UNIVERSITY OF
BIRMINGHAM

PRECIPITATION HARDENING IN AZ91 MAGNESIUM ALLOY

By

RUILIN ZENG

A thesis submitted to the University of Birmingham

for the degree of

DOCTOR OF PHILOSOPHY

School of Metallurgy and Materials

University of Birmingham

Edgbaston

Birmingham

B15 2TT

July 2013

PREFACE

The work described in this thesis was carried out by the author in the School of Metallurgy and Materials, the University of Birmingham from Sep. 2009 to Jul. 2013, under the supervision of Dr. Yulung Chiu and Prof. I.P. Jones.

The present work is original and no part of this work has been submitted for a degree at any other university. Wherever others' work has been drawn or cited, it is acknowledged in the text and a list of references is included at the end of this thesis.

Part of the present work has been published as follows:

R. Zeng, Y. Chiu, I. P. Jones, Characterisation of nano-sized Al–Mn–(Mg) particles in AZ91 and their effect on $Mg_{17}Al_{12}$ precipitation, Journal of Alloys and Compounds 579 (2013) 34–38.

ACKNOWLEDEGEMENTS

The author is grateful to my supervisors, Dr. Y. L. Chiu and Prof. I. P. Jones, for their constant supervision, guidance and encouragement. Their vast acknowledge and experience was of considerable importance in helping me understand this project and transmission electron microscopy. They provided excellent support and sound advice and lots of good ideas during the research.

Several other people have made brief but important contribution to my research. In particular I would like to thank Dr. R. Ding, Dr. M. Chu and Dr. Y. Tse for helping me on the TEM and STEM operation skills.

My EM group members and all other friends in School of Metallurgy and Materials have ensured a pleasant working environment as well as being the source of many discussion on the practical aspect of my PhD research. All of the support is of great appreciation.

My appreciation also goes to the financial support from the School of Metallurgy&Materials and China Scholarship Council (CSC). These have helped me a lot to devoting all my time to this research work.

To my parents, my girlfriend and my brother.

ABSTRACT

The microstructure evolution of a sand cast AZ91 magnesium alloy during heat treatment (solution treatment and subsequent ageing) were characterized quantitatively using a combination of optical microscopy (OM), scanning electron microscopy (SEM) and transmission electron microscopy (TEM). The area fraction of discontinuous precipitates and number density of continuous precipitates (N_V) in the AZ91 alloys with and without pre-deformation were measured using OM and TEM, respectively. Based on these metallurgical evidences, the existing precipitation strengthening mode for AZ91 was modified and the effect of pre-deformation on the precipitation strengthening of AZ91 was investigated. Meanwhile, attention was also paid to the low N_V of CPs in AZ91 compared with current Al alloys.

Al-Mn-(Mg) particles in the size range of 20-200 nm have been found in the as-cast AZ91. Their morphologies, chemical composition and structures were investigated using TEM. It was found that these particles have a chemical composition of $(Al_{6.52}Mn)_{1-x}Mg_x$ ($x < 0.13$) and a decagonal quasi-crystalline structure. These particles were stable during a solution treatment at 420 ℃ for 72 h and acted as preferential nucleation sites for continuous $Mg_{17}Al_{12}$ precipitates during the subsequent ageing. The potential effect of these Al－Mn－(Mg) particles on the strengthening of AZ91 magnesium alloys is discussed.

The results obtained using two electron tomography (ET) approaches were also summarized in this thesis. One uses HAADF-STEM for $Mg_{17}Al_{12}$ precipitates on Al-Mn-(Mg) particles. In this part, the attachment between $Mg_{17}Al_{12}$ and Al-Mn-(Mg) particles and rod shape of the Al-Mn-(Mg) particles were confirmed. Various projections of these particles in conversional

2D TEM observation are explained using the 3D information obtained and the reason for various shapes of the projections is also discussed. The other technique is BF-STEM applied to study $Mg_{17}Al_{12}$ precipitates on the dislocations. In this part, a diffraction alignment technique was used to obtain the 3D morphology of dislocations at the same time as the $Mg_{17}Al_{12}$ precipitates. Combined with 2D TEM information, some W-shaped dislocations are proved to have a spiral morphology composed of a number of basal and non-basal segments. The formation of such a morphology is probably related to the difference in the dislocation mobility between the basal and non-basal segments. However, $Mg_{17}Al_{12}$ precipitates are not reconstructed well in these two tomograms; the reasons are discussed and some suggestions are given to improve the tomograms.

Contents

Chapter 1 Introduction 1
Chapter 2 Literature review 4
2.1 Magnesium 4
2.1.1 History 4
2.1.2 Atomic properties 4
2.1.3 Structural properties 5
2.1.4 Mechanical properties 5
2.1.5 Deformation behaviour 5
2.2 Magnesium alloys 7
2.3 AZ91 7
2.3.1 Chemical composition 8
2.3.2 Mechanical properties 8
2.3.3 Microstructure evolution during heat treatment 9
2.3.4 Continuous and discontinuous precipitation (CP and DP) 10
2.3.5 Strengthening mechanism in AZ91 12
2.3.6 Pre-deformation and Precipitation 16
2.4 Aluminium alloys and their precipitation hardening 17
2.4.1 Aluminium and its alloys 17
2.4.2 Precipitation hardening in aluminium alloys 18
2.5 Al-Mn intermetallics in Mg-Al alloys 20
2.6 Quasicrystals 20
2.6.1 Structure and morphology 20
2.6.2 Composition and preparation 22
2.6.3 Physical properties of QC 22
2.6.4 Applications of QCs 23
2.7 Electron tomography 25
2.7.1 Tomography 25
2.7.2 Electron tomography 26
2.7.3 Limitations of electron tomography 26
2.7.4 Applications of electron tomography 28
2.8 Aims and objectives 30
Chapter 3 Experimental 57
3.1 Raw materials 57
3.2 Processing of materials 57
3.2.1 Route I 57
3.2.2 Route II 58

3.3 Microstructure characterisation 58
3.3.1 Optical microscopy (OM) 58
3.3.2 Scanning electron microscopy (SEM) 59
3.3.3 Transmission electron microscope (TEM) 60
3.4 Electron tomography 61
3.5 Hardness measurement 63
3.6 Particle number density 63
3.6.1 Thickness measurement 64
3.6.2 Counting the number of precipitates 65
Chapter 4 Precipitation hardening of deformed and undeformed AZ91 75
4.1 Introduction 75
4.2 As cast AZ91 (as-received) 75
4.3 Solution treated AZ91 76
4.4 Precipitation hardening of undeformed AZ91 77
4.4.1 Hardness 77
4.4.2 Discontinuous precipitation 77
4.4.3 Continuous precipitation 78
4.4.4 Thickness 80
4.5 Precipitation hardening of AZ91 after deformation 81
4.5.1 As-rolled samples 81
4.5.2 Hardness 82
4.5.3 Discontinuous precipitation 83
4.5.4 Continuous precipitation 83
4.5.5 Precipitates on twin boundaries 84
4.6 Discussion 84
4.6.1 The number density of continuous precipitates (Nv) 84
4.6.2 The calculated strength of AZ91 90
4.6.3 The number density of precipitates in AZ91 and Al alloys 93
4.6.4 Effect of pre-deformation on the precipitation hardening 95
4.7 Conclusions 98
Chapter 5 Characterisation of nano-sized Al-Mn-(Mg) particles in AZ91 and their effect on $Mg_{17}Al_{12}$ precipitation 134
5.1 Introduction 134
5.2 Precipitation of CP on the nano-sized particles containing Al and Mn 135
5.3 Chemical composition of nano-sized particles 136
5.4 Morphology and structure 138
5.5 Discussion 139

5.5.1 Morphology and structure of the Al-Mn-(Mg) particle 139
5.5.2 Quantitative chemical composition 140
5.5.3 EDX and SAD of nano-sized particles 141
5.5.4 Potential effect on the strength of AZ91 143
5.6 Conclusions 144
Chapter 6 3D TEM characterization of $Mg_{17}Al_{12}$ precipitation on Al-Mn-(Mg) particles and dislocations in AZ91 155
6. 1 Introduction 155
6.2 3D TEM characterisation of joined Al-Mn-(Mg)-CP particles 156
6.3 3D characterization of the continuous precipitates on dislocations 159
6.4 Discussion 164
6.4.1 The projections of Al-Mn-(Mg) particles 164
6.4.2 Deficiencies in the HAADF tomography 165
6.4.3 3D dislocation network 166
6.4.4 Problems in dislocation tomography 168
6.5 Conclusions 169
Chapter 7 Conclusions and suggestions for future work 188
7.1 Conclusions 188
7.2 Suggestions for further work 192
Appendices 195
Appendix A: Symmetry restriction of crystals 195
Appendix B: How to tilt nano-sized Al-Mn-(Mg) particles 198
Appendix C: Design of TEM tomography holder 205
References 207

Chapter 1 Introduction

The demand for reducing fuel consumption and CO_2 emission from engines calls for a range of lightweight alloys. Magnesium is the lightest of all the metals used for construction. Its alloys have excellent specific strength and stiffness, exceptional dimensional stability, high damping capacity and recyclability. Therefore, magnesium has been widely used in the transportation industry over past decades [1-4].

Magnesium must be alloyed with other metals for engineering applications. The most popular commercial magnesium alloys include AZ series (Mg-Al-Zn), AM series (Mg-Al-Mn), AE (Mg-Al-RE), EZ (Mg-RE-Zn), ZK (Mg-Al-Zr) and WE (Mg-RE-Zr) [1, 4]. Among the various magnesium alloys developed, AZ91, containing about 9 wt.% Al and 1 wt.% Zn, is the most widely used, not only for making automotive components but also for other structural components because of its combination of excellent castability and reasonable mechanical properties at room temperature with good corrosion resistance. About 90% of the magnesium cast products currently used are made of AZ91 [3].

The precipitation hardening response of AZ91 results from $Mg_{17}Al_{12}$ precipitates and is weaker than for many heat treatable aluminium alloys. The main reason for the poor hardening effect is that the number density of precipitates (N_V) in AZ91 is much lower than that in these aluminium alloys. This has been reported in some researches on AZ91 [5, 6], but few studies explain the reason for the low N_V. It could be beneficial to increase N_V in AZ91 and thus improve its precipitation hardening.

Recently, electron tomography (ET), a technique which was pioneered originally for imaging

three dimensional (3D) structures in life sciences, has been modified for the analysis of inorganic materials [7]. Since it is difficult to understand some fine features, such as particles and dislocations, completely via two dimensional observations, it is of our interest to study them in 3D.

This project focuses on two $Mg_{17}Al_{12}$ precipitation modes in AZ91. One is along dislocations and the other is on nano Al-Mn-(Mg) quasicrystal (QC) particles. Firstly, some issues concerning the precipitation hardening of undeformed AZ91 will be considered, including the modification of the precipitation hardening model and the reasons for low N_V. Secondly, the precipitation hardening response of deformed AZ91 will be studied quantitatively. Thirdly, the newly discovered Al-Mn-(Mg) QC particles and $Mg_{17}Al_{12}$ precipitation on them will be characterized. Finally, electron tomography will be used to characterise the two preferential precipitation modes in 3D.

The outline of the thesis is as follows:

Chapter 2 presents an overview of the literature on precipitation and strengthening in AZ91 and an introduction to electron tomography and quasicrystals.

Chapter 3 summarizes the materials and methods used in the current study.

Chapter 4 describes the precipitation hardening of the deformed and undeformed AZ91 and discusses a modification to the existing strengthening model, the reasons for low N_V and the effect of pre-deformation on ageing of AZ91.

Chapter 5 characterises the newly discovered Al-Mn quasicrystal particles in AZ91 and $Mg_{17}Al_{12}$ precipitation on these particles.

Chapter 6 presents the electron tomography of $Mg_{17}Al_{12}$ precipitates on nano Al-Mn-(Mg) quasicrystal (QC) particles and dislocations. The 3D morphologies of these particles and dislocations will be discussed.

Chapter 7 draws some conclusions and gives some suggestions for future work.

Chapter 2 Literature review

2.1 Magnesium

2.1.1 History

The history of magnesium starts in 1755, when it was discovered as a new element in magnesia. Magnesium could not be isolated until Sir Humphrey Davy extracted the metal successfully by decomposing wet magnesium sulphate by electrolysis in 1808. Before 1945, magnesium was mostly used as powder or ribbon for flashlights in military and other pyrotechnical purposes. After World War II, magnesium industry declined, because the producers failed to find an economical way to extract the metal to make its price competitive with that of aluminium [8, 9]. In recent years, magnesium alloys have enjoyed a renaissance in many manufacturing industries, such as the automotive and aerospace industries, since the need for reducing fuel consumption and CO_2 emission calls for light weight structural materials. Meanwhile, much research on magnesium has been carried out to improve its strength, corrosion resistance and creep resistance at elevated temperatures [1, 4, 10].

2.1.2 Atomic properties

Magnesium is number 12 in the periodic table of the elements. The isotopes 24, 25 and 26 exist naturally with a ratio of around 7:1:1, therefore, giving an atomic weight 24.32. The twelve orbital electrons in the free atom occupy the states $1s^2 2s^2 2p^6 3s^2$. The x-ray emission lines K_α and K_β are at 9.889 Å and 9.558 Å respectively. The K-absorption edge for x-rays is 9.512 Å [11].

2.1.3 Structural properties

Liquid magnesium freezes to hexagonal close-packed crystals at 650 ℃ with a density increase of about 4%. The lattice parameters of pure magnesium at room temperature are: a = 0.32092 nm and c = 0.52105 nm. The c/a ratio is 1.624 which is close to the ideal value of 1.633. Therefore, magnesium is considered as perfectly close packed [11]. The principal planes in the magnesium unit cell are shown in Figure 2.1 [11] and listed in Table 2.1[11].

2.1.4 Mechanical properties

The mechanical properties of pure magnesium are listed in table 2.2 [9]. The strength of pure magnesium is too low for most industrial applications. Therefore, magnesium is usually alloyed with other elements to improve its mechanical properties, as well as its corrosion resistance [9]. The major alloying elements used in magnesium alloys include aluminium, beryllium, zinc, silicon and calcium.

2.1.5 Deformation behaviour

According to von Mises [12] more than 5 independent slip systems must operate for polycrystals to deform uniformly and without failure at grain boundaries. Magnesium has a close packed hexagonal structure and the number of independent basal slip systems is thus less than that required. It is necessary that other non-basal slip systems are activated or that deformation occurs by twinning [9].

2.1.4.1 Plastic Deformation by Slip

Slip can be defined macroscopically as the irreversible shear of part of a crystal with respect to another under a shear stress without the breaking of a large number of inter-atomic bonds

(fracture) or changing the crystallographic orientation (twinning) [11]. In the HCP structure, the shortest slip vector preserving the ABAB close-packed plane stacking is $\frac{a}{3}\langle 11\bar{2}0\rangle$. Its strain energy can be reduced by the dissociation of the basal dislocations into two partial dislocations with slip vectors $\frac{a}{3}\langle 10\bar{1}0\rangle$. A stacking fault is produced as a narrow ribbon and separates the two partial dislocations. The distance between these two partials is determined by the stacking fault energy γ, which varies with material [11]. Seeger estimated its value in magnesium to be in the range 0.2-0.4 J/m^2 [13]. This leads the distance between these two partials to be of the order of atoms.

Apart from basal $\frac{a}{3}\langle 11\bar{2}0\rangle(0001)$ slip, first order prismatic slip, $\frac{a}{3}\langle 11\bar{2}0\rangle\{10\bar{1}0\}$, and first order pyramidal slip, $\frac{a}{3}\langle 11\bar{2}0\rangle\{10\bar{1}1\}$, also play a significant role in the deformation behaviour of hcp metals and their alloys. Meanwhile, first order pyramidal slip system, $\frac{1}{3}\langle 11\bar{2}3\rangle\{10\bar{1}1\}$, and second order pyramidal slip system, $\frac{1}{3}\langle 11\bar{2}3\rangle\{11\bar{2}2\}$,with a $\langle \vec{c} + \vec{a}\rangle$ slip direction can also operate to accommodate the strain along c-axis. In order to improve the plasticity of magnesium, it is necessary to increase the activity of these slip systems.

2.1.4.2 Deformation Twinning

Due to the limitation of dislocation slip in HCP, twinning is common in the deformation of magnesium. The most common twins in magnesium are $\{10\bar{1}2\}\ \langle 10\bar{1}1\rangle$, also called “tension” twins. This twinning system only operates when deformation gives an extension along the c-axis [14]. When there is compression along the c-axis, another twinning called “contraction” twins or “compression banding” would operate. This twinning system can be a complex doubly twinned structure [15], which is a nucleation of secondary twins inside the primary

twin domains.

2.2 Magnesium alloys

Magnesium alloys can be categorised according to the alloying elements and are named based on the conventions defined by the American Society for Testing and Materials (ASTM). This naming method is a three-part letter-number-letter system [16]. An example of such an alloy designation is shown in Figure 2.2. The first part consists of letters indicating the two principal alloying elements listed in order of decreasing alloying content as shown in Table 2.3 [16]. The second part consists of the weight percentages of these two elements rounded off to the nearest whole number and listed in the same order as the code letters. The third part consists of an assigned letter beginning with "A" to distinguish between alloys having the same nominal designation. Sometimes a letter plus a digit follows to indicate the Temper designation of the alloy.

In terms of processing, magnesium alloys can be divided into cast and wrought alloys. Wrought alloys are initially cast as ingots or billets and subsequently hot or cold worked mechanically into the desired form. Cast alloys are cast directly into their final form by one of the various methods such as sand-casting, die or pressure die casting. Casting is used for complex product shapes. The main commercial magnesium alloys include the AZ series (Mg-Al-Zn), AM series (Mg-Al-Mn), AE series (Mg-Al-RE), EZ series (Mg-RE-Zn), ZK series (Mg-Zn-Zr) and WE series (Mg-RE-Zr) [4].

2.3 AZ91

Among the various magnesium alloys developed, AZ91, containing about 9 wt.% Al and 1 wt% Zn, is the most popular commercial magnesium alloy. Statistically, more than 90% of

magnesium cast products are made of this alloy [1, 3].

2.3.1 Chemical composition

Aluminium is used to enhance the corrosion resistance and strength of magnesium alloy [10, 11]. According to the Mg-Al phase diagram shown in Figure 2.3 [6], aluminium is soluble up to 12 wt% in magnesium at 430℃, but only up to 3.2 wt% at 200℃. This introduces a large volume fraction of β-$Mg_{17}Al_{12}$ precipitates, which can act as a barrier to deformation. Meanwhile, the aluminium atoms in solution in the magnesium matrix also improve the strength of this alloy.

In AZ91, zinc usually takes the place of Al in $Mg_{17}Al_{12}$ in AZ91, creating a ternary intermetallic compound $Mg_{17}(Al,Zn)_{12}$ [17]. Thus, AZ91 can be treated as a Mg-Al binary alloy, as shown in Figure 2.3[18].

Meanwhile, a small amount of manganese is added to improve the corrosion resistance by removing iron [1], but manganese combines easily with aluminium and forms various Al-Mn intermetallic phases. This will be summarized in detail in §2.4.

2.3.2 Mechanical properties

With its 9 wt% aluminium, 1 wt% zinc and a small amount of manganese, AZ91 exhibits a good combination of excellent castability with reasonable mechanical properties at room temperature. Typical room-temperature mechanical properties of cast AZ91 are listed in Table 2.4[16]. However, at temperatures above 130℃, its strength decreases significantly. This is probably due to the poor thermal stability of $Mg_{17}Al_{12}$ precipitates at elevated temperatures [3, 5, 6].

2.3.3 Microstructure evolution during heat treatment

Aluminium is fully miscible with molten magnesium [9]. There are three steps in the formation of the microstructure of as-cast AZ91. Firstly, α-Mg nucleates at 600℃ and grows dendritically during solidification, forming primary α-Mg. Secondly, a divorced eutectic reaction takes place, forming eutectic α-Mg and β_{-eut} ($Mg_{17}Al_{12}$) due to the non-equilibrium solidification. After solidification, when the cooling rate of the casting is sufficiently slow, discontinuous precipitation (lamellar β $Mg_{17}Al_{12}$ precipitates) occurs within the eutectic α-Mg phase in regions adjacent to the β_{-eut} phase. Thus, the as-cast AZ91 microstructure consists of the primary α-Mg grains, surrounding eutectic (containing eutectic α-Mg and β_{-eut} phase) and finally lamellar β precipitates. A typical as-cast AZ91 microstructure is shown in Figure 2.4 (a) [19]. In addition, some Al-Mn intermetallic compounds will form before the primary α-Mg, if Mn is added to AZ91 [20].

In order to redistribute the β phase, as-cast AZ91 needs to be heat treated. The conventional heat treatment involves solution treatment at about 420℃ for a minimum of 24 h, followed by ageing at a temperature between 100 and 300℃. As shown in Figure 2.4 (b) [21], solution treatment causes complete dissolution of the α + β eutectic, leaving only α-Mg matrix (supersaturated solid solution). During further ageing, β phase precipitation occurs in two ways: discontinuously and continuously. Figure 2.4 (c) [17] is a TEM bright field image showing both the continuous precipitates (CP) and discontinuous precipitates (DP) after heat treatment. Unlike the precipitation in Al alloys, no Guinier-Preston zones [22, 23]or other metastable phases are reported during the β phase precipitation.

2.3.4 Continuous and discontinuous precipitation (CP and DP)

β-phase ($Mg_{17}Al_{12}$) has a complex body-centred cubic (bcc) structure with lattice parameter a=1.056 nm (space group I-43*m*). One unit cell of β-phase contains 34 Mg atoms and 24 Al atoms [5].

2.3.4.1 Continuous precipitation

Continuous precipitation generally takes place within grains, preferentially at defects, such as vacancies and dislocations and therefore pre-deformation before ageing can accelerate continuous precipitation [24]. In addition, it is reported that a relatively high ageing temperature (623K) results in more CPs [25].

According to previous reports [5, 26], there are several types of continuous precipitates. Most of them are lath-shaped (so-called Widmänsttten morphology [27]) lying on the basal plane of the Mg matrix. They have a Burgers orientation relationship (OR) ($(0001)_m \parallel (011)_p$ and $[2\bar{1}\bar{1}0]_m \| [1\bar{1}1]_p$, [24, 28, 29]) with the matrix. A small number of them is rod-shaped. Their long axes are either parallel to $[0001]_m$ or at a certain angle to $[0001]_m$. The $[0001]_m$ rods are of the form $(1\bar{1}00)_m \parallel (1\bar{1}1)_p$ and $[0001]_m \parallel [111]_p$, which is identical to the Crawley OR [28]. Other rods have another orientation relationship $(0001)_m \parallel (1\bar{1}5)_p$ and $[10\bar{1}0]_m \parallel [110]_m$, which is the Porter OR [30]. Other ORs have also been reported in Mg-Al alloys, such as Gjönmes-Ostrmoe OR [31] and Potter OR [32].

These rod-shaped CPs are more effective than lath-shaped CPs at strengthening the alloy, since they can efficiently block basal slip [5, 6, 33]. According to Celotto [5], low temperature ageing, such as at 100℃, increases significantly the proportion of rod-shaped CP, but it takes a very long time (3 years in his particular case) to get the maximium hardening

response.

2.3.4.2 Discontinuous precipitation

Discontinuous precipitation is the cellular growth of alternating plates of the secondary and near-equilibrium matrix phase at high angle boundaries [21]. This heterogeneous reaction leads to the formation of a lamellar structure behind a moving grain boundary (also called reaction front, RF). Figure 2.5 (a) shows a possible way in which discontinuous precipitation takes place [27]. The discontinuous precipitates nucleate at the grain boundary, and then grow with the grain boundary migration. Such migration should be associated with production of more stable microstructure or reduction of interfacial energy [34]. In this precipitation case, the diffusion of solute via grain boundary is considered to be more efficient than that through the lattice, which makes the matrix composition right up to the advancing grain boundary remain unchanged [27]. This is confirmed by EELS (electron energy loss spectroscopy) across the advancing grain boundary in Figure 2.5 (b) [27]. Due to the discontinuous change of the matrix composition when passing the reaction front, this precipitation case is called discontinuous precipitation. In AZ91, discontinuous precipitates have the same orientation relationship (Burgers OR) with the matrix as most CPs [24, 28, 29]. Apart from the lamellar DPs, some globular precipitates are also reported, surrounding lamellae. These globular precipitates were proved to be $Mg_{17}Al_{12}$, but are completely non-coherent with the matrix [28]. The growth mechanism of these globular precipitates is still unknown.

2.3.4.3 Competition between CP and DP

CP and DP occur simultaneously and competitively over a wide range of ageing temperatures [21, 25]. The competition between CP and DP was studied by Duly *et al.* in Mg-Al alloys with different Al contents and at various ageing temperatures [35]. A map representing such

temperatures and compositions is shown in Figure 2.6. For AZ91, the temperatures dependence of the morphology is as follows:

When 100 ℃ $< T < T_{d1}$, both CP and DP are observed. The volume fraction of the sample occupied by DP increases with T;

When $T_{d1} < T < T_{d2}$, the whole sample is occupied by discontinuous precipitation;

When $T_{d2} < T < T_{c2}$, both CP and DP may again be observed.

When $T_{c2} < T < T_s$, T_s being the solvus temperature, the whole sample is occupied by continuous precipitation.

However, this result has not been fully confirmed by different experiments. According to the ageing (within 30 hours) on AZ91 in current work, both CP and DP were observed at 150 ℃, 200 ℃ and 250 ℃, and only CP were observed at 100 ℃. The former is in accordance with Figure 2.6, while the later is not.

2.3.5 Strengthening mechanism in AZ91

Several different strengthening mechanisms exist in AZ91, including grain size strengthening, solid solution strengthening, Orowan strengthening and continuum effect (work hardening) [6].

2.3.5.1 Grain size strengthening

The well-known Hall-Petch relation is used to express the grain size yielded strengthening of a polycrystalline material. For AZ91, a lot of work has been done to refine the grains by adding of various elements, such as Mn, Ca, RE and Zr [36].

$$\sigma_{gs} = \sigma_0 + kd^{-1/2} \quad \text{(Equation 2.1)}$$

where d is the grain size. The intrinsic lattice resistance to basal slip, σ_0, and k were estimated to be 11 MPa [37] and 0.37 MPam$^{1/2}$, respectively, by Caceres et al. [38].

2.3.5.2 Solid Solution strengthening

In Caceres and Rovera's investigation [39], the solid solution strengthening for a series of polycrystalline Mg-Al alloys with different Al contents was in good agreement with the single crystal data of Aktar and Teghtsoonian [40], when a Taylor factor of 5 is used for the polycrystalline aggregate. The solid solution strengthening is given by Equation 2.2, where X is the atomic fraction of solute and C is 197 MPa$X^{-2/3}$.

$$\sigma_{ss} = CX^{2/3} \quad \text{(Equation 2.2)}$$

2.3.5.3 Orowan strengthening

The interaction between dislocations and precipitates was firstly suggested by Orowan [41] in 1947. In his theory, a critical size was designated. Dislocations can shear through particles smaller than this size and bow around particles larger than this size. In AZ91, there is no experimental measurement of this critical size, but Hutchinson et al. [6] estimated a critical size for $Mg_{17}Al_{12}$ of around 3 nm using a force balance between the stress of a curved dislocation and the yield stress of the precipitates, as shown in Equation 2.3.

$$\frac{G_m\, b}{R} = \frac{G_P}{15} \quad \text{(Equation2.3)}$$

where G_m is the shear modulus of the matrix [42], G_P is the shear modulus of the precipitates [42], b is the Burgers vector and R is the radius of curvature of the dislocation.

Since this critical size is smaller than that of $Mg_{17}Al_{12}$ precipitates in AZ91, dislocations will

tend to bow around the precipitates and form "Orowan loops" instead of shearing through the precipitates. In the case of the bowing of dislocations, the Orowan stress for a spherical particle is [43]

$$\sigma_{Orowan} = \frac{MGb}{2\pi\sqrt{1-\nu}} \frac{1}{\lambda} \ln\left(\frac{d_A}{r_0}\right) \quad \text{(Equation 2.4)}$$

where M is Taylor factor (taken as 5 in [6]); G is the shear modulus of the matrix; b is the Burgers vector of the dislocation; ν is Poisson's ratio; λ and d_A are, respectively, the mean spacing and mean diameter of particles in the slip plane and r_0 is the inner cut-off radius of the dislocation, taken equal to b.

In AZ91, Hutchinson et al. approximated $Mg_{17}Al_{12}$ precipitates as elliptical discs with a length/width (l:w) aspect of 4 and got $d_A = \frac{3.6w}{2}$ [6]. Within the (0001) plane, the mean particle spacing, $\boldsymbol{\lambda}$, can be expressed as:

$$\lambda = \frac{1}{\sqrt{N_V t}} - d_A = \frac{1}{\sqrt{N_V t}} - \frac{3.6w}{2} \quad \text{(Equation 2.5)}$$

where t is the particle thickness. Therefore, the contribution from the precipitation hardening can be obtained by measuring the number density and size of the particles.

2.3.5.4 Continuum effect (work hardening)

Typical magnesium alloys show an extended elastic-plastic transition, generally with no well-defined yield point in standard tensile tests. This is because that during deformation of aged AZ91, the different deformation behaviours of the matrix and precipitates result in the development of an internal stress in the matrix, which opposes further flow. This issue was investigated by Brown and Clark [44]. They concluded that in the absence of plastic

relaxation, the internal stress is proportional to the particle volume fraction, Young's modulus of the precipitate and the applied plastic strain, as shown in Equation 2.6:

$$\sigma_{Backstress}=E^{\beta}\ V_f^{\beta}\varepsilon \qquad \text{(Equation 2.6)}$$

2.3.5.5 Total calculated strength

After combining together these different strengthening values, Hutchinson et al. [6] compared the calculated strength and the reported experimental results and found they are in good agreement, as shown in Figure 2.7. This result also indicates the poor precipitation-hardening response of AZ91.

Compared with most precipitation-hardenable Al alloys, AZ91 has a considerable precipitate volume fraction but presents a low tensile strength [5, 6]. Celotto [5] attributed this to the low number density of $Mg_{17}Al_{12}$ precipitates. He measured the number of continuous precipitates per unit volume, N_v, at different ageing temperatures for different ageing times and found N_v in most samples is between 10^9 and $10^{10}mm^{-3}$, which is much less than that of most Al alloys. A comparision of N_v between AZ91 and 7075, a typical precipitation-hardenable Al alloy, is shown in Table 2.5 [6]. Nie [33] shows that another reason for this poor precipitation hardening is the basal orientation of the $Mg_{17}Al_{12}$ precipitate plates, which increases the effective inter-particle spacing and results in a low Orowan increment.

Both Celotto [5] and Hutchinson et al. [6] listed several ways to enhance the precipitation hardening response of AZ91. (1) Micro-alloying: new alloying elements may dope the precipitates and vary their lattice parameter to change the basal orientation of the $Mg_{17}Al_{12}$ laths. (2) Pre-deformation after solid solution: Based on the preferential nucleation of CP on dislocations, this method will introduce dislocations and provide more heterogeneous nucleation sites for $Mg_{17}Al_{12}$ precipitates.

Apart from these two methods, some recent studies reported that the addition of well distributed particles [45, 46] and a quasicrystal-containing magnesium-based master alloy [47] can improve the precipitation strengthening of AZ91. Both of them introduce extra dispersed particles with heat resistance, resulting in enhancement of strength at both room and elevated temperatures.

2.3.6 Pre-deformation and Precipitation

As mentioned above, cold deformation prior to ageing in precipitation-hardenable alloys is a useful way to tailor their microstructure and enhance their precipitation hardening response. This method is widely used in aluminium alloys. Many quantitative investigations have been carried out on the effect of pre-deformation on the microstructure and mechanical properties of various aluminium alloys [48-53]. In these cases, the pre-deformation accelerates the precipitation, leading to an earlier ageing peak and a more dispersed and uniform distribution of precipitates. This results in an increase in hardness and tensile strength. However, pre-deformation decreases the ductility and excessive pre-deformation causes coarsening and a heterogeneous distribution of precipitates, which reduces the strength of the alloy. Therefore, an optimum pre-deformation is often defined for a given alloy under a given conditions [52].

Compared with these aluminium alloys, AZ91 exhibits a relatively low ageing hardening effect and this may be improved by pre-deformation, as suggested by Celotto[5], Nie [33] and Hutchinson et al. [6]. However, the reported research work on the effect of pre-deformation on precipitation in AZ91 is meagre. To the author's knowledge, there are only two papers relevant to this study. One was by Clark in 1968 [24]. He found that continuous precipitation occurs along the dislocations introduced by pre-deformation. 5% rolling can accelerate the precipitation of AZ91 but only increase its peak hardness by 5%. The other paper is by Duly

in 1995 [54], who concluded that the twinning produced in the pre-deformation can restrict the growth of DPs and be helpful for continuous precipitation. So far, there are no detailed hardness measurements or quantitative precipitate analysis for ageing of pre-deformed specimens.

2.4 Aluminium alloys and their precipitation hardening

As another popular group of light alloys, many aluminium alloys are also strengthened by precipitation. Thus these aluminium alloys often compare and compete with magnesium alloys in industry. In the current work, the reason for the poor precipitation hardening of AZ91 alloys (compared with popular precipitation-hardenable aluminium alloys) is discussed. Therefore, it is worth introducing the aluminium alloys and their precipitation hardening first.

2.4.1 Aluminium and its alloys

Similar to magnesium, pure aluminium in the annealed condition presents a low yield strength (7-11MPa) [55] and need to be alloyed with other elements. Mg, Cu, Zn and Si, which have sufficient solid solubility are the most commonly used alloying elements in aluminium alloys. Cr, Mn and Zr are also used, primarily to form compounds which control the microstructure.

Similar to magnesium alloys, aluminium alloys are also namely classified into wrought alloys and cast alloys. Both of them can be further designated by a four digit number defined from AAA (Aluminium Association of America) [56]. This classification is adopted by the International Alloy Development System (IADS) and by most of the countries in the world [56]. The first digit specifies the major alloying element(s) and their atomic symbol(s) are shown in Table 2.6 and 2.7 [56].

According to the heat treating status, the aluminium alloys can be also divided into two groups: heat-treatable and non heat-treatable [55]. Heat treatable alloys usually refers to the alloys which can be strengthened by heat treatment. When this term is used for aluminium alloys, it refers to the alloys which can be strengthened significantly by precipitation. Heat-treated aluminium alloys are required to have (a) a decreasing equilibrium solid solubility with decreasing temperature; (b) precipitation of coherent/partially coherent phase by decomposition of the supersaturated solid solution [55, 56].

2.4.2 Precipitation hardening in aluminium alloys

Although there are various aluminium alloys, only these heat-treatable wrought aluminium alloys (2xxx, 6xxx and 7xxx) have sufficient strength for structural components in aerospace applications. Table 2.8 shows the mechanical properties of some representing precipitation-hardening aluminium alloys together with AZ91 [27]. There are various strengthening mechanisms in these alloys, including solution strengthening, grain boundary strengthening, precipitation strengthening and work hardening, but precipitation hardening usually plays the most important role.

Precipitation in these commericial aluminium alloys usually starts with the formation of GP zones [22, 23], which are considered as fully coherent metastable precipitates and have a very low interfacial energy. Subsequent evolution of the microstructure involves the precipitation of other transition phases to replace the GP zones and the formation of equilibrium phases. Table 2.9 shows the precipitation sequences of several aluminium alloys [27]. The classic example of such multi-stage precipitation is the precipitation sequence in Al-Cu alloys. The whole precipitation process can be written [27]:

$$\alpha_0 \rightarrow \alpha_1 + \text{GP zones} \rightarrow \alpha_2 + \theta'' \rightarrow \alpha_3 + \theta' \rightarrow \alpha_4 + \theta$$

where α_0 is the composition of the matrix in the original supersaturated solid solution, α_1 is the composition of the matrix in equilibrium with GP zones, α_2 is the composition of the matrix in equilibrium with θ" and so on. The Al-Cu phase diagram with the metastable GP zone, θ", θ' and θ solvuses is shown in Figure 2.8.

Transition phases (θ" and θ') form, because their activation energy barrier for nucleation is lower than that of the equilibrium phase and the free energy of the alloy is reduced more rapidly via the transition phase than by direct transformation to the equilibrium phase. Taking Al-Cu for example, the GP zones form as the first precipitates because they are fully coherent with the matrix and therefore have a low interfacial energy. The crystal structures of θ", θ' and θ in comparison with the matrix are shown in Figure 2.9. θ" has a tetragonal unit cell which is essentially a distorted fcc structure. Compared with the atomic structure of the matrix, the (001) planes of θ" are identical, and (010) and (100) are very similar. There is only a small mismatch in the [001] direction. θ' is also tetragonal and its (001) planes that are identical with the {001} of α, but its (100) and (010) planes are different from those of the matrix. The equilibrium θ has a complex body-centred tetragonal structure and there are no planes having good match with the matrix, so the interfaces between θ and the matrix are almost incoherent or at best semi-coherent [26]. It is found that θ" are nano-sized (10-100nm) and have a fine distribution. Both θ' and θ are μm sized and distribute sparsely [27]. Figure 2.10 shows the relationship between the microstructure and properties of an Al-Cu alloy during ageing. It is noted that the peak hardness corresponds to the formation of θ" and the hardness decreases with the precipitation of coarse θ' and θ [27]. This relationship between the fine distribution of precipitates and the peak hardness exists in many other Al alloys, such as Al-Zn, Al-Mg and Al-Ag.

2.5 Al-Mn intermetallics in Mg-Al alloys

As mentioned in 2.3.1, Mn is usually added to AZ91 to enhance the corrosion resistance, which is also common in other Mg-Al based alloys. This leads to various Al-Mn intermetallic phases in these alloys, since Al combines easily with Mn [45, 46, 57-59]. Table 2.10 [59] summarizes these reported Al-Mn intermetallic phases. As shown in Table 2.10, these Al-Mn phases are often 0.1 ~ 30 μm in size and present various morphologies [59]. Apart from the corrosion resistance, it has been reported that some Al-Mn intermetallic compounds, such as the hcp ε-AlMn phase, can be favourable sites for heterogeneous nucleation of the α-Mg grains and thereby reduce the grain size [58]. However, most of them are μm sized and located at grain boundaries, which is often detrimental to plasticity. Therefore, on balance, they are detrimental to the mechanical properties of the alloys.

2.6 Quasicrystals

All the Al-Mn compounds mentioned in the previous section are crystalline, but quasicrystals (QC) are also widely reported in rapidly cooled Al-Mn alloys [60-66]. QC is a third form of solid matter apart from crystalline and amorphous [66]. The discovery of QC in 1984 provoked a lot of research on the structure, properties and applications of these "new materials.

2.6.1 Structure and morphology

A crystal is defined as a three-dimensional periodic arrangement of atoms with translational periodicity along its three principal axes. Thus it is possible to obtain an infinitely extended crystal structure by aligning unit-cells until space is filled [67, 68]. A crystal can possess only certain symmetries (one fold, two fold, three fold, four fold and six fold) because there are a

limited number of ways that identical unit cells can be assembled to form a solid (detailed proof shown in Appendix 1). Diffraction patterns, produced either by X-ray, electron or other rays and particles are used to identify crystallographic point symmetries [69].

In 1982, Schechtman and his colleagues obtained an electron diffraction pattern with five-fold rotation symmetry from a rapidly cooled Al-Mn alloy, which marked the discovery of quasicrystals [60]. Since then, not only a large number of QCs have been found in various multi-component alloy systems, which are refered as “hard QCs”, but also an increasing number of “soft QCs” have been identified recently with self-assembled quasiperiodic structures, such as structures of supramolecular dendrimer and ABC star terpolymers on the mesoscale [70]. Although the atomic structure of quasicrystals has not been well understood so far, several models, such as Penrose tiling [71], have been proposed. In summary, we can state with confidence that quasicrystals are materials with perfect long-range order, but with no three-dimensional translational periodicity. The former is manifested in the occurrence of sharp diffraction spots and the latter in the presence of a non-crystallographic rotational symmetry [72].

According to their quasi-periodicity in three dimensions, QCs can be classified into three types: The first type is three dimensional QCs, also known as the icosahedral. They are quasi-periodic in three dimensions with twelve five-fold, twenty three-fold and thirty two-fold symmetry axes. The second type is two dimensional QCs with axes of eight, ten or twelve-fold symmetry (octagonal, decagonal and dodecagonal phases, respectively), They are periodic along these axes and quasiperiodic in the other two perpendicular directions. The third and last type is one dimensional QCs (trigonal and digonal QC). They are only quasiperiodic along a single direction and periodic along all other directions [73, 74].

Among these intermetallic QCs, the icosahedral (IQC) and decagonal (DQC) ones are the most common. Figure 2.11 (a) and (b) show the morphologies of single grain of an IQC and a DQC, respectively [75, 76]. As shown in Figure 2.11 (b), the ten fold symmetry axis (also known as "decagonal axis") is generally perpendicular or inclined to the quasiperiodic layers. Due to such a "periodic stacking of quasiperiodic layers" structure, the DQCs are generally needle-like or rod-like [70].

2.6.2 Composition and preparation

In many early researches on QCs, most QCs were generally obtained by rapidly cooling binary alloys. For example, the first IQC [60] and DQC [61] were found in Al-Mn and the first dodecagonal phase was produced in the Ni-Cr system [77]. They are metastable and convert into a normal crystal when heated up to certain temperatures. Later on, a large number of stable QCs were found in ternary and quaternary alloys under normal casting conditions. Most of them were ternary intermetallic compounds containing Al [70]. In a recent research, a new family of QCs has been discovered in Mg-Zn-RE alloys cast into metallic moulds. These QCs are stable, finely distributed and finely-sized [78-81]. Table 2.11 summarizes QCs with various chemical compositions in different systems [68, 72].

The preparation methods for metastable QCs can be classified into two categories. One is rapid cooling, such as melt spinning and vacuum evaporation; the other is solid state inter-diffusion, such as crystallization of an amorphous glass [82]. Stable QCs usually form in the second way.

2.6.3 Physical properties of QC

Due to their unique structures, QCs have unusual physical properties different from

crystalline and amorphous phases. Table 2.12 shows a comparison of various physical properties between selected QCs and relevant conventional materials at room temperature [68].

In the hardness section, it is shown that QCs are hard. QCs also present a low coefficient of friction, which suggests that QCs can potentially be used as a low friction coating in industry. Finally, the Young's modulus of QCs, which reflects their elasticity, is comparable with those of conventional metals.

Compared with their mechanical properties, the transport properties of QCs are rather surprising, as shown in Table 2.12. Although most QCs are binary and ternary alloys of metallic elements, they exhibit poor thermal conductivity. The thermal conductivity of QC containing more than 70 at.% aluminium is two orders of magnitude lower than that of aluminium. This suggests that they can probably be used as a thermal barrier.

Finally, some surface properties of QCs also have drawn a lot of attention. Table 2.12 shows the surface energy of selected QCs and some benchmark materials. Compared with typical metals, the surface energies of QCs are low and comparable with that of PTFE, a coating material resistant to water, oil and dust. Meanwhile, some QCs, such as i-Al-Pd-Mn and i-Al-Cu-Fe, are resistant to oxidation [83].

2.6.4 Applications of QCs

Given such special properties, QCs, nowadays, are not of academic interest only, but are also ready to be applied by industry. The three main current applications are listed below [83, 84].

2.6.4.1 Surface coating

As mentioned previous section, QCs have a good combination of desirable physical

properties for a surface coating, including high hardness, low coefficients of friction and surface energy, good resistance to oxidation and low thermal and electrical conductivity. The most well-known example is a QC coating for frying pans. A French company called Sitram has sold these QC coated frying pans [85].

2.6.4.2 Alloy strengthening

Qualitative research reported that lots of nano-sized QC precipitates are found in steel, Al and Mg alloys [47, 78-81, 86]. Since QCs are generally hard and difficult to be sheared or cut by dislocations, they produce a high strength for those alloys. On the other hand, probably due to their low surface energy, they are resistant to coarsening during prolonged tempering. This makes these alloys resistant to over-ageing. The first application of these QC strengthened alloys is in some steel medical instruments produced by Sandvic-Steel in the 1990s. After decades of research on QC strengthened alloys, many such materials are, nowadays, available [85].

2.6.4.3 Energy storage and absorption

Besides applications based on their mechanical properties, potential uses in hydrogen storage and as solar aborption materials have also been explored recently. It is reported that the titanium QCs, such as Ti-Zr-Ni, have a good combination of a hydrogen-favoured chemistry and a structural unit with lots of tetrahedral sites. Ti-Zr-Ni QCs can store nearly double the weight of hydrogen as $LaNi_5$, which is used in the rechargeable batteries in laptops. In addition, the potential of QCs for solar selective absorbers has been highlighted by some researchers. Eisenhammer in Germany reported that a thin-film stack, composed of a layer of Al-Cu-Fe between two layers of dielectric alumina, deposited on a reflective metal, achieved a good combination of a high solar absorbance and a low emittance [85].

Despite the properties and applications described above, more effort can be made on new avenues for QC research, such as introducing fine QC particles into commercial alloys and exploring the growth of different QCs by three dimensional techniques. As a “novel material” with various specific properties, exciting developments for QCs are ahead.

2.7 Electron tomography

Conventional TEM and STEM are powerful tools for imaging micro- and nano-scale features in materials science, but they only provide 2D projections of 3D features and the information along the beam direction is still missing. In order for a complete determination of the 3D morphology of these features, electron tomography, a technique for obtaining detailed 3D structures of objects using an electron beam, has been applied to reveal the 3D structures of features in material science [87, 88].

2.7.1 Tomography

Tomography is defined as a method for reconstructing a 3D object from a series of 2D projections or slices. Its mathematical principle was first proposed in 1917 [89], and it was used for the application until the 1960s [90]. Since then this technique has developed rapidly and has been widely used in radiology, archaeology, biology, geophysics, oceanography, materials science and astrophysics. Tomography can be classified according to different physical phenomena. Table 2.13 lists the common types of tomography [87, 88].

Although these techniques are based on different signals, all of them will work only if each image of the object fulfils the “projection requirement”, which states that the projection signal must be a monotonic function of a projected physical quantity [87, 88, 90]. For example, the intensity of the HAADF-STEM signal varies monotonically with the thickness

and atomic number distribution of the object, which matches the projection requirement [90].

2.7.2 Electron tomography

Most electron tomography is undertaken in TEM and STEM. In the process, a beam of electrons passes through the sample which is tilted at incremental degrees around its centre. This information is collected and used to reconstruct a 3D image of the target. The resolution of these ET systems is typically in the 5-20 nm range, suitable for examining precipitates, catalysts and dislocations in materials science [88].

Tomography in TEM and STEM is different from the others in several aspects. The source (electron gun) and detector are fixed and cannot be scanned around the sample as in medical X-ray tomography, while the sample is instead rotated by tilting the specimen holder to obtain a series of images at different tilt angles, which is called a 'tilt series'. The electron tomography process is defined in Figure 2.12.

Apart from data acquisition in TEM and STEM, another method to acquire 2D data for reconstruction is dual beam FIB/SEM tomography [91]. In this methodology, a clean surface is imaged by SEM and then removed by ion milling. The imaging and removing procedure is repeated hundreds of times and a stack of images is created. The plane of the SEM image defines the x-y planes of the image stack while the milling direction defines the thickness (z-direction) of the stack. After aligning and stacking these images together, the 3D morphology can be obtained [91].

2.7.3 Limitations of electron tomography

2.7.3.1 Limitation of ET in TEM and STEM – Missing wedge

Because of the limited space between the two pole pieces, most of the specimen stages or

holders in TEM used for electron tomography achieve a maximum tilt range of about ±45 º-±80 º. Some modified holders with a narrow profile give a maximum tilt range of ±80 º. At a high tilt angle, the projection thickness increases dramatically and the features of interest become blurred or invisible. All this implies a restriction on how far the specimen can be tilted inside the microscope, and this limited range of tilt causes a wedge of missing data, known as a "missing wedge", as shown in Figure 2.13 [88, 92]. Because of the incomplete data, reconstructed objects are elongated parallel to the optic axis by a factor e, which is a function of the maximum tilt angle α, and is given by Equation 2.7 [88].

$$e = \sqrt{\frac{\alpha + \sin\alpha\cos\alpha}{\alpha - \sin\alpha\cos\alpha}} \qquad \text{(Equation 2.7)}$$

Recently, some novel techniques have been applied to solve this problem: one uses a 360 º-tilt specimen holder and a slab-like specimen in an ultrahigh-voltage electron microscope [93]; the other way is to acquire data from two perpendicular tilt axes, a technique called "dual axis tomography"[94].

2.7.3.2 Limitations in FIB/SEM tomography

There are also two limitations for FIB/SEM tomography. Firstly, in order to keep the magnitude of the z direction similar to the pixel resolution in the *x–y* imaging plane, the thickness removed each time is usually less than 10 nm, in high resolution tomography. This makes the milling process very time consuming when large (several tens of micrometres) volumes are analysed. Secondly, the milling process is easily affected by the drift caused by either mechanical or electromagnetic instabilities of the system. Hence precise control over the Ga-ion milling process and the drift during serial sectioning are needed. This now can be partially achieved with the new generation of high stability/high flux Ga-ion columns and

high stability FIB stages [95].

2.7.4 Applications of electron tomography

In the last couple of years, electron tomography using various imaging modes has been used widely in materials science: Bright Field (BF) TEM tomography, Energy Filtered (EF) TEM tomography, electron holographic tomography, High Angle Annular Dark Field (HAADF) STEM tomography and Annular Dark-Field Scanning Transmission Electron Microscopy (ADF-STEM) tomography techniques have been applied successfully to characterize different features in materials, such as nano particles and dislocations.

2.7.4.1 Electron tomography on nano-particles

Due to its high resolution (5-20 nm), electron tomography is suitable for 3D characterization of nano-size particles in catalysis, glasses and alloys. In the case of catalysts, the reactivity of a catalyst structure depends on its total active surface area. Features, such as rough surface, pores and regular channels, can increase the total active surface area. Due to the overlapping in the TEM 2D projection, these features cannot be viewed in detail. Therefore, 3D characterization using electron tomography is necessary for catalysts [90]. For particles (precipitates) in alloys, their 3D shape, size and distribution determine the strength of the dispersion-hardening alloys and thus it is important to explore the 3D aspect of these particles to gain a better understanding of strengthening mechanisms [91].

Early applications of electron tomography for these particles were generally undertaken using BF TEM [7]. However, since most of these particles are crystalline, diffraction contrast typically dominates the BF image. This contrast does not vary monotonically during the tilt acquisition, if not controlled properly. Therefore, some artefacts are generated in the subsequent reconstruction [96]. In order to avoid artefacts, some other imaging modes, such

as EF-STEM [90, 96] and HAADF-STEM [90, 96-98], have been used. The intensity in these images was found to satisfy the projection requirement, at least within certain limits, and removed most of the artefacts in reconstruction.

2.7.4.2 Electron tomography of dislocations

Another application of electron tomography is to reveal the true 3D complexity of dislocation structures. Unlike particles, whose images always contain mass-thickness contrast, the contrast of dislocations comes entirely from phase contrast. In order to make a series of dislocations usable for 3D tomographic reconstruction, the diffraction condition is usually kept constant during the tilting by orienting the sample properly. The first work on electron tomography of dislocation was published in 2006 by Barnard et al [99]. They applied a weak beam dark field (WBDF) image tilt series with a constant g vector to dislocations in a GaN epilayer and successfully reconstructed the 3D network. Although WBDF can give nice images of dislocations [100], it requires an exact diffraction condition alignment. The contrast was not consistent enough for the acquisition software to correct the specimen drift during tilting. Later on, some other image modes were tried: ADF-STEM and BF-STEM. These approaches are less sensitive to the diffraction contrast due to beam convergence and allow a relatively large deviation from the exact Bragg condition [101].

There are several works reported on 3D characterization of dislocation [99, 101, 102]. Although the 3D information obtained has rarely been applied to real material science issues, electron tomography is still a powerful tool to investigate the 3D morphology of dislocation and will be useful to sort out some materials science issues with the further development of this technique.

2.8 Aims and objectives

1. To clarify several issues about the precipitation strengthening of AZ91: (1) to gain a better understanding of the current precipitation strengthening modelling of AZ91; (2) to consider the reason for the poor precipitation hardening effect of AZ91 and propose a way towards improving the mechanical properties of aged magnesium alloys; (3) to investigate the role of cold work before ageing on the mechanical properties and microstructure of AZ91 after ageing (including the effect of pre-deformation on hardness, size, distribution and percentage of CP and DP).

2. To characterize the observed QC particles in AZ91 and their role on the precipitation of $Mg_{17}Al_{12}$ and to discuss their potential effect on the strengthening of AZ91.

3. To gain a better understanding of the Al-Mn-(Mg) QC particles and dislocations in AZ91 using the 3D information obtained from electron tomography.

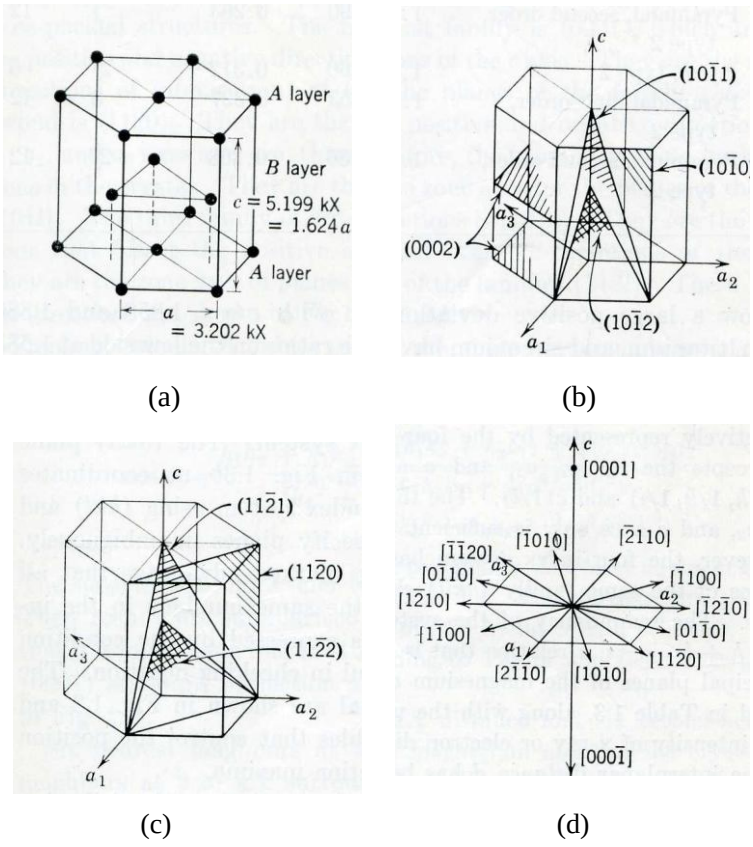

Figure 2.1. The magnesium crystal structure. (a) Atomic positions; (b) principal planes of the $[1\bar{2}10]$ zone axis; (c) principal planes of the $[1\bar{1}00]$ zone axis; (d) principal directions. (1kX = 0.1nm) [103].

Table 2.1. The principal atomic planes of magnesium crystal [11].

$\{hkil\}$	Name	d, nm	$(\sin\theta)/\lambda$	Structure Factor, F	Multiplicity
$\{0001\}$	Basal	0.520	0.096	0	2
$\{10\bar{1}0\}$	Prism, type 1	0.277	0.180	f	6
$\{0002\}$	Basal	0.260	0.192	2f	2
$\{10\bar{1}1\}$	Pyramidal, first order, type 1	0.245	0.204	$\sqrt{3}$f	12
$\{10\bar{1}2\}$	Pyramidal, second order, type 1	0.190	0.263	f	12
$\{11\bar{2}0\}$	Prism, type 2	0.160	0.312	2f	6
$\{11\bar{2}1\}$	Pyramidal, first order, type 2	0.153	0.327	0	12
$\{11\bar{2}2\}$	Pyramidal, second order, type 2	0.136	0.368	2f	12

f: one atomic scattering factor, which varies with the scattering angle.

Table 2.2. Mechanical properties of pure magnesium (99.9 wt%) [8]

	Tensile strength (MPa)	Tensile yield strength (MPa)	Compressive yield stress (MPa)	Elongation (%)	Brinell Hardness (500 kg/10 mm)
Sand cast, thickness 13 mm	90	21	21	2-6	30
Extrusion, thickness 13 mm	165-205	69–105	34–55	5–8	35
Hard rolled sheet	180–220	115–140	105–115	2–10	45–47
Annealed sheet	160–195	90–105	69–83	3–15	40–41

Table 2.3 Code letters for the designation system of magnesium alloys [16].

Letter	**Alloying Element**
A	Aluminium
C	Copper
E	Rare earth metals
K	Zirconium
L	Lithium
M	Manganese
Q	Silver
S	Silicon
W	Yttrium
Z	Zinc

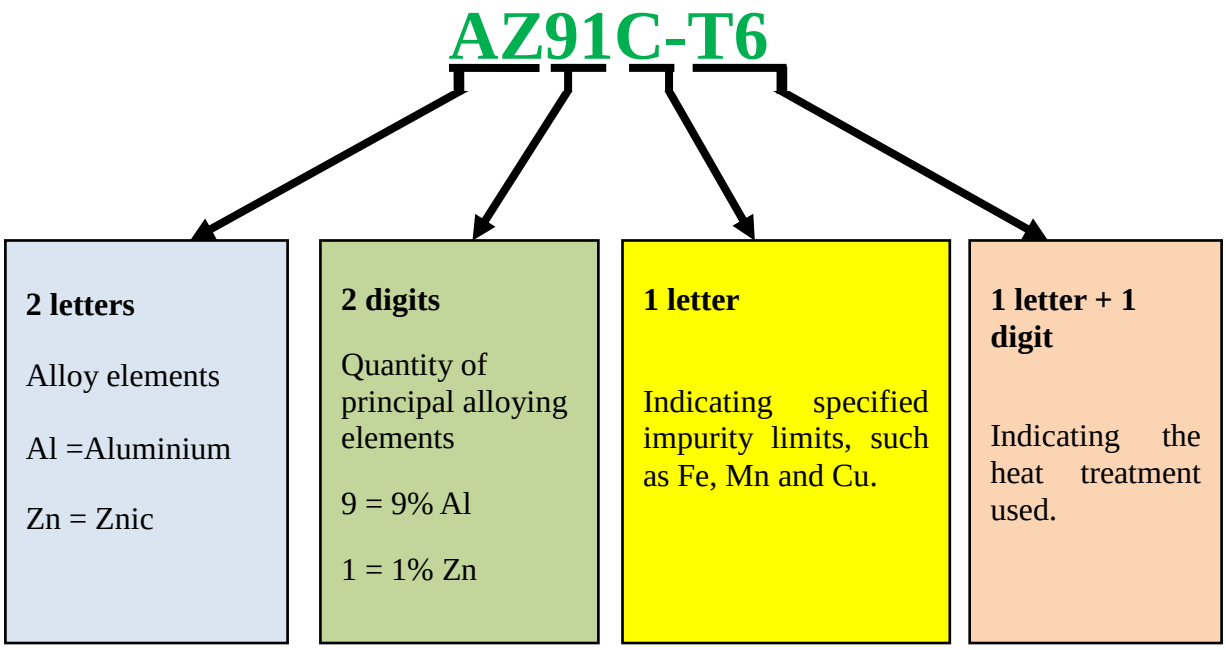

Figure 2.2. An example of a magnesium alloy designation .

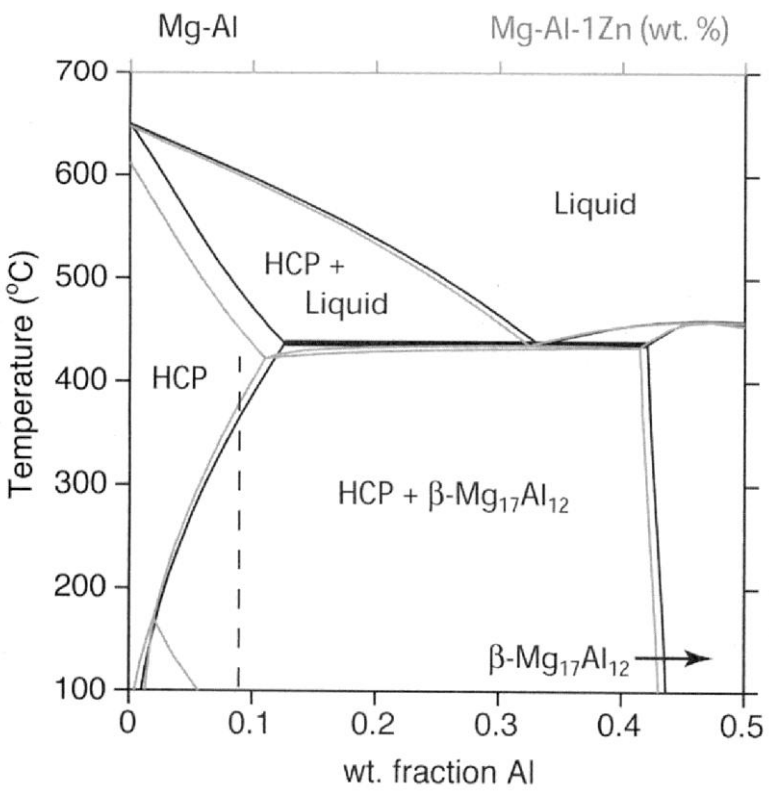

Figure 2.3. Mg-rich end of the Mg-Al and Mg-Al-Zn phase diagrams. The dashed line indicates the bulk Al content of AZ91 and the grey line illustrates the shift of solvus line due to Zn addition [18]. The Al content of $Mg_{17}Al_{12}$ is 44.26 wt%.

Table 2.4. Typical room-temperature mechanical properties of cast AZ91 (F: As-cast condition; T4: Solution treated Condition; T6: Solution treated and aged condition.) [16].

Properties	**Die Castings**	**Sand Castings**		
	F	**F**	**T4**	**T6**
Tensile strength	230 MPa	165 MPa	275 MPa	275 MPa
Tensile yield strength	150 MPa	97 MPa	90 MPa	145 MPa
Elongation of 50 mm	3%	2.5%	15%	6%
Compressive yield strength	165 MPa	97 MPa	90 MPa	130 MPa
Shear strength	140 MPa	---	---	---
Hardness	75 HRE	66 HRE	62 HRE	77 HRE
Tension elastic modulus	45 GPa			
Shear elastic modulus	17 GPa			
Principal fracture mode	Cleavage usually along {0001}			

HRE: the hardness of metallic materials on the Rockwell E scale.

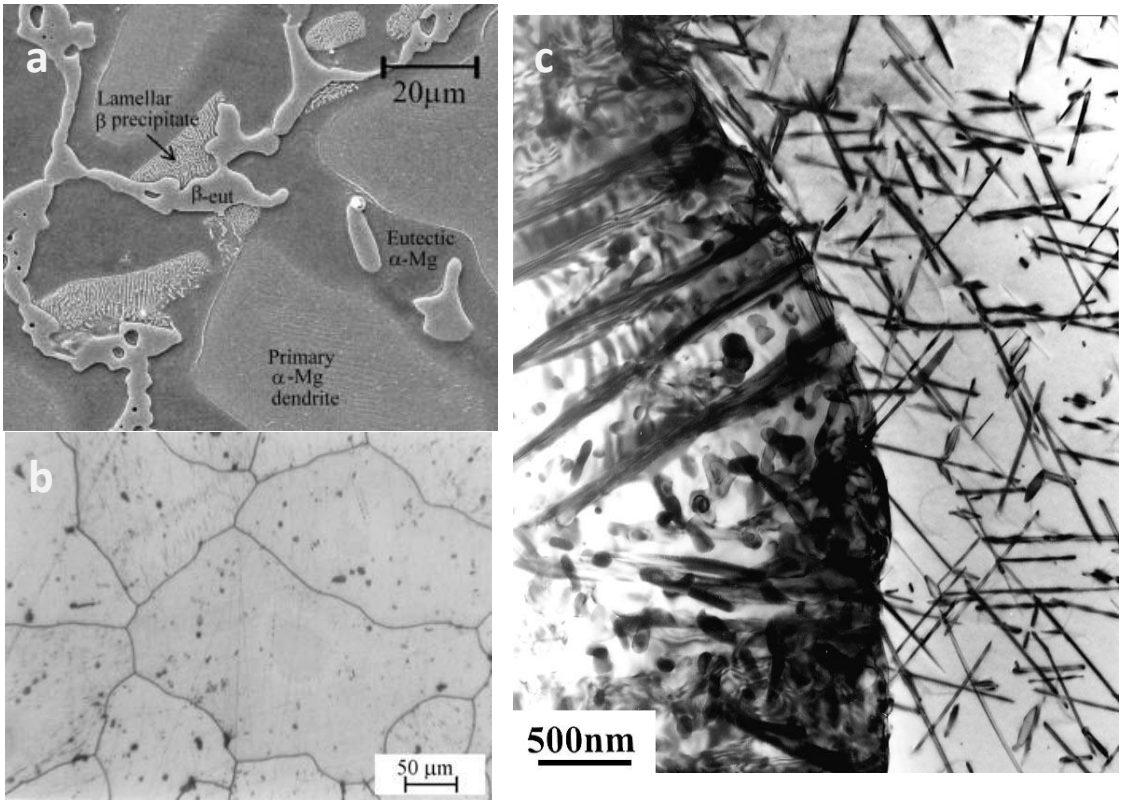

Figure 2.4. Microstructure of AZ91 during heat treatment: (a) SEM micrograph showing primary α-Mg, eutectic α-Mg and β−eut phases and lamellar β precipitates in a sand cast AZ91 [19]; (b) Optical micrograph showing the dissolution of the eutectic structure in AZ91 solid solution treated at 420℃ for 24h [21]; (c) TEM micrograph showing a region of discontinuous (left) and continuous (right) precipitation in AZ91 aged at 200℃ for 4 h [17].

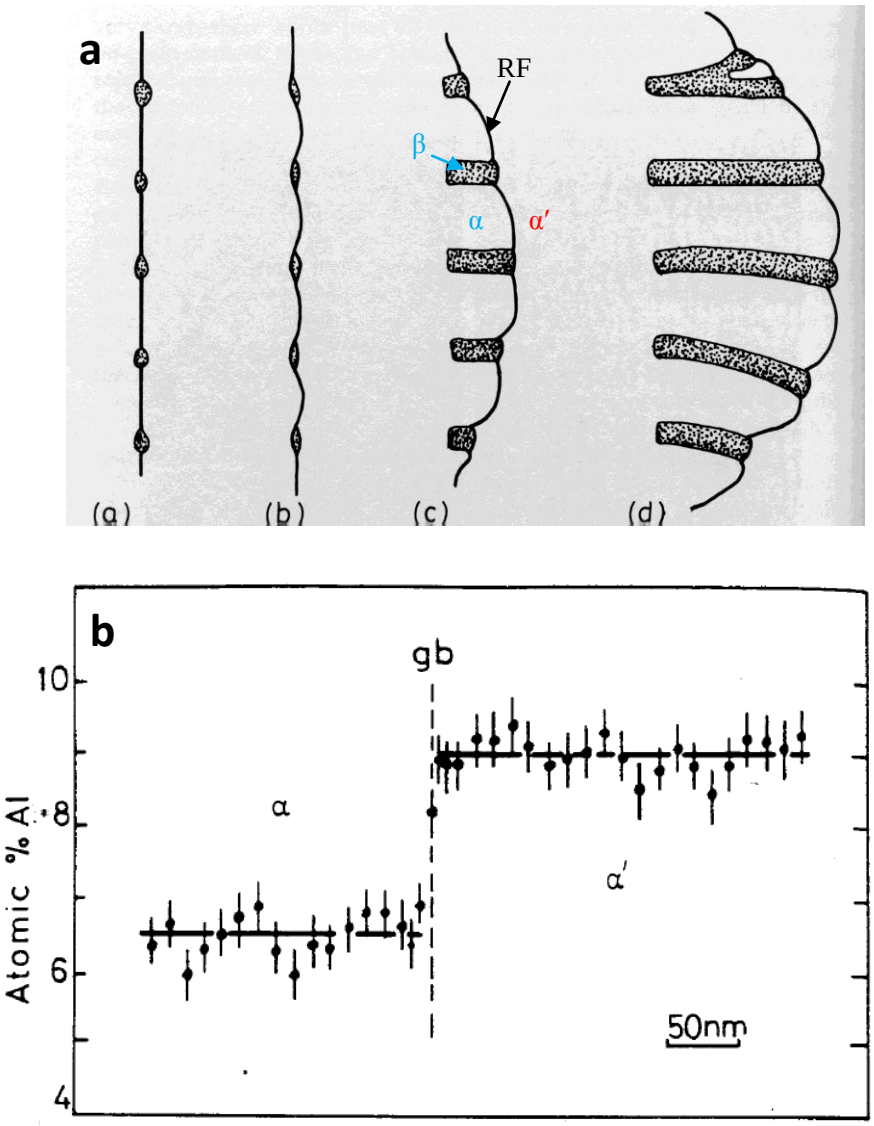

Figture 2.5. (a) A schematic diagram showing a possible sequence of steps during cellular precipitation [27]. Different phases (α′, α and β) and the reaction front (RF) are indicated. (b) The variation of aluminium concentration across an moving grain boundary midway between two precipitate lamellae [27].

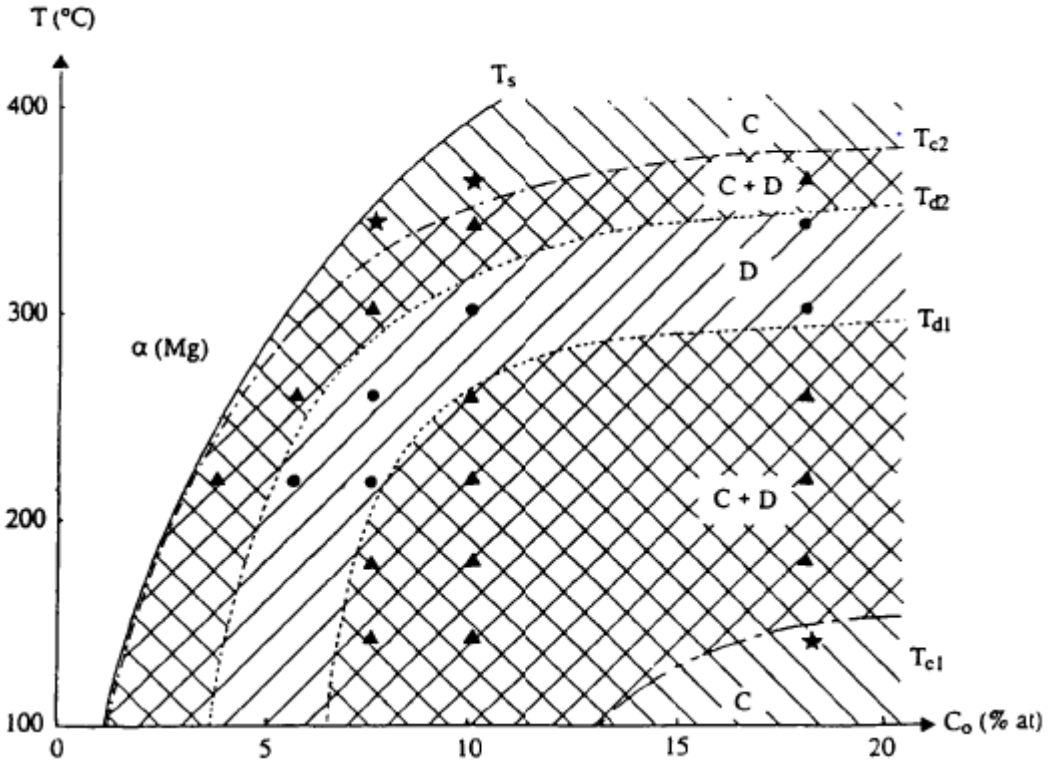

Fig. 2.6. Precipitation morphology diagram (C_0: Content of Al in Mg-Al alloys; T: Temperature of ageing). Circles, triangles and stars respectively correspond to the experimental points for which were observed discontinuous precipitates (D) only, both continuous and discontinuous precipitates (C+D), and continuous precipitates (C) only [35]. For the meaning of T_{c1}, T_{d1}, T_{d2} and T_{c2}, see text in §2.3.4.3.

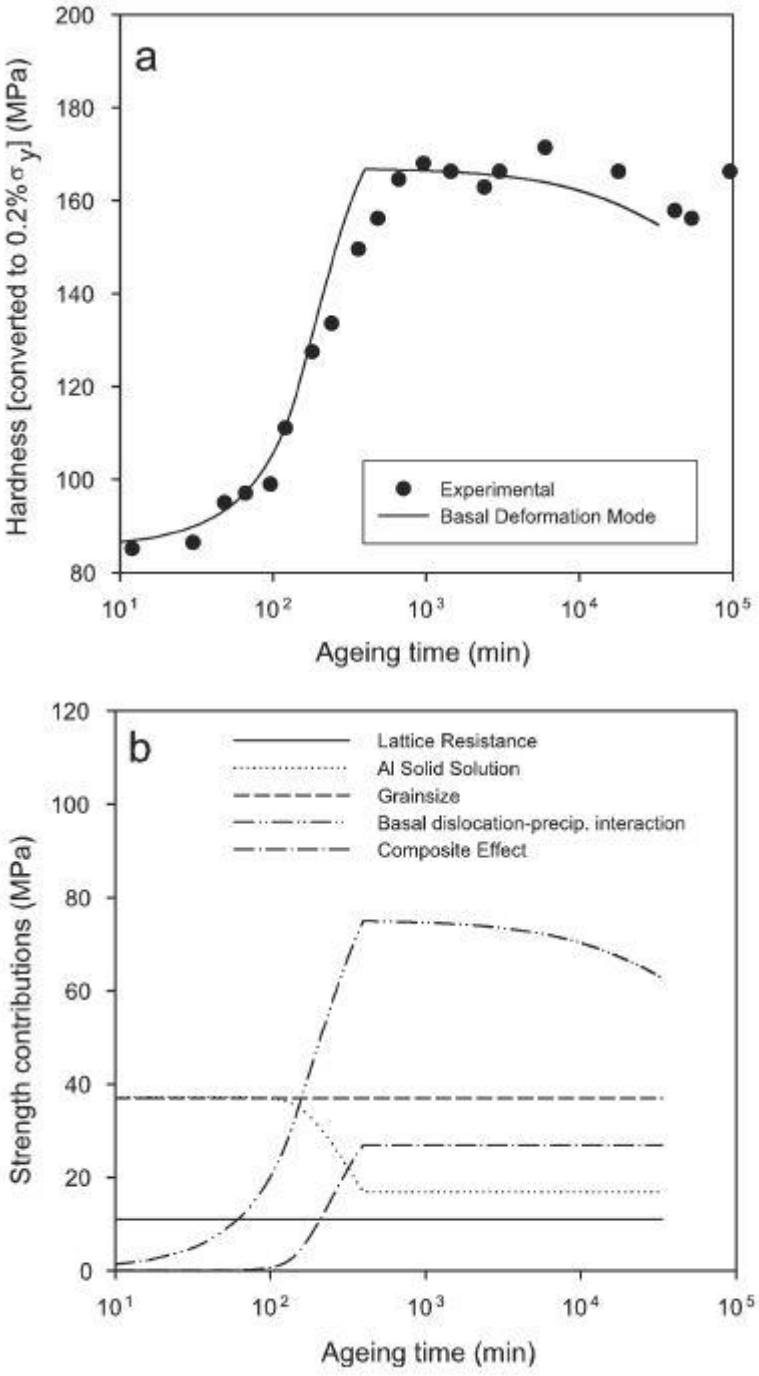

Fig. 2.7. (a) Comparison of the calculated room-temperature yield strengths for alloy AZ91 as a function of ageing time at 200 ℃ using Eqs. 2.1 to 2.6 and the experimental data reported by Celotto [5]. (b) Individual contributions to the overall calculated yield strength [6]. Composite effect is the continuum strengthening effect (work hardening) described in §2.3.5.4.

Table 2.5. Comparison of precipitation-hardening between AZ91 magnesium alloy and 7075 aluminium alloy aged at 200 ℃ [6]. (The yield strengths of pure magnesium [35] and aluminum [52] are also listed)

	AZ91	7075	Pure magnesium	Pure aluminium
Equilibrium volume fraction	~15%	~5%	NA	NA
precipitates per unit volume, Nv	~ $10^{10}mm^{-3}$	~ $10^{12}mm^{-3}$	NA	NA
Yield strength	150 MPa	600 MPa	11 MPa	7-11 MPa

Table 2.6. Classification of wrought Al alloys [56].

Series	Element Names (in order of %)	Heat-treatable Status
1xxx	Super- or commercial-purity aluminum	Non-heat-treatable
2xxx	Aluminum-Copper-Magnesium	Heat-treatable
3xxx	Aluminum-Manganese-Magnesium	Non-heat-treatable
4xxx	Aluminum-Silicon	Non-heat-treatable
5xxx	Aluminum-Magnesium	Non-heat-treatable
6xxx	Aluminum-Magnesium-Silicon	Heat-treatable
7xxx	Aluminum-Zinc-Magnesium-Copper	Heat-treatable
8xxx	Aluminum-Lithium- Etc…	Non-heat-treatable

The second digit indicates modification of the alloy or impurity limits. The last two digits identify aluminum alloy or indicate the alloy purity.

Table 2.7. Classification of cast Al alloys [56].

Series	Element Names (in order of %)	Heat-treatable Status
1xx.x	Super- or commercial-purity aluminum	Non-heat-treatable
2xx.x	Aluminum-Copper	Heat-treatable
3xx.x	Aluminum-Silicon –(Copper/Magnesium)	Non-heat-treatable
4xx.x	Aluminum-Silicon	Non-heat-treatable
5xx.x	Aluminum-Magnesium	Non-heat-treatable
6xx.x	Unused series	Heat-treatable
7xx.x	Aluminum-Zinc	Heat-treatable
8xx.x	Aluminum-Lithium- Etc…	Non-heat-treatable

The second two digits identify the aluminum alloy or indicate the alloy purity. The last digit indicates the product form: casting (designated by “0”) or ingot (designated by “1” or “2”, depending on chemical composition limits.)

Table 2.8. Mechanical properties of some commercial precipitation-hardening Al alloys [27].

Alloys	2024	6061	7075	AZ91-T6
Composition (wt %)	Al-4.5Cu-1.5Mg-0.6Mn	Al-1.0Mg-0.6Si-0.25Cu-0.2Cr	Al-5.6Zn-2.5Mg-1.6Cu-0.2Mn-0.3Cr	Mg-9%Al-1%Zn
Precipitate	S' (Al_2CuMg)	β' (Mg_2Si)	η' ($MgZn_2$)	β ($Mg_{17}Al_{12}$)
Yield Strength* (MPa)	390	280	500	145
Ultimate Tensile Strength* (MPa)	500	315	570	275
Elongation* (%)	13	12	11	6%

* At peak hardness and tested at room temperature.

Table 2.9. Some precipitation sequences in Al alloys [27]

Alloys	Precipitation Sequence
Al-Ag	GP zone (spheres) → γ' (plates) → γ (Ag_2Al)
Al-Cu	GP zone (discs) → θ'' (discs)→ θ' (plates) → θ ($CuAl_2$)
Al-Cu-Mg	GP zone (rods) → S' (laths)→ S ($CuMgAl_2$) (laths)
Al-Zn-Mg	GP zone (spheres) → η' (plates) → η ($MgZn_2$)
Al-Mg-Si	GP zone (rods) → β' (rods)→ β (Mg_2Si) (plates or rods)

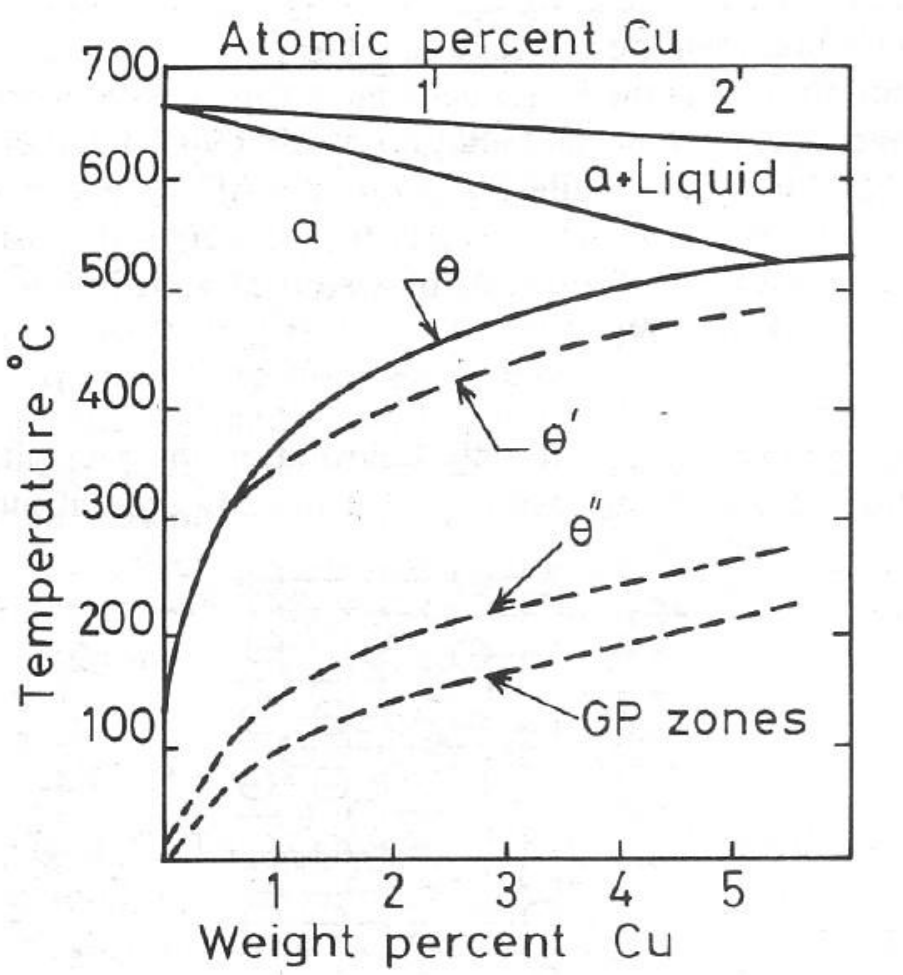

Figure 2.8. The Al-Cu phase diagram with the metastable GP zone, θ", θ' and θ solvuses [27].

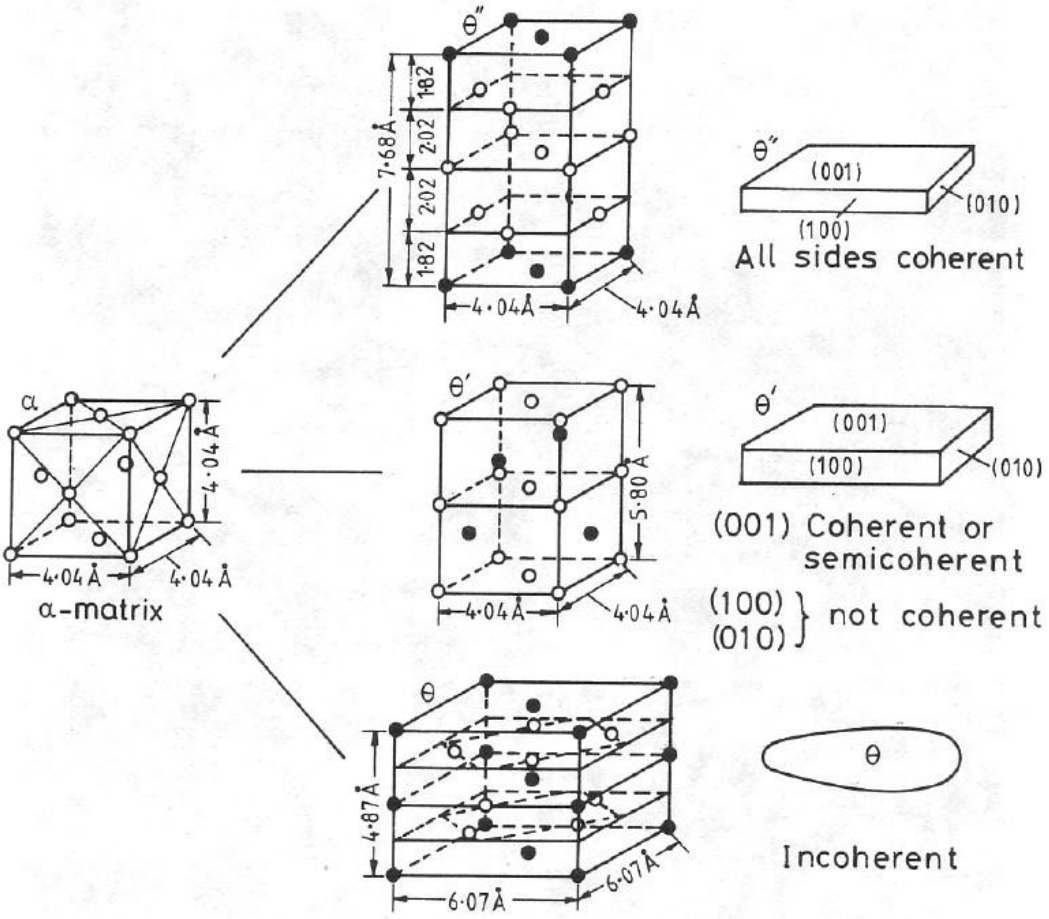

Figure 2.9. Structure and morphology of precipitates in Al-Cu (○Al, ●Cu) [27].

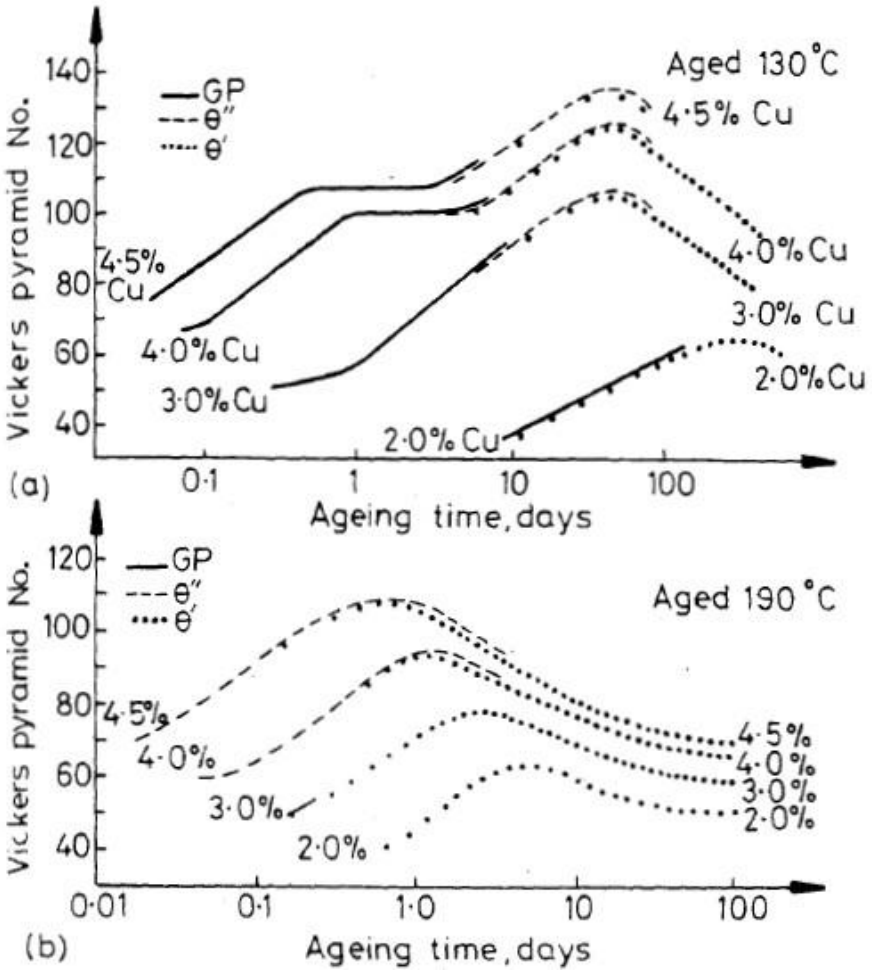

Figure 2.10. Precipitation and hardness evolution of various Al-Cu alloys at (a) 130 ℃ and (b) 190 ℃ [27].

Table 2.10. Manganese-containing particles reported in Mg-Al based alloys [46].

Production method	Alloy	Particle type	Particle size (μm)	Particle morphology	Particle Location
Die-casting	AZ31	Al_8Mn_5 β-Mn	~1	Not mentioned	Preferentially at grain boundaries and inside grains
Die-casting	AZ91D	Al_8Mn_5	0.1-0.2	Angular block morphology	Not mentioned
Die-casting	AZ91	Al-Mn-(Fe)	0.1-1	Flower-like structure	On coarse $Mg_{17}Al_{12}$ phase and grain boundaries
Rapid solidified ribbons	AZ91	Al-Mn-Fe	N/A	Cross-shaped features	Not mentioned
Cone ladle	AM60	$Al_8(Mn,Fe)_5$	10-30	Spherical or flower-like	Not mentioned
Semi-solid	AZ91	$Al_8(Mn,Fe)_5$	N/A	Not mentioned	Within primary Mg phase

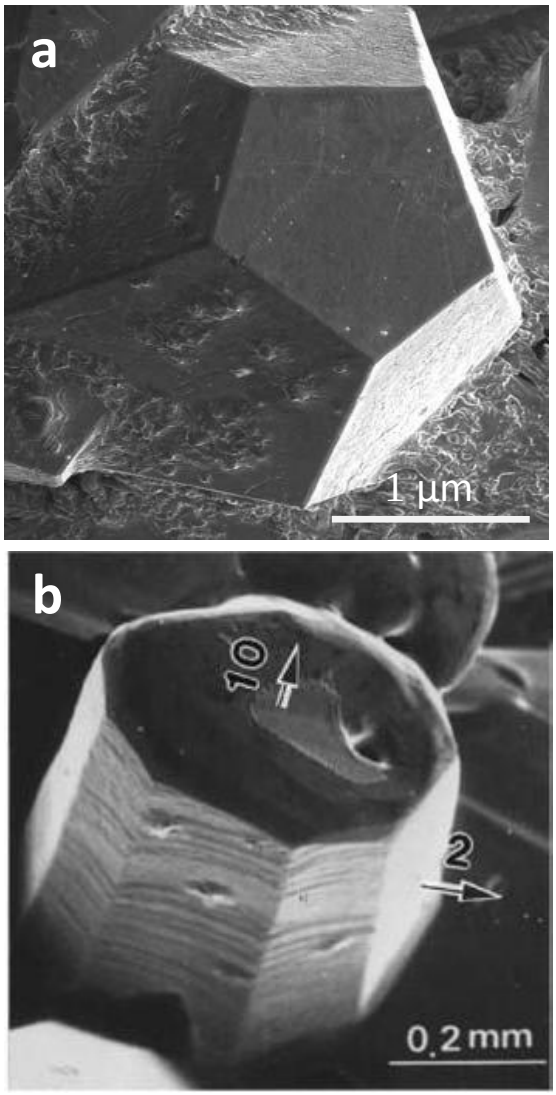

Figure 2.11. Scanning electron microscopy (SEM) micrographs showing a single grain of (a) icosahedral Al-Pd-Re [75] and (b) decagonal Al-Ni-Co quasicrystals [76]. The arrows in (b) correspond to the high symmetry axes.

Table 2.11. QCs with various chemical compositions in different systems [68, 72].

Types of QCs	Alloy systems of QCs
Octagonal QC	V-Ni-Si, Cr-Ni-Si, Mn-Si, Mn-Si-Al, Mn-Fe-Si
Decagonal QC	Al-TM (TM=Ir, Pd, Pt, Os, Ru, Rh, Mn, Fe, Co, Ni, Cr), Al-Ni-Co *, Al-Cu-Mn, Al-Cu-Fe, Al-Cu-Ni, Al-Cu-Co *, Al-Cu-Co-Si *, Al-Mn-Pd *, V-Ni-Si, Cu-Ni
Dodecagonal QC	Cr-Ni, V-Ni, V-Ni-Si
Icosahedral QC	Al-Mn, Al-Mn-Si, Al-Li-Cu *, Al-Pd-Mn *, Al-Cu-Fe, Al-Mg-Zn, Zn-Mg-RE * (RE=La, Ce, Nd, Sm, Gd, Dy, Ho, Y), Ti-TM (TM=Fe, Mn, Co, Ni), Nb-Fe, V-Ni-Si, Pd-Ni-Si

* : stable phase.

Table 2.12. Comparison of physical properties between selected QCs and relevant conventional materials at room temperature [68].

Physical Properties	Materials	Value
Hardness (HV)	Diamond	6000-10000
	i-Al-Cu-Fe	800 – 1000
	i-Al-Pd-Mn	700 – 800
	low-carbon steel	70 – 200
	Copper	40 -105
	Aluminum	25 – 45
Coefficient of friction (unlubricated with a diamond pin)	Copper	0.42
	aluminium alloy	0.37
	low-carbon steel	0.32
	i-Al-Cu-Fe	0.05-0.2
Young's modulus (GPa)	stainless steel	31
	i-Al-Pd-Mn	29
	Copper	19
	Aluminum	10
Thermal conductivity ($W \cdot m^{-1} \cdot K^{-1}$)	Copper	390
	Aluminium	170
	low-carbon steel	50
	i-Al-Cu-Fe	2
Surface energy (mJ/m^2)	Iron	2480
	Copper	1830
	i-Al-Pd-Mn (air-oxidized)	24-25
	PTFE (similar to Teflon)	17-18

Table 2.13 Different types of modern tomography [87, 88].

Image medium	Type of tomogram
gamma rays	SPECT (Single photon emission computed tomography)
electron-positron annihilation	PET (Positron emission tomography)
X-rays	CT (Computed Tomography)
electrons in SEM	FIB/SEM tomography
electrons in S/TEM	Electron tomography or 3D ET
ions	atom probe

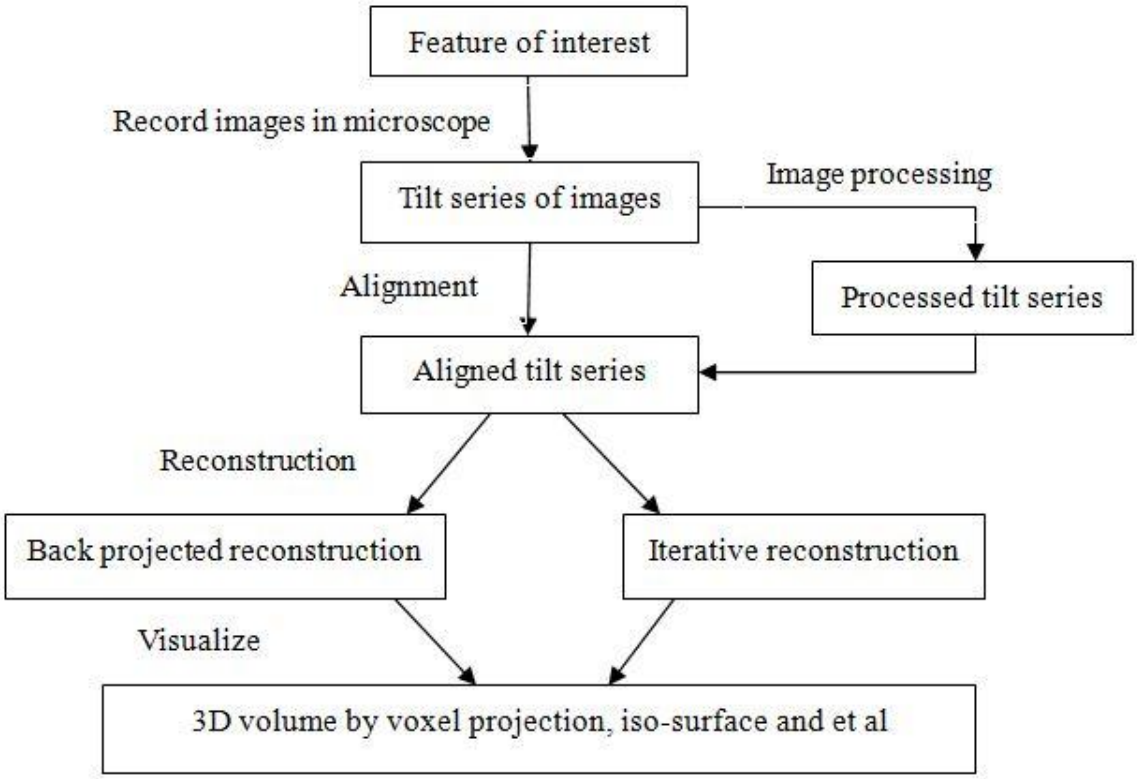

Figture 2.12. Flowchart showing steps required for electron tomography

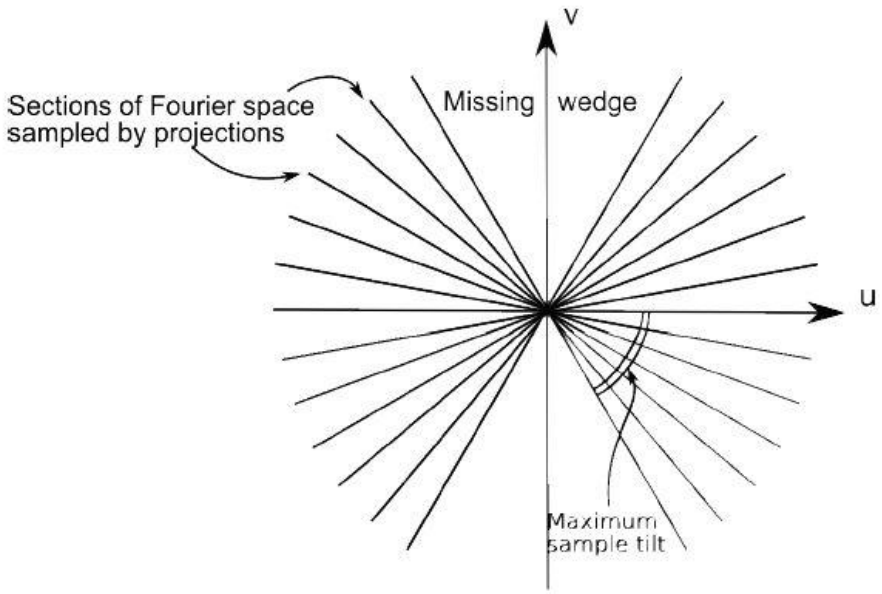

Figure 2.13. Diagram showing the effect of restricted tilt angle on the ability to fill Fourier space with data about the object. Lines plotted on these u-v spatial frequency axes are slices through the object. The relatively larger number of data points at low frequencies results in a blurred reconstruction [88, 92].

Chapter 3 Experimental

3.1 Raw materials

The material used in this work was a sand-cast AZ91E alloy ingot with dimensions of 560 mm × 60 mm × 60 mm, as shown in Figure 3.1. The actual chemical composition of the alloy is shown in Table 3.1. The element contents are consistent with standards listed in the literature for this alloy [16]. In experiments involving the as-cast alloy, specimens were cut from the ingot without any further treatment.

3.2 Processing of materials

The as-cast alloy was cut into small pieces of 100 mm × 60mm × 60 mm and solution treated at 420℃ for 72 hours followed by water quenching. During the solution treatment, the materials were covered by graphite powder to minimize oxidation which occurs rapidly above 370℃ [5]. The as-cast and the solution treated materials were used to study the morphology, chemical composition and structure of Al-Mn-(Mg) nano-particles. After solution treatment, the materials were processed via two different processing routes, as shown in Figure 3.2.

3.2.1 Route I

The solution treated materials were aged at 100 ℃, 150 ℃, 200 ℃ and 250 ℃ in air for 0.5 h, 1 h, 3 h, 5 h, 10 h, 15 h and 30 h, as shown in Figure 3.3. These samples were used to study the precipitation hardening response of AZ91 without pre-deformation and the precipitation of $Mg_{17}Al_{12}$ on the Al-Mn-(Mg) particles.

3.2.2 Route II

The solution treated materials were either cold rolled or compressed before ageing. During the cold rolling (multiple pass), the thicknesses reduction was set at 5%, 10%, 15% and 20%. The as-rolled samples were then aged at 200℃ in air for 0.5 h, 1 h, 3 h, 5 h, 10 h, 15 h and 30 h. These samples were used to investigate the effect of the pre-deformation on the mechanical properties and microstructure of AZ91 after the ageing and the precipitation of $Mg_{17}Al_{12}$ on defects. During the compression, the sample thickness was reduced by 0.6% to introduce dislocations with a proper density. The as-compressed sample was then aged at 200℃ in air for 1 h. This sample was used to characterise the precipitation of $Mg_{17}Al_{12}$ on dislocations via electron tomography.

3.3 Microstructure characterisation

3.3.1 Optical microscopy (OM)

OM was used for general microstructure observations and discontinuous precipitation area measurement because of its large field of view. The specimens for OM were cold mounted and mechanically ground using water and silicon carbide paper with increasing fineness from P800 to P4000. After that, the samples were polished with water-free cream containing diamond powder (1 μm) and ethanol until a mirror-like surface finish was achieved. It should be noticed that water was avoided during the polishing, since it might oxidize the surface of the polished samples. Instead of water, ethanol was used to clean all polished samples.

In order to reveal the microstructure of the samples, several etchants were used for different OM samples [102]. A nitric acid solution (4 ml nitric acid and 100 ml ethanol) was used to etch the as-cast OM samples for 30s. An acetic acid solution (1 ml acetic acid, 50 ml distilled

water and 150 ml ethanol) was used to etch the OM samples after solution treatment for 50s: A phosphor-picral etchant (0.7 ml phosphoric acid, 4g picric acid and 100ml ethanol) was used to etch the OM samples after ageing for 10s [16]. To etch the samples, the polished surface was immersed in the etchant with gentle stirring for the required time and then washed with ethanol, followed by drying with cool air. OM observation was performed on a Zeiss Axioskop optical microscope. Figure 3.4 is a typical image showing how the area fraction of discontinuous precipitation was measured using ImageJ [104]. A typical OM (Figure 3.4 (a)) image shows the discontinuous precipitation area (indicated by red arrows) in an AZ91 aged at 200 ℃ for 5 h. Figure 3.4 (b) is a SEM image showing a typical discontinuous precipitation area in the same sample with (a). These discontinuous precipitation areas were selected manually and then their contrast was enhanced in ImageJ to separate them from the other area, as shown in Figure 3.4 (c). Finally, the area fraction of the discontinuous precipitation was obtained using the "area fraction" function in ImageJ.

3.3.2 Scanning electron microscopy (SEM)

To study details of the morphologies of the β precipitates, a JEOL 7000 SEM and a PHILIPS XL 30 SEM were also used. Generally, suitably prepared OM samples were also good for SEM observation. But, due to the non-conducting nature of the cold mounted materials, silver paint was used to connect the polished surface to the bottom of the SEM samples. In the SEM (secondary electron imaging), β precipitates present as bright and magnesium matrix appears dark in the etched samples. This is due to the different height of the β precipitates and magnesium matrix and the edge effect gives the contrast. Energy dispersive X-ray spectroscopy can be employed to determine the chemical composition. During EDX measurement, the operating voltage was 20kV and the dead time was usually maintained between 25 and 35%.

3.3.3 Transmission electron microscope (TEM)

For high spatial resolution chemical analysis and microstructural characterization, such as defect analysis and structure determination of nano sized Al-Mn-(Mg) particles, both JEOL 2100 HT and TECNAI F20 (200kV) transmission electron microscopes were used. Bright-field (BF) and dark field (DF) imaging techniques were used to observe the morphology of precipitates and defects. Weak beam dark field (WBDF) imaging was used to investigate dislocations. Selected area diffraction (SAD) patterns were used to determine the structure of the precipitates. Convergent beam electron diffraction (CBED) was used to determine the thickness of the samples. Quantitative chemical analysis was carried out by using energy dispersive X-ray (EDX) analysis. The nano-sized Al-Mn-(Mg) QC particles close to the hole of the sample were chosen for the analysis of their chemical composition and structure, to minimize the influence from the Mg matrix. Dislocations were all imaged under two-beam conditions [100].

Scanning transmission electron microscopy (STEM) was also used on the TECNAI F20. High angle annular dark field STEM (HAADF-STEM) imaging was used to observe the relationship between the β precipitates and Al-Mn-(Mg) QC particles. Line scanning and element mapping in STEM were also used to analyse the chemical variation across the samples. Bright-field STEM (BF-STEM) was used to study dislocations. All the detailed operations of the TEM and STEM follow Williams and Carter [100].

To prepare TEM samples, thin slices were cut from bulk specimens using electro-discharge machining. 3 mm diameter discs were punched out from these thin slices and mechanically ground down to less than 200μm on P4000 grade paper. Final thinning was performed by twin-jet electro-polishing with a solution containing 10% perchloric acid and 90% acetic acid

at 223 K [5]. Liquid nitrogen was used to cool the electrolyte to the desired temperature. During the twin-jet electro-polishing, the current was maintained between 0.5-1 A with an applied voltage around 20 V. Once removed from the jet polisher, the specimens had a black opaque layer on the surface which was removed by dipping for 1~2 s into a 20 vol. % nitric acid-80 vol. % ethanol solution. Finally, the specimens were cleaned using a Gatan precision ion polishing system (PIPS) 691 at a beam voltage of 4.0 kV and an incidence angle of 4 ° for about 30 min on both sides of the samples.

3.4 Electron tomography

In order to investigate the 3D morphology of nano-sized Al-Mn-(Mg) QC particles and dislocations, electron tomography (ET) was performed using the TECNAI F20 transmission electron microscope. Data collection for ET was carried out by tilting the samples in various high tilt tomography holders with respect to the electron beam. After the calibration, the X tilt axis was found to be 0.9° clockwise from the vertical line of the images obtained using Tecnai F20 TEM at used magnifications. The resolution and quality of the reconstructed volume are determined not only by image resolution but also by the angular increment and range of the tilt series [98]. Typically, a tilt series includes a collection of images obtained at 1-2 ° angular intervals over an angular range from -70 ° to 70 °. However, it should also be noted that the distance which the electron beam goes through in the sample increases with increasing angle from the zero tilt position, thus the images at high tilting angles often get blurred. Due to different contrast mechanisms, different specimen holders and imaging modes were used for particles and dislocation tomography in the current work.

For electron tomography of the Al-Mn-(Mg) QC particles, HAADF-STEM imaging (based on Z contrast) was used. In this case, the foils were placed on a Gatan high tilt tomography

holder model 914 (tilt range from -80 ° to 80 °), as shown in Figure 3.5. HAADF STEM tilt series were recorded in a Gatan slow scan CCD from -60 ° to +60 ° with a 2 ° interval using an HAADF detector. The HAADF detector collects the electrons with a high scattering angle, which make its signal approximately proportional to Z^2. The HAADF signal suppresses the coherent diffraction contrast and is therefore useful for studies on crystalline materials [97].

Unlike particles, dislocation imaging relies on diffraction contrast. Dislocations are largely invisible if their Burgers vectors are perpendicular to the diffraction vectors. Therefore, the diffraction vectors should be carefully selected. In the case of Mg, for example, a two beam condition using g= $10\bar{1}1$ enables one to view most $< a >$ type and $< c + a >$ type dislocations. Before the tilt acquisition, diffraction condition alignment was performed on a HATA (High Angle Triple Axis) holder, shown in Figure 3.6 [105, 106]. A schematic diagram of the geometry of the bright field STEM and diffraction alignment of g = $10\bar{1}1$ is shown in Figure 3.7. The coarse rotation of samples was by hand, followed by fine rotation using an off-line index dock system [105]. The accuracy of the alignment was checked finally in the microscope with a quick tilt from -60 ° to 60 °. Diffraction condition alignment in these tilt series was not always perfect. s , the deviation parameter, varies a little bit during each tilt series, which will be mentioned in Chapter 6. Therefore, BF STEM was chosen to image dislocations to reduce the effect of varying s on the dislocation contrast.

After the tilt acquisition, the data sets were transferred into a workstation (DELL precision T3500) for alignment, reconstruction and tomogram slicing using IMOD software [107, 108], which uses the weighted back projection (WBP) and simultaneous iterative reconstruction technique (SIRT) method to reconstruct the tomogram. The signal-to-noise ratio of the 3D reconstruction is strongly dependent on the precise alignment of all the images of the tilt series. The alignment can be done automatically using cross-correlation of the images or

manually if some small misalignments need to be corrected. Both methods are available in IMOD [107].

3.5 Hardness measurement

All specimens for hardness testing were ground using a series of waterproof silicon carbide papers of different grits, viz. P120, P240, P400, P800, P1200 and P2400, followed by diamond paste polishing down to 0.5 μm grade to produce a mirror-like surface. Hardness testing was performed on the polished surface using a Mitutoyo MVK-H1 micro-hardness tester fitted with a Vickers indenter with a load of 500 g for 10 s.

3.6 Particle number density

In order to know the effect of pre-deformation on the number density of continuous precipitates (CP), it is necessary to measure the precipitate number density in the aged AZ91 with and without pre-deformation. For a perfectly random arrangement of particles, the following relationship is expected to be satisfied [109]:

$$N_V = \frac{N_A}{t} \qquad \text{(Equation 3.1)}$$

where N_V is the number of particles per unit volume in a foil and N_A is the number of the particles per unit area, t is the specimen thickness.

Based on the equation, the number of particles per unit volume, N_V, can be calculated with N_A and t obtained in TEM. N_A can be obtained by measuring the number of the particles in each TEM image and the size of the images. Thickness measurement can be achieved by

several means, such as EELS and thickness fringes, but the most reliable method has been found to be convergent beam electron diffraction (CBED) [109, 110].

3.6.1 Thickness measurement

CBED makes use of the intensity oscillations present in convergent beam diffraction patterns. An equation deriving from the two beam dynamical theory of electron diffraction shows the relationship between ξ_g, t and the position of the minima in intensity oscillations in the diffraction disc, which is as follows:

$$\left(\frac{s_i}{n_i}\right)^2 + \left(\frac{1}{n_i}\right)^2 \left(\frac{1}{\xi_g}\right)^2 = \frac{1}{t^2} \qquad \text{(Equation 3.2)}$$

where s_i is the deviation parameter of the ith minimum for the reflection g. s_i can be measured directly from the spacing of the fringes in the convergent beam pattern and n_i is the number of the fringes counting outwards from the mid-line. s_i can be determined by:

$$s_i = \frac{\lambda}{d^2}\left(\frac{\Delta\theta_i}{2\theta_d}\right) \qquad \text{(Equation 3.3)}$$

where d is the plane spacing of the operating reflection and λ is the wavelength. $\Delta\theta_i$ is the distance to the chosen minimum from the mid-line and $2\theta_d$ is the distance between the centre spot and the diffracted spot. Plotting $(s_i/n_i)^2$ versus $(1/n_i)^2$, the foil thickness is given by the intercept of the resulting straight line with the $(s_i/n_i)^2$ axis if n gives a straight line. The method is illustrated in Figure 3.8. Very large d values (very low hkil values) must be avoided in this technique due to multiple scattering from systematic reflections. In this study, thickness measurements were carried out near the $[1\bar{2}10]$ zone axis using g = $10\bar{1}3$. An example of a thickness measurement will be shown in §4.4.4.

3.6.2 Counting the number of precipitates

Transmission electron microscopy (TEM) is by far the most widely applied technique for measuring the size and number of the micro or nano particles due to its high resolution. However, even the best TEM suffers from the overlapping and truncation of the precipitates. In this study, bright field images taken at magnification of 8k and 10k were used to measure the number of β precipitates. In order to reduce overlap of the precipitates, all the images were taken with a beam direction close to $\langle 1\bar{2}10 \rangle$. The foil normals of all the samples used are within 30 ° of $\langle 1\bar{2}10 \rangle$.

Figure 3.1. The as-cast AZ91 magnesium alloy ingot (as-received material).

Table 3.1. The actual chemical composition of the AZ91 used in this work.

Element	Composition (wt. %)
Aluminium	9.12
Zinc	0.643
Silicon	0.001
Manganese	0.237
Copper	0.0008
Iron	0.0005
Nickel	0.0004
Magnesium	Balance

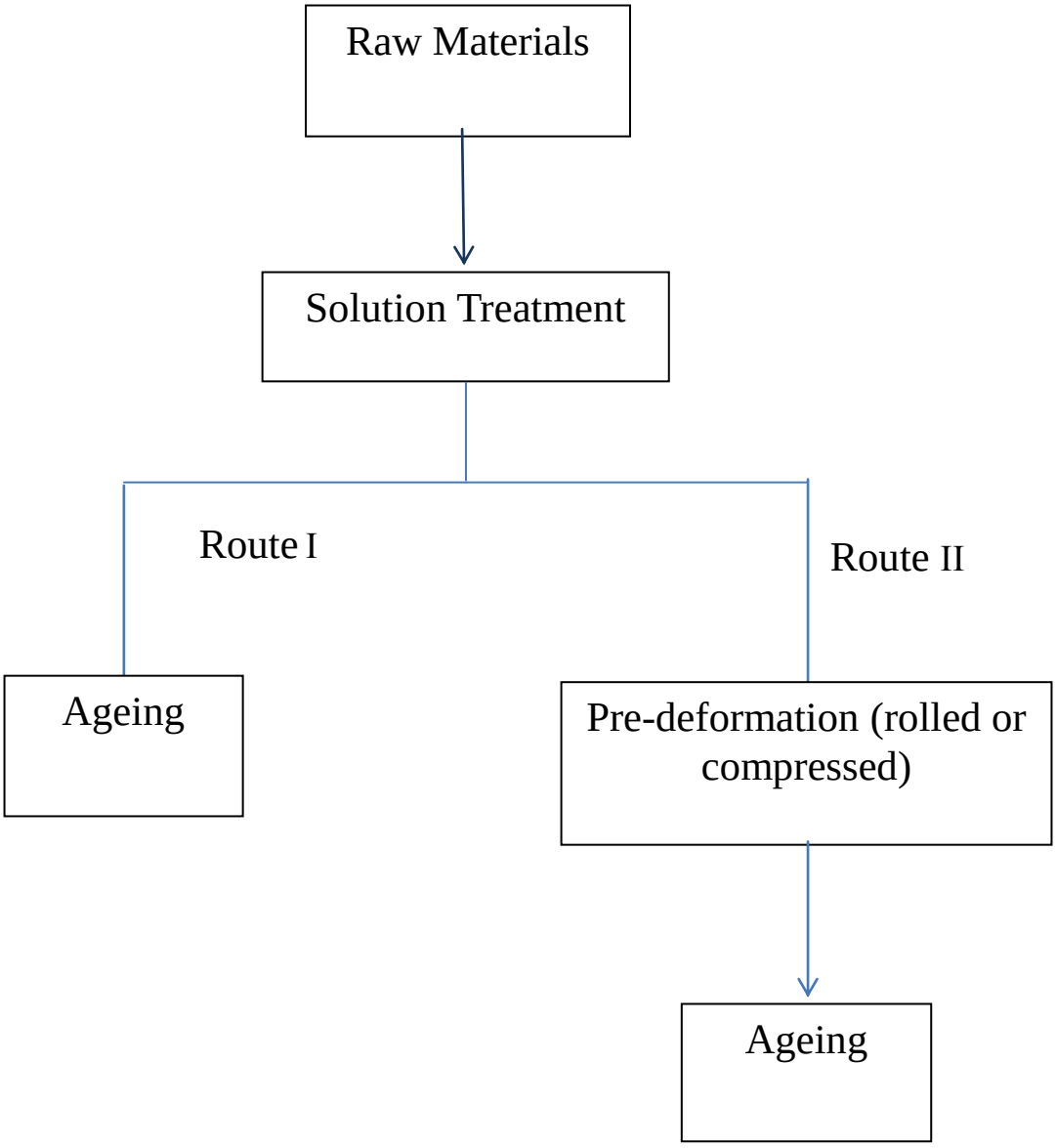

Figure 3.2. Processing routes.

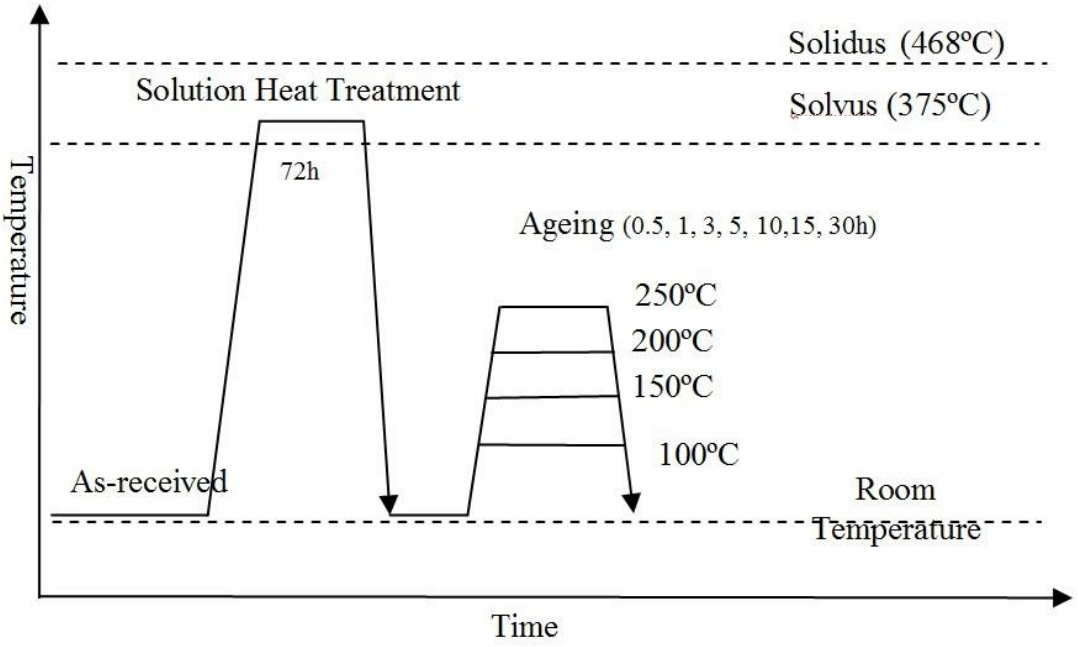

Figure 3.3. A schematic diagram showing the heat treatment procedure.

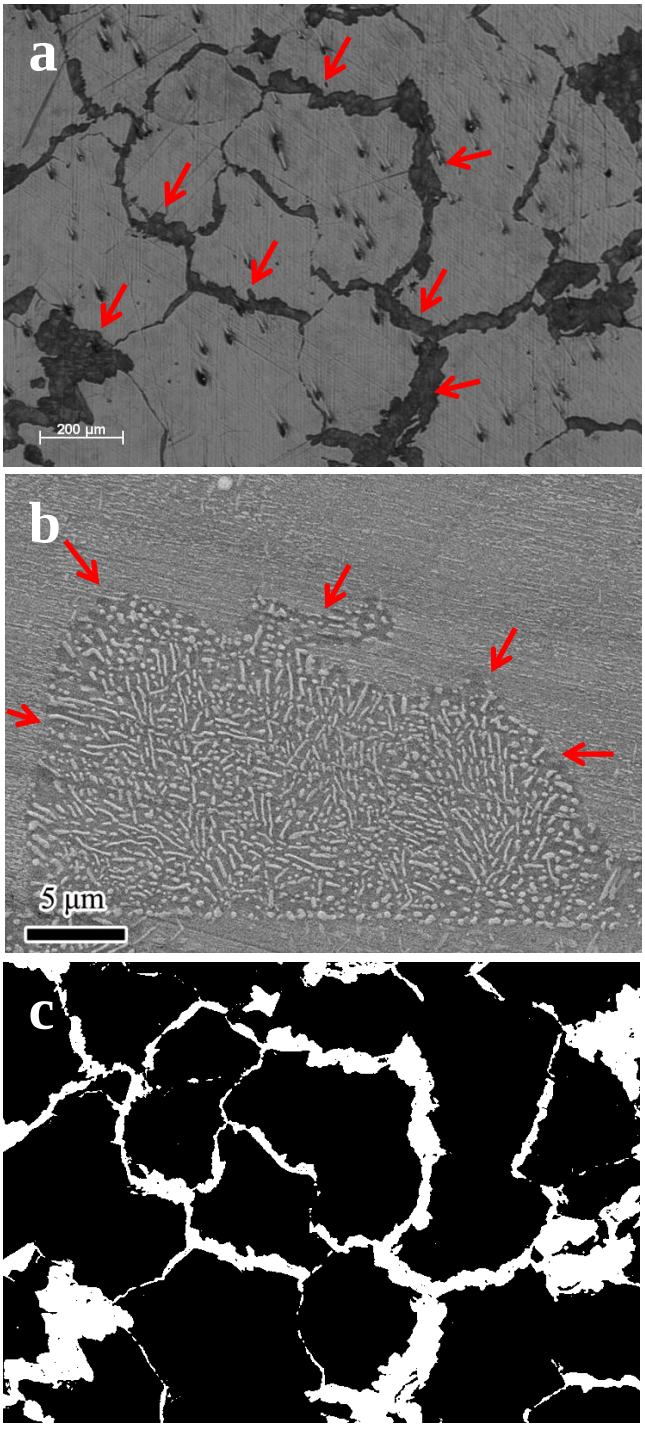

Figure 3.4 (a) An optical microscope image showing the discontinuous precipitation (DP) area (dark area) in the AZ91 alloy aged for 5 hours. Most of the discontinuous precipitation is located along the grain boundaries, as indicated by the red arrows. (b) A high magnification SEM image shows a typical DP area in the same sample with (a); (c) The image (a) after processing by ImageJ. The discontinuous precipitation area is now white.

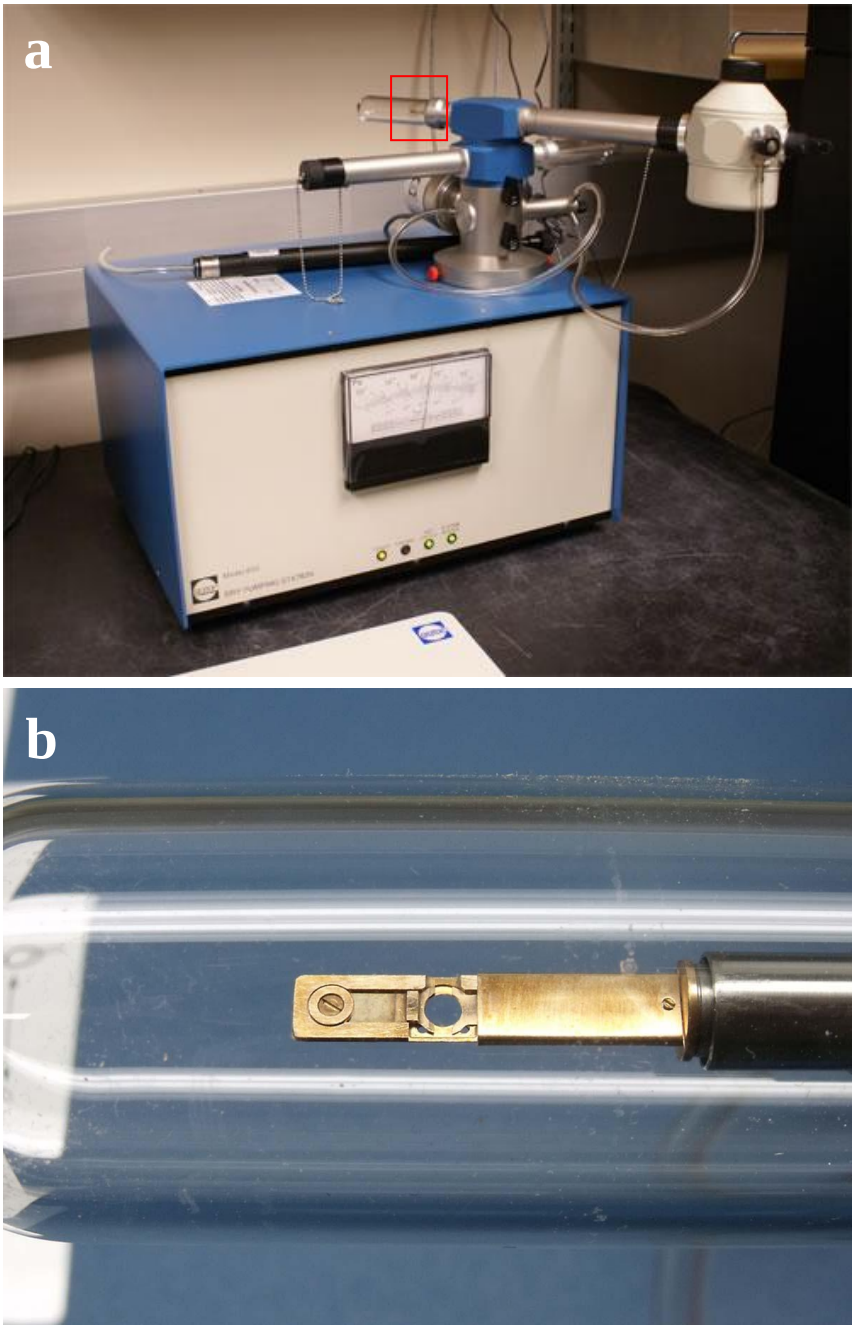

Figure 3.5. (a) Gatan model 914 High Tilt Liquid Nitrogen Cryo Transfer Tomography Holder and Gatan model 655 Dry Pumping station equipped with two holder mainfolds for storing the cryo holders. (b) The tip of the Gatan model 914 cryo holder (showing the detail of the part within the red box in (a)).

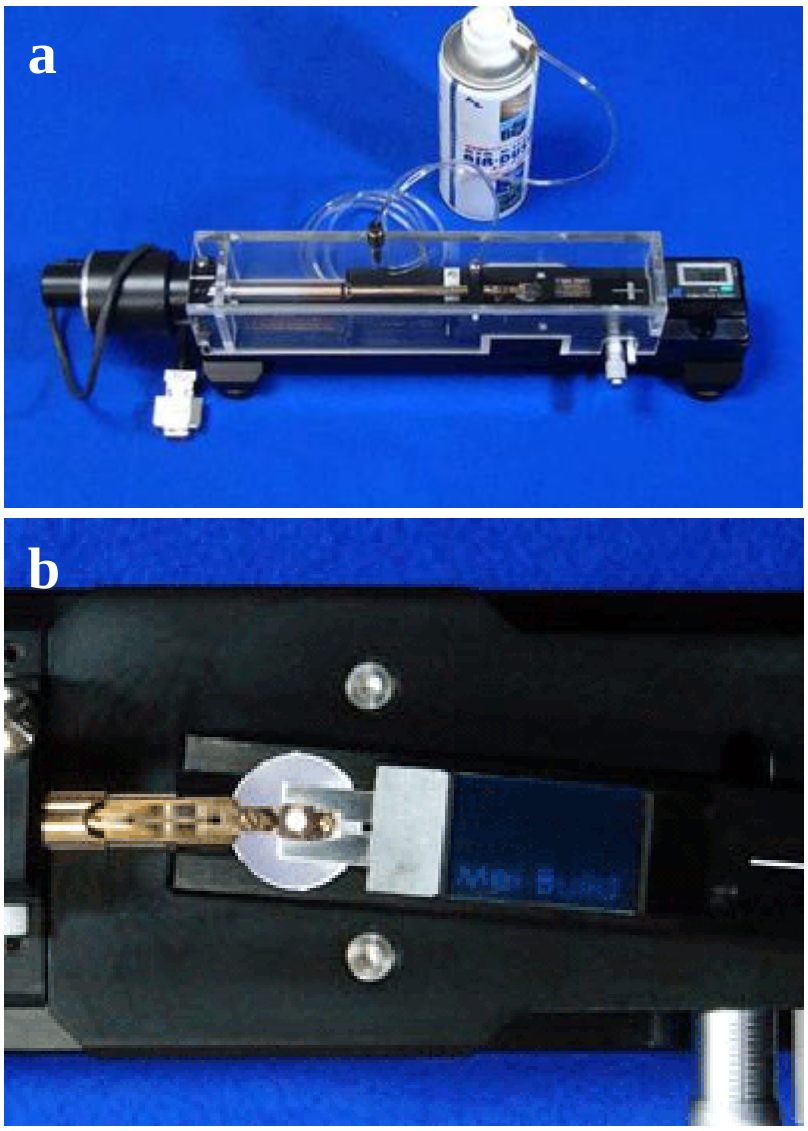

Figure 3.6. (a) High Angle Triple Axis (HATA) Holder and Index Dock System; (b) The rotation of the specimen stage in HATA holder using the micrometer in the Index Dock System.

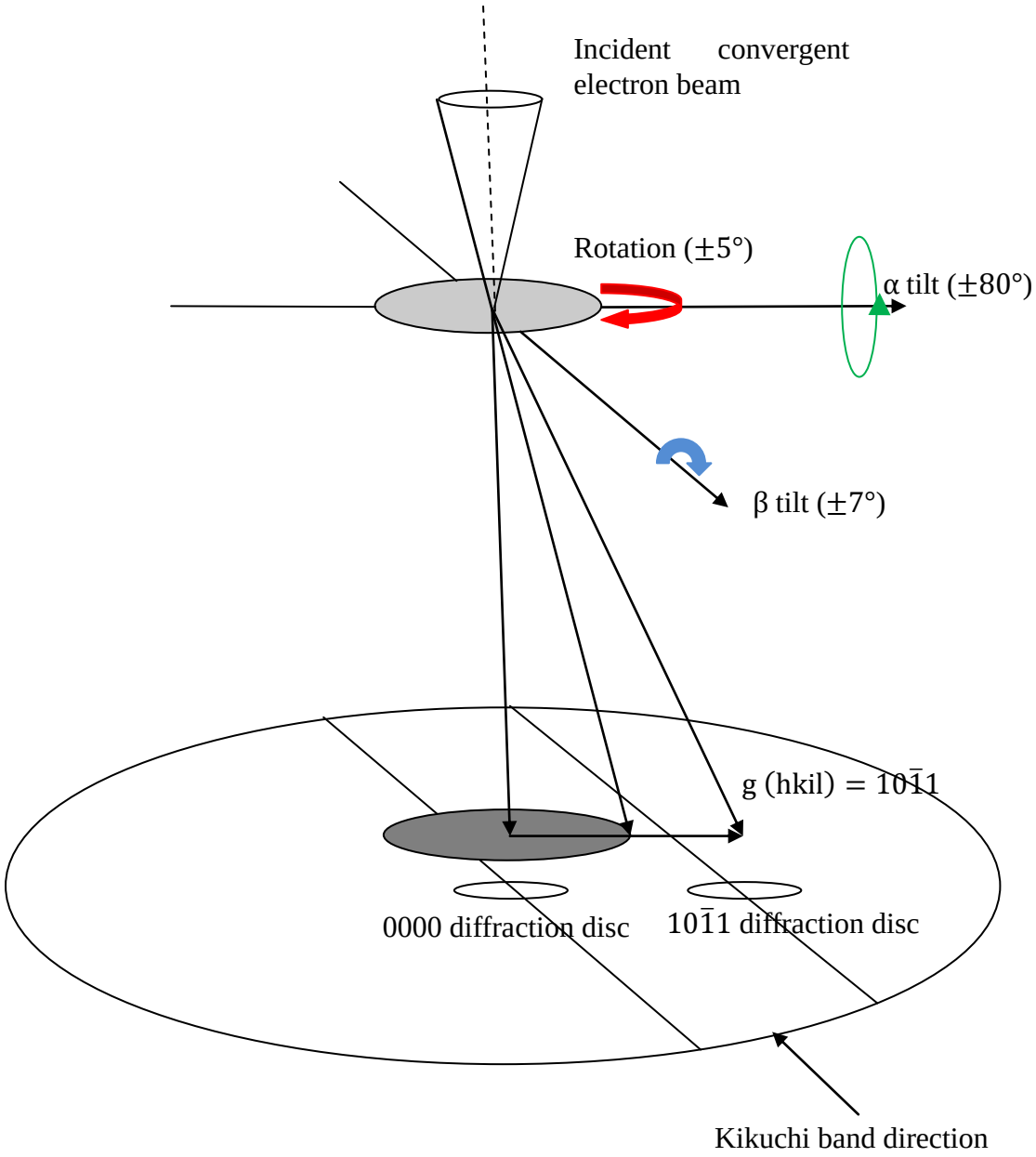

Figure 3.7. Schematic diagram of the geometry of the bright field in STEM and diffraction disk of g (hkil) = 10$\bar{1}$1. The direction of g (hkil) = 10$\bar{1}$1 is aligned with the α tilt axis of the HATA holder.

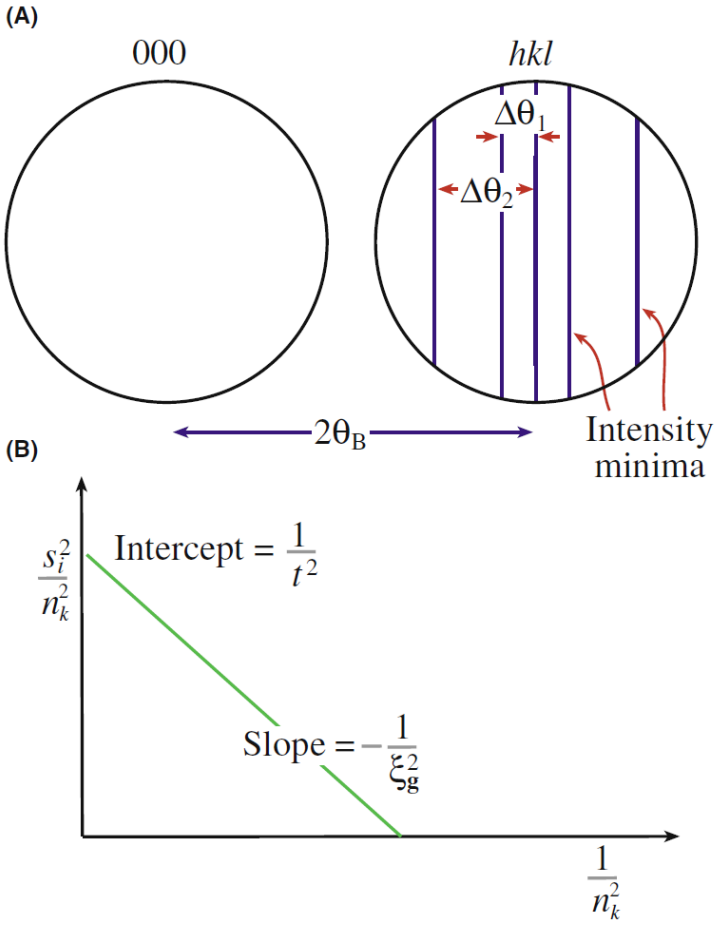

Figure 3.8. Schematic drawing illustrating the foil thickness measurement using a two beam condition convergent beam electron diffraction. (A) The measurements necessary to extract thickness (t) from K-M fringes. From n_i measured space of $\Delta\theta_i$, determine the deviation parameters s_i, then (B) plot $(s_i/n_i)^2$ against $(1/n_i)^2$. If the plot is a straight line, extrapolate to the ordinate to find t^{-2}. Hence t can be obtained.

Chapter 4 Precipitation hardening of deformed and undeformed AZ91

4.1 Introduction

Continuous precipitates (CP) contribute most hardening response of AZ91 during ageing [5], so their number density (N_V) and volume fraction are vital to its strength. In this study, two cases of preferential precipitation of CPs were observed. One is along dislocations; the other is on Al-Mn-(Mg) nano-sized particles, which are due to the Mn addition to AZ91. Since both of them can potentially increase the number density of CPs, the effect of these two mechanisms on the strength of the AZ91 are investigated here.

In this chapter, the microstructures of the undeformed and deformed AZ91 alloys during heat treatment were characterized quantitatively using a combination of OM, SEM and TEM. Based on the microstructural information obtained in the current work, some issues on the precipitation hardening of AZ91 were investigated. Firstly, some modifications were made in the published precipitation hardening model for undeformed AZ91 [6]. Secondly, attention was paid to the low N_V of CPs in AZ91. Thirdly, the role of cold work on the ageing of AZ91 was studied, including the effect of pre-deformation on (1) hardness and (2) the distribution and fraction of continuous and discontinuous precipitates.

4.2 As cast AZ91 (as-received)

Figure 4.1 (a) shows the general microstructure of the as-cast AZ91 alloy. There are many dendrites over the microstructure. Figure 4.1 (b) is a high magnification micrograph

illustrating the dendrites. According to the report in Chapter 2, the dendrite consists of eutectic α-Mg and β-$Mg_{17}Al_{12}$, which are the products of the eutectic reaction. Both of them are labeled in Figure 4.1 (b).

Figures 4.2 (a) and (b) are scanning electron microcopy (SEM) images showing the precipitates in the eutectic α-Mg of the as-cast AZ91. Both discontinuous (Figure 4.2a) and continuous precipitates (Figure 4.2b) were observed. The discontinuous precipitates (DPs) are in the size of 1-20 μm, while the continuous precipitates (CPs) are less than 5 μm. Both of them should form during the solidification after the eutectic reaction.

Typical energy dispersive x-ray (EDX) spectra obtained in Transmission Electron Microscopy (TEM) from discontinuous $Mg_{17}Al_{12}$ precipitates and the matrix are shown in Figure 4.3. The weight percentage of magnesium decreases from $(90 \pm 1.2)\%$ in the matrix to $(53 \pm 1.8)\%$ in the precipitates, while the aluminium increases from (9 ± 0.6) to $(46 \pm 1.2)\%$.

Apart from the $Mg_{17}Al_{12}$ precipitates, some other Al and Mn rich particles were also observed in the TEM, as shown in Figure 4.4. Some of them are μm in size, as shown in Figure 4.4 (a). The EDX result (Figure 4.4 (c)) from this particle shows the atomic number ratio between Al and Mn is around 59: 41, close to 8:5 and it is probably the reported Al_8Mn_5, one of the Al-Mn intermetallic phases in Mg-Al alloys [20]; the others are finely-sized (20-200nm) and exhibit various morphologies, as shown in Figure 4.4 (b). The characterization of these particles will be presented in Chapter 5.

4.3 Solution treated AZ91

Figure 4.5 (a) shows a general view of the microstructure of the AZ91 alloy after solution-

treatment and water quenching. In this optical micrograph, there are no dendrites, indicating that all the $Mg_{17}Al_{12}$ precipitates dissolved into the matrix and that a supersauturated solid solution formed.

Figure 4.5 (b) is a TEM image showing dislocations and fine particles in the solution-treated AZ91. The dislocations may be introduced by the water quenching after the solid solution, while the morphologies of the fine particles is very similar to that shown in Figure 4.4 (b). These particles will be investigated in Chapter 5.

4.4 Precipitation hardening of undeformed AZ91

4.4.1 Hardness

The age-hardening curves of the solution-treated AZ91 are shown in Figure 4.6. When aged at 200℃, the hardness of AZ91 increases steadily as a function of ageing time before reaching the peak hardness at 10h and then decreases slowly. The 250℃ ageing curve has the same tendency as that at 200℃, but the hardness values are lower. The peak hardness for 250℃ ageing was achieved after about 5h, which is 5h earlier than that at 200 ℃. This indicates an accelerated age-hardening response at higher temperature for AZ91. No hardness peak was observed for AZ91 aged at 100℃ and 150℃ within 30h, although the hardness increases steadily with ageing time. This suggests that the age hardening at these two temperatures was relatively slow. According to Celotto's study [5], the peak hardnesses at 100℃ and 150℃ reach around 85HV and 100HV after ageing for 1000h and 10000h, respectively.

4.4.2 Discontinuous precipitation

Figure 4.7 shows optical micrographs of the area taken up by discontinuous precipitates (DP)

in the AZ91 alloy aged at 200 ℃ for different times. These figures show that all the discontinuous precipitates (black area) are located on the grain boundaries and that the discontinuous precipitation area increases with ageing time. A quantitative description of the area fraction of the discontinuous precipitation is shown in Figure 4.8. In this figure, it is seen that the area fraction of the discontinuous precipitates increases rapidly from 1h to 10h and then keeps nearly constant after that. This suggests that most of the discontinuous precipitation occurs before 10 hours at 200℃.

Figures 4.9 (a) and (b) illustrate the morphologies of the discontinuous precipitates during ageing. In the early stage of ageing, nucleation of discontinuous precipitates occurs on the grain boundaries and some nodules form. They present a polygonal shape at high magnification, as shown in Figure 4.9 (a). After ageing for another 9 h, these nodules grow and form a lamellar structure, as shown in Figure 4.9 (b). This process probably corresponds to the illustration in §2.3.4.2.

4.4.3 Continuous precipitation

Due to their relatively small size, the observation of continuous precipitates by optical microscopy is difficult. The continuous precipitates are therefore characterized by SEM and TEM here. Figure 4.10 (a) is an SEM image showing both continuous and discontinuous precipitation in the AZ91 aged at 200℃ for 3h, from which a boundary can be seen between the discontinuous and continuous precipitation area. This type of boundary is illustrated in more detail using TEM at a high magnification in Figure 4.10 (b). A line scan in Figure 4.10 (c) and (d) shows that there is a change for the chemical composition of the Mg matrix across this boundary in Figure 4.10 (c) and (d). Meanwhile, the examination of Kikuchi maps reveals that there is also a change of matrix orientation between CP and DP area. These

indicate that this boundary is actually a moved grain boundary, according to the illustration in §2.3.4.2 [27].

Differently from the preferential precipitation of DP on the grain boundaries, continuous precipitation tends to happen on the dislocations in the early stage of ageing in AZ91, as shown in Figure 4.11. At this stage the precipitates are very thin and strain contrast is a better way of seeing them than absorption contrast.

In Figures 4.12, TEM images show the distribution of the continuous precipitates in samples aged for 10h at 200℃ with the beam direction close to $[0001]_m$. As can be seen from the bright field image in Figure 4.12 (a), the precipitates are closely distributed and overlap each other. In order to separate the precipitates, dark field images, figures 4.12 (b) to (d), are used. The precipitates are lath-shaped. There are three variants of CPs with their long axes close to the $\langle 11\bar{2}0\rangle_m$. These variants are separated in (b), (c) and (d). This all agrees with previous reports [5, 6].

Figure 4.13 (a) is a TEM image showing the distribution of the continuous precipitates in another sample aged for 10h at 200℃, but the beam direction is close to $[11\bar{2}0]_m$. At such a beam direction, the continuous precipitates look less closely-distributed and overlap less frequently than in Figure 4.12 (a), even though the heat treatments are identical. In addition, some other rod-shaped continuous precipitates not lying on the basal plane are also observed. Most of these are lying along $[0001]_m$, indicated by red arrows in Figure 4.13 (b). A small of fraction of them is lying at a certain angle to $[0001]_m$, as shown in Figure 4.13 (c). A 3D schematic diagram in Figure 4.13 (d) summarizes the morphologies of the continuous precipitates.

In Figure 4.12 and 4.13, the measurement of the dimensions (including length, width and thickness) of CPs is indicated with arrows. With a series of such images taken along $[0001]_m$ and $[\bar{2}110]_m$ at different ageing times, the number density and dimensions of CPs during ageing can be obtained. Figure 4.14 shows an example with beam direction close to $[11\bar{2}0]_m$. All the obtained data are listed in Table 4.1 for the calculation in §4.6.1 and §4.6.2.

The relationship between the number density of the continuous precipitates (N_V) and the ageing time is shown in Figure 4.15. $N_{current}$ and $N_{celotto}$ refer to the Nv measured in the current work and Celotto's work, respectively. In both these two cases, Nv increases rapidly from 1h to 5h, followed by a slow increase from 5h to 10h, and after that it starts to decrease slightly. The rapid increase of N_V during the first 5h ageing happens because defects, such as vacancies and dislocations, in the water-quenched samples will promote the nucleation by reducing the energy barrier. As Celotto reported [5], the number of these defects in the as-quenched AZ91 was about $10^8\ m^{-3}$. After these defects are consumed, nucleation in the defect-free matrix becomes difficult and the nucleation rate slow down. The decrease in N_V is probably due to the coarsening of the CPs, which makes some of them combine together and form larger particles.

4.4.4 Thickness

Because the measurement of N_V in TEM requires a knowledge of the foil thickness, so an example of a thickness measurement using CBED is shown in Tables 4.2 & 4.3 and Figure 4.16. Figure 4.16 (a) is a CBED pattern taken close to the $[\bar{2}110]$ using $g = 0\bar{3}31$ in AZ91 aged at 200 ℃ for 5h. The reciprocal of the inter-planar spacing, $1/d_{30\bar{3}1}$ is 6.78908 nm^{-1}. s_1, s_2 and s_3 are calculated according to Equation 3.3 [110] and listed in Table 4.2. In general, the integer 1 is assigned to the first fringe. With values of n_i = 1, 2, 3, 4, the values of

s_i^2/n_i^2 were obtained and are listed in the Table 4.2. However, it can be seen that these data are not monotonously decreasing and thus cannot plot as a straight line against $1/n_i^2$. Values of n_i = 2, 3, 4, 5 are then assumed and the corresponding values of s_i^2/n_i^2 are shown in Table 4.3. In this case, a straight line was obtained, as shown in Figure 4.16 (b). The intercept of the straight line with the ordinate, $1/t^2$, is 9×10^{-6} nm^{-2}, so the foil thickness, t, is equal to 333 nm. Due to the small atomic number of Mg, the scattering of electrons is relatively weak. Therefore, the observable sample thickness in TEM can be as thick as 450nm, according the author's experience. The thicknesses of measured area in the current work are mainly between 150 and 300 nm in the aged sample, which can normally achieve a balance between a reasonable N_A and too much overlapping of CPs.

4.5 Precipitation hardening of AZ91 after deformation

4.5.1 As-rolled samples

Figure 4.17 shows an optical micrograph obtained from a cold-rolled AZ91 with the thickness reduction of 5%. Twinning is observed in the micrograph, as indicated by the red arrows.

Transmission electron micrographs of the as-rolled AZ91 (5%) are shown in Figure 4.18. Figures 4.18 (a) and (b) show that one twin always terminates on either a grain or twin boundary. Fine dislocation arrangements can also be seen all over the matrix and within the twins. Figure 4.18 (c) is a high magnification image showing the dense dislocation arrangement in the matrix.

The dislocation substructures developed in the rolled AZ91 with 5% thickness reduction are analysed in Figures 4.19. Each of these images has been taken near the zone axis $[2\bar{1}\bar{1}0]$ in the same area. In Figure 4.19 (a), the diffraction vector $g = 01\bar{1}1$ has been used. Under this

condition, all the dislocations except some $\langle a \rangle$ types are visible. In order to know the Burger vectors of these dislocations, it is necessary to use other diffraction vectors $g = 0002$ and $g = 01\bar{1}0$. With $01\bar{1}0$ diffraction vector, all the $\langle c \rangle$ dislocations are out of contrast and only a part of $\langle a \rangle$ and $\langle c + a \rangle$ can be seen, as shown in Figure 4.19 (b). With the 0002 diffraction vector, all $\langle a \rangle$ dislocations are invisible and only $\langle c \rangle$ or $\langle c + a \rangle$ are visible, shown in Figure 4.19 (c). After comparison with these images, it is noted that most of dislocation present in Figure 4.19 (a) are $\langle a \rangle$ type dislocations, because they are not visible in Figure 4.19 (b). Also, this identifies the existence of $\langle c \rangle$ or $\langle c + a \rangle$ types dislocations in the as-rolled samples, as indicated by the red arrow in Figure 4.19 (c).

4.5.2 Hardness

Figure 4.20 shows the hardness of the as-rolled AZ91 alloys. It is shown that the hardness of the AZ91 increases from 62.0 HV to a relatively high value (from 80.2 to 94.0 HV). This indicates that the AZ91 was work-hardened. According to the reports on the strain-hardening of polycrystalline Mg [4, 5], the hardening response of Mg is mainly due to the interaction of glide basal dislocation with forest dislocations. Also, it is seen that the hardness of AZ91 increases slowly after 10% thickness reduction. This happens because the work hardening has a square root dependency on the number of dislocations [111]. Even though the number of dislocations increases with further deformation due to the multiplication of dislocations at grain boundaries and forest dislocations, the increase in strength of the alloy is limited. Since the ductility of a work-hardened material decreases with increasing deformation, 10% would be optimum the cold rolling amount (under the current experimental conditions) for AZ91 in consideration of both strength and ductility.

Figure 4.21 illustrates the hardness evolution of the AZ91 alloys with and without pre-

deformation during ageing at 200℃. It is shown that the times for all the deformed AZ91 to reach the peak hardness are reduced to 5h. In addition, the peak hardness also increases from 90 HV to nearly 110 HV. The peak hardnesses of the AZ91 with 10%, 15% and 20% rolling are very close to each other.

4.5.3 Discontinuous precipitation

Figure 4.22 shows discontinuous precipitation in the rolled AZ91 alloys at peak hardness. In these images, all the discontinuous precipitation areas are still distributed along the grain boundary, and no discontinuous precipitation is seen on the twin boundaries. Compared with Figure 4.7 (c), the discontinuous precipitation area in rolled AZ91 is substantially reduced, especially for the AZ91 with more than 5% rolling reduction. Little discontinuous precipitation can be seen in Figure 4.22 (b), (c) and (d). The area fraction of the discontinuous precipitate of AZ91 versus amount of deformation at peak hardness point is shown in Figures 4.23. Thus, for example, the area fraction of the discontinuous precipitates drops from 29.7 % to 4.4 % after 5% pre-deformation. With increasing pre-deformation, the area fraction of DP continues to decrease. With more than 10% rolling, the area fraction of DP in the whole microstructure is less than 1%. Therefore, the pre-deformation suppresses the discontinuous precipitation.

4.5.4 Continuous precipitation

Figure 4.24 shows the distribution of the continuous precipitation in the rolled AZ91 with 5% and 10% thickness reduction, after ageing at 200℃ for 1h and 5h. It can be seen that the continuous precipitates in the deformed AZ91 have a smaller size and a finer distribution than in undeformed AZ91 (as shown in Figure 4.13 and 4.14).

The relationship between the Nv and ageing time at AZ91 with 10% rolling is shown in Figure 4.25. Compared with the undeformed AZ91, it is noted that the N_V in the 200℃-5h aged alloy increases from $1.97 \times 10^{11}\ mm^{-3}$ for the undeformed AZ91 to $2.73 \times 10^{11}\ mm^{-3}$ for AZ91 with 10% rolling. The largest gap of N_V between the deformed and undeformed AZ91 happens at 1 hour ($2.54 \times 10^{10}\ mm^{-3}$ vs $1.65 \times 10^{11}\ mm^{-3}$), which corresponds to the large hardness gap at 1 hour in Figure 4.21. In the early stages of ageing, there is still a remarkable dislocation density in the deformed AZ91 and the promoting effect of dislocations on precipitation is obvious. As the ageing goes on, lots of dislocations are consumed by recovery. The promoting effect of the defects on precipitation goes down, which results in the gap in N_V between deformed and undeformed AZ91 declining.

4.5.5 Precipitates on twin boundaries

Figure 4.26 shows some nodular precipitates along a twinning boundary in the deformed AZ91 with 5% thickness reduction after 1h at 200℃. They are also common in other deformed AZ91. Compared with CPs in the matrix and twin, these precipitates are coarse. After EDX investigation, it is found that these particles only contain Mg and Al and the atomic number ratio of Mg to Al is close to that in $Mg_{17}Al_{12}$. This indicates that these precipitates are also $Mg_{17}Al_{12}$. Due to their coarse size and location, they will not strengthen the alloy so effectively as CPs.

4.6 Discussion

4.6.1 The number density of continuous precipitates (Nv)

It is shown in Figure 4.13 that the number density of continuous precipitates (N_V) during ageing at 200 ℃ from the current work, $N_{current}$, is between 2.48×10^{10} and $1.5 \times$

$10^{11}\ m^{-3}$. It is larger than $N_{celotto}$, N_V in Celloto's work [5] (4×10^9 to $8.2 \times 10^9\ m^{-3}$) , by one order of magnitude, but it is in agreement with the N_V in a recently published work on AZ91 by Stanford et al. [112]. In both this and Celotto's work, N_V is measured according to Equation 3.1 by TEM [5]. The exact way of N_V measurement in Stanford et al.'s work is not given, but it is also based on TEM [112]. In the following discussion, several factors will be considered and they may account for the large gap between $N_{current}$ and $N_{celotto}$ in Figure 4.15.

Firstly, different crystallographic directions are used to view the continuous precipitates. The foil normals of the specimens in Celotto's work were within 25° of $[0001]_m$, so N_A is counted using images taken along $[0001]_m$ and nearby. In contrast, the N_A in the current work is measured around $[11\bar{2}0]_m$, which is 90° away from $[0001]_m$. It is already known that most continuous precipitates are laths parallel to the basal plane, forming a Widmanstätten morphology [27, 113], as illustrated in Figures 4.12-4.14. A TEM image presents a 2D projection of a 3D object. Therefore, the projections of these continuous precipitates present a parallelogram shape along $[0001]_m$ and a strip shape along $[11\bar{2}0]_m$. This results in one CP lath having different projection areas along different crystallographic directions. A comparison of the total the projected area of the CPs along $[0001]_m$ and $[11\bar{2}0]_m$ is given as follows.

It is assumed that there are N precipitates lying on the basal planes within bulk AZ91. As shown in Figure 4.27, the projection of each precipitate along $[0001]_m$ is approximated as a parallelogram according to previous studies [5, 6] and the current observation. The two pairs of opposite angles of these parallelograms were assumed as 60 ° and 120 °, respectively. The directions of the long edges of these parallelograms are assumed to lie exactly and evenly along each $\langle 11\bar{2}0\rangle_m$. Figure 4.28 illustrates the dimensions of these CPs and their projections

when viewed along $\langle 11\bar{2}0\rangle_m$.

When viewed along $[0001]_m$, each precipitate takes up the projected area, l × w. The sum of the projection area of the CPs is:

$$s_{0001} = N \times l \times w$$

When viewed along one of the $\langle 11\bar{2}0\rangle_m$, one third of the CPs lie along the viewing direction and each of them has a projected area, w × t, such as A and B in Figure 4.27. Another one third of CPs are not lying along the viewing direction, such as C and F in Figure 4.27. Their long edges are 60° away from the viewing direction and the projected area for each of them is $\frac{\sqrt{3}}{2} l \times t$. For the remaining one third of CPs, marked D and E, their long edges are also 60° away from the viewing direction, but their projection is longer than that of C and F by a length of w, as indicated in Figure 4.28. Consequently, the sum of the projected area of these CPs is:

$$s_{11\bar{2}0} = \frac{1}{3} N \times w \times t + \frac{1}{3} N \times \frac{\sqrt{3}}{2} l \times t + \frac{1}{3} N \times \left(\frac{\sqrt{3}}{2} l + w\right) \times t$$

Thus,

$$\frac{s_{11\bar{2}0}}{s_{0001}} = \frac{\frac{1}{3} N \times w \times t + \frac{1}{3} N \times \frac{\sqrt{3}}{2} l \times t + \frac{1}{3} N \times \left(\frac{\sqrt{3}}{2} l + w\right) \times t}{N \times l \times w}$$

$$= \frac{\frac{1}{3} N \times w \times t + \frac{2}{3} N \times \frac{\sqrt{3}}{2} l \times t + \frac{1}{3} N \times w \times t}{N \times l \times w}$$

$$= \frac{2t}{3l} + \frac{\sqrt{3}t}{3w}$$

Due to the lath shape of the continuous precipitates, a relationship $l > w > t$ is always satisfied. Meanwhile, as shown in Table 4.1, $\frac{t}{w}$ is always around 1/3 and the maximum $\frac{t}{w}$ is 51/146 at 15h.

Therefore,

$$\frac{t}{l} < \frac{t}{w} \leq \frac{51}{146}$$

And

$$\frac{2}{3} + \frac{\sqrt{3}}{3} \approx 1.244$$

So,

$$\frac{s_{11\bar{2}0}}{s_{0001}} = \frac{2t}{3l} + \frac{\sqrt{3}t}{3w}$$

$$< \frac{2t}{3w} + \frac{\sqrt{3}t}{3w} = \left(\frac{2}{3} + \frac{\sqrt{3}}{3}\right) \times \frac{t}{w}$$

$$\leq \left(\frac{2}{3} + \frac{\sqrt{3}}{3}\right) \times \frac{51}{146} \approx 0.434$$

$$< 1$$

That is $s_{11\bar{2}0} < s_{0001}$

This indicates that the sum of projection area of all precipitates along the $\langle 11\bar{2}0\rangle_m$ is always smaller than that along $[0001]_m$. For example, according to literature [5], the ratio between l, w and t was 11:2.5:1 in the peak aged AZ91 at 200℃ (10h). With such a ratio, the value of $\frac{s_{11\bar{2}0}}{s_{0001}}$ is close to 1/4, which means that projected area of precipitates along $\langle 11\bar{2}0\rangle_m$ is only one fourth of that along $[0001]_m$. Since the viewing area at a given magnification in a TEM micrograph is fixed, a smaller projected area of the CP can reduce the possibility of overlapping of the CPs and the area of overlap. Thus, the CPs would look less crowded along $\langle 11\bar{2}0\rangle_m$ than along $[0001]_m$, and this makes the CPs easier to distinguish from each other. This can be verified in the real microstructures shown in Figure 4.12 and 4.13. In Celotto's work, most precipitates are imaged along $[0001]_m$. This condition may make some small precipitates invisible, thus underestimating N_V.

Secondly, some nano Al-Mn particles were found in the current work. Their behaviours during heat treatment will be studied in Chapter 5. One aspect is that they can be preferential nucleation sites for the continuous precipitates. This will potentially increase N_V. In Celotto's work [5], such preferential nucleation of CP was not reported. Therefore, the extra nucleation sites for CP in the current work may contribute to make the $N_{current}$ larger than $N_{celotto}$.

The last, but only a possible reason is that most of the images provided in Celotto's paper were dark-field TEM images. With N_A in these dark field TEM images and an estimated foil thickness (150-250nm), an N_V in the range from 10^9 to 10^{10} m^{-3} can be obtained, which is in good agreement with Celotto's result. If such an imaging mode were used to measure N_A in Celotto's work, the $N_{celotto}$ will be largely underestimated, because one dark field image makes only a fraction of precipitates visible. An example was shown in Figure 4.12.

As seen for Figure 4.15, the gap between $N_{current}$ and $N_{Celotto}$ increases with the ageing

time at 200℃. This is because different factors affecting N_V dominate at different stages of ageing. In the initial stage of ageing (within 1hour), precipitates are few and far away from each other, as shown in Figure 4.14 (a) and (b), so the probability of overlapping is small. Under this situation, it is easy to distinguish one precipitate from the others along both $\langle 0001 \rangle_m$ and $\langle 11\bar{2}0 \rangle_m$. However, due to preferential precipitation of CPs on the Al-Mn-(Mg) particles, the nucleation rate of CP in the current work is increased. In the initial stages of ageing, most of the $Mg_{17}Al_{12}$ precipitates in a discontinuous way on the grain boundaries. This is probably because the high diffusion rate of Al along the grain boundary makes the discontinuous precipitation easier than continuous precipitation. Even though the Mn content is limited in the current AZ91 alloy, the Al-Mn-(Mg) particles are locally distributed. This means that they have a remarkable number density in a local volume and can provide considerable extra nucleation sites for CPs. Therefore, even a limited number of Al-Mn-(Mg) nano-sized particles can increase $N_{current}$ significantly in local volume of the AZ91.

As the ageing goes on, more and more precipitates nucleate and grow to a larger size, as shown in Figures 4.12 (b)-(d). Overlapping of precipitates becomes more and more frequent in the TEM images. Apart from the influence from the Al-Mn-(Mg) particles, the viewing direction starts to affect the measured N_V. As discussed above, $N_{Celotto}$ may be an underestimate due to the increasing overlapping of CPs along $[0001]_m$, while $N_{current}$ is less influenced, because there would be less overlap along $\langle 11\bar{2}0 \rangle_m$. Therefore, the gap between $N_{current}$ and $N_{Celotto}$ increases with the growth of CPs.

In summary, more than one of the factors mentioned above may have contributed to the difference between $N_{celotto}$ and $N_{current}$ and they dominate at the different stages of ageing. It is also worth noting that an appropriate crystallographic direction for measuring N_V can reduce effectively the probability of overlap of the precipitates and make the measured N_V

more accurate.

4.6.2 The calculated strength of AZ91

In previous years, several models have been used for predicting the strength of AZ91 [6, 38]. In these models, the total strength of AZ91 after ageing originates from grain size strengthening, solid solution strengthening, Orowan strengthening and work hardening, as shown in Equation 2.2. In Hutchinson et al's work [6], the estimated strength is in good agreement with the converted experimental strength. However, according to the author's understanding, the N_V and percentage of CPs used in this model are inaccurate and they need to be modified.

Firstly, most data used in this work, including the N_V, were based on Celotto's paper [5]. According to Equation 2.1, N_V is crucial for the strengthening contribution from the precipitates, σ_{Orowan}. Due to the large difference between $N_{celotto}$ and $N_{current}$, as discussed in the last section, it is necessary to re-visit the model using the parameters measured here.

Since the composition and ageing temperature in the current work were the same as those in Hutchison et al.'s work [6], the estimated strengthening contributions from the solid solution strengthening and work hardening are reproduced here as he had them. The contributions from the precipitation and grain size are calculated using the parameters measured here. The strength derived from the hardness in [6] is also used to compare with the calculated strength in the current work.

Grain size strengthening:

According to grain size measurements of the solution treated AZ91, such as that shown in Figure 4.5 (a), the grain size, d, for the AZ91 is round 300 μm. Therefore, the grain size

strengthening is

$$\sigma_{gs} = \sigma_0 + kd^{-1/2} \quad \text{(Equation 4.1)}$$

$$= 11 + 21.3 = 32.3 \text{ MPa}$$

Orowan strengthening:

The calculation of the strength from the Orowan strengthening is based on Equation 4.2 [43].

$$\sigma_{\text{Orowan}} = \frac{\text{MGb}}{2\pi(1-\nu)^{\frac{1}{2}}} \frac{\ln(d_A/r_0)}{\lambda} \quad \text{(Equation 4.2)}$$

where M is the Taylor factor (taken as 4.5 [114]), G is the shear modulus of the matrix; b is the Burgers vector of the dislocations; ν is Poisson's ratio; λ and d_A are, respectively, the mean spacing and mean diameter of the particles in the slip plane and r_0 is the inner cut-off radius of the dislocations taken equal to b.

According to the approximation in [6], the λ and d_A were calculated using Equations 4.3 and 4.4 [6], respectively.

$$d_A = \frac{3.6w}{2} \quad \text{(Equation 4.3)}$$

$$\lambda = \frac{1}{\sqrt{N_V t}} - d_A = \frac{1}{\sqrt{N_V t}} - \frac{3.6w}{2} \quad \text{(Equation 4.4)}$$

Nv, t and w are taken from Table 4.1. The contributions of each strengthening mechanism and the overall strength of the alloy are shown in Table 4.4.

The overall strength is plotted against the ageing time, referred to as "all CP mode" in Figure 4.29. Compared with the strength converted from the hardness, referred as to "Experimental" in Figure 4.29, the "all CP mode" predicts a higher strength than "Experimental". This may

be attributed to the difference in the consideration of DP and CP between the model and the real microstructure, which will be discussed in the following paragraph.

It is known that both CPs and DPs co-exist in the aged AZ91 over a wide range of temperatures [25, 35], as illustrated in Figure 4.30. In many studies of precipitation hardening in AZ91 [5, 6, 38], CPs are considered to be responsible for most of the strengthening due to their fine distribution. The contribution of DPs to strength is always neglected. This is actually a reasonable approximation, because DPs have a much larger size than CPs, as shown in Figure 4.10. In Hutchinson et al.'s model [6], equation 4.2-4.4 were used with Nv of the continuous precipitates only. This actually assumes that all the $Mg_{17}Al_{12}$ are CPs over the whole microstructure. Such an "all CP mode" forces all the DP in the microstructure to be replaced by CP, as shown in Figure 4.30, rather than the contribution of strengthening from DP being ignored. In fact, there is a noticeable presence of discontinuous precipitates during ageing of the undeformed AZ91 (~ 30%) at 200℃, as shown in Figure 4.7 and 4.8.

To include the presence of DPs in the alloy, it is necessary to modify the contribution of the Orowan strengthening. In the current work, the contribution of Orowan strengthening was reduced according to the equilibrium proportion of the CP in the microstructure, as shown in Equation 4.5. This is actually a "Partial CP model".

$$\sigma_{Orowan} = (1 - \alpha) \times \sigma_{Orowan}^{CP} \qquad \text{(Equation 4.5)}$$

where σ_{Orowan}^{CP} is the contribution of the Orowan strengthening calculated based on Equation 4.2 and with the measured precipitate density and dimensions. α is the equilibrium area fraction of the DP in the microstructure.

According to Figure 4.8, the equilibrium area fraction of the DP in the microstructure at

200℃ is around 30%. Therefore, the increment of strength from precipitation in table should be reduced by 30%. As shown in Figure 4.29, the resulting calculation from the "Partial CP model" is closer to the experimental results.

However, the calculated strength is still a drift from the experimental data at some points, such as 1h and 10h. This is because there are still several problems existing in the current model. Firstly, the total strength is the direct sum of all the strength mechanisms and the interaction between these mechanisms is not considered. Secondly, α is an equilibrium area fraction of DPs. Whether the contribution of the Orowan strengthening should be reduced proportionally by α still needs to be considered.

4.6.3 The number density of precipitates in AZ91 and Al alloys

Previous studies [5, 6] reported that compared with many widely used Al alloys, CPs in AZ91 has a low number density of precipitates and this results in a low strength of AZ91. However, the reason for the low number density of CPs has not been clearly discussed yet. In this section, this issue is considered and two possible reasons are discussed.

4.6.3.1 Precipitation Sequences

As mentioned in Chapter 2, many Al alloys have a precipitation sequence as follows:

GP zones→ transition phase → equilibrium phase.

With such a sequence, especially the GP zones, the activation energy barrier for nucleation is lower than that for the direct precipitation of the equilibrium phase. This increases the nucleation rate and therefore results in a fine precipitate distribution.

Table 4.5 [115] indicates the precipitation sequences in some common magnesium alloys. It

is evident that GP zones are also common in Mg alloys. However, AZ91 is an exception. The equilibrium phase, $Mg_{17}Al_{12}$, precipitates directly from the matrix without GP zones or any transition phase. Most $Mg_{17}Al_{12}$ precipitates have a Burgers OR ($(0001)_m$// $(0\bar{1}0)_p$ and $[2\bar{1}\bar{1}0]_m$//$[111]_p$) with the matrix [5, 6, 116], and the interfaces between the matrix and them are either semi-coherent or incoherent [27]. The activation energy barrier for nucleation of such precipitates is much higher than for a coherent GP zone. Therefore, the nucleation rate is lower, resulting in a small number density of coarse precipitates. Actually, similar situations also happen for some Al alloys quenched and aged above the GP zone solvus. For example, when a typical Al-Zn-Mg alloy is heated to above ~155℃, no GP zone forms during the heat treatment[117]. There are no easy nucleation sites for the subsequent precipitation, which results in a coarse dispersion of precipitates with nucleation on the dislocations [117]. On the other hand, some RE containing magnesium alloys with GP zone or other coherent precipitates have quite good precipitation hardening strength [118-121]. One of the example is the reported Mg-Gd-Y alloy shows high tensile strength exceeding 400 MPa after rolling and heat treatment [121].

4.6.3.2 Diffusion Rate

The formation of the $Mg_{17}Al_{12}$ precipitates in AZ91 depends on the diffusion of Al atoms through the Mg matrix. Recently, Brennan et al. [122] estimated the impurity diffusion coefficients of Al in Mg, D_{Al}^{Mg}, and Mg in Al, D_{Mg}^{Al}, which agree well with previous work [123]. They found that D_{Al}^{Mg} is an order of magnitude lower than D_{Mg}^{Al}, as shown in Table 4.6 [122]. The slow diffusion of Al through Mg makes the nucleation of the $Mg_{17}Al_{12}$ precipitates difficult compared with that of precipitates in Al-Mg alloys in the early stages of ageing, which leads to a low nucleation rate and precipitate number density.

In summary, no nucleation of GP zones during $Mg_{17}Al_{12}$ precipitation and the relatively low diffusion of Al through Mg matrix are two reasons for the low precipitate number density in AZ91.

4.6.4 Effect of pre-deformation on the precipitation hardening

§4.5 demonstrated that pre-deformation can be used to modify the hardness and microstructure of AZ91 during ageing. This effect will be discussed here.

4.6.4.1 The optimum pre-deformation for hardness (on a macroscopic scale)

As mentioned in Chapter 2, pre-deformation can lead to a more dispersed and uniform distribution of precipitates in many Al and Mg alloys, but excessive pre-deformation often causes coarsening and a heterogeneous distribution, which are deleterious to the strength of the alloy [52]. In the current study, upon 10% pre-deformation, AZ91 can achieve a maximum peak hardness of 108.6 HV during ageing at 200 ℃. Although 15% and 20% rolling can achieve a similar peak hardness (108.0 HV and 108.8 HV), the large deformation makes the alloy suffer the risk of cracking due to the lower ductility. Therefore, in consideration of the combination of strength-ductility of the alloy, a favourable pre-deformation for AZ91 is about 10% for subsequent ageing at 200℃, which increases the peak hardness by 13.7%. This is attributed to the "grain refinement" effect from twins and the increased N_V of the continuous precipitates, which will now be discussed.

4.6.4.2 The control of CP and DP by pre-deformation (on a microscopic scale)

Due to its poor strengthening effect, the DP is preferably to be avoided or at least reduced, while CP is desirable. In previous studies [25, 35], it was found that the ageing temperature can affect the volume ratio between CP and DP. High ageing temperature (i. e. close to solves

temperature) and low temperature are reported to encourage CP and suppress DP, while an intermediate temperature is good for discontinuous precipitation [35]. However, reducing DP via temperature control during ageing is limited and may cause either fast coarsening of CPs or a considerably long ageing time. Therefore, other effective and economical ways to remove DPs from the microstructure are needed.

In the current study, pre-deformation was found to suppress the DP effectively. The DP can almost be avoided by pre-deformation, as shown in Figure 4.22. As seen in Figure 4.23, the DP area fraction can be reduced to less than 1% by cold rolling with 10% thickness reduction using rolling. This potentially provides a way of tailoring the microstructure of the AZ91. There are two reasons for this.

Firstly, twin boundaries can impede the growth of DP. Due to the limited slip systems, twinning is desirable for the coordination of strain in hcp materials. As shown in Figure 4.22, twins are increasingly prominent with increasing deformation, especially noticeable after 5% rolling. Lamellar DPs always start on grain boundaries and move towards the grain interiors. It is therefore likely that they interact with the twin boundaries close to the grain boundaries. According to previous studies [54, 124], the lamellar DPs will stop when coming to a twin boundary and such a mechanism will therefore suppress the growth of DP.

Secondly, the rolling introduces a high density dislocation network, as shown in Figure 4.18 (c). These dislocations provide easy nucleation sites for CPs, accelerating the continuous precipitation. In comparison to the undeformed AZ91, both the number density and the CP area fraction are increased, as shown in Figures 4.23 and 4.25. Since the Al content in the alloy is fixed, the increased continuous precipitation will suppress the discontinuous precipitation.

Since DPs are nearly removed and CPs has a finer distribution due to pre-deformation, the strength of AZ91 is supposed to be largely increased after pre-deformation. However, as shown in Figure 4.21, all the peak hardnesses of the deformed AZ91 are less than 110HV. Compared with the undeformed AZ91 (95.2 HV), the increment is limited. This happens because many coarse $Mg_{17}Al_{12}$ nodules form on the twin boundaries, as show in Figure 4.26. Although these $Mg_{17}Al_{12}$ nodules may have certain strengthening effect against twin growth, they do not act as such a good strengthener as the CPs for slip due to their coarse size. Meanwhile, the formation of these nodules consumes a large amount of Al and compresses the continuous precipitation. This may be responsible to the slight increase for the N_V in the deformed AZ91, as shown in Figure 4.25 and thus make the increment of the peak hardness not so large as expected. In addition, it is also worth to notice that the increase of the peak hardness should be partially attributed to the high dense twins in the deformed AZ91. This is because each twin can be considered as a "grain" with different orientation with the adjacent matrix. The bulk materials would be strengthened by finer "grain size". This strengthening contribution can be estimated by calculation of hardness-converted yield stress (e. g. Figure 4.29) and the contribution of other strengthening mechanisms (e. g. Table 4.4).

4.6.4.3 Precipitation and Recovery

It is also worth noting that no recrystallization has been observed in all the cold-rolled samples during ageing at 200 ℃. In addition, it can be seen in Figure 4.18 (c) and Figure 4.22 that the dislocation density is reduced largely during the ageing. This indicates that recovery takes place. Therefore, the ageing process of deformed AZ91 at 200℃ actually involve both precipitation (hardening) and recovery (softening). The hardness increment in Figure 4.21 is thus the combined result of both hardening and softening.

4.7 Conclusions

1. The range of N_V measured in the current work is larger than that in Celotto's work by one order of magnitude. The $\langle 11\bar{2}0\rangle_m$ viewing direction and the existence here of Al-Mn-(Mg) nano-sized particles are probably the main causes.

2. The crystallographic direction used for viewing the precipitates affects the overlapping of the precipitates when N_V reaches a certain level. Compared with [0001], $[11\bar{2}0]$ can significantly reduce such overlapping in AZ91.

3. Compared with most precipitation hardenable Al alloys, N_V in AZ91 is still low. No GP zones and the relatively low diffusion rate of Al in Mg are the likely reasons.

4. In Hutchinson et al's modelling of the precipitation hardening, DP is replaced by CP, rather than being ignored. Here the DPs are ignored and the calculated strength from CPs (based on Equation 4.2) is reduced according to the metallographic evidence.

5. Pre-deformation increases the hardness of the aged AZ91. 10% rolling reduction is considered to be a favourable amount of pre-deformation under the current experimental conditions, increasing the peak hardness of AZ91 by 13.7%.

6. Twins play an important role in the precipitation of deformed AZ91. Although they impede discontinuous precipitation and increase the area fraction of CPs, they promote nucleation and coarsening of $Mg_{17}Al_{12}$ nodules, which decreases the strength. The high density dislocations increase the N_V of the CPs in the deformed AZ91.

7. The early stage of ageing of deformed AZ91 at 200℃ actually involves both precipitation (hardening) and recovery (softening). The hardness is a combined result of both the hardening and softening.

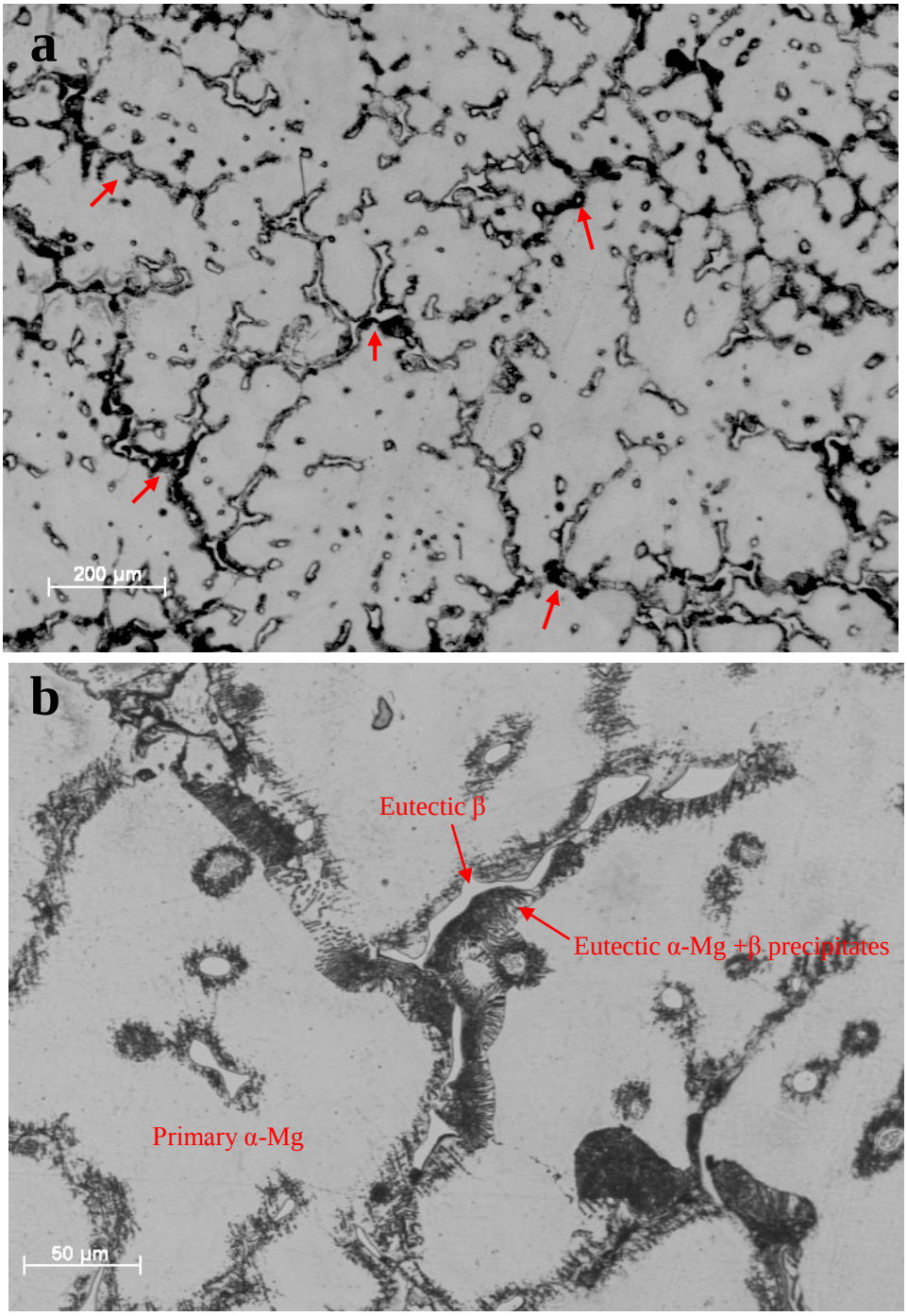

Figure 4.1. Optical microscopy images showing (a) the general microstructure of the as-cast AZ91 alloy (some of the dendrites are indicated by the red arrows). (b) dendrite structure composed of eutectic α-Mg and β-$Mg_{17}Al_{12,}$ both indicated by red arrows.

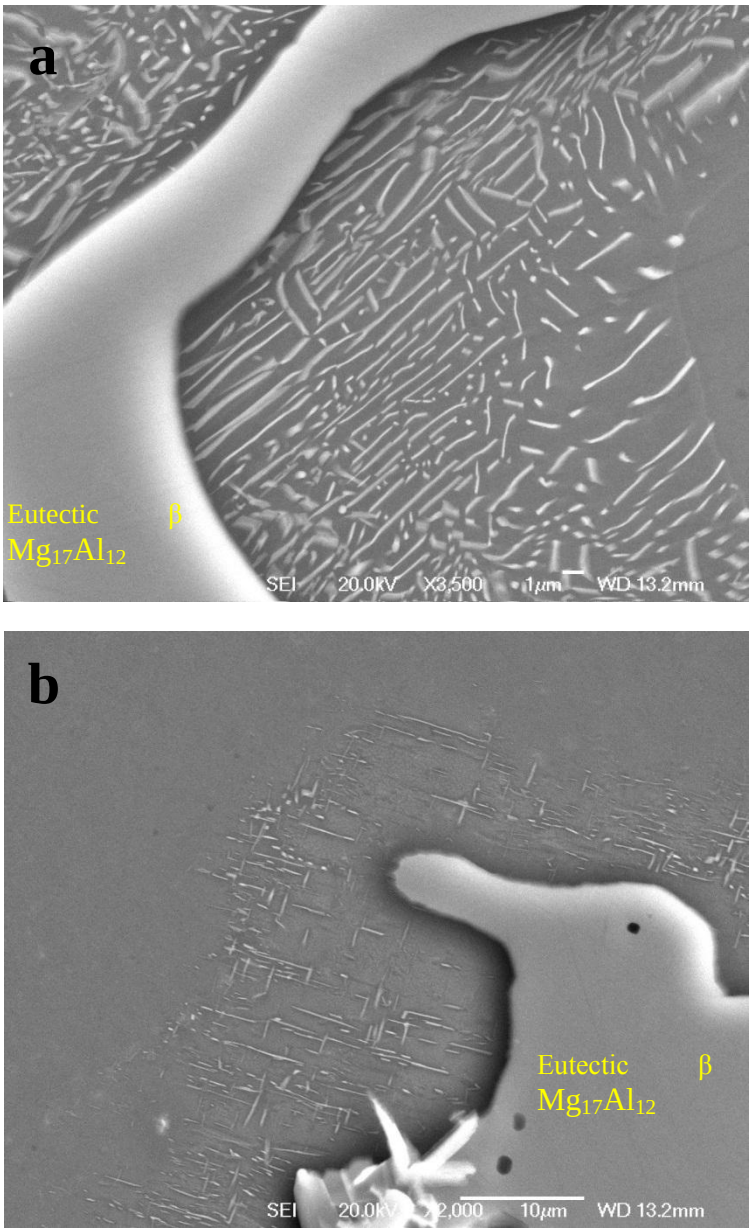

Figure 4.2 SEM images showing the morphologies of (a) DP (discontinuous precipitates) and (b) CP (continuous precipitates) in the eutectic α-Mg of the as cast AZ91.

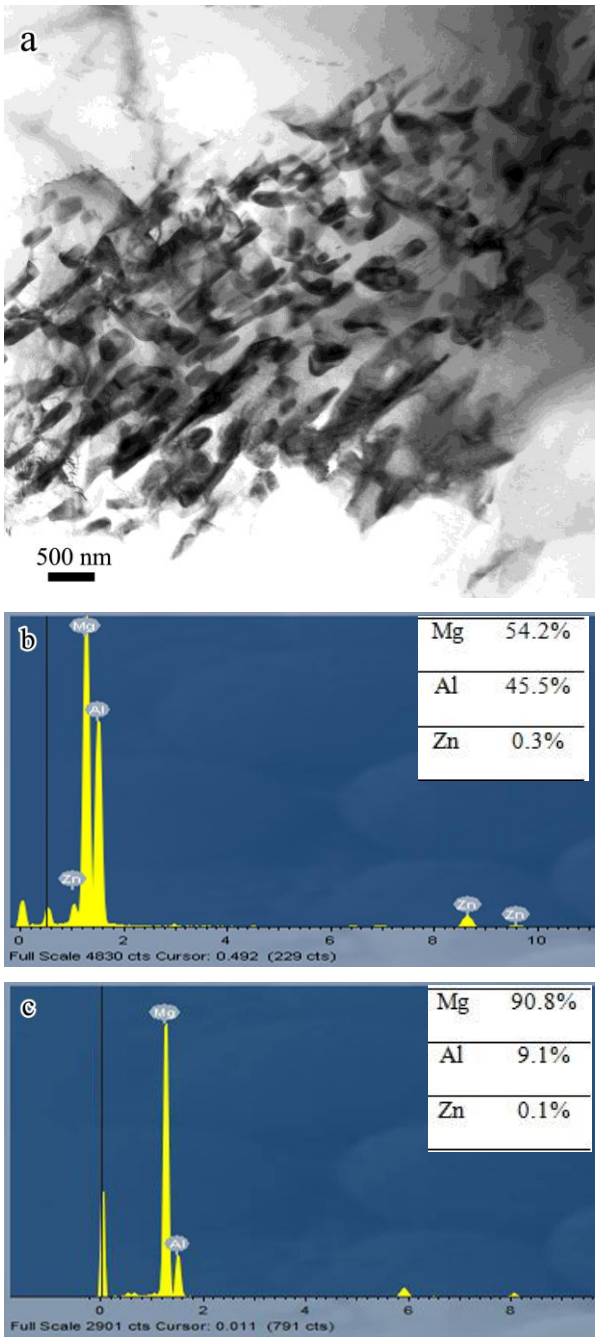

Figure 4.3. (a) The typical TEM image showing DPs in the as-cast AZ91 and EDX results obtained from (b) the precipitates and (c) the Mg matrix. The weight percentage of each element is shown in the inside in Figure (b) and (c).

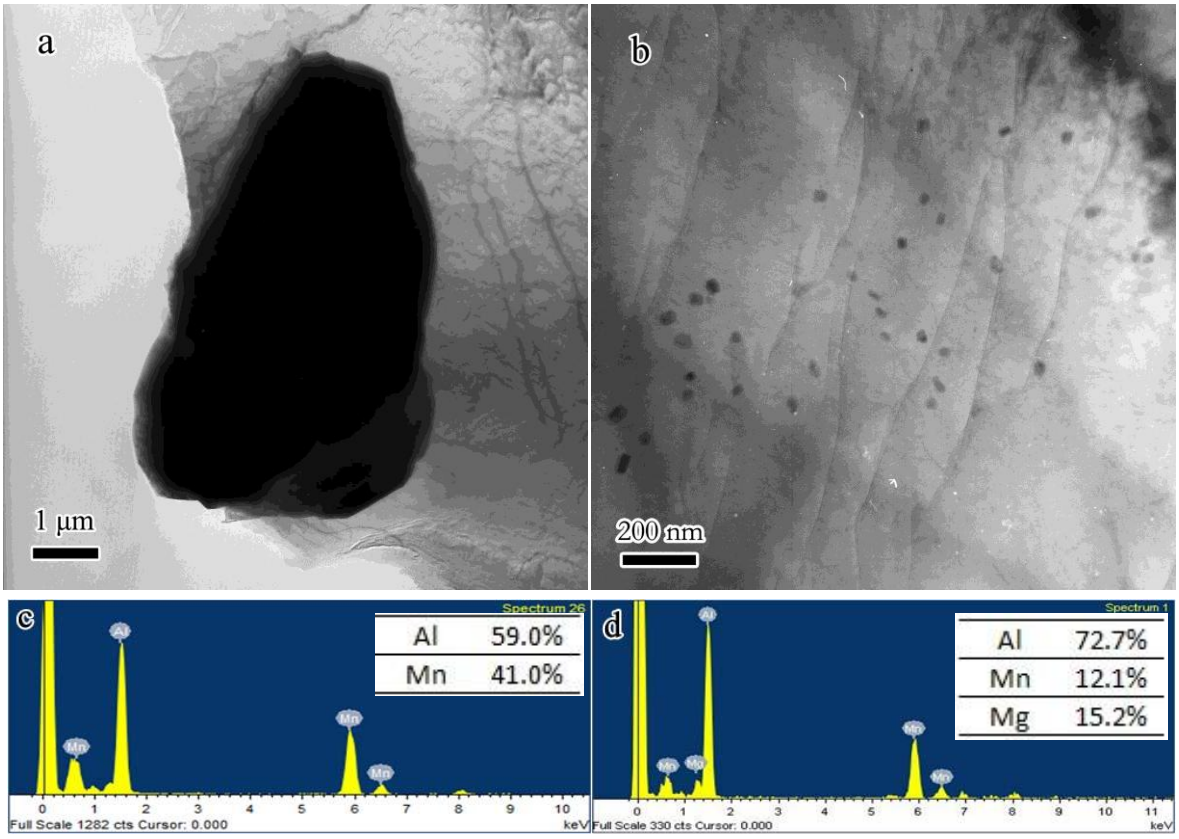

Figure 4.4. TEM images showing the existence of Al-Mn containing particles with different sizes in the as-cast AZ91: (a) micron-sized and (b) nano-sized. (c) and (d) are the corresponding EDX spectrums obtained from the particles in (a) and (b), respectively. The atomic percentage of each element is shown in the inside in Figure (c) and (d).

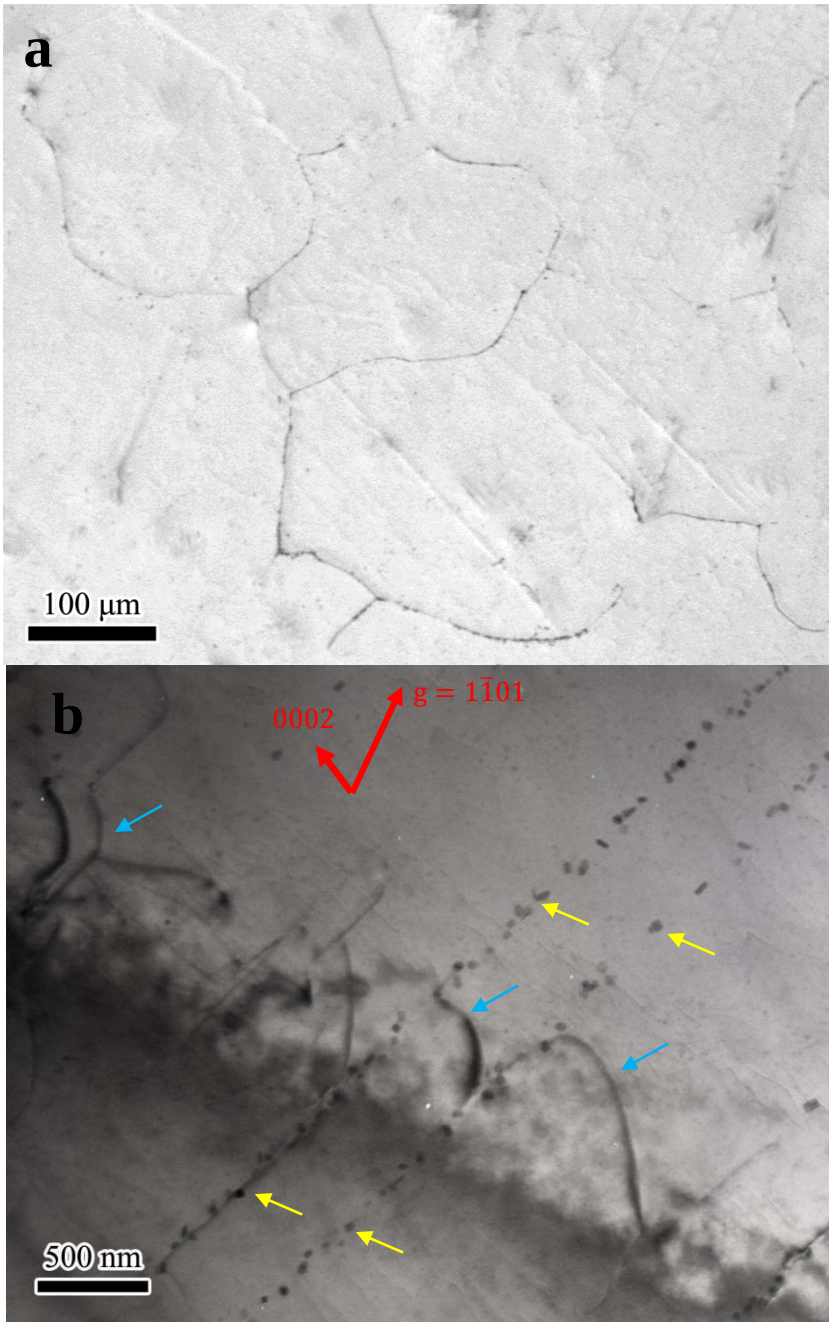

Figures 4.5. Microstructure of the solution-treated AZ91: (a) An optical image showing the absence of a dendrite network; (b) A TEM micrograph showing dislocations and fine-sized particles, indicated by blue and yellow arrows, respectively. BD~ $[11\bar{2}0]$ and g = $1\bar{1}01$.

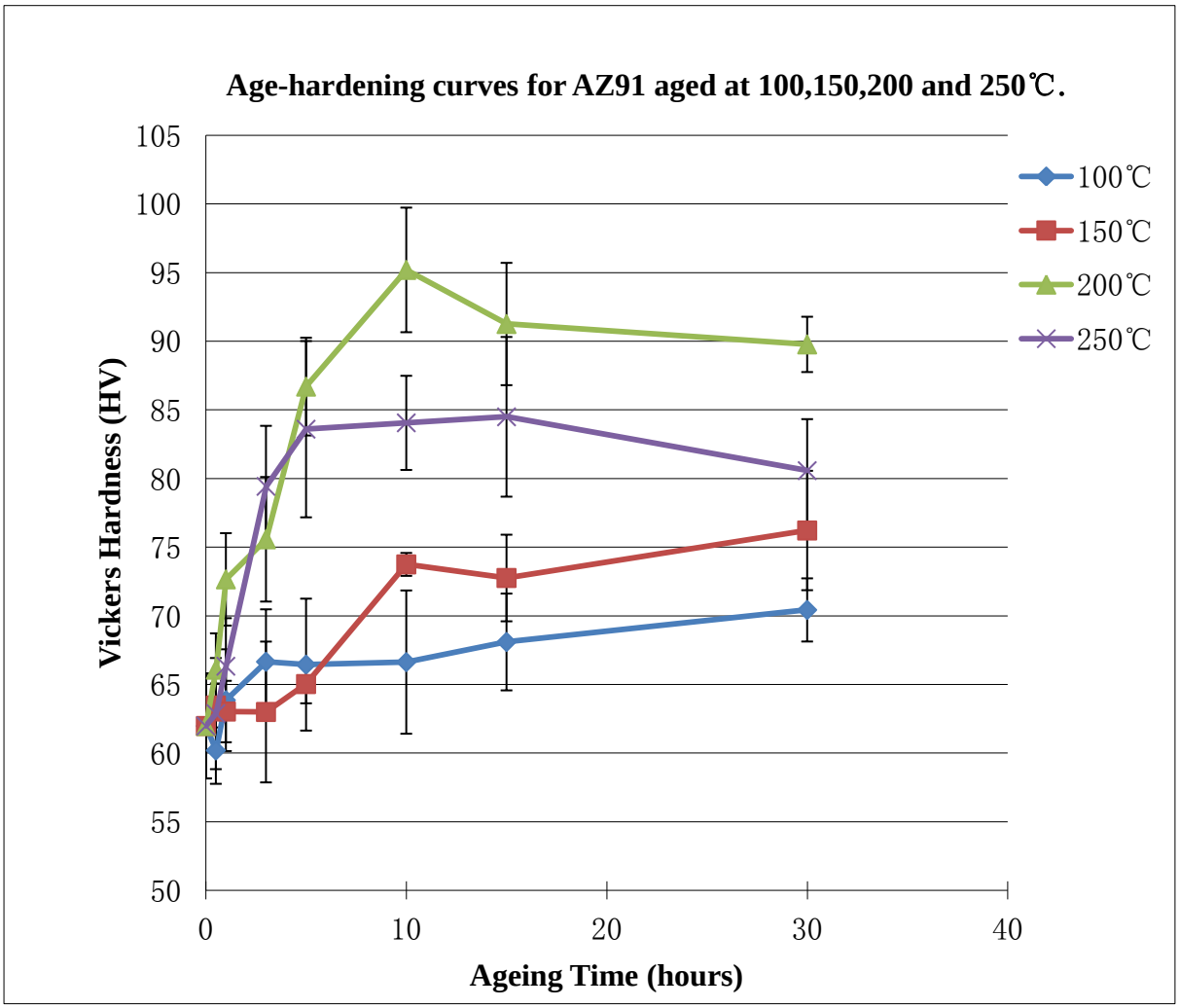

Figure 4.6. Hardness evolution of undeformed AZ91 during ageing at 100 ℃, 150 ℃, 200 ℃ and 250 ℃. (Note that the hardness is on a scale from 50 to 105 HV.)

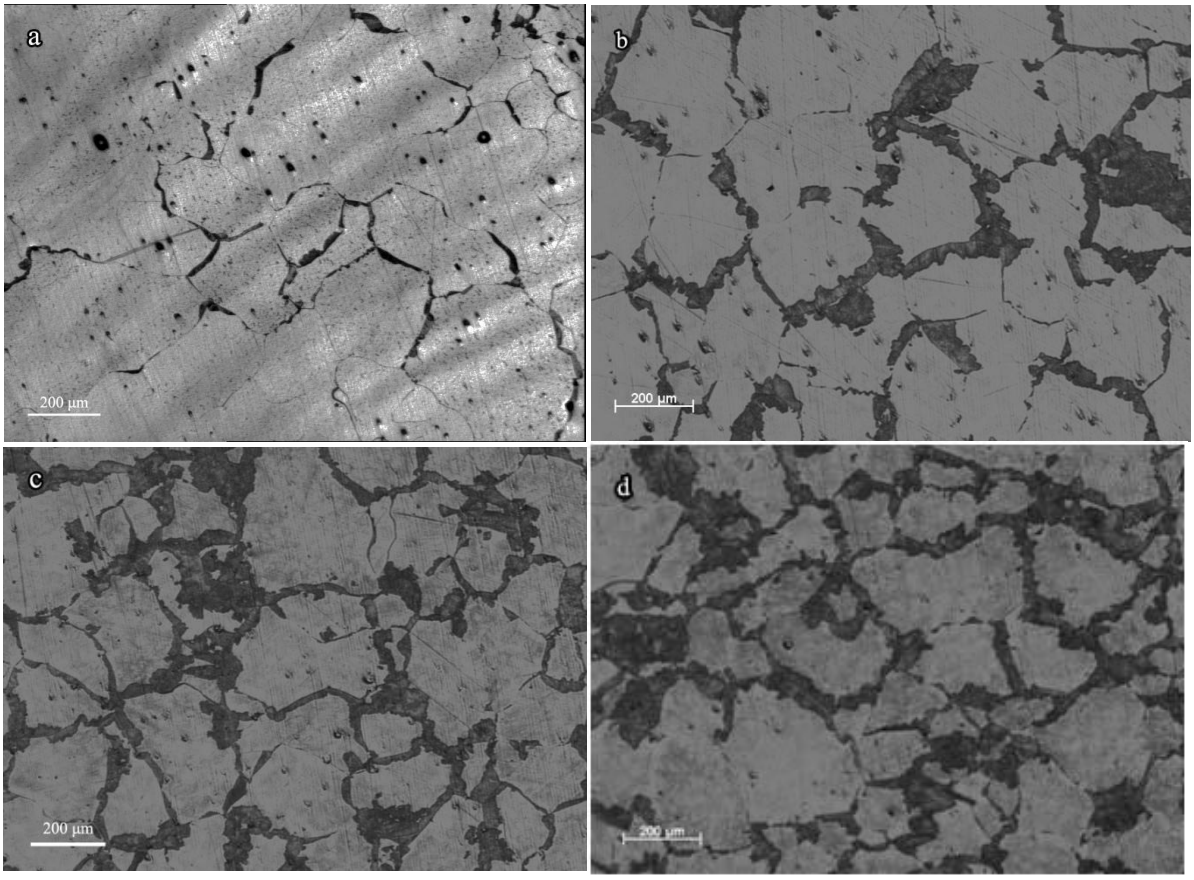

Figure 4.7. Optical micrographs showing the evolution of the discontinuous precipitation during ageing at 200℃ for (a) 1h; (b) 5h; (c) 10h; (d) 30h. The area with low intensity along the grain boundaries in the micrographs is taken up by discontinuous precipitates. The stripe contrast in (a) is probably due to the strain introduced during sample preparation.

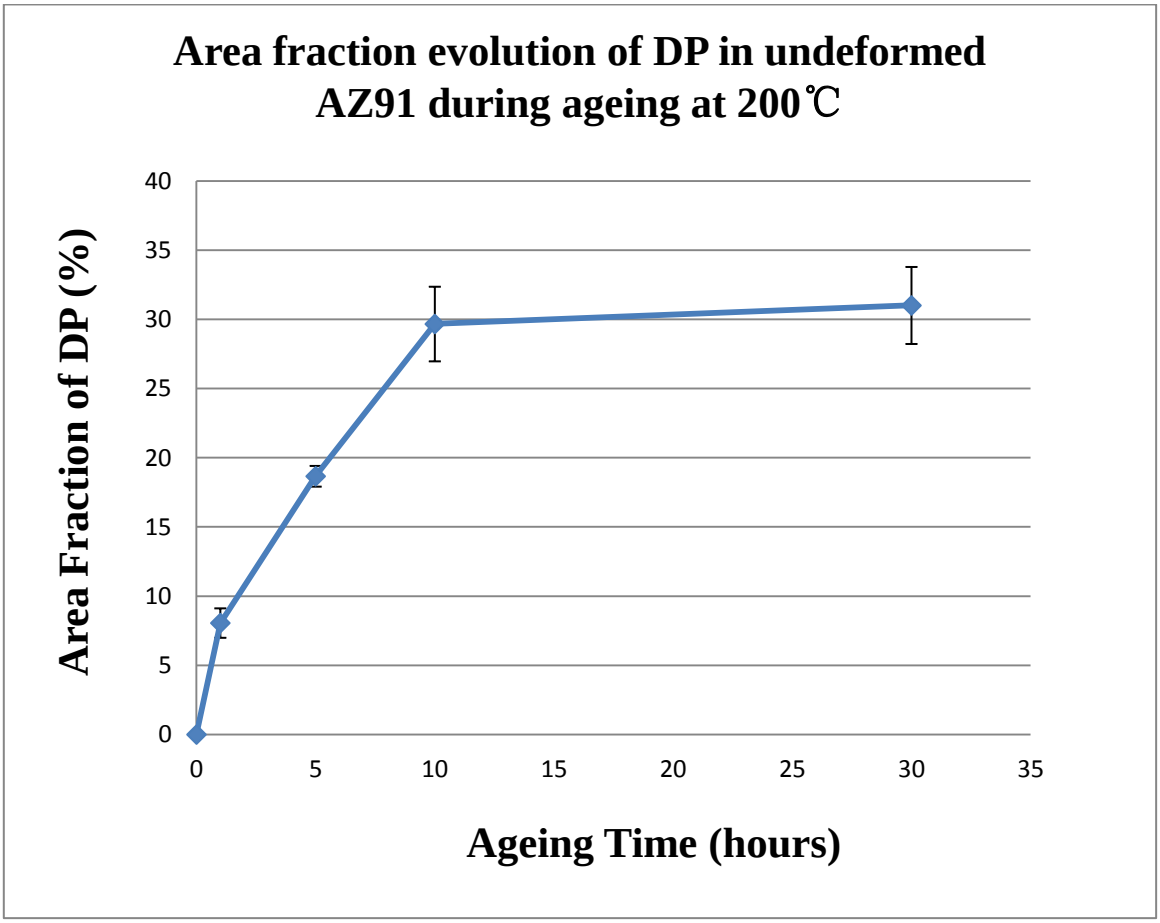

Figure 4.8. The evolution of the DP area fraction during the ageing at 200℃

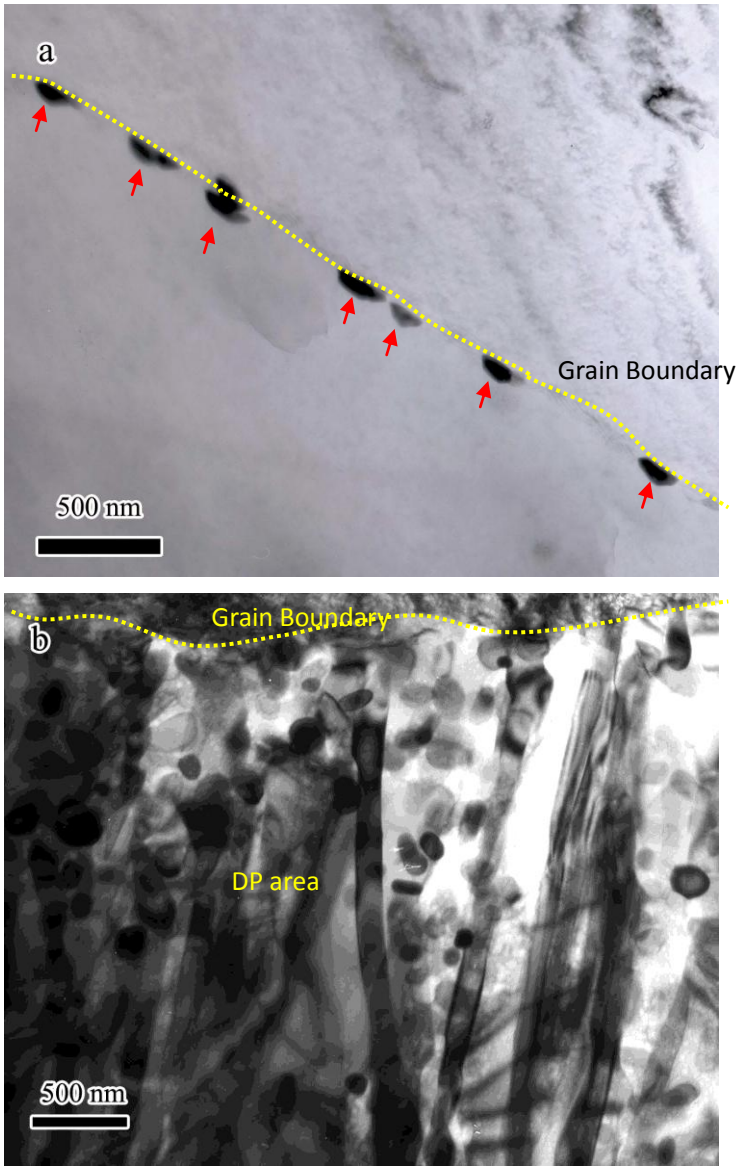

Figures 4.9. TEM micrographs showing (a) a possible area where discontinuous precipitates nuclei, indicated by red arrows, are located along a grain boundary after ageing at 200℃ for 1h and (b) the morphology of the discontinuous precipitates after ageing at 200℃ for 10h. The trace of the grain boundary is indicated by yellow lines.

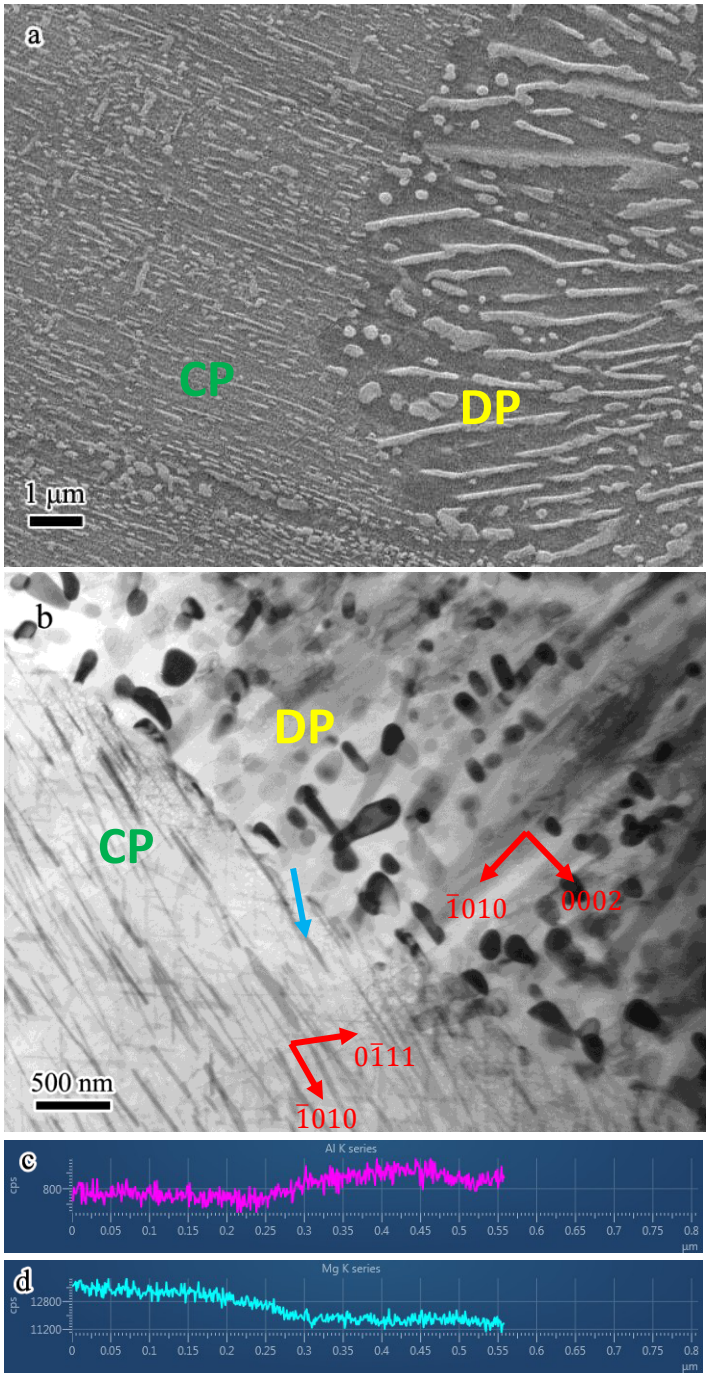

Figure 4.10. SEM (a) and TEM (b) images showing the boundary between CP and DP in the AZ91 aged at 200℃ for 3h. In this case, the boundaries are the moving grain boundary (reaction font) accoding to the orientation of the precipitates. Line scan for Al (c) and Mg (d) shows the difference in chemical composition across the boundary. The blue arrow indicates the line scan distance and direction (from DP area to CP area).

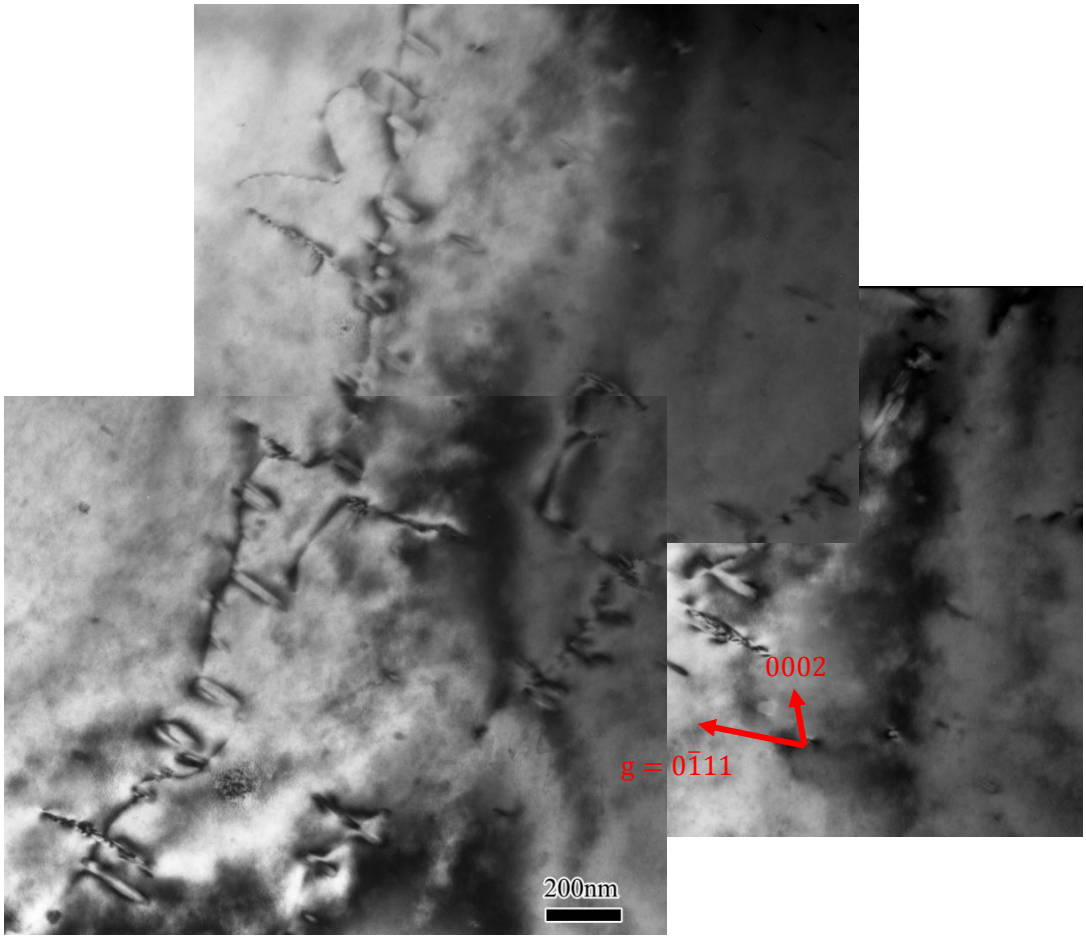

Figure 4.11. A bright field image with two beam condition showing the preferential precipitation of CPs on dislocations in the AZ91 aged at 200℃ for 1h. g = 0$\bar{1}$11; BD~ [$\bar{2}$110].

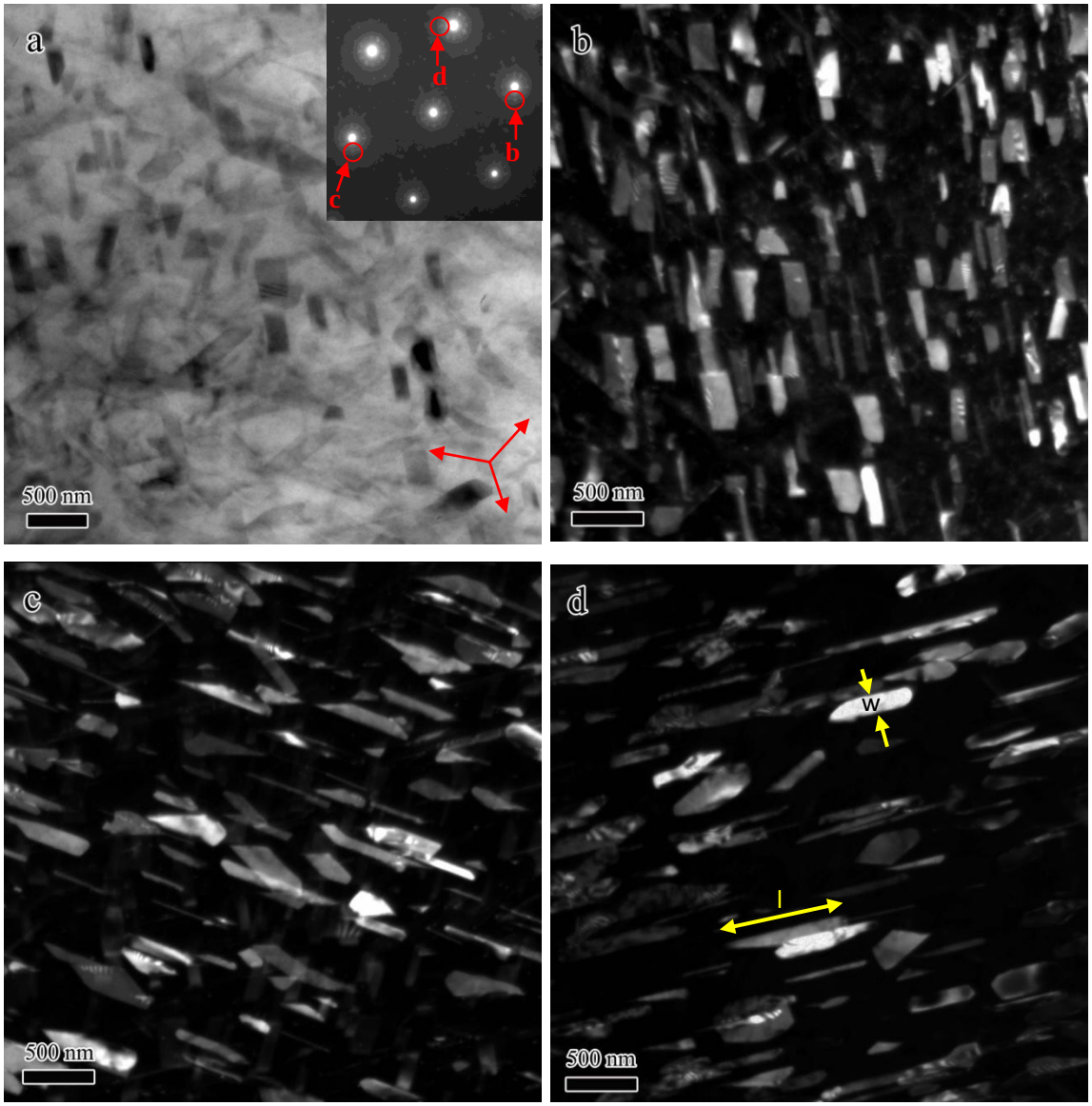

Figure 4.12. The TEM images showing the morphology of CPs with beam direction close to the [0001]. (a) A bright field image illustrating all the CPs; the insert is the diffraction pattern along [0001]; red arrows indicate three $\langle 11\bar{2}0 \rangle$. (b)-(d) Dark field images illustrating CP with different variants separately; Their long axes are close to $\langle 11\bar{2}0 \rangle$. The diffraction spots used in (b)-(d) are indicated with red circles in the insert in (a); The length (l) and the width (w) of CPs are indicated with yellow arrows in (d). All of these images were taken in AZ91 aged at 200℃ for 10h.

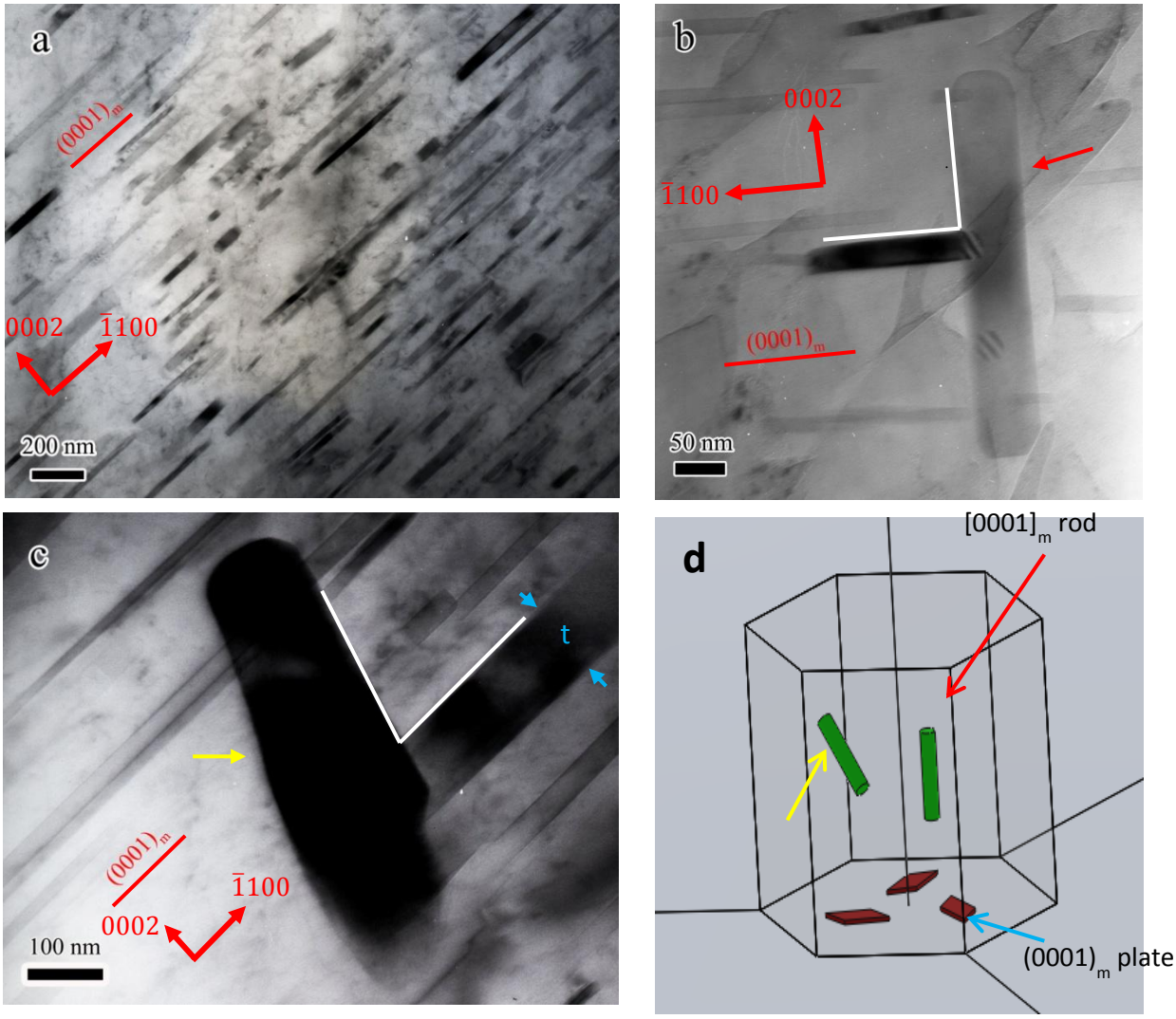

Figure 4.13. (a) Low magnification TEM image showing the morphology of CPs with the beam direction close to [11$\bar{2}$0]; (b) TEM image showing a rod-shaped CP perpendicular to the basal plane; (c) TEM images showing a rod-shaped CP lying at a certain angle to the basal plane. (d) A schematic diagram summarizing different types of CPs. The thickness (t) of CPs lying on the basal plane are indicated with blue arrows in (c). All of images were obtained from the AZ91 aged at 200℃ for 10h.

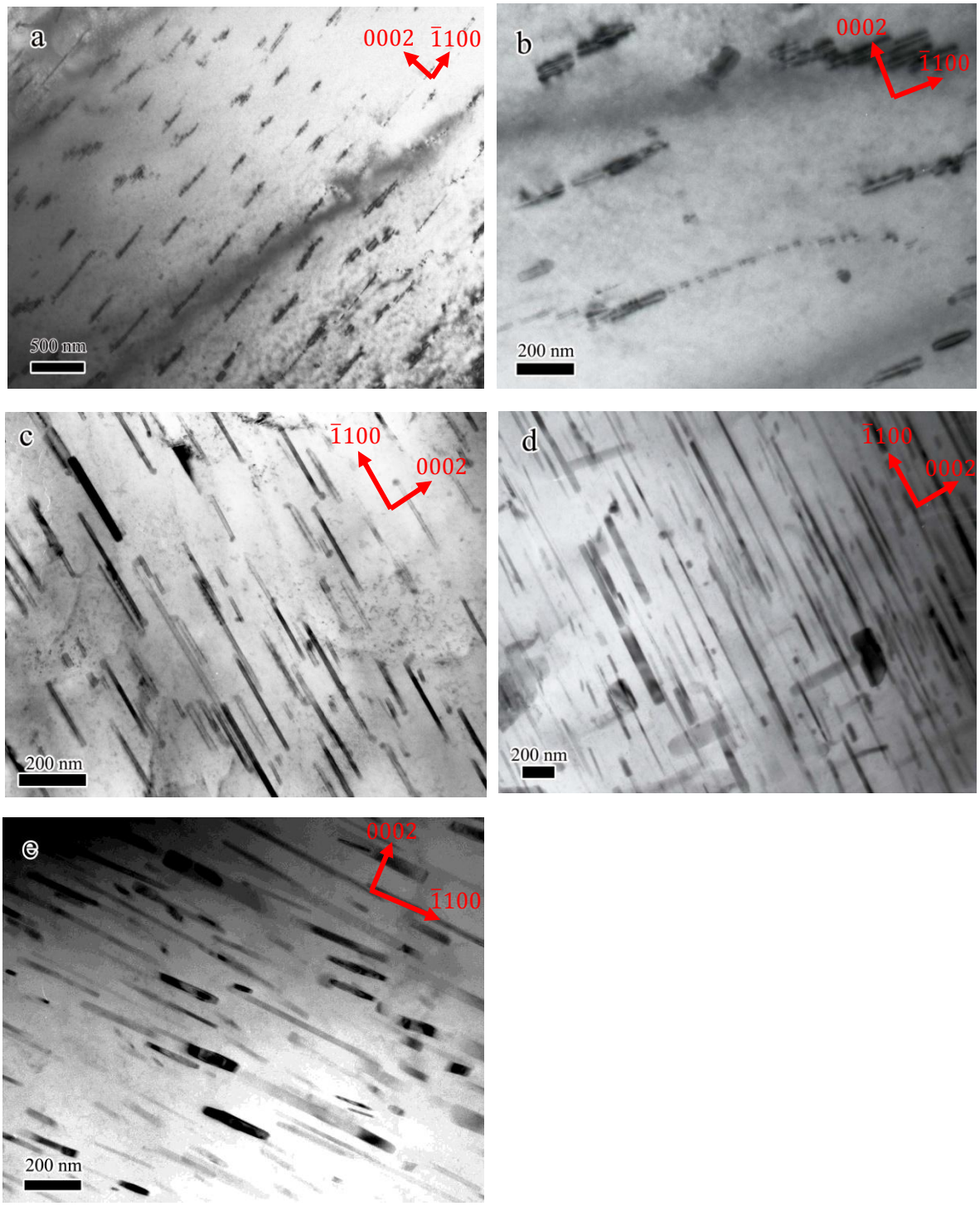

Figure 4.14. TEM images showing the distribution of CPs during ageing for different times. (a) and (b): 1h; (c) 3h; (d) 5h; (e) 15h. BD~ $[11\bar{2}0]$ in the all the images.

Table 4.1.Lath shaped precipitate dimensions and number density in the aged AZ91 measured from TEM micrographs (dimensions are defined in Figure 4. 27).

Ageing time	N_v (mm^{-3})	l (nm)	w (nm)	t (nm)	l/w
1h	2.54×10^{10}	165	40	12	4.12
3h	7.83×10^{10}	363	90	15	4.03
5h	1.37×10^{11}	510	122	20	4.18
10h	1.97×10^{11}	560	125	40	4.48
15h	1.77×10^{11}	620	146	51	4.24

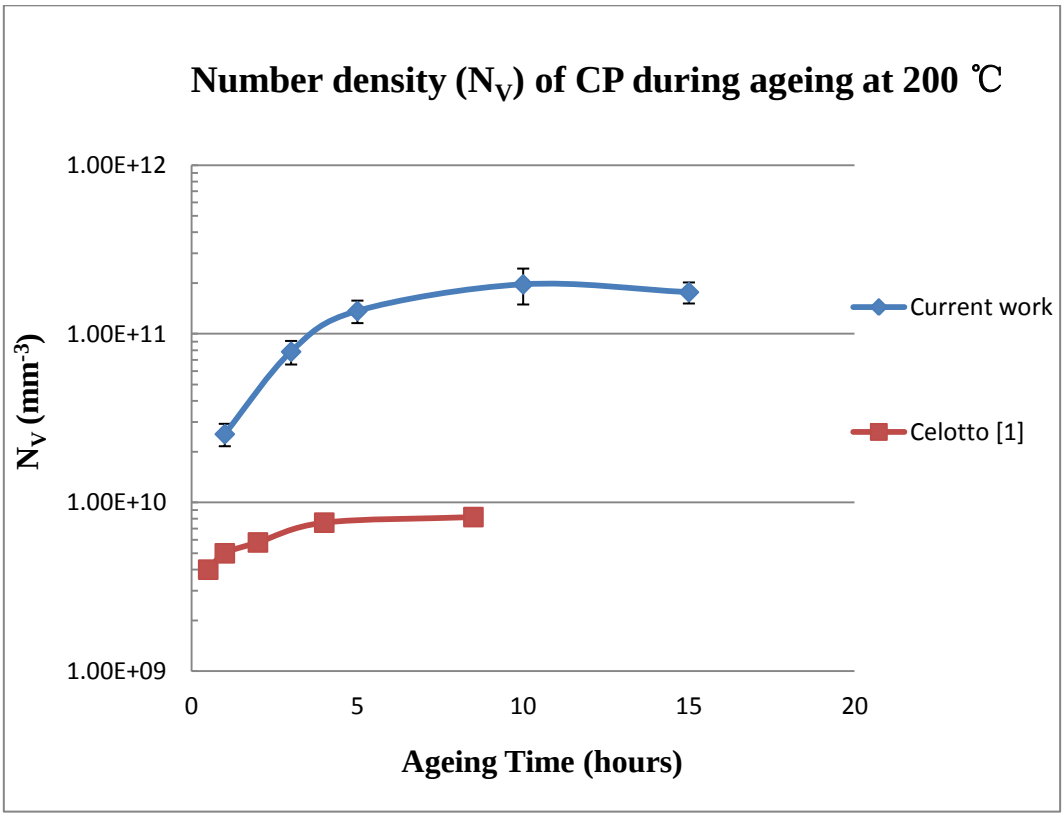

Figure 4.15. The evolution of N_V of CPs in current work and as reported from Celotto [5] during the ageing at 200℃.

Table 4.2 CBED data for thickness determination

s_i (nm^{-1})	n_i	s_i^2/n_i^2 (nm^{-2})
0.0036	1	1.27×10^{-6}
0.0076	2	1.43×10^{-6}
0.0111	3	1.38×10^{-6}
0.0144	4	1.30×10^{-6}

Table 4.3 Alternative CBED data for thickness determination

s_i (nm^{-1})	n_i	s_i^2/n_i^2 (nm^{-2})
0.0036	2	3.17×10^{-6}
0.0076	3	6.37×10^{-6}
0.0111	4	7.75×10^{-6}
0.0144	5	8.29×10^{-6}

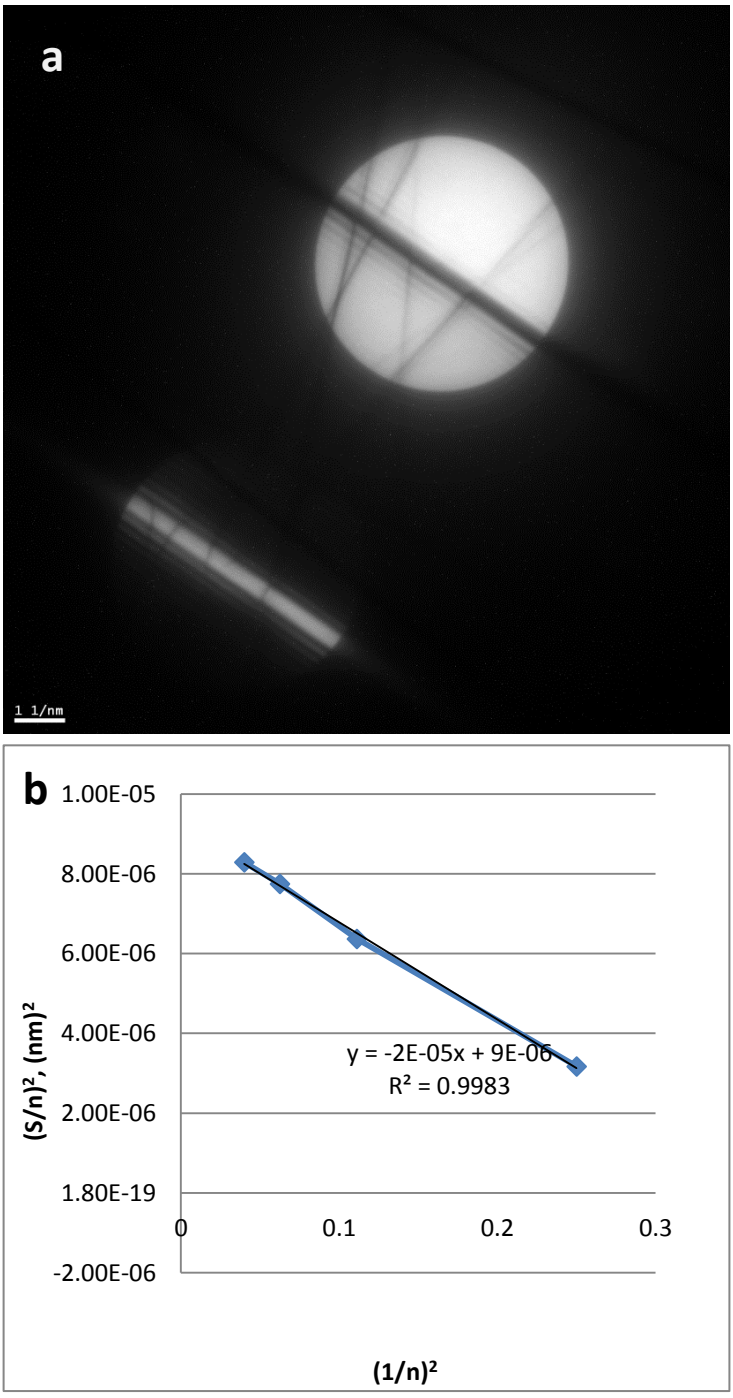

Figure 4.16. (a) A CBED pattern taken the close to $[\bar{2}110]$ using g = $0\bar{3}31$ in a AZ91 aged at 200℃ for 5h. (b) s_i^2/n_i^2 was plotted as a function of $1/n_i^2$; the intercept of the straight line with the s_i^2/n_i^2 axis is $1/t^2$.

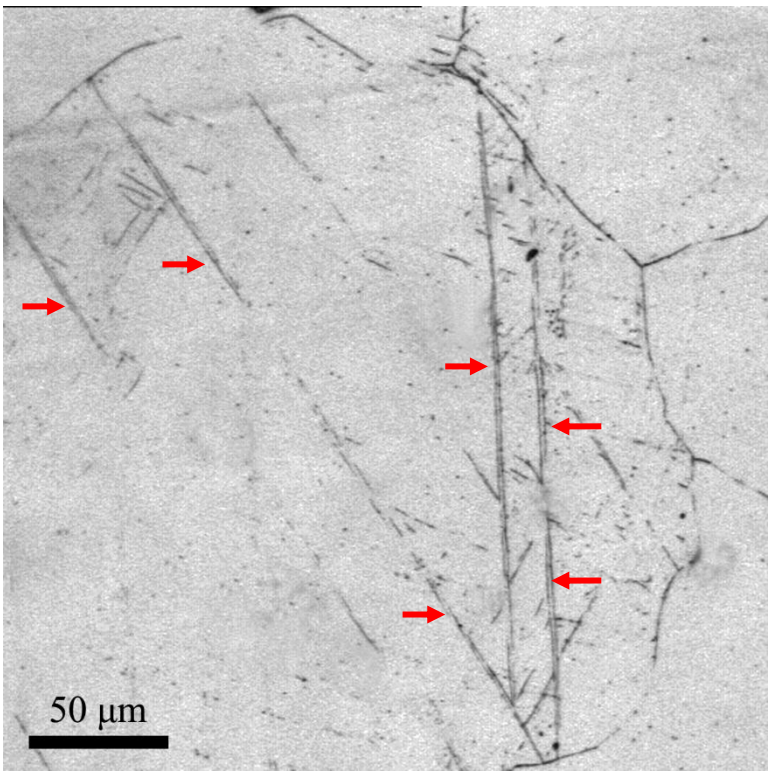

Figure 4.17. An optical images showing the microstructure of as-rolled samples with 5% thickness reduction. Twins are indicated by red arrows.

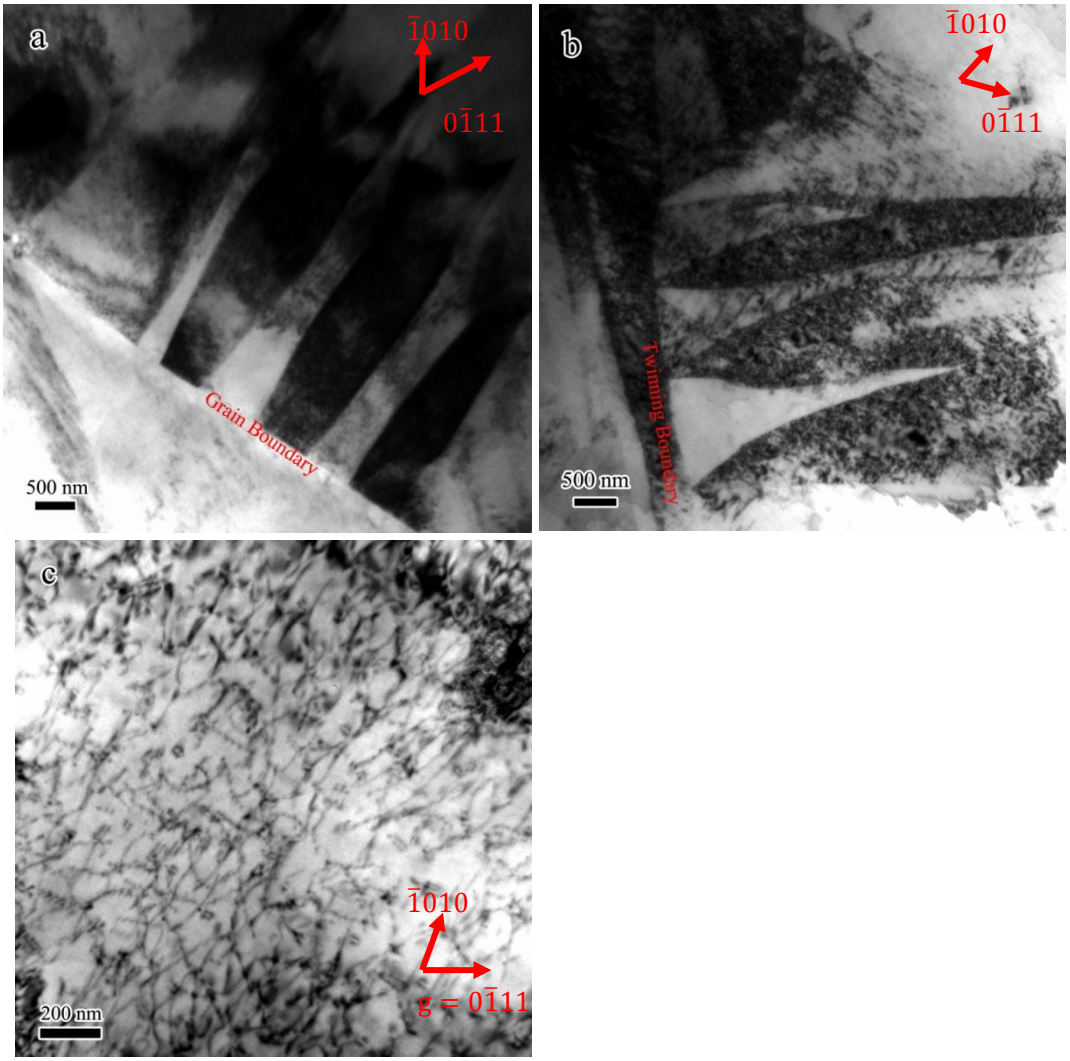

Figure 4.18. TEM images showing the twin and dislocations. (a) and (b) show that the twins end on either grain boundaries or other twin boundary. BD~ $[1\bar{2}1\bar{3}]$. (c) illustrates the dislocation arrangement in the matrix. BD~ $[1\bar{2}1\bar{3}]$ and $g = 0\bar{1}11$.

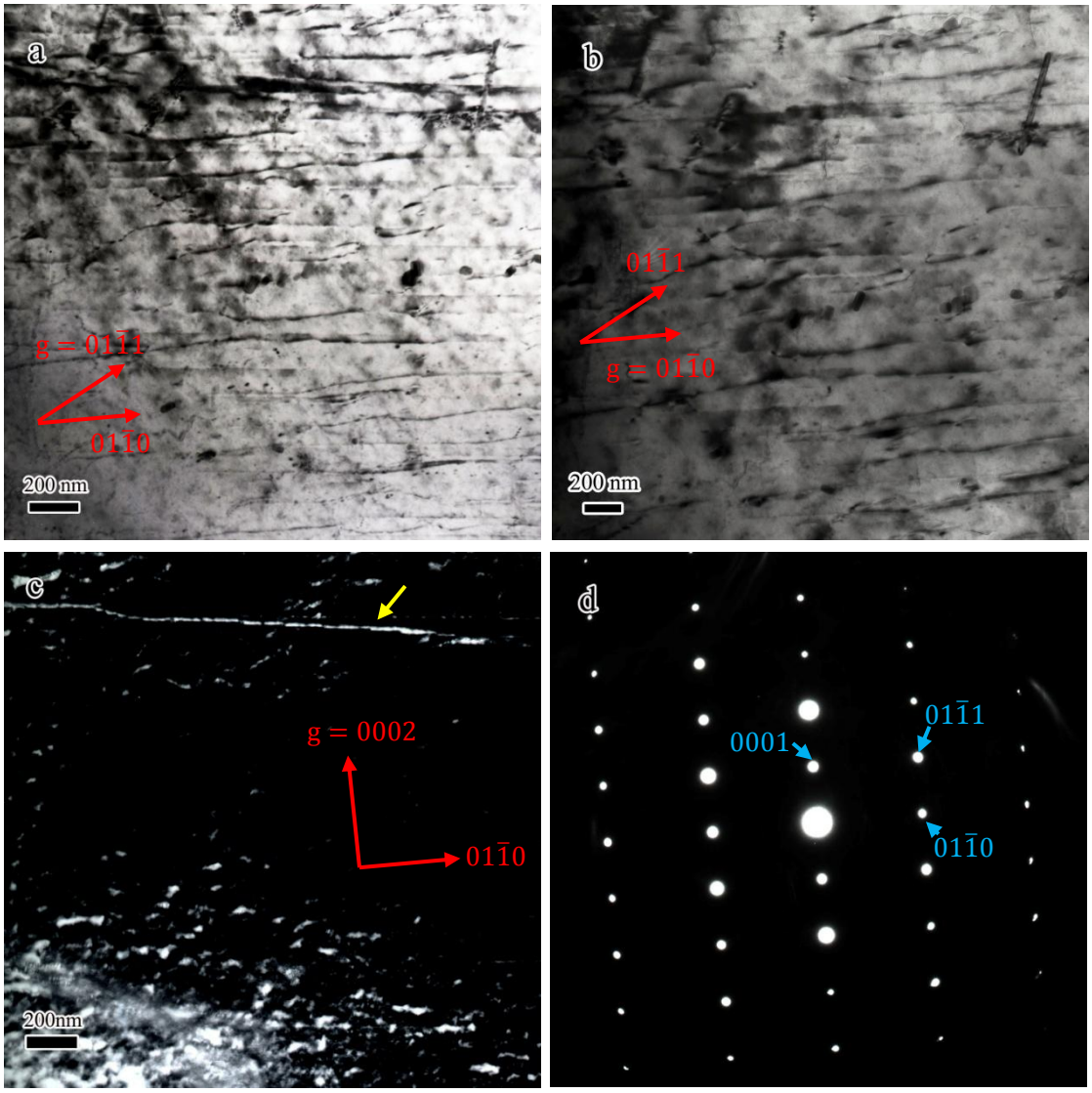

Figure 4.19. The dislocation substructures developed in the AZ91 with 5% rolling. (a) Bright field image with $g = 01\bar{1}1$; (b) Bright field image with $g = 01\bar{1}0$; (c) Dark field image with $g = 0002$.The only visible dislocation was indicated by yellow arrow. (d) Diffraction pattern in the $[2\bar{1}\bar{1}0]$ zone axis. The g vectors in Figure (a)-(c) are indicated with red arrows.

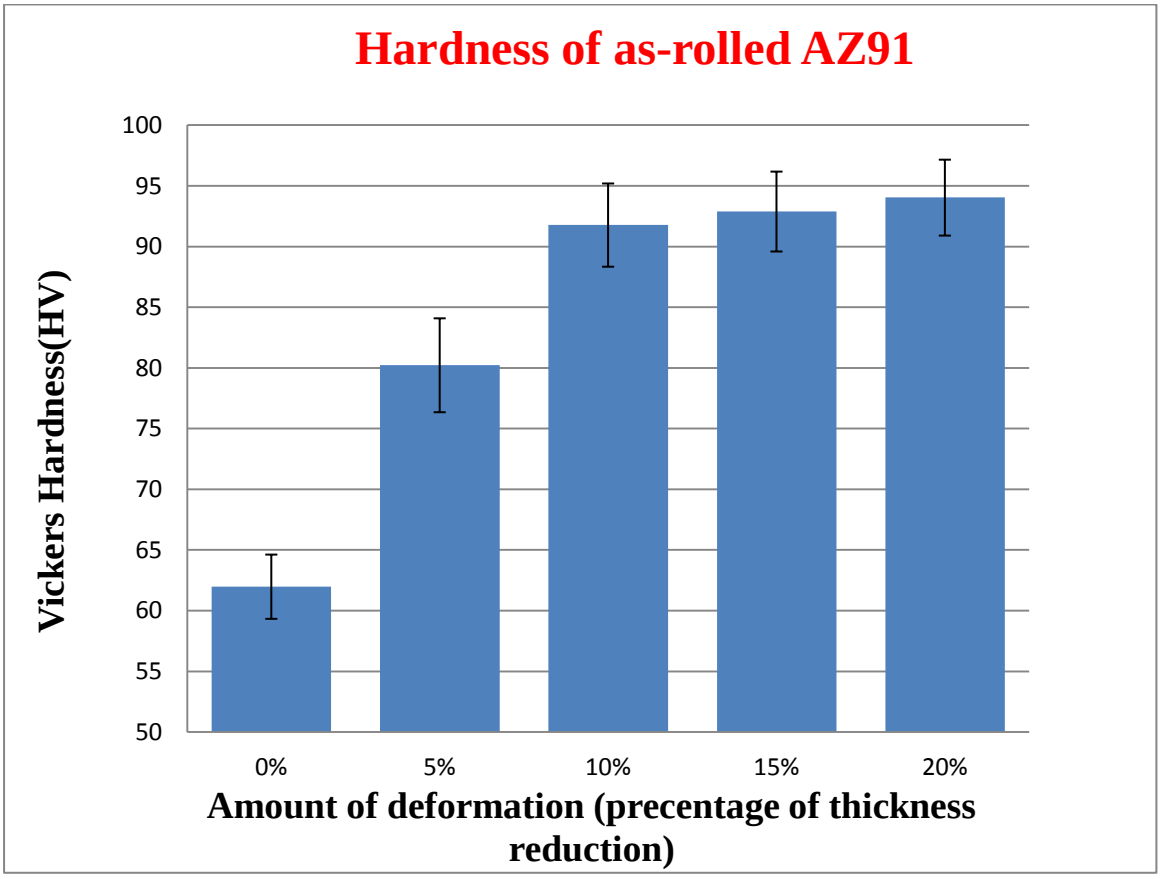

Figure 4.20. The hardness of the as-rolled AZ91 with different amounts of rolling reduction.

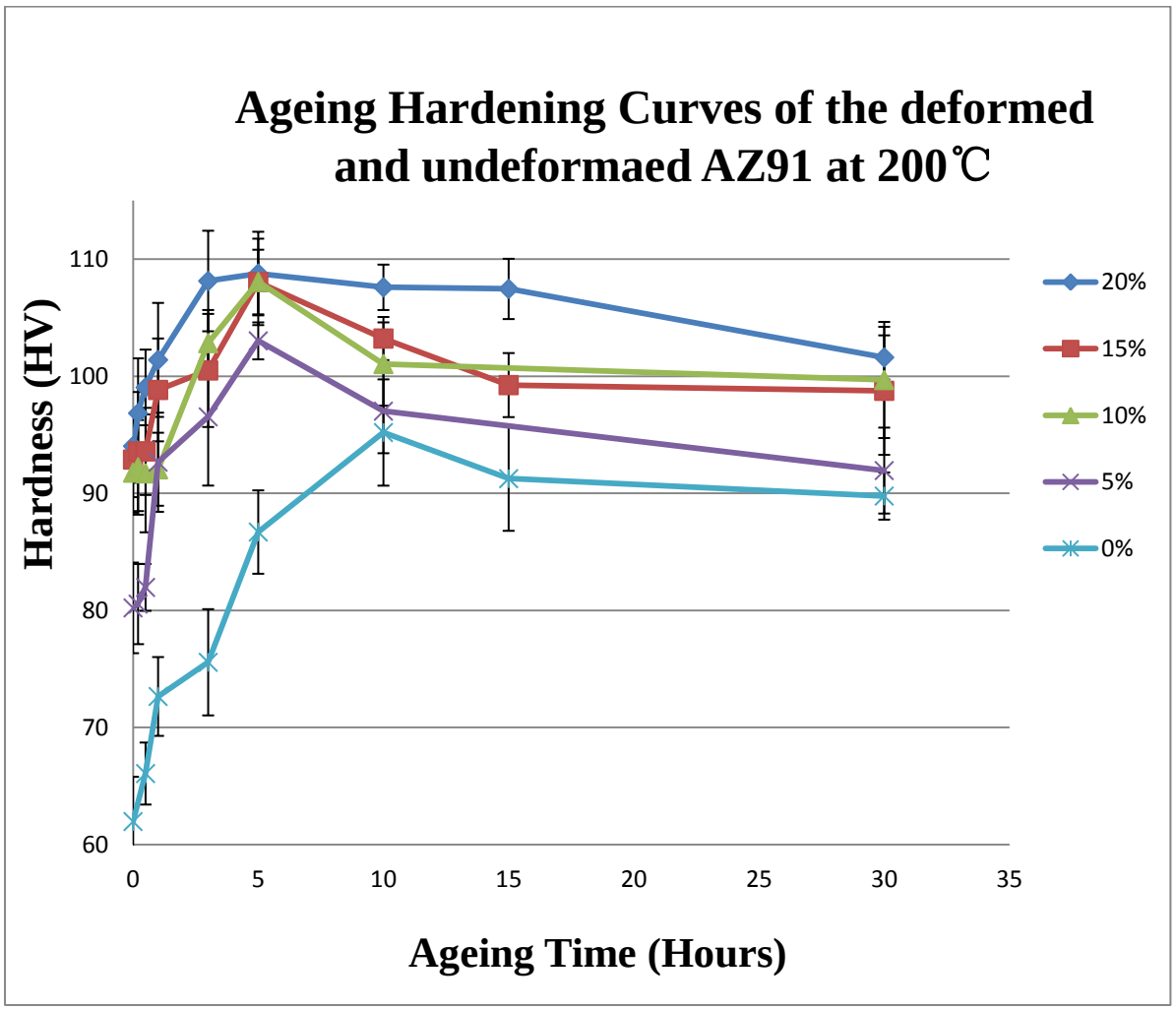

Figure 4.21. The hardness evolution of the deformed AZ91 during ageing at 200℃. The right end shows the cold rolling thickness reduction.

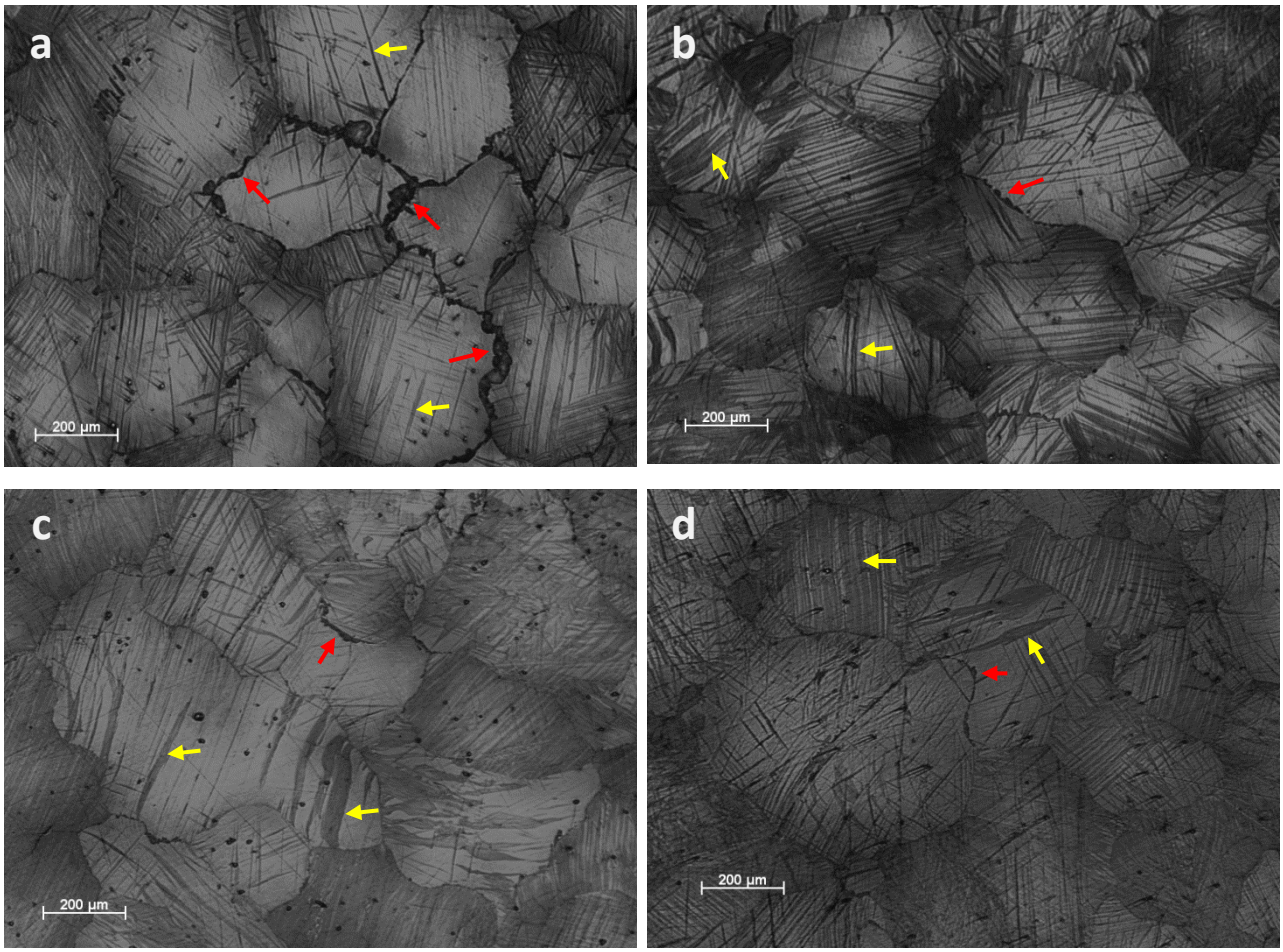

Figure 4.22. Optical micrographs showing the discontinuous precipitation in the peak aged AZ91 with various pre-deformation during ageing at 200℃. (a) 5%; (b) 10%; (c) 15%; (d) 20%. The discontinuous precipitates are always along the grain boundary, as indicated by red arrows. Some of the twins are also labelled with yellow arrows. The uneven contrast within grains is probably due to the Al solute segregation near the grain boundary and high strain within twins, which alters the corrosion resistance of the Mg matrix.

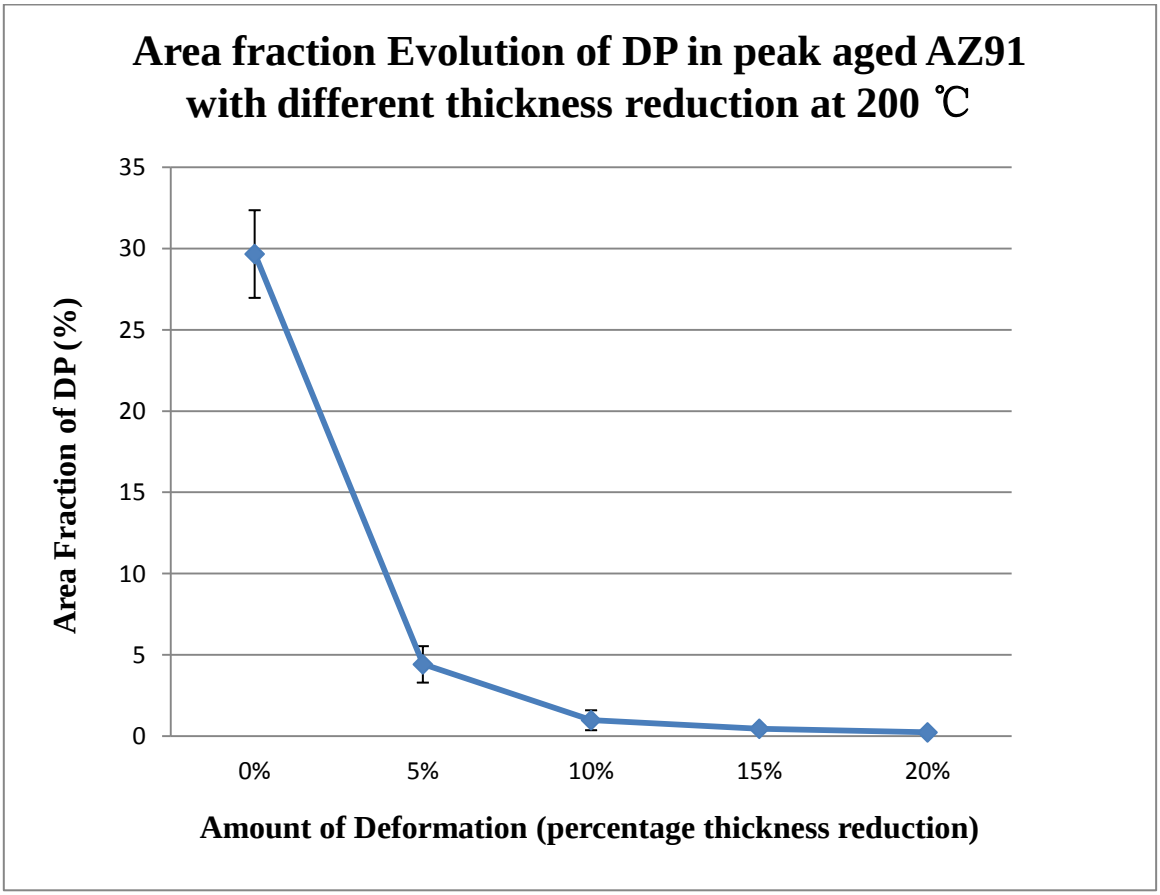

Figure 4.23. Area fraction of discontinuous precipitation in the peak aged AZ91 with various amounts of pre-deformation.

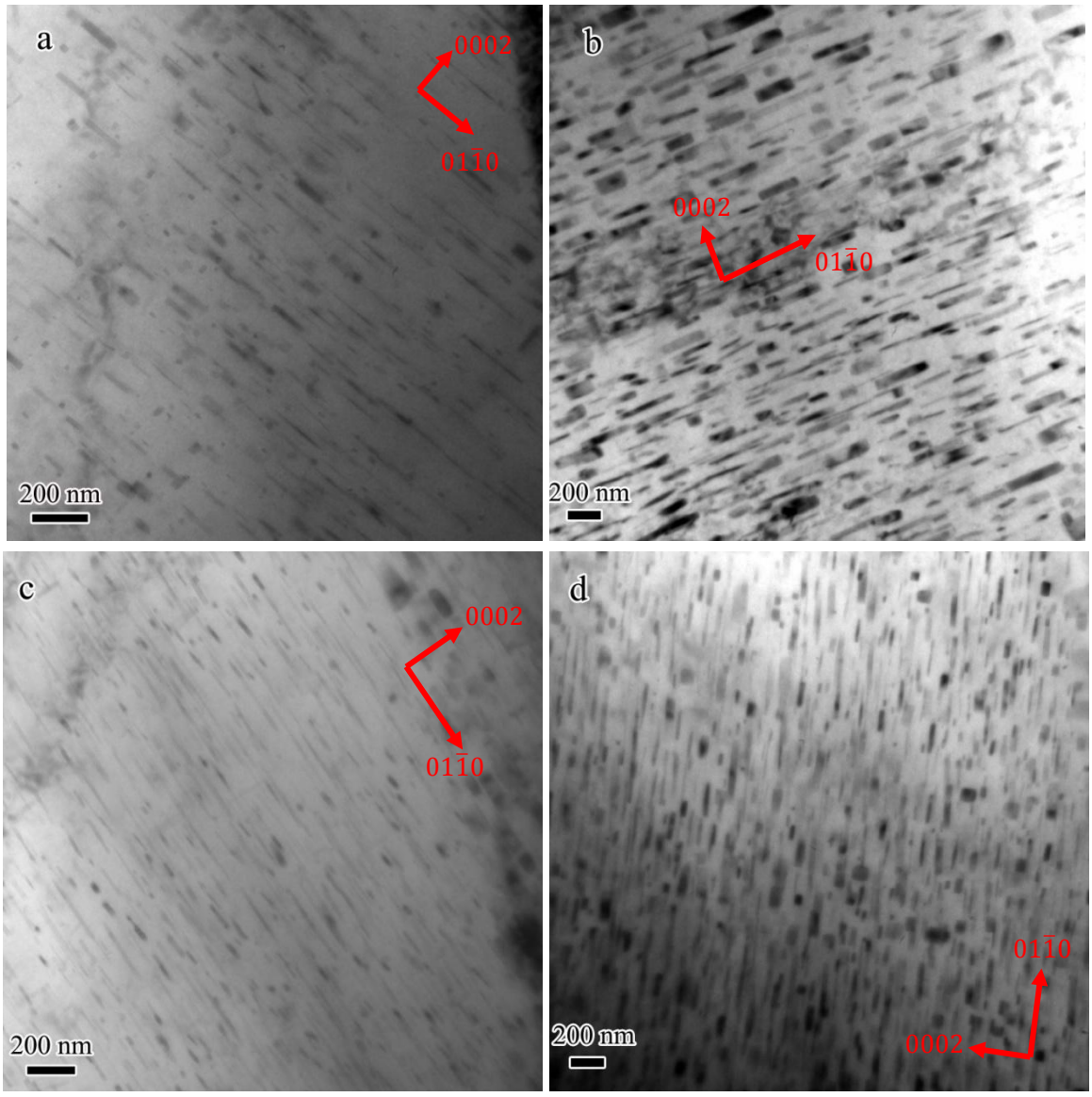

Figure 4.24. TEM micrographs show the distribution of CPs in the AZ91 with pre-deformation during ageing at 200℃. (a) 5% rolling+ 1h ageing; (b) 5% rolling + 5h ageing; (c) 10% rolling + 1h ageing; (d) 10% rolling + 5h ageing. BD ~ [$\bar{2}$110].

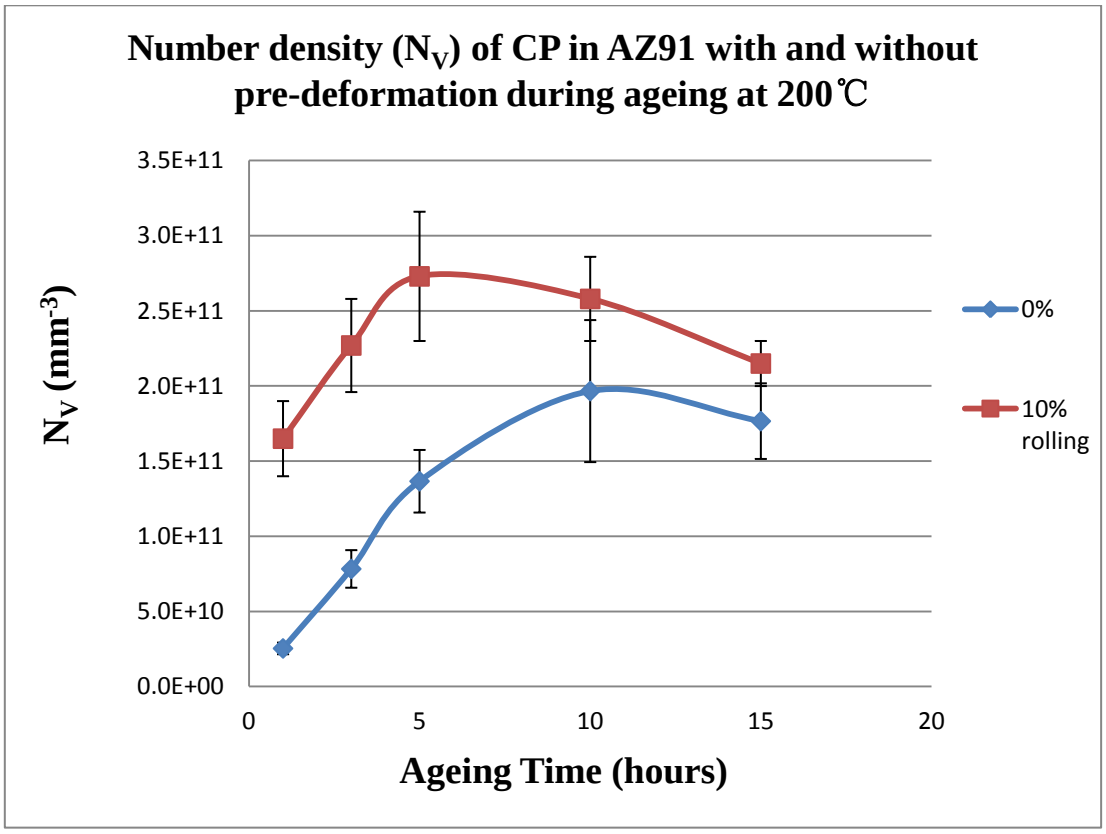

Figure 4.25. The comparison of N_V of AZ91 with and without 10% rolling during ageing at 200℃.

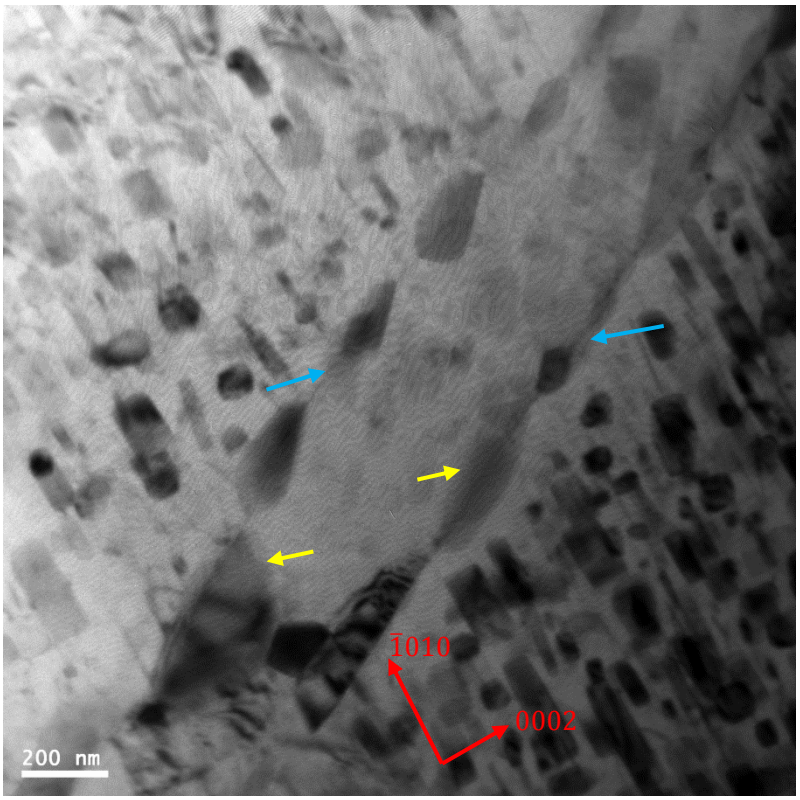

Figure 4.26. Precipitation of $Mg_{17}Al_{12}$ (indicated by yellow arrows) on the twin boundaries (indicated by blue arrows) in 5% rolled AZ91 after ageing at 200℃ for 5h. BD~ $[1\bar{2}10]$ in the matrix.

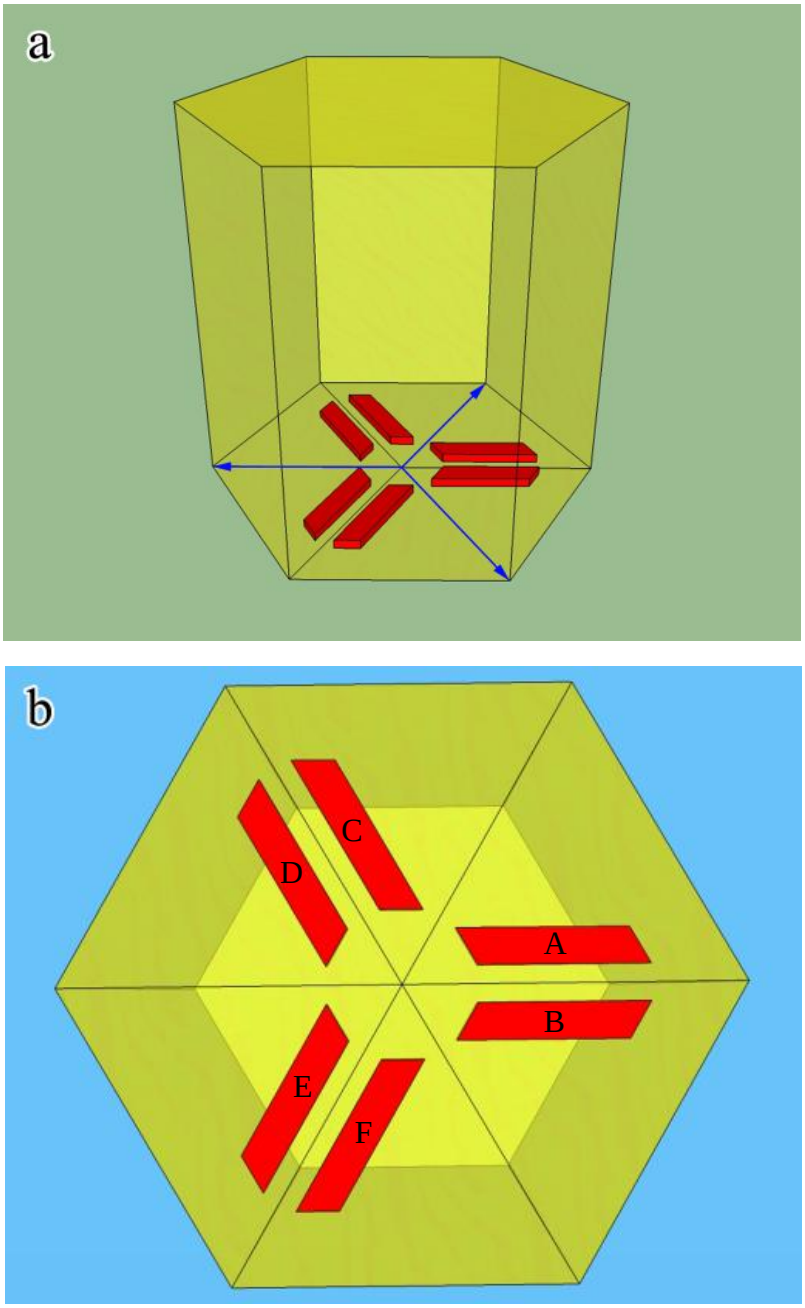

Figure 4.27. 3D schematic diagrams showing the approximation for the CP (red lath) distribution along the direction (a) close to $[20\bar{2}1]$ (b) along $[0001]$. The hcp unit is used to indicate crystallographic directions.

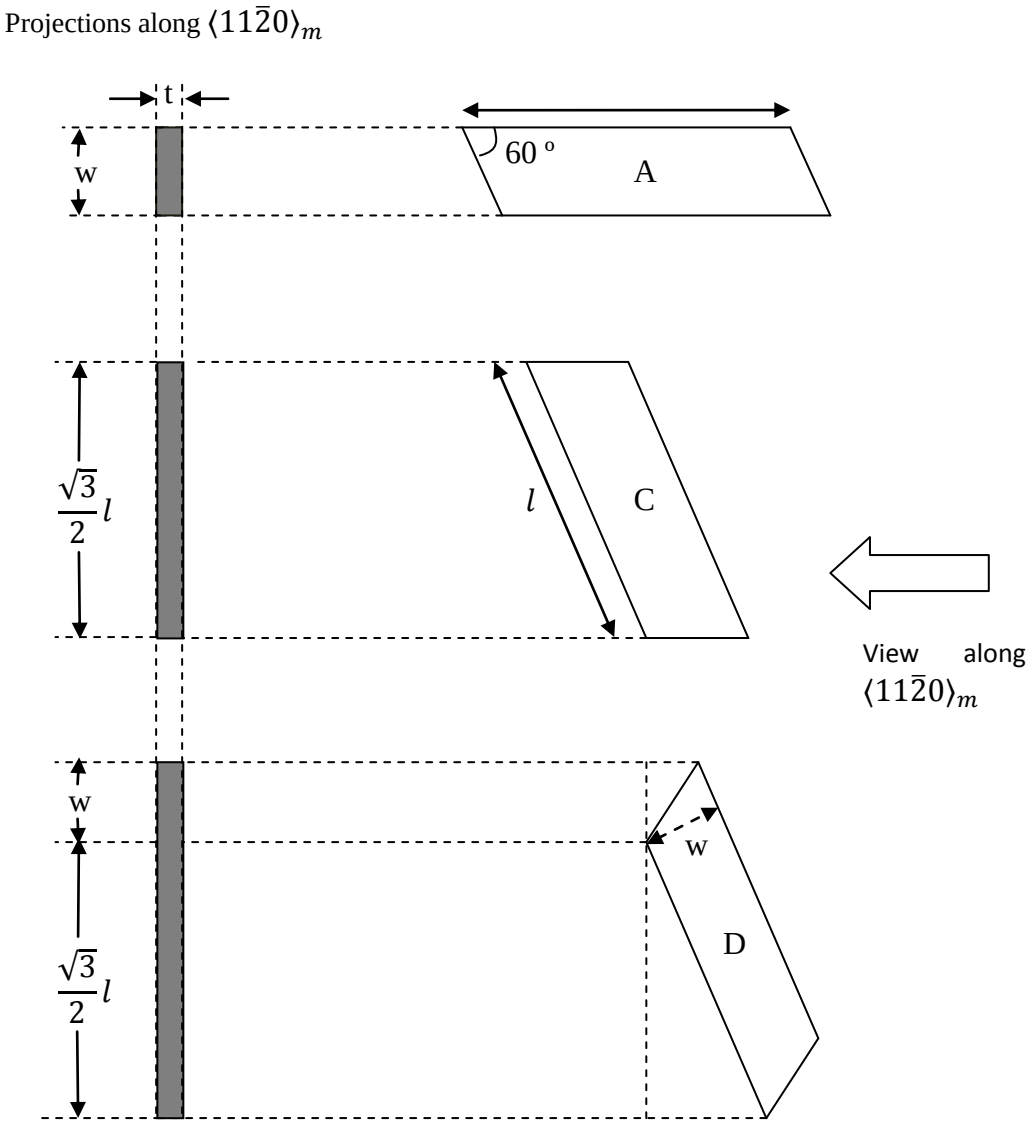

Figure 4.28. Schematic diagrams showing the dimensions of the CPs and their projections along $\langle 11\bar{2}0\rangle_m$ l, w and t represent the length, width and thickness of the CP.

Table 4.4 The calculated strength from each strengthening model of AZ91 during ageing.

Ageing time	Grain size (Current work) (MPa)	Work hardening [6] (MPa)	Solid solution [6] (MPa)	Precipitation hardening (Current work) (MPa)	Sum (MPa)
1h	32.30	0	38	15.75	86.05
3h	32.30	8	30	80.96	151.12
5h	32.30	16	20	96.57	164.87
10h	32.30	28	16	140.85	217.15

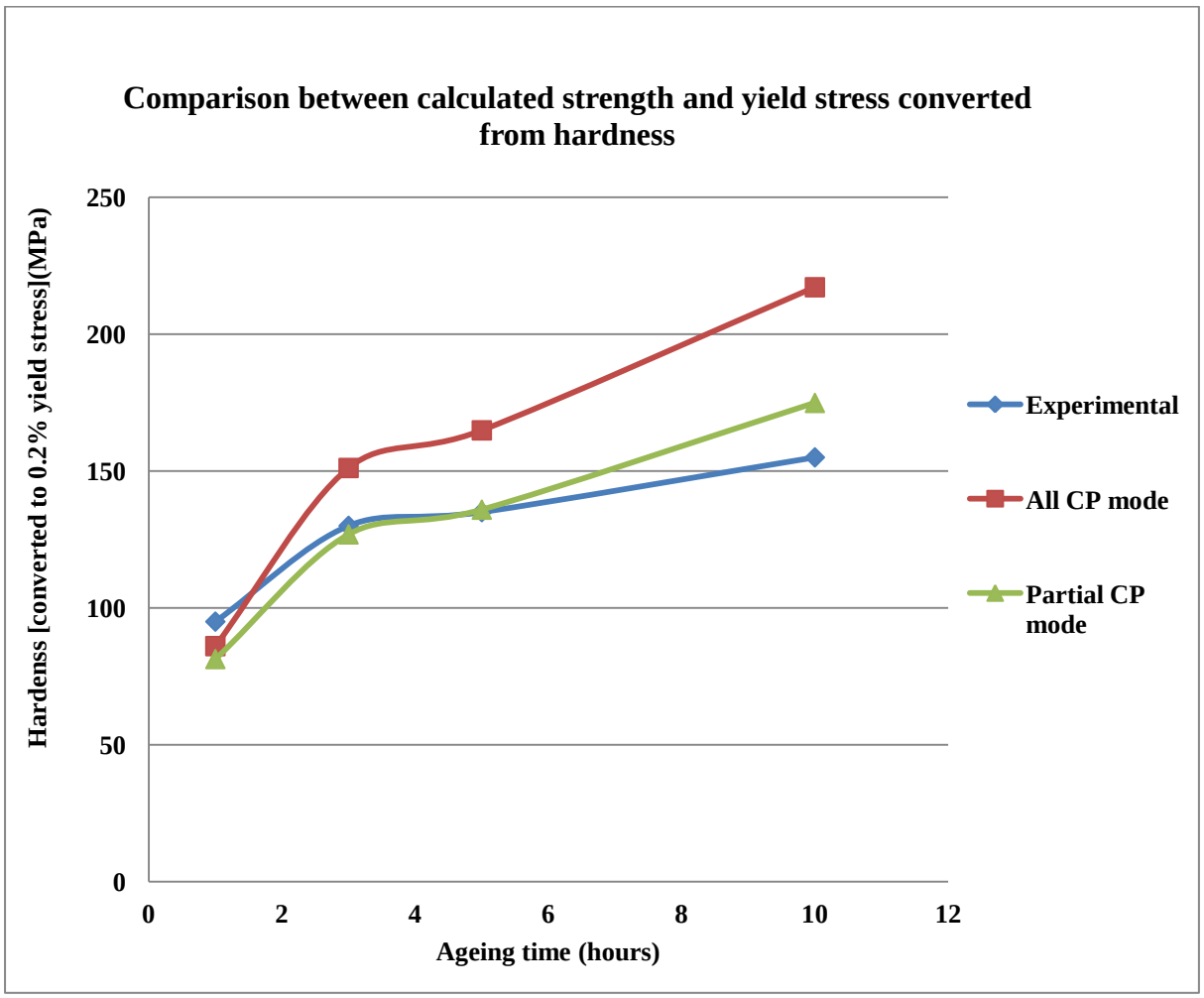

Figure 4.29. The comparison of the calculated strengths with all CP and partial CP with the strength converted from the hardness reported in [5] using the hardness-yield strength relationship in [125] (yield stress $\approx$ proof stress $= 569\,(0.003)^{n}$, $n = 1.528 - 0.684\,\log(H_v)$, H_v: Vickers hardness).

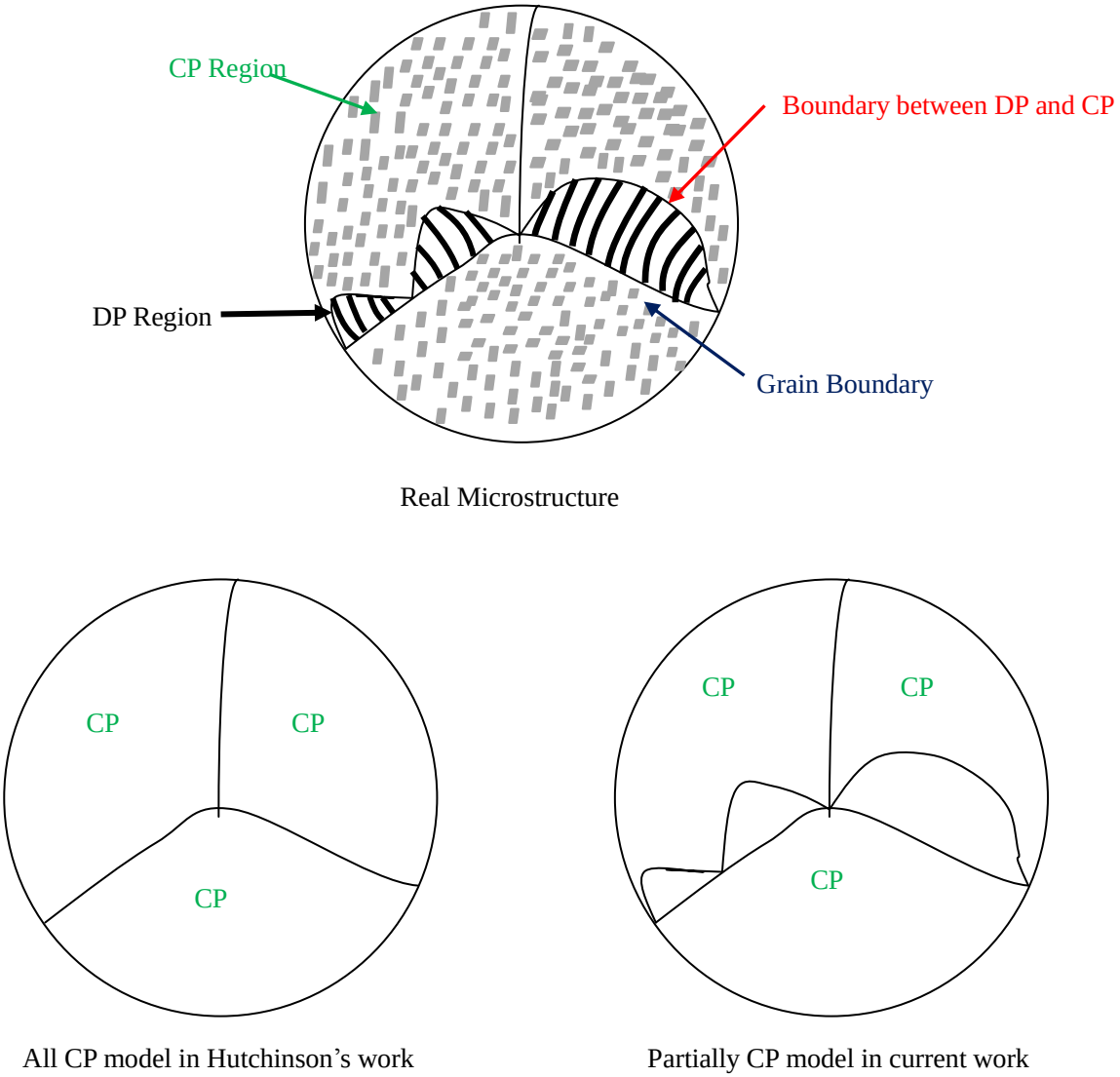

Figure 4.30. Schematic diagrams showing the microstructure of the real AZ91, Hutchinson's model and the current model.

Table 4.5. Possible precipitation processes in some magnesium alloys [115].

Alloys	Precipitation process
Mg-Al (i.e. AZ91)	SSS[1)] → $Mg_{17}Al_{12}$
Mg-Zn(-Cu)	SSS→GP zones → $MgZn_2$ (rods, coherent) → MgZn(disc, semicoherent) → Mg_2Zn_3 (trigonal, incoherent)
Mg-RE(Nd)	SSS → GP zones → Mg_3Nd (*[2)],hcp) → Mg_3Nd (fcc,semicoherent) → $Mg_{12}Nd$ (incoherent)
Mg-Y-Nd	SSS→β` ($Mg_{12}Nd$) → β_1 ($Mg_{14}Nd_2Y$, *) → β ($Mg_{14}Nd_2Y$)
Mg-Ag-RE(Nd)	SSS → GP zones (coherent) → γ` (*, conherent) SSS →GP zones (coherent) → β (*, semicoherent) → $Mg_{14}Nd_2Ag$(incoherent)

[1)] SSS, supersauturated solid solution; [2)] *, questionable, needs further investigation.

Table 4.6. Extrapolated impurity diffusion coefficients of Al in Mg, D_{Al}^{Mg}, and Mg in Al, D_{Mg}^{Al} and the corresponding activation energies [122].

Temperature	D_{Al}^{Mg}	D_{Mg}^{Al}
673 K (400 ℃)	5.5×10^{-16} m^2/s	9.4×10^{-15} m^2/s
623 K (350 ℃)	8.0×10^{-17} m^2/s	2.9×10^{-15} m^2/s
573 K (300 ℃)	1.5×10^{-17} m^2/s	4.3×10^{-16} m^2/s
Q (kJ / mol)	114.7	98.9

Chapter 5 Characterisation of nano-sized Al-Mn-(Mg) particles in AZ91 and their effect on $Mg_{17}Al_{12}$ precipitation

5.1 Introduction

In this chapter, the second case of preferential precipitation of CP (continuous $Mg_{17}Al_{12}$ precipitates) referred to in Chapter 4, is considered i.e. on the pre-exsiting nano particles. It was mentioned in Chapter 4 that some nano-sized (20-200nm) particles containing Al and Mn were found in the as-cast and solution-treated AZ91 alloy. In the current chapter, these particles (including their morphology, structure and chemical composition) and their behaviour during heat treatment of the AZ91, are characterized. Based on such information, the potential effect of these particles on the strength of AZ91 is discussed.

The current investigation shows that these particles were stable after a solution treatment at 420℃ for 72hours and acted as preferential nucleation sites for $Mg_{17}Al_{12}$ precipitates during the subsequent ageing treatment. The particles themselves have a rod-like morphology and a decagonal quasicrystalline structure. Their chemical composition can be written as $(Al_{6.52}Mn)_{1-x}Mg_x$ ($x<0.13$). No well-defined orientation relationship is found between these nano particles and the attached CP or with the matrix. In addition, the chemical analysis of the nano-sized particles was also

discussed.

5.2 Precipitation of CP on the nano-sized particles containing Al and Mn

The HAADF-STEM images in Figure 5.1 were taken from an area containing continuous precipitation in the AZ91 alloy aged at 200℃ for 0.5 hour. In such an imaging mode, diffraction contrast can be suppressed and most of the contrast is due to the difference of atomic numbers in the different phases, which is referred as "Z contrast" [100]. In these figures, CPs ($Mg_{17}Al_{12}$) exhibit a lath-shape and weak Z contrast, while the nano-sized Al-Mn containing particles are short, rod-like and have a strong Z contrast. Figure 5.1 (a) shows a general view of CPs and Al-Mn containing particles at a low magnification with the beam direction close to $[0001]_m$ (m refers to matrix). Each CP is associated with an Al-Mn containing particle. CPs without accompanying Al-Mn containing particles are rarely seen. This indicates that the Al-Mn containing particles are preferential nucleation sites for the $Mg_{17}Al_{12}$ precipitates. Such nucleation precedes that in the matrix and accelerates the continuous precipitation. Figure 5.1 (b) is a high magnification image obtained with the electron beam direction close to $[11\bar{2}0]_m$, showing the details of the attachment between the two phases. One $Mg_{17}Al_{12}$ precipitate is always attached to one Al-Mn containing particle. Such an attachment is also confirmed to be genuine (rather than just overlap) in three dimensions by the tomography work reported in Chapter 6. As mentioned

above, the nano-sized particles and CPs display Z contrast in HAADF-STEM images, indicating their different chemical compositions. In order to know the detailed chemical composition of these particles, a series of investigations in both TEM and STEM modes were performed.

5.3 Chemical composition of nano-sized particles

Figure 5.2 (a) is a typical HAADF-STEM image showing CPs and attached Al-Mn containing particles at high magnification with beam direction close to $[0001]_m$. A yellow line goes across an Al-Mn containing particle, indicating the distance where line scan takes place. The variation of the chemical composition along the yellow line is presented in Figure 5.2 (b). It can be seen that compared with the matrix, the nano-sized particles are rich in Al and Mn and poor in Mg. The same result is also illustrated in the element map shown in Figure 5.3. The abundance of Mn in the locations of the nano-sized particles is obvious. Increased Al and lower Mg can also be seen. Since the enriched Al-Mn content is certain and the Mg content is undetermined for these particles, they are referred to as Al-Mn-(Mg).

In the above cases, the overlap of the Al-Mn-(Mg) particles and the CP (Al rich phase) may affect the EDX results. In order to remove the influence of the attached CPs and obtain a quantitative chemical composition for the Al-Mn-(Mg) particles, an SDD-

EDX investigation was performed on these nano-sized particles in the solution-treated and as cast AZ91, where there are no $Mg_{17}Al_{12}$ precipitates.

Figure 5.4 shows an example of such an experiment in solution-treated AZ91. Figure 5.4 (a) shows three Al-Mn-(Mg) particles (marked A, B and C) at different distances from the edge of the sample. The concentrations of Mg, Al and Mn measured from these particles are shown in Figure 5.4 (b). It can be seen that the Mg content (at. %) increased from 18.62% to 43.55%, while the Al, Mn content (at. %) declines from 70.11% to 48.98% and from 11.14% to 7.33%, respectively with the increasing distance from the edge. This is because there is more Mg matrix in the detected volume due to the increasing foil thickness, as illustrated in Figure 5.5 (a). This will be discussed in detail in §5.5.3.

During acquisition of the EDX spectrum, beam damage of the particles is common. Figure 5.6 illustrates a hole on one particle after acquisition for 100s. In order to avoid the Mg matrix around the particles, a small probe size (normally nano-probe size 6) was used in the current work. This small beam size concentrates the electrons in a small area and the beam current becomes high. Thus it is easy to sputter out the atoms in the particles [126].

In spite of this, some useful information can still be obtained by EDX. Figure 5.7

shows the SDD-EDX results obtained from these particles in the as-cast (black spot) and the solution-treated (green spot) AZ91 plotted on an Mg-Al-Mn ternary diagram. Each point in the diagram represents the Al, Mn and Mg concentration from a particle and the unavoidable matrix. These dots are distributed along a straight line extending from the composition of the matrix, indicated by a blue arrow, to that of the particles (if it were Mg free), indicated by a green arrow. This indicates that these particles have a fixed Al/Mn ratio (of ~ 6.52). It can also be seen that the Mg content in these SDD results ranges from 13 to 55 at. %.

5.4 Morphology and structure

Figure 5.8 (a) is a high magnification TEM micrograph showing a typical rounded rectangular particle in Figure 1 along one of its zone axes. After tilting to another zone axis, it is found that the particle presents an irregular round shape, as shown in Figure 5.8 (b). Both these two shapes simultaneously present in Figure 4.4 (b) and Figure 4.5 (b).

The diffraction patterns corresponding to Figures 5.8 (a) and (b) are shown in Figure 5.9 (a) and (b), respectively. Figures 5.9 (a) presents two-fold symmetry, while Figure 5.9 (b) shows a typical pseudo five-fold symmetry. The tilt angle between Figure 5.9 (a) and (b) is 37.45 °. Another zone axis with two-fold symmetry, as shown in Figure 5.9 (c), was found at 35.41 ° away from that in Figure 5.9 (a). Parallel diffuse streaks are seen in all these diffraction patterns. Similarly to EDX, the SAD was also affected

by the Mg matrix. Some strong diffraction spots in the pattern are actually from the Mg matrix.

5.5 Discussion

5.5.1 Morphology and structure of the Al-Mn-(Mg) particle

As shown in Figures 5.8 (a) and (b), both the rounded rectangle and irregular rounded projections can be achieved from one particle by tilting, thus in three dimensions the particle is a short rod with a rounded cross section. The different shapes in Figure 5.8 (a) and (b) are actually two dimensional projections of such a rod along different viewing directions.

As shown in Figure 5.9 (b), pseudo five-fold symmetry is observed in the diffraction pattern of the particle. This indicates that the particle have a quasicrystalline structure. The tilt angle between the two axes with two-fold symmetries is 35.41°, which is close to that of DQCs ($360°/10 = 36°$). Meanwhile, the angles between the zone axis with two-fold symmetry and that with pseudo five-fold symmetry (37.47° and 36.75°) also match the reported decagonal symmetry [74]. In addition, parallel diffuse streaks in these diffraction patterns are a typical feature of DQCs. This is due to the layered structure of the DQCs and is present in every diffraction pattern except along the decagonal axis [74]. The rod shape of the particle is also in accordance with the morphology of DQCs [70, 73, 74]. Therefore, both the morphology and diffraction

information obtained from these Al-Mn-(Mg) particles suggest a DQC structure. In fact, Figure 5.8 (a) shows the projection of the rod when its decagonal axis is perpendicular to the electron beam and Figure 5.8 (b) shows the projection of the rod when its decagonal axis is inclined to the electron beam (about 63 ° between these two).

5.5.2 Quantitative chemical composition

It is shown in Figure 5.7 that the ratio between Al and Mn is fixed (around 6.52), while the Mg content is various. This is because the composition of the Al-Mn-(Mg) particles is mixed with that of the Mg matrix. Since there is only limited Al (less than 9 wt%) and nearly no Mn in the Mg matrix, the ratio Al:Mn is hardly affected by the matrix. But the massive Mg matrix can strongly influence the Mg signal in the spectrum and be difficult to avoid. Therefore, in Figure 5.7, the points close to the Mg corner (with high Mg content) indicate that the particles were located in a thick area of the TEM foil, such as the particle C in Figure 5.4, while the points far away from the Mg corner (with low Mg content) represent those particles in a thin area, such as the particle A in Figure 5.4. The minimum Mg content in Figure 5.7 is around 13 at. %. This can be considered as the case involving the minimum Mg matrix or possibly no Mg matrix under the current experimental conditions. Therefore, the maximum possible Mg content in the Al-Mn-(Mg) particle is around 13 at. %, and the chemical composition can therefore be written as $(Al_{6.52}Mn)_{1-x}Mg_x$ ($x<0.13$).

According to the previous studies, most Al-Mn QCs are not stable, but can be stabilized by adding some other element. For instance, the metastable Al-Mn i-phase becomes stable after substituting part of the Al by Pd. The third element is generally used to tune the electron concentration and increase the entropy by chemical disorder [70]. Since these quasicrystalline Al-Mn-(Mg) particles are stable throughout the heat treatment used here, it would be of fundamental interest in the future to investigate whether Mg helps to stabilize the Al-Mn phase.

5.5.3 EDX and SAD of nano-sized particles

5.5.3.1 Influence on the EDX results

In the current work, EDX on the nano-sized Al-Mn-(Mg) particles was influenced by several factors. The first factor is the foil thickness, as mentioned in §5.5.2. Figure 5.5 (a) illustrates a cross section showing three QC particles with the same size located in different areas in a wedge-shaped TEM foil. It can be understood that the closer the particle is to the hole, the less Mg matrix will be involved in the interaction with the electron beam. Therefore, the particle A will receive the smallest influence from the matrix and thus have normally a small Mg content. This is confirmed in real experiments, as shown in Figure 5.4. Because of this, particles close to the edge of the hole in TEM, such as the particle A in Figure 5.4, are normally selected for EDX experiments to minimize the influence of the Mg matrix. However, due to their small size, even the particle on the edge of the TEM foil cannot guarantee the excluding of

the Mg signal from the matrix. So whether these particles are truly Mg free or not is still debatable. To resolve this, the most convincing way is to extract the particles from the Mg matrix, for example, by using some solution to remove the Mg and leave the Al-Mn-(Mg) particles.

Apart from the foil thickness, the location and size of the particle also affect the experimental results. Figure 5.5 (b) shows three QCs particles in an area with uniform thickness. It can be seen that the large QC, marked by D, has less Mg matrix above and below and thus would be less influenced by matrix. Particles E and F are two particles with the same size, but located in different parts of the sample: particle F is close to the bottom of the foil, while particle E is close to the top of foil. According to previous research [126], the high energy electron beam can easily make a hole from the bottom of the sample. Due to different location, the hole is easy to take place on particle F, while the particle E will not lose its volume until the matrix below it is consumed. With the acquisition going on, the spectrum of F obtains less and less signal from the particle, while the spectrum of E gets less and less signal from the matrix. Therefore, the EDX result of E can be less affected by the matrix, compared with that of F. In addition, even for one particle, Al is easy to remove by the electron beam. This decreases the signal from Al and affects the measured percentage of Al. If the particle is Mg-containing, the same problem will happen in the measured percentage of Mg. In order to avoid the hole in the particle, a short acquisition time and low accelerating voltage can be used, but this will reduce the total counts in the

spectrum. In the current work, 100s and 200kV were used as acquisition time and accelerating voltage.

5.5.3.2 SAD experiment (how to tilt a nano-sized particle)

SAD also suffers from the same problem as EDX. The diffraction patterns from these particles are always mixed with that from the matrix. However, in this case, they can be distinguished by taking a diffraction pattern from the matrix nearby. The real difficulty in the SAD experiment is how to tilt the particles to zone axes. How to resolve these two issues is shown in Appendix C step by step.

5.5.4 Potential effect on the strength of AZ91

Compared with most precipitation-hardenable Al alloys, AZ91 shows poor precipitation hardening. There are two reasons: one is that the number density of precipitates in AZ91 is much lower than in Al alloys; the other is that most $Mg_{17}Al_{12}$ precipitates lie on the basal plane and are thin and thus are not effective obstacles to the motion of dislocations along the basal plane [5]. Meanwhile, the coarsening of $Mg_{17}Al_{12}$ precipitates at elevated temperature also limits the application of AZ91 [1]. It has been explained above that Mn additions can introduce fine Al-Mn-(Mg) QC particles into AZ91. QC particles normally have unusual properties, such as high hardness and thermal stability [68]. Thus these Al-Mn-(Mg) QC particles could potentially play an important role in strengthening AZ91. Firstly, their quasiperiodic nature will make them resistant to shear by dislocations, strengthening the alloy. A

recent study reported that the hardness and toughness of AZ91 were much improved by addition of an Mg-Zn-Y-Mn master alloy containing spherical QCs [47]. Secondly, it has been shown above that they are stable up to about 420℃ and resistant to coarsening. This will be helpful to the mechanical properties of AZ91 at elevated temperatures. Thirdly, it is reported that some Al-Mn compounds, such as the hcp ε-AlMn phase, can be favourable sites for heterogeneous nucleation of the α-Mg grains and thus reduce the grain size [58]. Hence, the Al-Mn-(Mg) QC particles can potentially be a grain size refiner for AZ91. Finally, $Mg_{17}Al_{12}$ precipitates preferentially on the Al-Mn-(Mg) QC particles and thus more such particles may result in a finer distribution of $Mg_{17}Al_{12}$ precipitates. Hence, if more ultrafine Al-Mn-(Mg) QCs with an even distribution could be introduced into AZ91 by a greater Mn addition, for example, the mechanical performance of AZ91 at room and elevated temperature may be improved.

5.6 Conclusions

Ultrafine Al-Mn-(Mg) particles have been found in sand cast AZ91. They are rod shaped and have both two-fold and pseudo five-fold symmetries. Compared with many other Al-Mn intermetallic phases in Mg-Al alloys containing Mn, these Al-Mn-(Mg) particles are small (20-200 nm). Their structure and morphology indicate that they are decagonal quasicrystals with a partial crystalline structure. A rough chemical composition, $(Al_{6.52}Mn)_{1-x}Mg_x$ ($x<0.13$), has been obtained for them, though the

existence of Mg within these particles is still debatable.

These particles are stable after a solution treatment at 420℃ for 72h. During ageing, $Mg_{17}Al_{12}$ precipitates on pre-existing ultrafine Al-Mn-(Mg) particles have been observed. If introduced as an even distribution and in a larger amount, these ultrafine Al-Mn-(Mg) particles should improve the mechanical performance of AZ91 at both room and elevated temperatures.

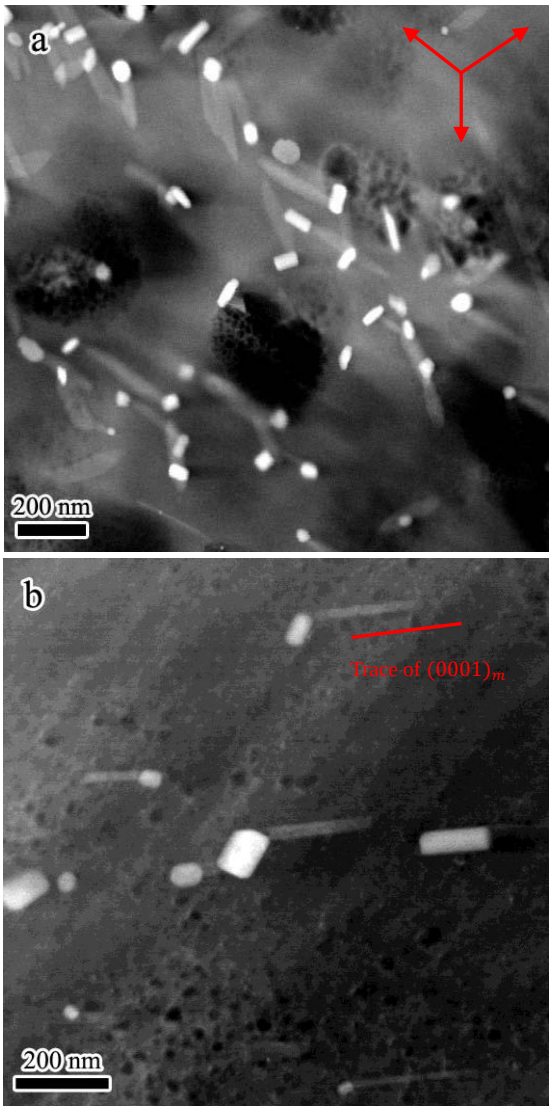

Figure 5.1. HAADF-STEM images showing $Mg_{17}Al_{12}$ precipitates attached to Al-Mn containing particles: (a) low magnification with BD~ $[0001]_m$ and (b) high magnification with BD ~$[11\bar{2}0]_m$. The small, white particles are Al-Mn-(Mg) QC; the larger, grey particles are the $Mg_{17}Al_{12}$. $\langle 11\bar{2}0\rangle_m$ in (a) and the trace of $(0001)_m$ in (b) are indicated by red arrows and lines, respectively.

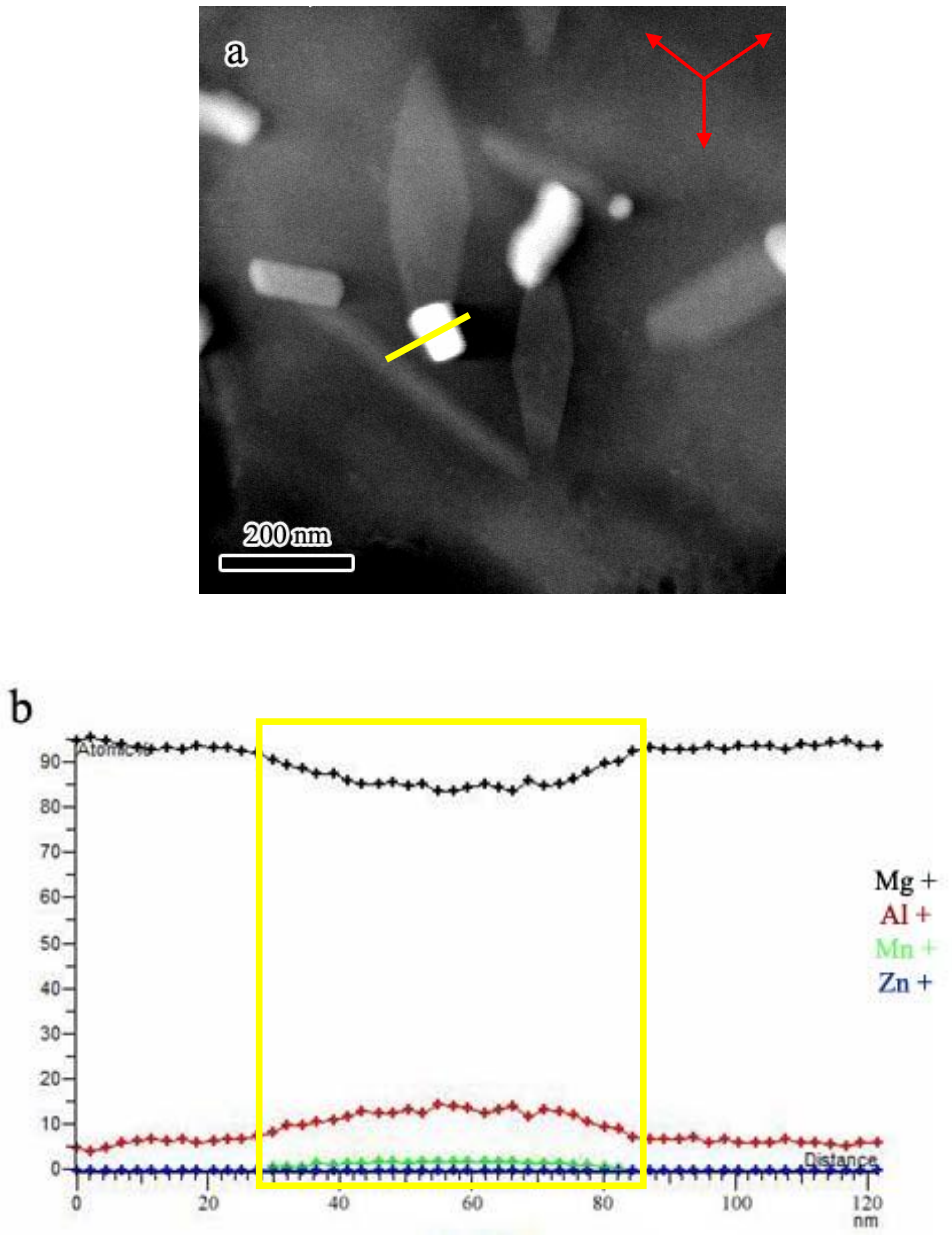

Figure 5.2. (a) A HAADF-STEM image showing CPs and attached Al-Mn containing particles at high magnification with BD ~ $[0001]_{\mathrm{m}}$. The yellow line indicates where the line scan took place. Red arrows indicate the $\langle 11\bar{2}0\rangle_m$ directions. (b) Line scans showing the variation of chemical composition across the nano-sized particles in (a). The yellow box delineates the particle.

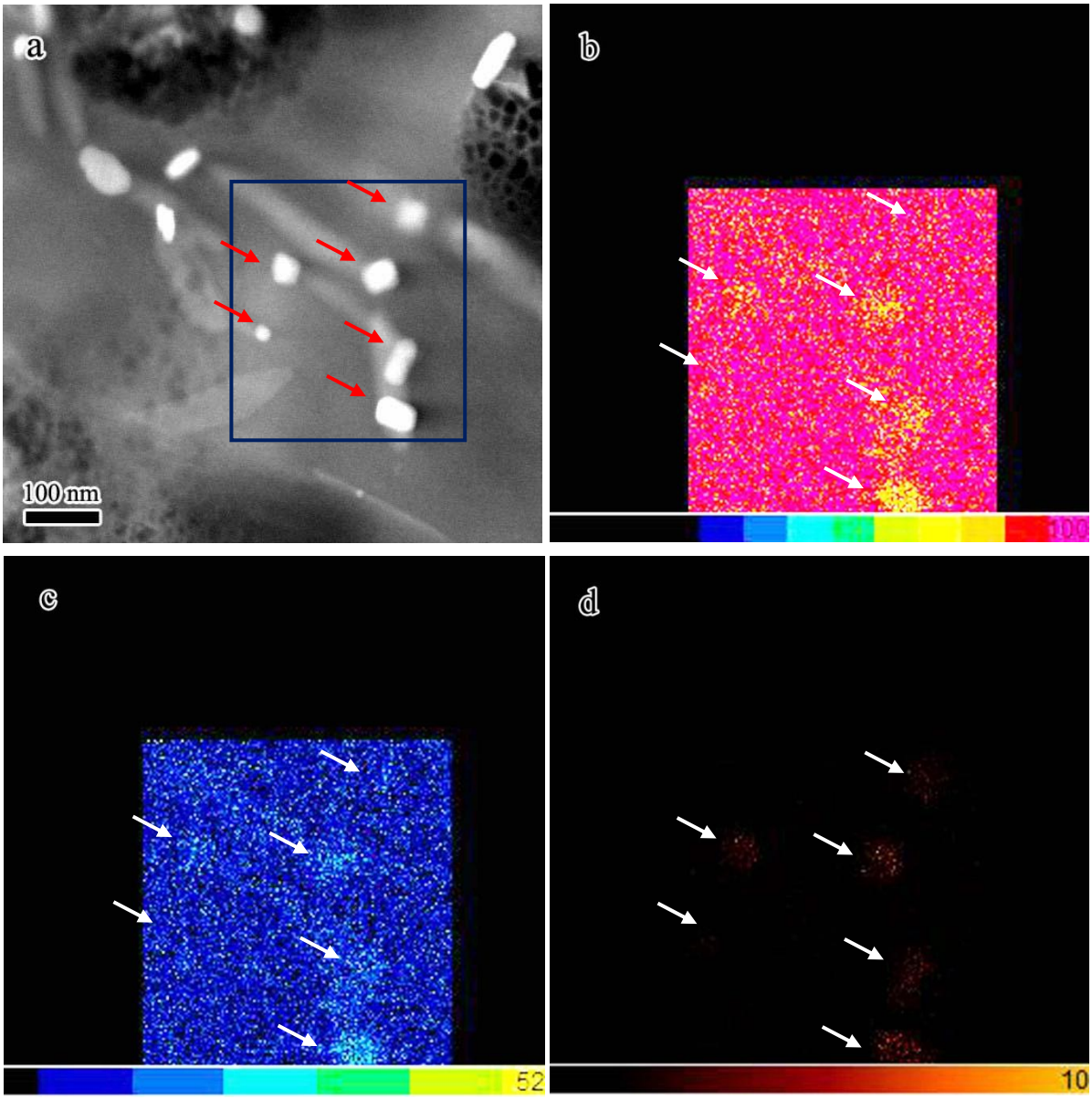

Figure 5.3. (a) HAADF-STEM image at high magnification showing an area containing CPs and attached Al-Mn containing particles, BD ~ $[0001]_m$. The blue box indicates the element mapping area. (b)-(d) Element mapping in STEM for Mg, Al and Mn in the area within the blue box in (a), respectively.

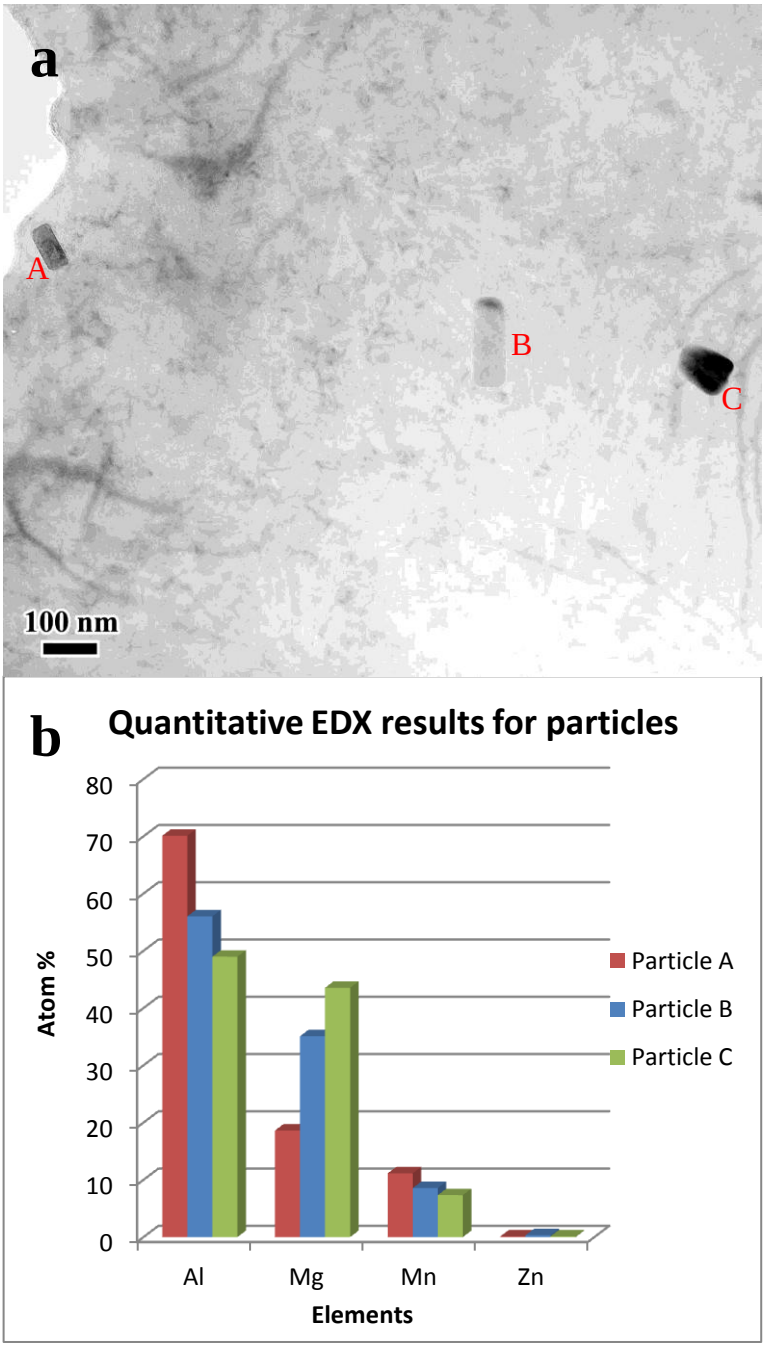

Figure 5.4. An typical EDX experiment performed for the Al-Mn containing particles with different locations. (a) a TEM bright-field image showing three Al-Mn particles, marked A, B and C. (b) SDD-EDX results showing the Mg, Al, Mn and Zn atomic percentages for particles A, B and C, respectively.

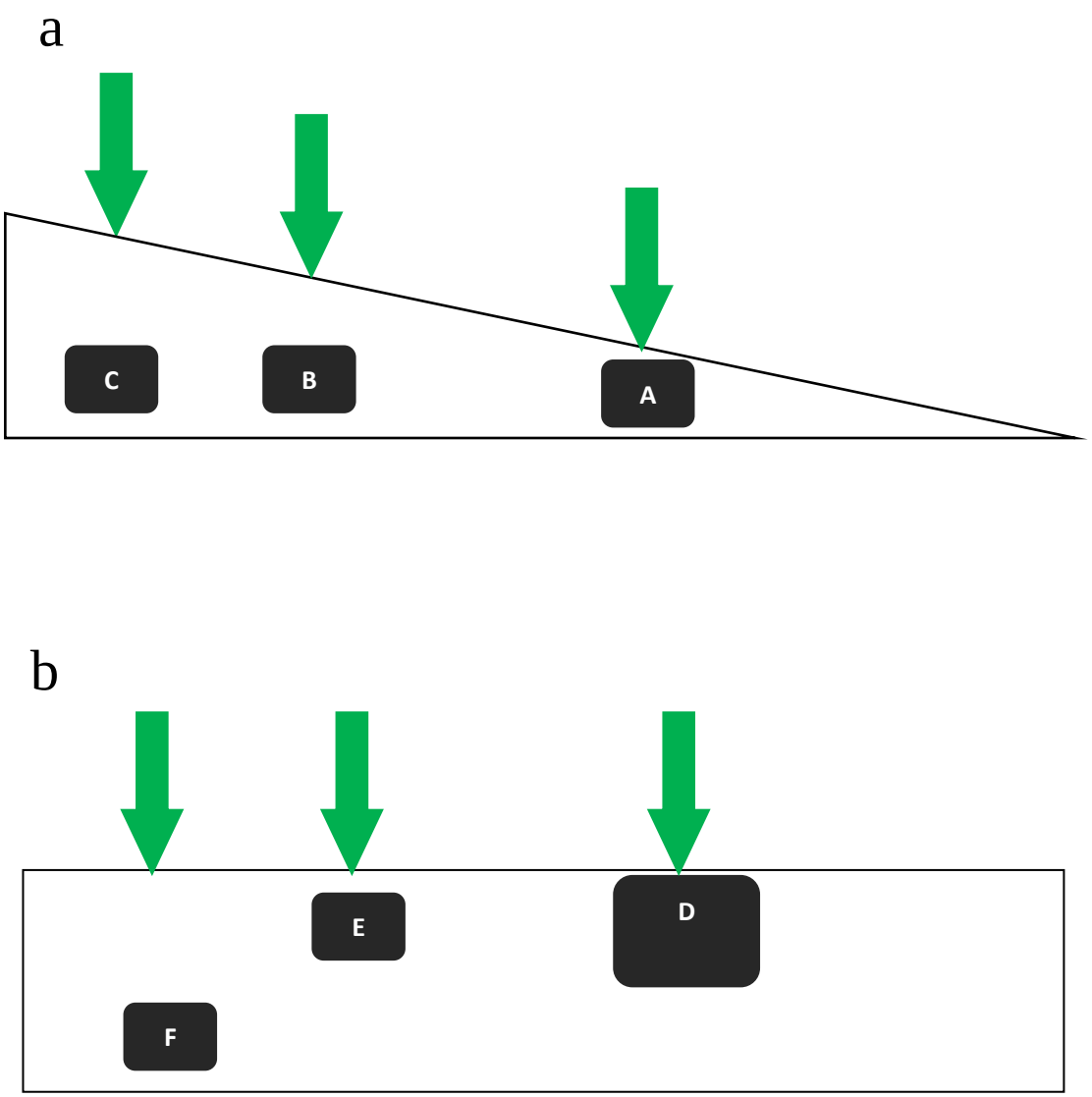

Figure 5.5. Schematic diagrams showing (a) the same sized particles with different TEM foil thicknesses and (b) particles with different sizes and locations in a TEM foil with uniform thickness.

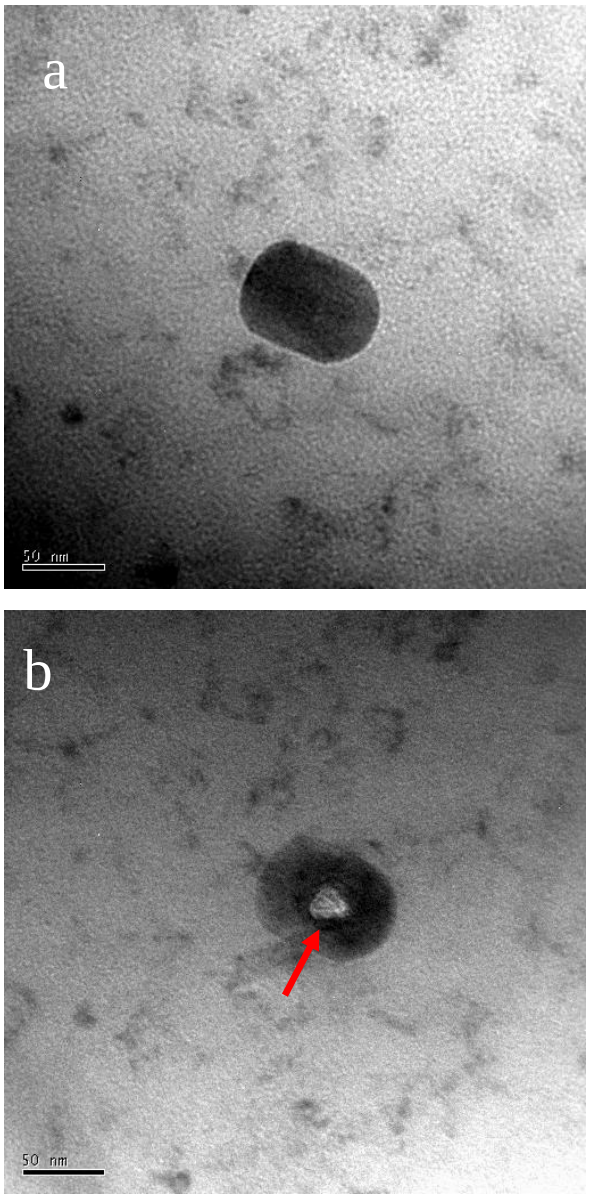

Figure 5.6. Bright-field images showing a typical Al-Mn containing particle (a) before and (b) after SDD-EDX (acquisition time: 100s). The red arrow indicates a hole on the Al-Mn-(Mg) particle due to the beam damage.

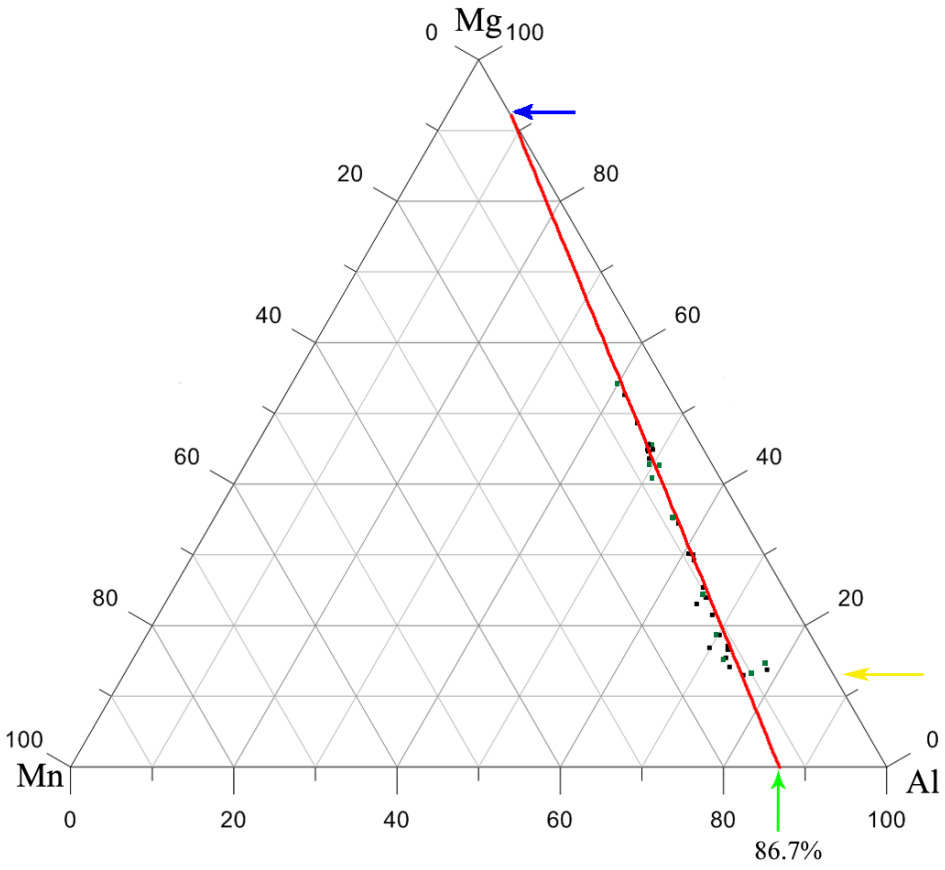

Figure 5.7. Representative quantitative TEM EDX results obtained from the particles (at.%) in the as-cast (black spots) and solution treated (green spots) AZ91. The red line indicates that these particles have the same Al/Mn ratio. The blue arrow indicates the chemical composition of the Mg matrix, while the green arrow indicates the chemical composition of the particles, assuming they are Mg free. The maximum possible Mg content measured from in the particles is indicated by a yellow arrow (around 13 at. %).

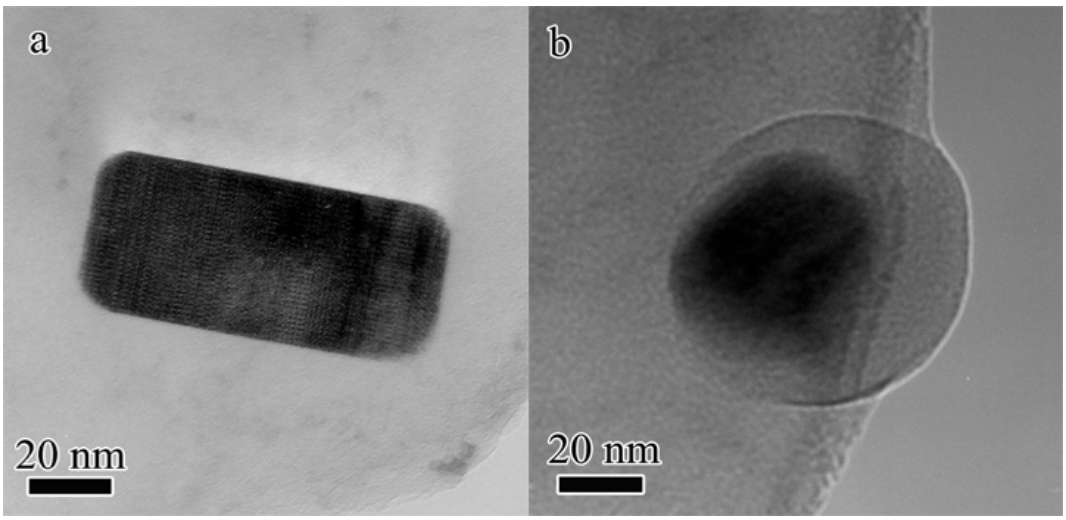

Figure 5.8. TEM micrographs showing different projected shapes of a nano-sized particle: (a) rounded rectangle shape; (b) irregular rounded shape. The inner part of the circle with high contrast is the particle, while the outer part is beam damage in the Mg matrix caused by the convergent electron beam.

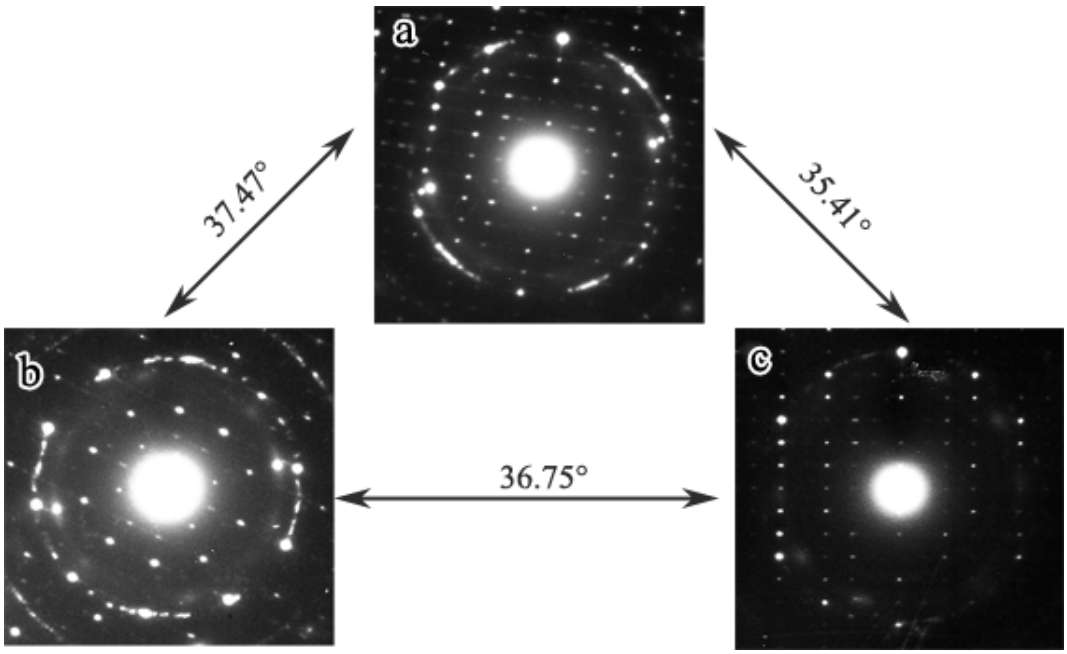

Figure 5.9. TEM diffraction analysis of the particle shown in Figure 5.8: (a) and (b) are the corresponding SAED diffraction patterns of Figures 5.8 (a) and (b), respectively. They show two-fold and pseudo five-fold symmetry, respectively; (c) is another diffraction pattern showing two-fold symmetry. The tilt angles between them are also labelled.

Chapter 6 3D TEM characterization of $Mg_{17}Al_{12}$ precipitation on Al-Mn-(Mg) particles and dislocations in AZ91

6. 1 Introduction

Continuous precipitation of $Mg_{17}Al_{12}$ on Al-Mn-(Mg) particles and dislocations is reported in the previous two chapters. However, both particles and dislocations are three dimensional objects and it is difficult to understand them completely via two dimensional images. Electron tomography is a technique for characterizing 3D nanostructures, and has therefore been used to study the $Mg_{17}Al_{12}$ precipitates in relation to Al-Mn-(Mg) QC particles and dislocations.

This chapter summarises the results obtained using two tomography approaches. One uses HAADF-STEM for $Mg_{17}Al_{12}$ precipitates on Al-Mn-(Mg) particles. In this part, the attachment between $Mg_{17}Al_{12}$ and Al-Mn-(Mg) particles was confirmed by a tilt series from 60˚ to -60˚. The Al-Mn-(Mg) particle is shown to be rod shaped, which agrees with its DQC structure [70]. Apart from the irregular rounded cross section mentioned in Chapter 5, the cross section of the rod is found to be a rounded rectangle here using electron tomography. Various projections of these particles are explained using the 3D information obtained and the reason for various shapes of the projections is also discussed. The other technique is BF-STEM applied to study $Mg_{17}Al_{12}$

precipitates on the dislocations. In this part, a diffraction alignment technique was used to obtain the 3D morphology of dislocations at the same time as the $Mg_{17}Al_{12}$ precipitates. Combined with 2D TEM information, these dislocations are proved to have a spiral morphology composed of a number of basal and non-basal segments. The formation of such a morphology is probably related to the difference in the dislocation mobility between the basal and non-basal segments. However, $Mg_{17}Al_{12}$ precipitates are not reconstructed well in these two tomograms; the reasons are discussed and some suggestions are given to improve the tomograms.

6.2 3D TEM characterisation of joined Al-Mn-(Mg)-CP particles

Before the application of electron tomography, various shapes of Al-Mn-(Mg) particles were observed by conventional 2D TEM, as shown in Figure 6.1. Irregular round particle and rounded rectangles, as illustrated in Figures 6.1 (a) and (b), are commonly seen in most areas of the samples. Some long strips, as shown in Figure 6.1 (c), are also observed. Apart from the strips, teardrops are often seen as well, especially in the areas close to the sample hole, as shown in Figure 6.1 (d). A small number of Al-Mn-(Mg) particles exhibit round square and hexagonal shapes, as shown in Figures 6.1 (e) and (f), respectively. Except the long strips, which are a few hundred nm in length, the other particles have a size in the range from 50 nm to 200 nm. All of these images are of course the projections of the 3D particles [100].

According to the tilting experiments of § 5.2, the decagonal Al-Mn-(Mg) particles have a short rod shape with an irregular rounded cross section and such particles present both irregular rounded and rounded rectangle projections. Thus, the observed shapes in Figure 6.1 (a) and (b) should be from Al-Mn-(Mg) rods with irregular round cross sections. The long strips, one of which is shown in Figure 6.1 (c), can also be understood as having the same 3D morphology as that in Figures 6.1 (a) and (b), but with a different length-to-width ratio. The teardrop shape, as shown in Figure 6.1 (d), shows a low contrast on one of its ends. As mentioned in Chapter 3, PIPS was used to clean the contamination from the TEM sample surfaces. The ion beam not only removes the oxide from the sample, but also inevitably removes a certain part of the sample including particles. The reduced thickness of the particle is likely probably for the low contrast. Meanwhile, the teardrop shows a great similarity to the rods at its other end. This suggests that it may also have had a rod shape before the PIPS cleaning, as illustrated in Figure 6.2, which contains two schematic diagrams illustrating how a teardrop projection is produced. Figure 6.2 (a) shows part of a short rod removed, producing a cylinder with a slope. Figure 6.2 (b) is a projection of the cylinder in Figure 6.2 (a), which presents a teardrop shape like that in Figure 6.1 (d).

The rounded square (6.1 (e)) and hexagonal (6.1 (f)) shapes require a different 3D particle morphology, which was determined using HAADF-STEM tomography. The sample used was solution treated and then aged at 200℃ for 0.5h. Figure 6.3 is part of an HAADF-STEM tomography tilt series, in which the $Mg_{17}Al_{12}$ and Al-Mg-(Mn)

particles can clearly be distinguished (except at -60 °). As mentioned before, compared with $Mg_{17}Al_{12}$ precipitates, Al-Mg-(Mn) particles have a strong Z contrast because of their high average atomic number as compared with the Mg matrix. Therefore, the bright particles are Al-Mn-(Mg) phase and the grey particles with low contrast are the $Mg_{17}Al_{12}$ precipitates. The attachment between the CP and Al-Mg-(Mn) particles was seen over the whole tilt series. This confirms the precipitation of $Mg_{17}Al_{12}$ on the Al-Mn-(Mg) particles. At -60 °, the lath-shaped $Mg_{17}Al_{12}$ precipitate is nearly vertical and its increased thickness along the beam direction raises its intersity in the image at -60 °. This makes its contrast close to that of the Al-Mg-(Mn) particle.

Figure 6.4 shows 3D views reconstructed from the tilt series in Figure 6.3. Since the $Mg_{17}Al_{12}$ precipitate has a weak Z contrast in the α-Mg matrix, its 3D morphology is difficult to produce even with a low threshold, but the 3D morphology of the Al-Mn-(Mg) particle can be seen clearly. This one is a short rod.

Figure 6.5 (a) shows another view of the particle, when the viewing direction is inclined to its long axis. The cross section of the particle presents an approximate rounded square shape, which corresponds to Figure 6.3 (e). Meanwhile, as shown in Figure 6.5 (a), the projection of the particle exhibits a hexagonal shape, which is close to Figure 6.1 (f). Thus, the hexagonal shape in Figure 6.1 (f) can be understood as a projection of a rod as in Figure 6.5 (a). Figure 6.5 (b) shows a slice through the

reconstructed particle. There is a notch in the particle, indicated by a green arrow in Figure 6.5 (a). The formation of such a notch will be discussed in §6.4.

According to the tomography as shown in Figures 6.3 to 6.5, the cross section through the Al-Mn-(Mg) rod does not present only an irregular rounded shape but also an approximate rounded square shape. Figure 6.6 illustrates how the projections observed in Figure 6.1 form from Al-Mn-(Mg) particles of different shapes and orientations in a wedge-shaped TEM sample. All the projections are actually from two kinds of rod-shaped particle.

In summary, although the Al-Mn-(Mg) particles in AZ91 present various 2D projections, all these particles actually have rod shapes in 3D, which agrees with the DQC structure [70]. The cross-sections of these rods are either irregular globular or rounded square. The length-to-width ratio of most rods is between 2 and 4, but this ratio for some long rods can be more than 10. Compared with the Al-Mn-(Mg) DQC particles, the $Mg_{17}Al_{12}$ precipitate is not reproduced well. This will be discussed in § 6.4.

6.3 3D characterization of the continuous precipitates on dislocations

The sample was solution treated, compressed by 0.6% and then aged at 200℃ for 0.5h. The foil normal of the sample at zero tilt was within 2 ° of $[11\bar{2}0]_m$. After diffraction

condition alignment, the sample was maintained at a two beam condition with $g = 1\bar{1}01$ and a similar Bragg deviation parameter for the whole tilt series. Some images close to low index zone axes were removed from the reconstruction.

Figure 6.7 is part of a BF-STEM tomography tilt series showing the dislocations along with continuous precipitation on them. The tilt acquisition extends from -52 °to 58 °. During the tilt acquisition and the reconstruction, two issues obtrude. Firstly, beam damage occurred after the first 10 images, as indicated by the red arrows in Figure 6.7. Secondly, the lower right corner of the area is too thick for the imaging of the dislocations and precipitates, especially at high tilt angles. Therefore, only the area within the yellow box is used in the reconstruction.

The zero tilt image in Figure 6.7 shows the dislocations when the beam direction is close to $[11\bar{2}0]_m$. The dislocations present three different morphologies. Some are straight lines following the trace of $(0001)_m$, as indicated by the blue line. Some are straight lines on $(0001)_m$ with oblique lines away from $(0001)_m$ between them, as indicated by the yellow line. The others are curved with a "W" shape, as indicated within the green box.

Figure 6.8 shows the 3D visualization reconstructed from the tilt series in Figure 6.7. It is seen that most dislocations are well reconstructed, but some dislocations appear discontinuous. The dislocations indicated by yellow and blue in Figure 6.7 are shadowed with yellow and blue lines, respectively in Figure 6.8. Both of them are

actually curved. The W shaped dislocation marked by a green box is not well imaged at such a low magnification. This will be remedied by imaging using high magnification in Figure 6.9. The beam damage also appears in the reconstructed volume as straight lines through the volume along the beam direction, as indicated by white arrows in Figure 6.8-6.11. Because long time ageing produces massive and coarse precipitates, as shown in Figure 4.14, and consumes lots of dislocations, which increases the difficulty of the reconstruction, a relatively short ageing time is used. However, due to this, some $Mg_{17}Al_{12}$ precipitates on the dislocations are so small that they are difficult to distinguish from the dislocations.

Figure 6.9 (a) is a BF-STEM image at high magnification of the area defined by the green box in Figure 6.8. Figure 6.9 (b) shows a 2D schematic diagram of the dislocation and precipitates in (a). In this area, the precipitates have a relatively large size and are marked A, B, C and D. The dislocations (black curves) and traces of the basal planes (marked with blue dashed lines) are also included in Figure 6.9 (b). Figure 6.9 (c) is the 3D reconstructed volume corresponding to the selected area. It can be seen that all the features in the area are reproduced clearly except for some dislocations in the upper left corner and the precipitate D in the lower right corner.

Figures 6.10 (a) and (b) show another two views of the reconstructed volume along the directions of the red and green arrows in Figure 6.9 (c). The discontinuous parts of

the dislocations are connected using white lines. The precipitates are indicated by light blue straight lines.

Figures 6.11 (a) and (b) are the two side-views of the reconstructed volume in Figure 6.9 (c) along the yellow and blue arrows. The dislocations and precipitates are shown schematically to the right of each image. Here the dislocations are curved lines and supposed to start from the top and end at the bottom of the volume, which is indicated using arrows.

From the reconstruction in Figures 6.10 and 6.11, it is found that there are actually two dislocations in the reconstructed volume: one is traced with white (left image) or black (right image) lines in Figures 6.11 (a) and (b). This dislocation presents a "W" shape in 2D along $[11\bar{2}0]_m$ projection, but actually it has a spiral structure in 3D. It goes from the upper left corner to the lower right corner in Figure 6.9, and is composed of spirals on the basal plane connected by segments between the basal planes; the other is a "U" shaped dislocation on the basal plane II in Figure 6.9 (a), which is indicated by green lines in Figure 6.11 (a) and (b). On the basal plane II, the interaction between a part of the spiral dislocation and the U-shaped dislocation can be seen, indicated by red arrows in Figure 6.10 and 6.11.

Figures 6.12 (a)-(b) and (c)-(d) are 3D schematic diagrams corresponding to Figures 6.10 (a)-(b) and 6.11 (a)-(b), respectively. The precipitates are simplified to purple lozenge plates and the dislocations are illustrated using black curves. These diagrams

illustrate the morphologies of the dislocation network and the precipitates in the reconstructed volume. The basal planes are also drawn to show the location of the precipitates and the basal-slip parts of the dislocations.

In order to simplify the depiction of the two dislocations, they are shown separately in Figures 6.13 (a)-(d). Figures 6.13 (a) and (b) visualize the morphology of the spiral dislocation when the beam directions are close to $[11\bar{2}0]_m$ and $[0001]_m$. Figures 6.13 (c) and (d) illustrate the morphology of the U-shaped dislocation when the beam directions also are close to $[11\bar{2}0]_m$ and $[0001]_m$.

The two dislocations interact with each other on the basal plane II. Figure 6.14 is a schematic diagram showing the dislocations on the basal plane II only.

Figure 6.15 is a high magnification BF TEM image showing another W-shaped dislocation with $g = 1\bar{2}10$ and beam direction close to $[10\bar{1}0]_m$. It is shown that the curved dislocation has a stair-like structure, composed of a number of basal or non-basal segments.

Figure 6.16 shows the reconstructed precipitate C in Figure 6.9 (b). In such an imaging mode, the precipitate is not imaged so well as the dislocations. The reconstructed $Mg_{17}Al_{12}$ precipitate presents part of its profile. Some parts in the centre, as indicated by the yellow arrow in Figure 6.16 (a), are not reproduced. This is due to its contrast mechanism in the imaging mode and will be discussed, particularly in §

6.4.4. Figure 6.16 (b) is a typical BF-TEM image showing the strain contrast between the $Mg_{17}Al_{12}$ precipitate and the Mg matrix.

In summary, the 3D morphology of dislocations in AZ91 has been reconstructed successfully, despite of some deficiencies, while some parts of the $Mg_{17}Al_{12}$ precipitates involved are not well reproduced.

6.4 Discussion

6.4.1 The projections of Al-Mn-(Mg) particles

As shown in Figure 6.6, the various shapes of the projection in Figure 6.1 correspond to the different orientations of the Al-Mn-(Mg) particles in the Mg matrix. Generally, the precipitates should show a uniform morphology along a certain crystallographic direction of the matrix, if they have a well-defined orientation relationship (OR) with the matrix. For example, most of the $Mg_{17}Al_{12}$ precipitates have a Burgers OR with the Mg matrix in AZ91 [5]. They always present a lozenge shape when imaged along $[0001]_m$ and a rod-shape along $[11\bar{2}0]_m$, as shown in Chapter 4. In the case of the Al-Mn-(Mg) particles, however, there is no well-defined OR between them and matrix. Thus the Al-Mn-(Mg) particles are oriented randomly in the matrix. This results in their various projections along a given viewing direction.

6.4.2 Deficiencies in the HAADF tomography

Although the 3D morphology of an Al-Mn-(Mg) particle has been determined using HAADF-STEM tomography, there are still some deficiencies in the technique as applied here. Firstly, imperfection of the sample leads to some false features in the reconstruction. As shown in Figure 6.5, there is a notch in one corner of the rod. This actually results from some pits on the surface of the sample, as indicated by red arrows in Figure 6.3. They should be produced during jet-electro-polishing, due to corrosion. The region with these pits has a low thickness and gives low intensity HAADF-STEM contrast, as shown more commonly in the low right corner of the images in Figure 6.3. During the tilting, they moved and overlapped with the Al-Mn-(Mg) particle sometimes. This decreases the intensity of some parts of the particles. In the reconstruction, the software recognizes these parts as a thin area, which results in some loss of thickness in the particle. The same problem also can be produced by the beam damage as indicated by green arrows in Figure 6.3. The pit indicated by white arrows in Figure 6.4 should result from the beam damage in the zero tilt image.

Secondly, the $Mg_{17}Al_{12}$ precipitates are not well reconstructed, which makes it difficult to observe how the $Mg_{17}Al_{12}$ precipitate connects with the Al-Mn-(Mg) particle. A different, low threshold has been tried to illustrate the $Mg_{17}Al_{12}$ precipitate separately from the Al-Mn-(Mg) particle, but it was not successful. This is due to the low Z contrast of the $Mg_{17}Al_{12}$ precipitate. According to previous studies [127-129],

the intensity of each point in an HAADF-STEM image is roughly proportional to Z^2. The $Mg_{17}Al_{12}$ precipitate has around 2/5 positions taken up by Al, but the atomic number of Al (Z=13) is very close to that of Mg (Z=12). Thus, it is difficult to distinguish the $Mg_{17}Al_{12}$ from the Mg matrix by HAADF-STEM. One possible way to sort out this problem would be tomography on these two types of particles separately using different image modes. Z contrast in HAADF-STEM can still be used for the Al-Mn-(Mg) particle, while diffraction contrast in the dark field in either TEM or STEM might be a candidate to reconstruct the $Mg_{17}Al_{12}$ precipitate. However, the diffraction alignment work could be as difficult as that in dislocation tomography. Finally, the two tomograms have to be combined together.

6.4.3 3D dislocation network

W-shaped dislocations are not only commonly observed in the compressed AZ91 but also in other deformed Mg alloys viewed along $[11\bar{2}0]$ [130-134]. Based on the dislocation tomography (Figure 6.10-6.13), the dislocation line was a 3D spiral structure. It contains 2D sections on the basal plane and links segments between these basal planes. The 2D curves must be basal-slip dislocations, while these linking segments are composed of a number of stair-like structures according to Figure 6.15. Each step contains a basal-slip segment and a non-basal segment. The 3D spiral structure of the dislocations may result from the different mobility of basal and non-basal slip segments during the deformation. Figure 6.17 illustrates a possible

mechanism.

After the water quench from solid solution, some dislocations together with lots of vacancies are produced. During the subsequent deformation, more dislocations are introduced. These dislocations consist of both basal and non-basal segments (Figure 6.17 (a)), but most of them are a-type, as mentioned in Chapter 4. A blue hexagon is used to indicate the basal plane of the hcp unit cell and the $\langle 11\bar{2}0\rangle$ directions. Here the Burgers vector and slip direction are simplified as the same direction, one of $\langle 11\bar{2}0\rangle$, as indicated with the red arrows. As the deformation continues, the dislocations start to move. The basal segments of the dislocations slip easily on the basal planes and bow out to produce some 2D curves on the basal planes (Figure 6.17 (b)). The movement of the non-basal segments can rely on two mechanisms: non-basal slip and climb. The non-basal slip is in either a $\{10\bar{1}0\}$ prismatic plane or $\{10\bar{1}1\}$ first-order pyramidal plane, but this slip is not so easy as basal slip at room temperature [11, 135]. Climb is an important mechanism for the deformation of the Mg at elevated temperatures [136, 137]. In this case, a large number of quenched-in excess vacancies exist in the alloy. These vacancies can interact with the dislocations either by the movement of the dislocation during deformation or their self-diffusion during the consequent ageing. Such an interaction induces climb of the dislocation. However, the mobility of the dislocations on the non-basal planes is not so high as on the basal plane, and some of them may remain still during the whole process, as indicated by the blue arrows in Figure 6.17 (c). The difference in mobility between

the basal and non basal segments produces a number of elbow-shaped dislocations (Figure 6.17 (c)), which looks like a W when viewed along the basal plane (Figure 6.17 (d)), but actually it has a spiral structure.

6.4.4 Problems in dislocation tomography

Although the 3D dislocation network has been reconstructed, some aspects of the technique can still be improved. Firstly, some reconstructed dislocations are discontinuous or not well imaged. This is because some dislocations have a poor contrast under the currently used diffraction condition. This may be partly resolved by rotating the sample, adding another tilt series with a perpendicular g vector and combining it with the previous tomogram. Secondly, some beam damage occurs during the tilt acquisition, which also is present in the reconstructed volume and makes some parts of the dislocations invisible. In order to reduce the beam damage, rapid focusing and acquisition of images should be employed. Finally, the $Mg_{17}Al_{12}$ precipitates in the BF-STEM are not well imaged. Most of them miss some parts of their profiles, as shown in Figure 6.16 (a). This results from the contrast mechanism of the $Mg_{17}Al_{12}$ precipitates in BF-STEM, which consists of both mass-thickness contrast and diffraction contrast. The $Mg_{17}Al_{12}$ phase has poor mass-thickness contrast in an Mg matrix, because it is composed of Mg and Al. Diffraction contrast makes the CPs sharp in some images only, and such a contrast is not well controlled and does not satisfy the projection requirement [88]. However, the $Mg_{17}Al_{12}$ phase

presents obvious strain contrast at the interface between itself and the Mg matrix in many images in the current tilt series. Figure 6.16 (b) shows an example. Such contrast is obvious, because the ageing time is limited (0.5h) for the current sample and the lattice strain between the two phases has not been reduced. Consequently, the strain contrast contributes to the obvious edges of the precipitates in the reconstructed results, while the weak thickness-mass contrast contribution leads to the missing parts of the precipitate profile. Finally, the stair-like structure has not been reproduced clearly in the current tomogram and tomography at high magnifications and with the diffraction conditions of Figure 6.14 is worth trying.

6.5 Conclusions

HAADF-STEM and BF-STEM tomography have been applied to the $Mg_{17}Al_{12}$ precipitates on the Al-Mn-(Mg) particles and dislocations in AZ91, respectively. In the HAADF-STEM tomography, the end-to-end connection between the CPs and the Al-Mn-(Mg) particles is confirmed. Meanwhile, it is found that apart from the irregular globular shape, the cross-section of the particle can also present as rectangular. The observed 2D projections of the Al-Mn-(Mg) particles are explained using the 3D morphologies of the particles. Because there is no well-defined OR between the Al-Mn-(Mg) particle and the matrix, the particles are oriented randomly in the matrix, resulting in 2D projections with various shapes.

In the BF-STEM tomography, a dislocation network in the compressed AZ91 is

imaged in 3D. The W-shaped dislocations are found to have a spiral structure composed of lots of basal and non-basal segments. Such a spiral structure results from the different mobilities of the basal and non-basal segments during the movement of the dislocations.

In both the tomography experiments, the $Mg_{17}Al_{12}$ precipitates are not well imaged due to their low contrast. Some suggestions towards resolving this issue and other problems are given in the discussion.

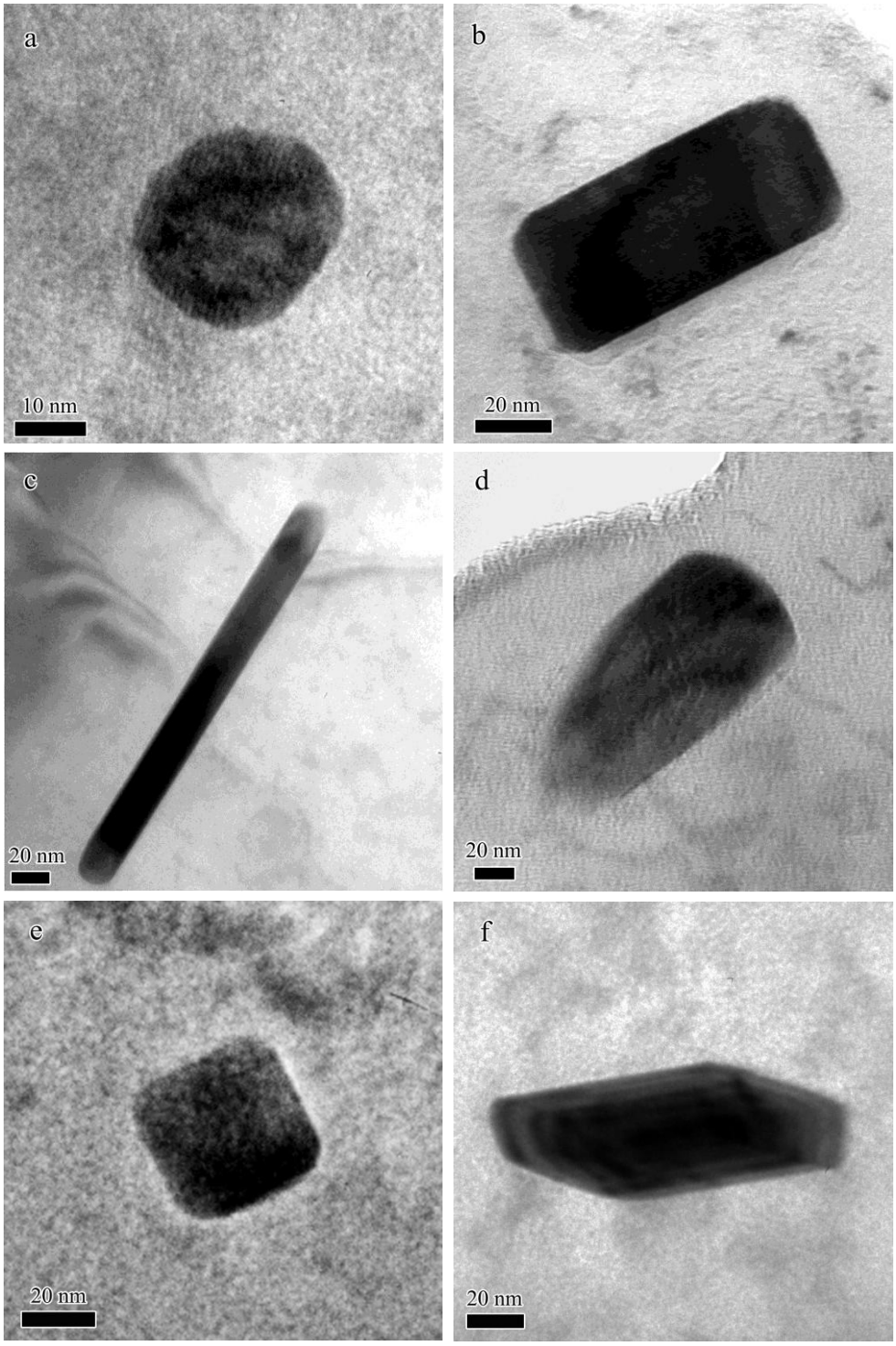

Figure 6.1. Images of various Al-Mn-(Mg) particles in the solution-treated AZ91 alloy obtained with BD~ $[11\bar{2}0]_m$: (a) irregular globule; (b) short rod; (c) long rod; (d) teardrop; (e) rounded rectangle; (f) irregular hexagon.

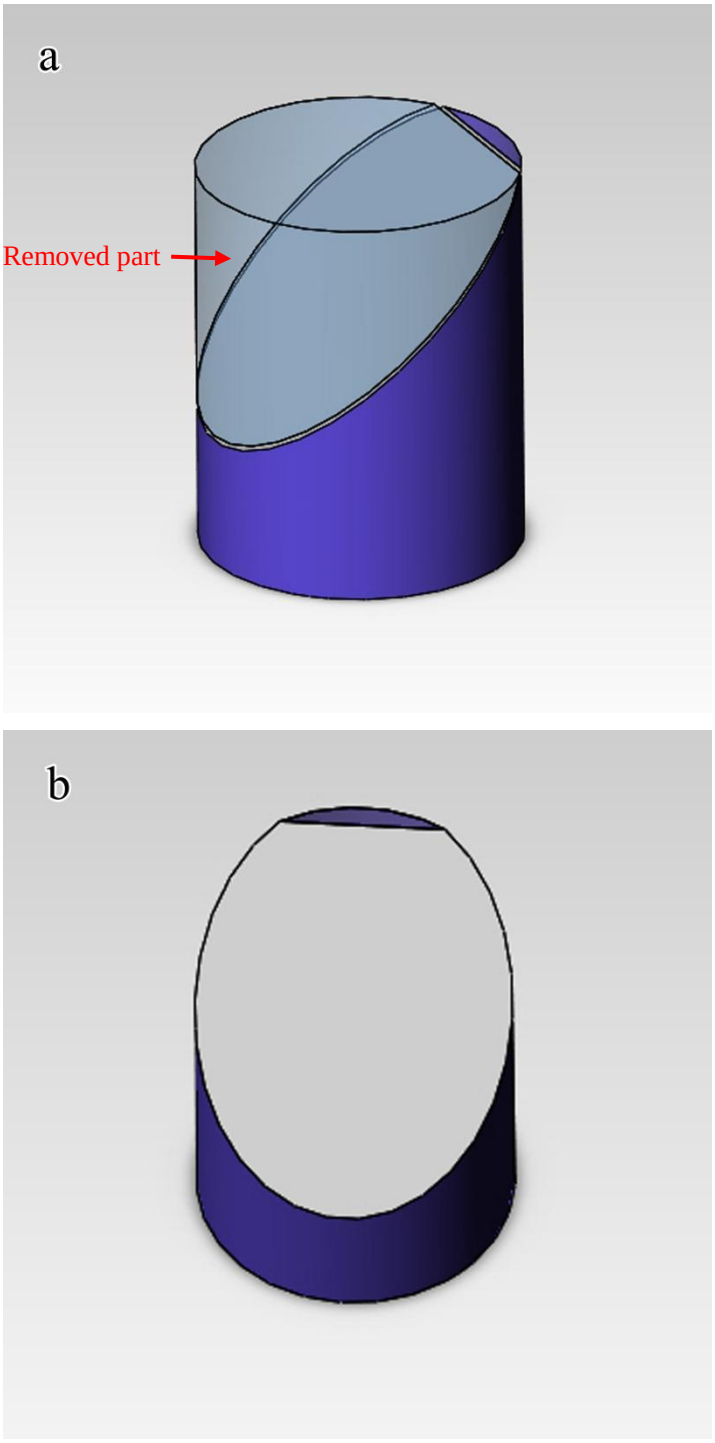

Figure 6.2. Schematic diagrams showing the possible formation process of the teardrop Al-Mn-(Mg) particle in AZ91 TEM samples: (a) 3D illustration of a rod-shaped particle with a part removed by PIPS; (b) a projection of the particle in (a) showing a teardrop shape.

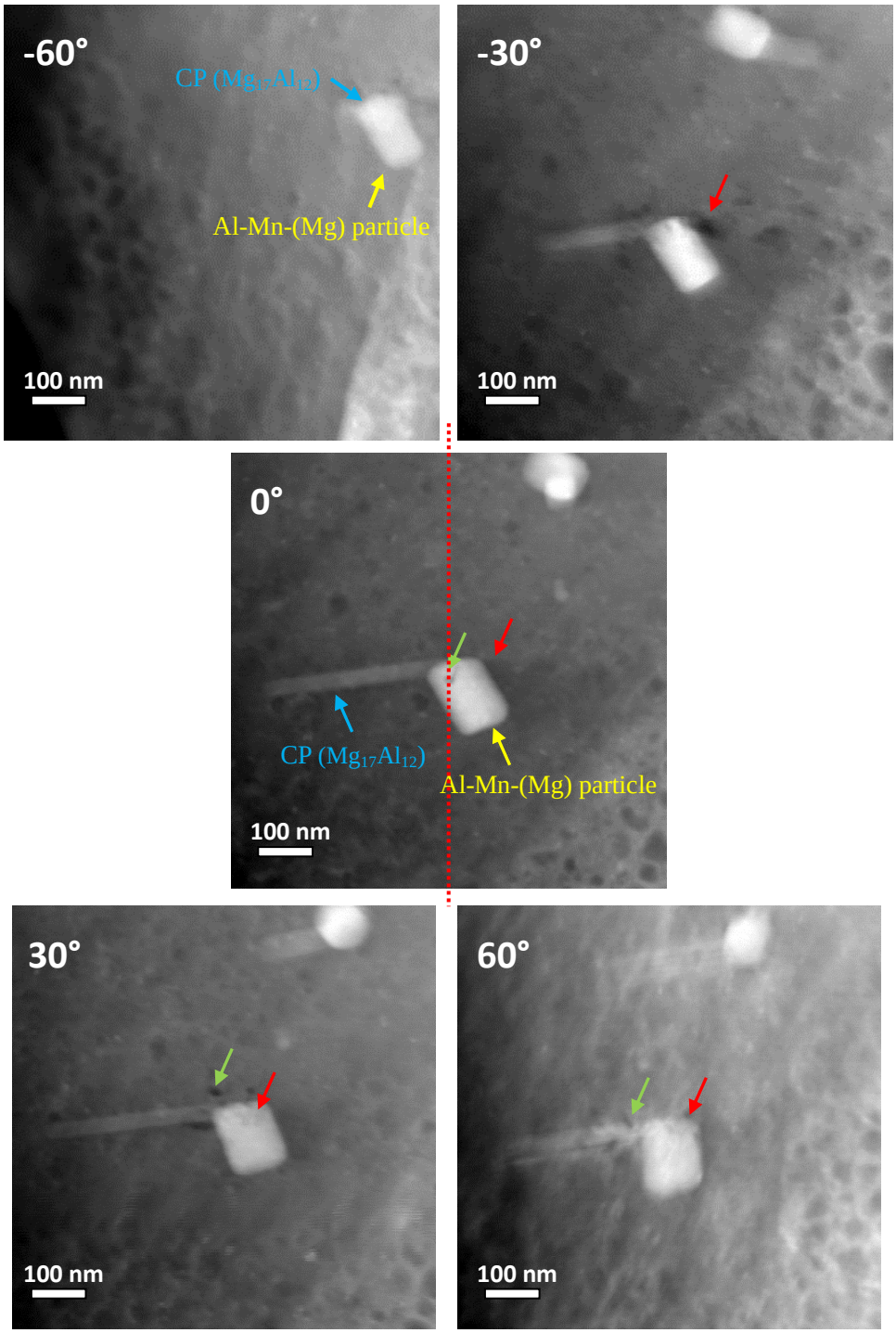

Figure 6.3. Part of an HAADF-STEM tilt series for a joined Al-Mn-(Mg) QC particle and $Mg_{17}Al_{12}$ precipitate. The tilt angle is given in each image. Corrosion pits and beam damage are indicated by red and green arrows, respectively. The $Mg_{17}Al_{12}$ precipitate and Al-Mn-(Mg) particle are indicated by blue and yellow arrows, respectively, at zero tilt. The red dash line in the zero tilt image indicates the tilting axis.

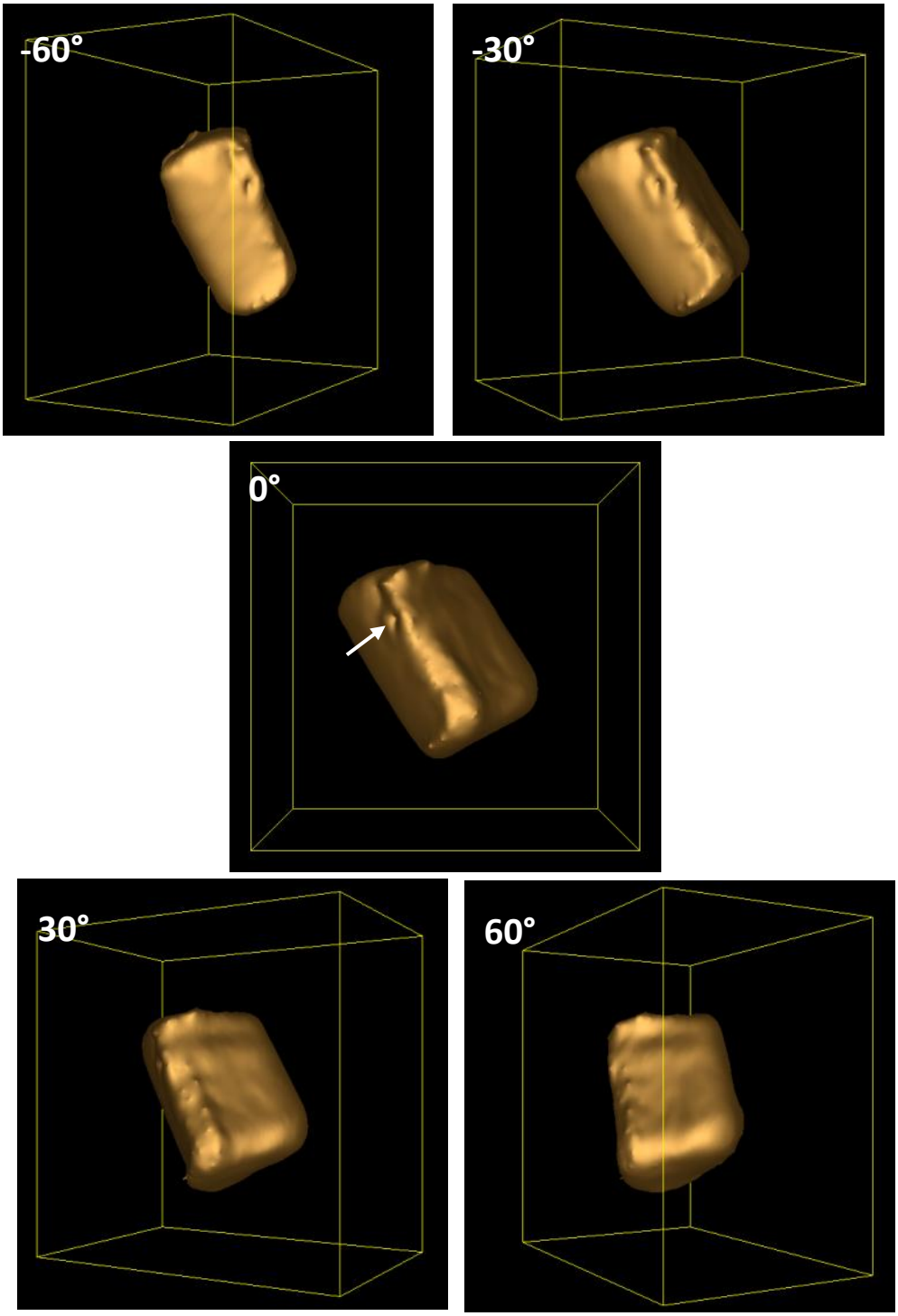

Figure 6.4. Reconstructed views of Al-Mn-(Mg) QC particle in Figure 6.3. The tilt angle is given in each image. The white arrow indicates a reconstructed artifact due to beam demage.

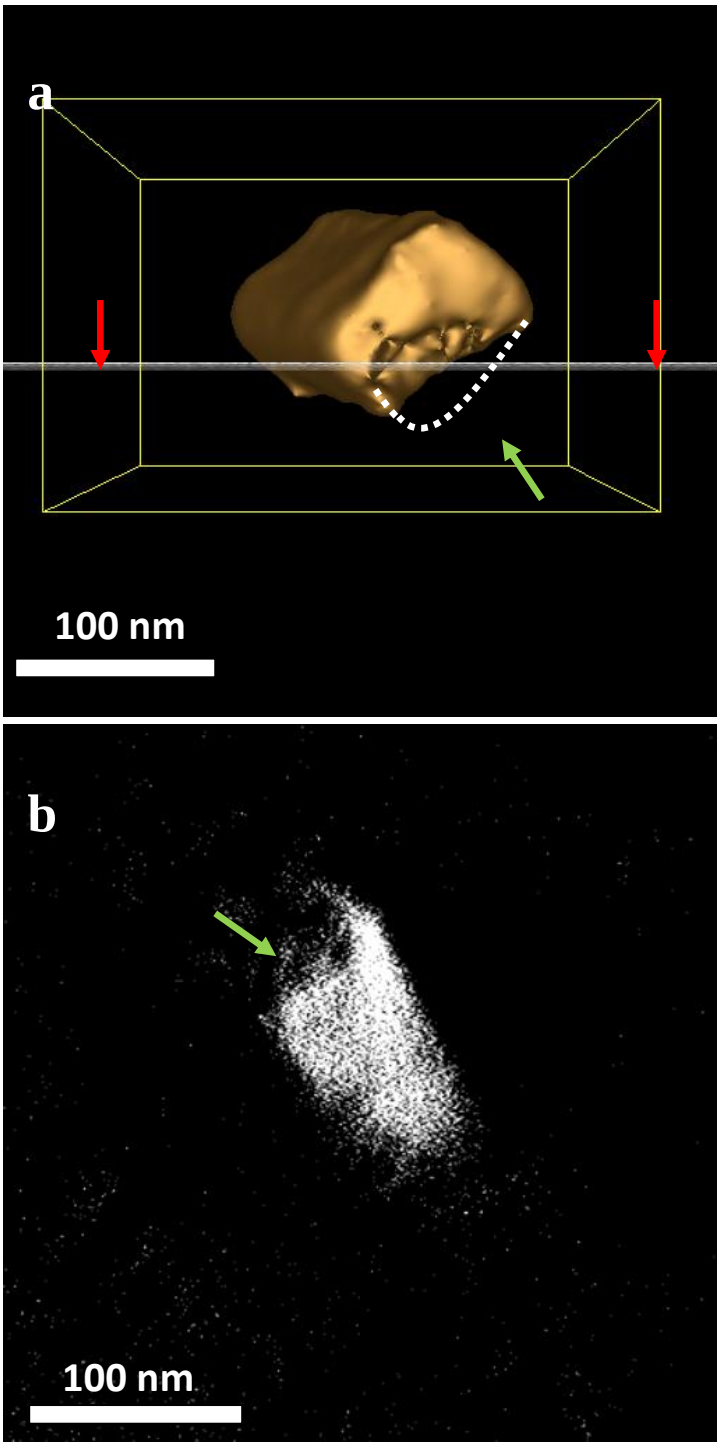

Figure 6.5. (a) The 3D reconstruction of Figure 6.3, showing the top surface and a hexagonal projection of the particle. A slice plane and a notch on the reconstructed particle are indicated with red and green arrows. The supposed complete particle is illustrated using a white dashed curve. (b) The intersection of the slice with the reconstructed particle is shown in (a). The green arrow indicates a reconstructed notch due to contamination on the sample.

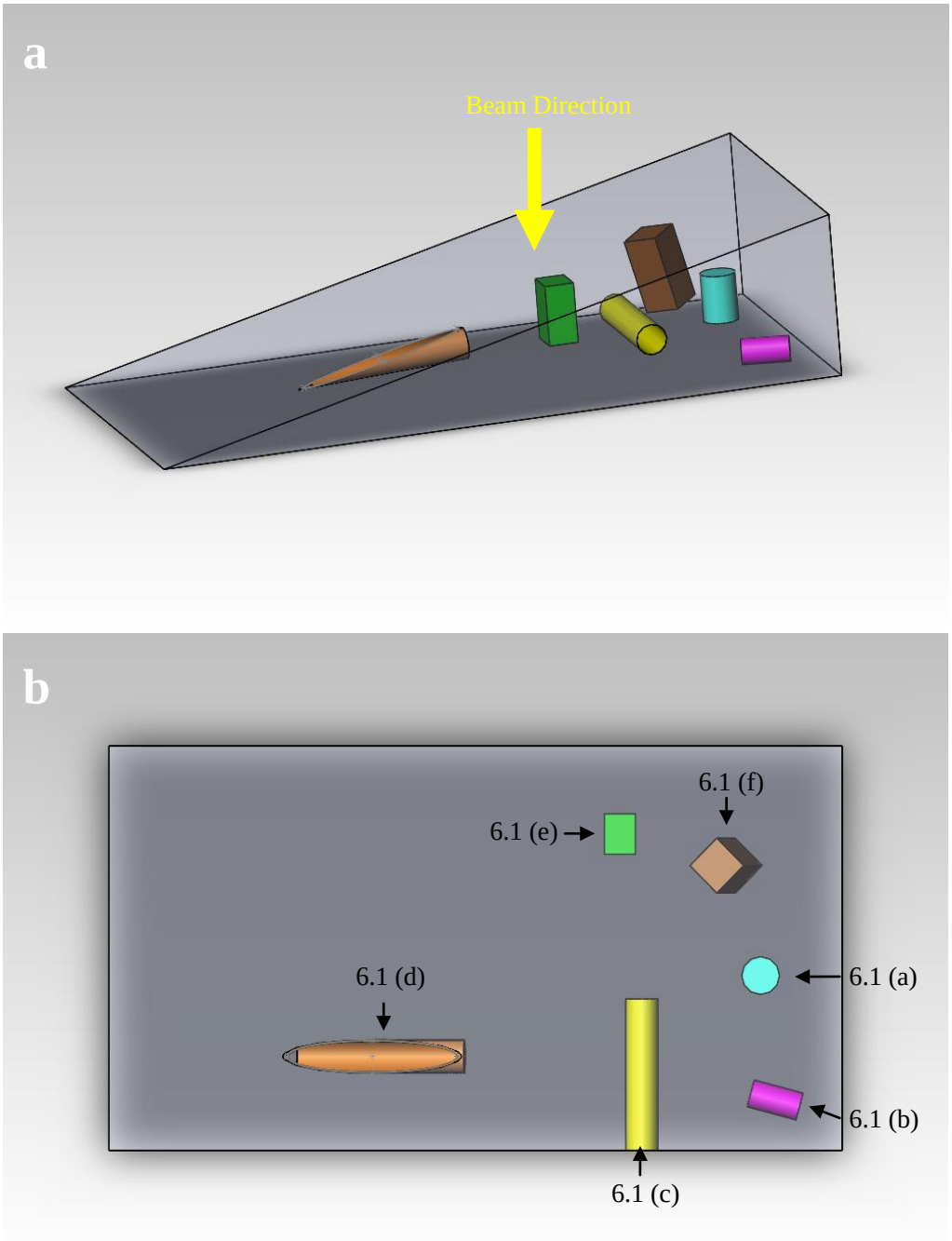

Figure 6.6. Schematic diagrams showing (a) a wedge-shaped TEM sample containing rod-shaped Al-Mn-(Mg) particles with different orientations. The yellow arrow indicates the beam direction; (b) a 2D projection of the sample in (a) along the beam direction. The projected shapes corresponding to Figure 6.1 (a)-(f) are indicated by arrows.

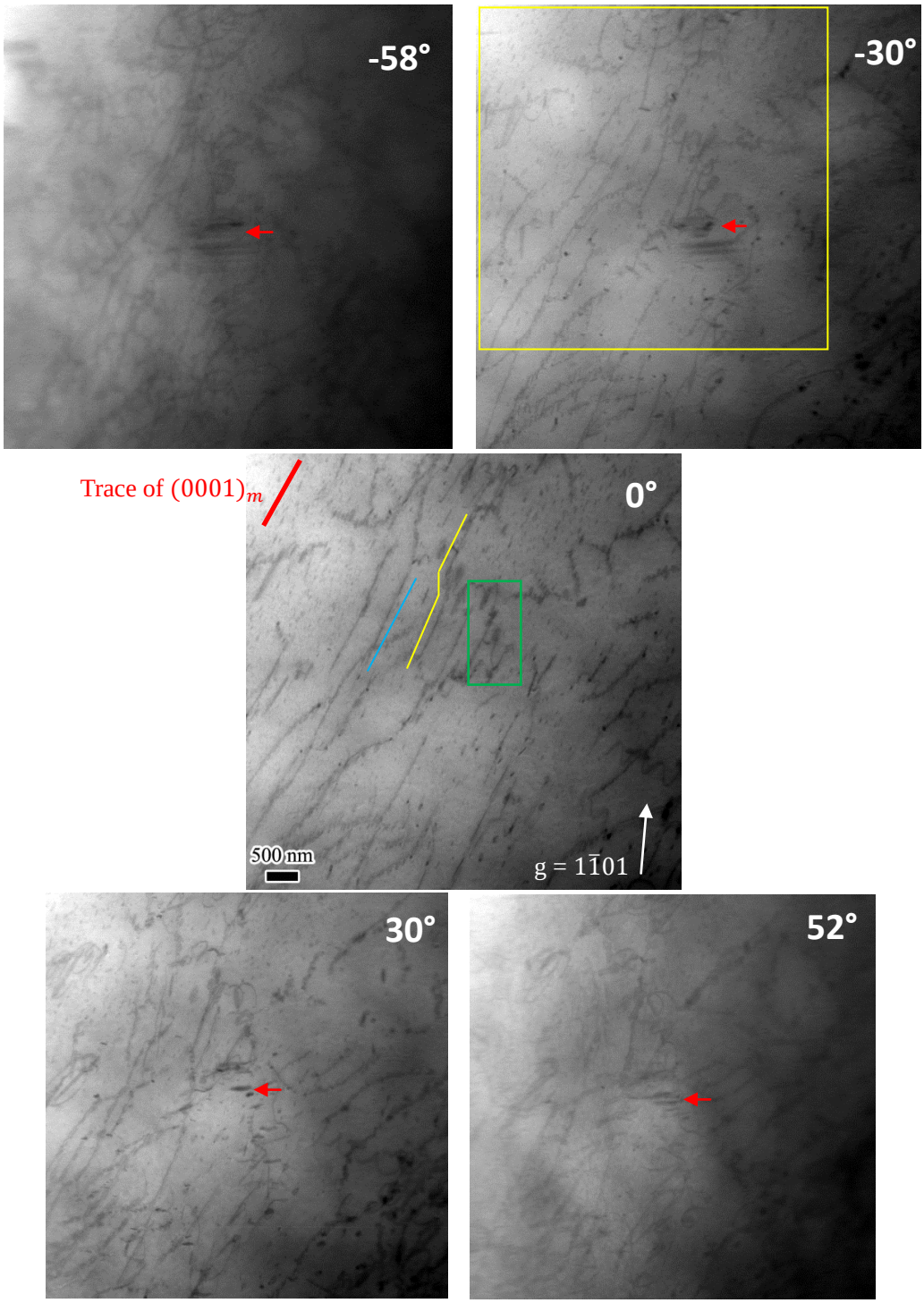

Figure 6.7. Selected BF-STEM images from the tilt series acquired for construction of the tomogram. A tilt angle is given in each image. The red arrows indicate beam damage. In the zero tilt image, dislocations of different morphologies and the trace of $(0001)_m$ are highlighted. The g vector is also indicated by a white arrow. The sample was solution treated and then compressed by 0.6% and aged at 200℃ for 0.5h.

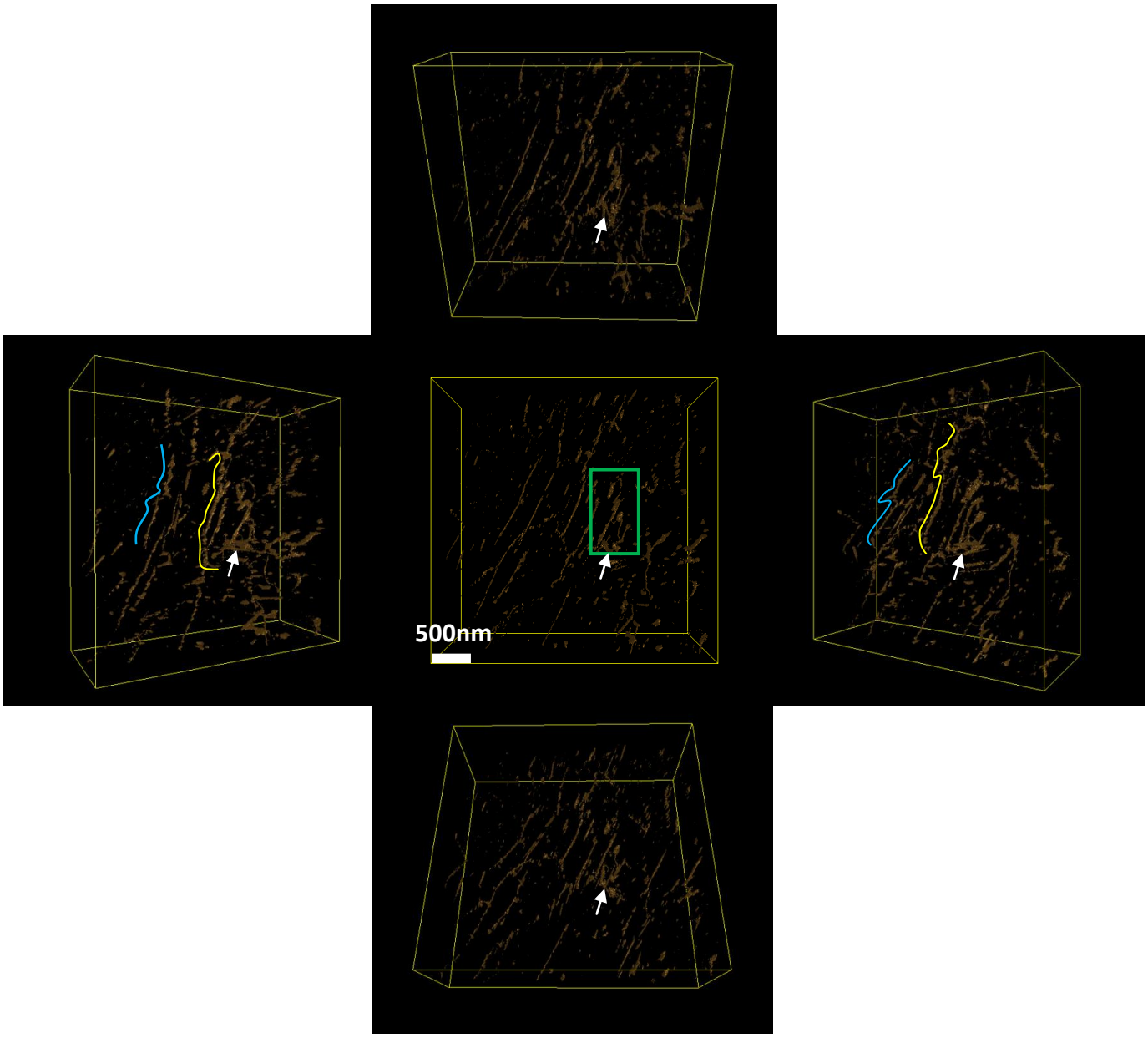

Figure 6.8. 3D reconstruction of tilt series in Figures 6.7, showing the dislocation network in the area within the yellow box. The blue and yellow dislocations in Figure 6.7 are indicated by blue and yellow curves, respectively. The green box corresponds to the green box in Figure 6.7. The white arrows indicate beam damage, which is also shown in Figure 6.9-6.11 at high magnification.

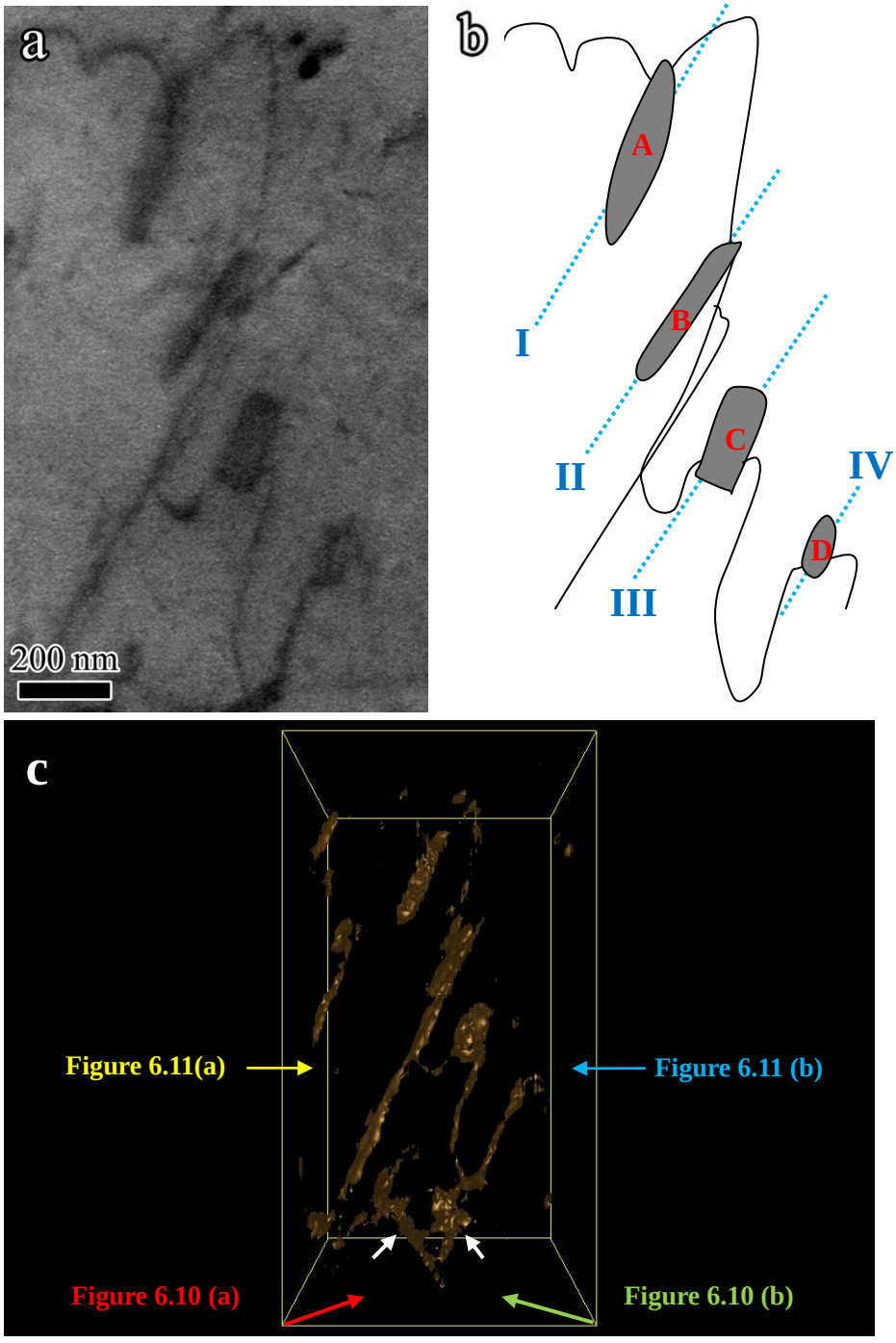

Figure 6.9. (a) A BF-STEM image at high magnification, showing the area marked in Figure 6.7. BD~$[11\bar{2}0]_m$ (b) A schematic diagram showing the dislocations and precipitates in (a). The four precipitates are marked A to D, and they lie on four basal planes, which are the traces marked I to IV. (c) A magnified view of the reconstructed volume for (a). The white arrows indicate beam damage. The viewing directions for Figures 6.10 and 6.11 are also marked with arrows.

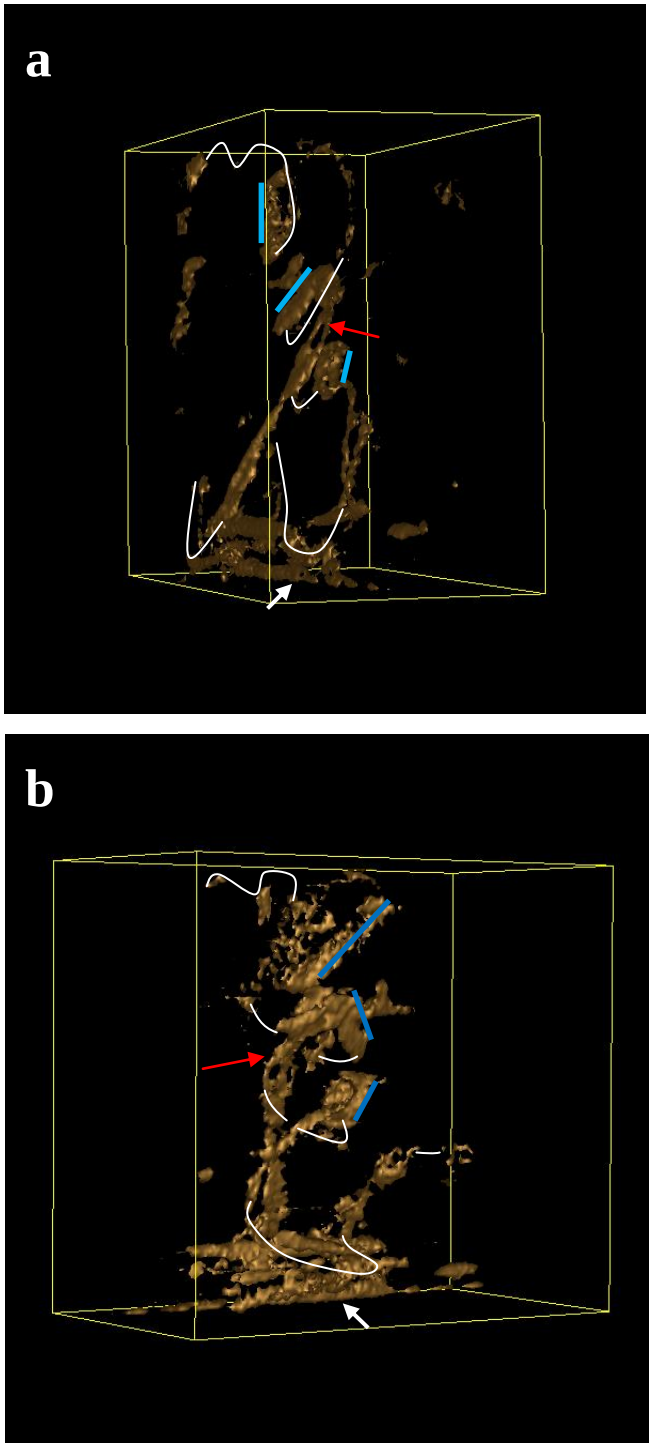

Figure 6.10. Two views of the reconstructed volume in Figure 6.9. The viewing directions accord with the arrows in Figure 6.9 (c). The precipitates, except D, are marked with light blue straight lines. The discontinuous segments of the dislocations are connected with white curves. The red arrows indicate the interaction of two dislocations. The white arrows indicate beam damage.

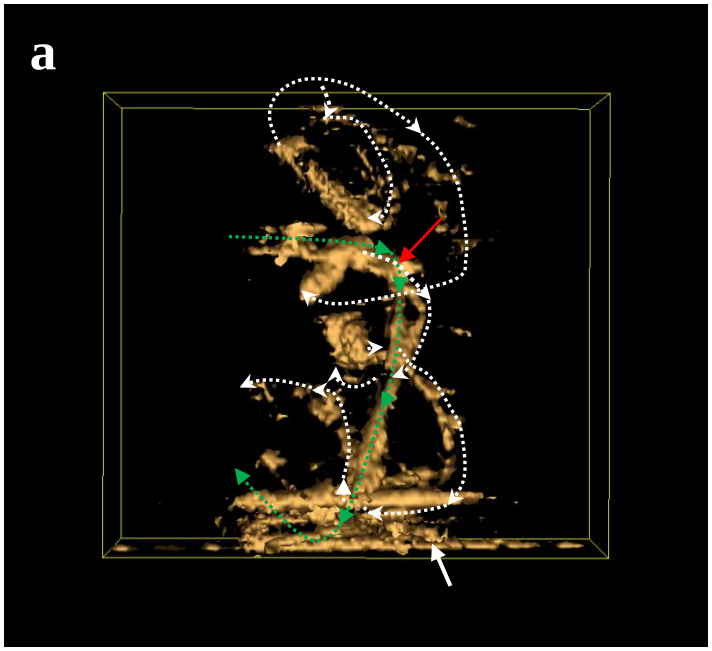

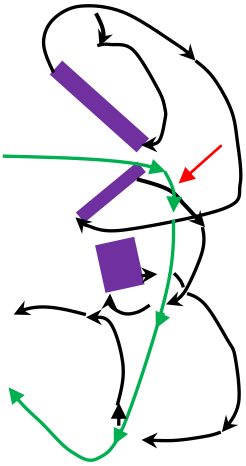

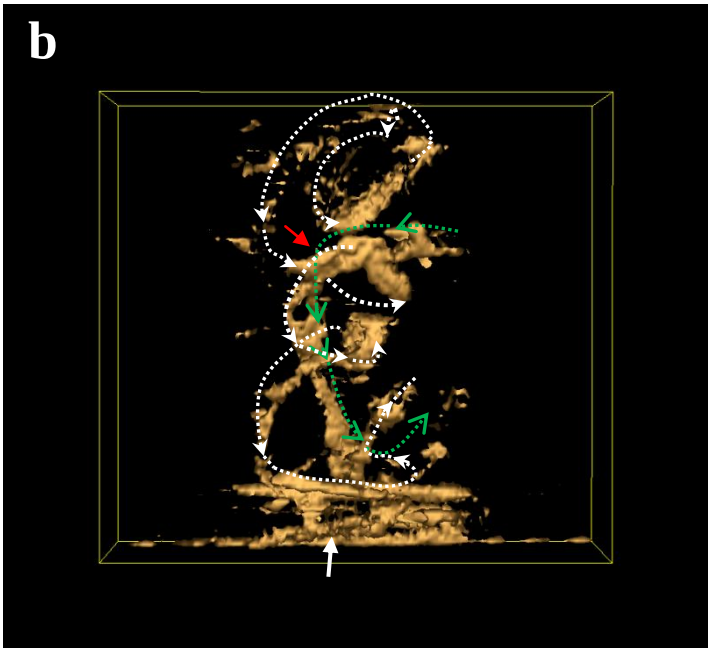

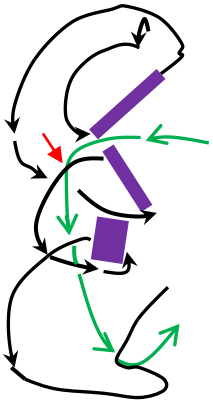

Figure 6.11. Two lateral views of the reconstructed volume, showing the dislocation lines. The viewing directions for (a) and (b) are shown in Figure 6.9 (c). The white and green dashed curves indicate the spiral and U shaped dislocations, respectively. It is supposed that the dislocation lines go from the top to bottom of the volume. The arrows on the dislocations indicate the direction along which the dislocations go through the volume. The white arrows indicate beam damage. A 2D schematic diagram for each image is given on the right. The red arrows indicate the interaction of two dislocations.

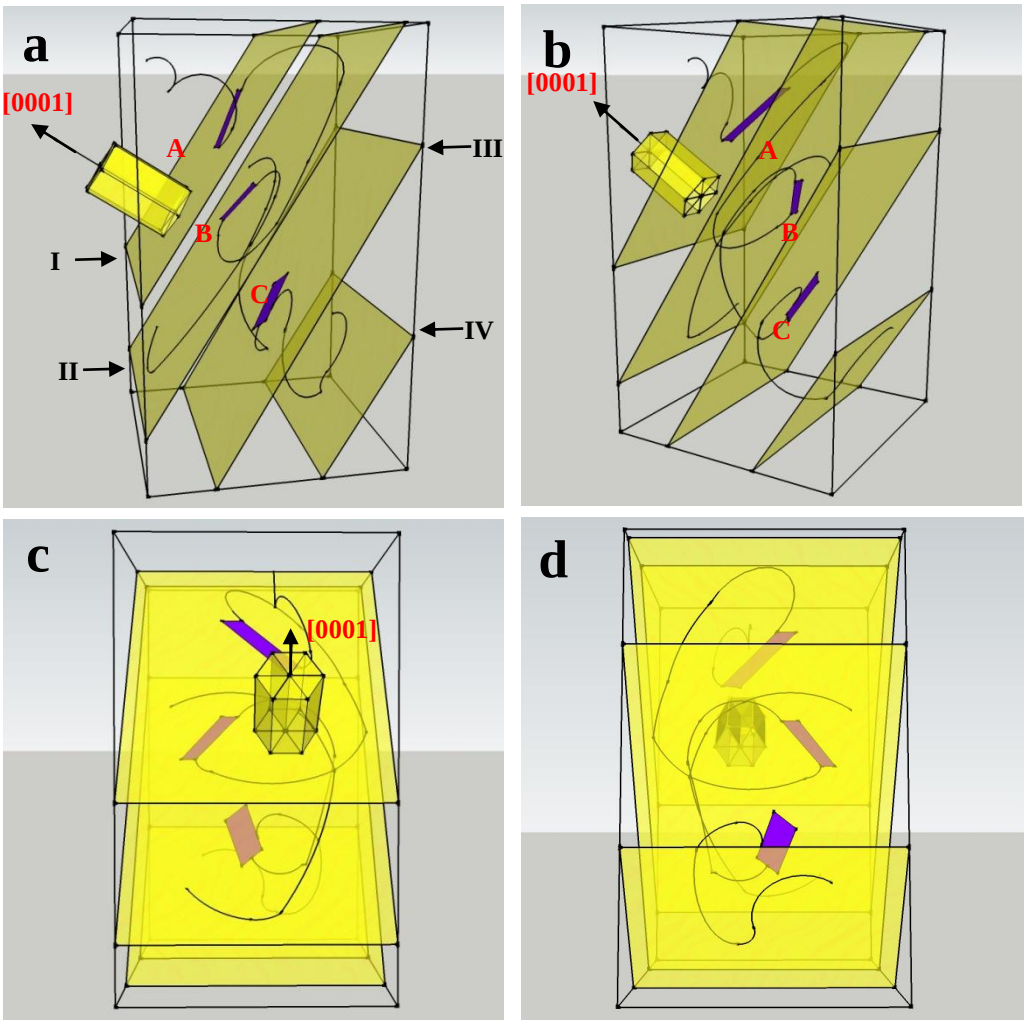

Figure 6.12. Four 3D schematic views showing the dislocations and precipitates. The black lines indicates the dislocations, the purple planes represent the precipitates; The basal planes I to IV are also marked. A hcp unit cell is created to indicate the crystallographic orientations. The black arrow indicates[0001]. (a) and (b) correspond to Figure 6.10 (a) and (b); (c) and (d) correspond to Figure 6. 11 (a) and (b).

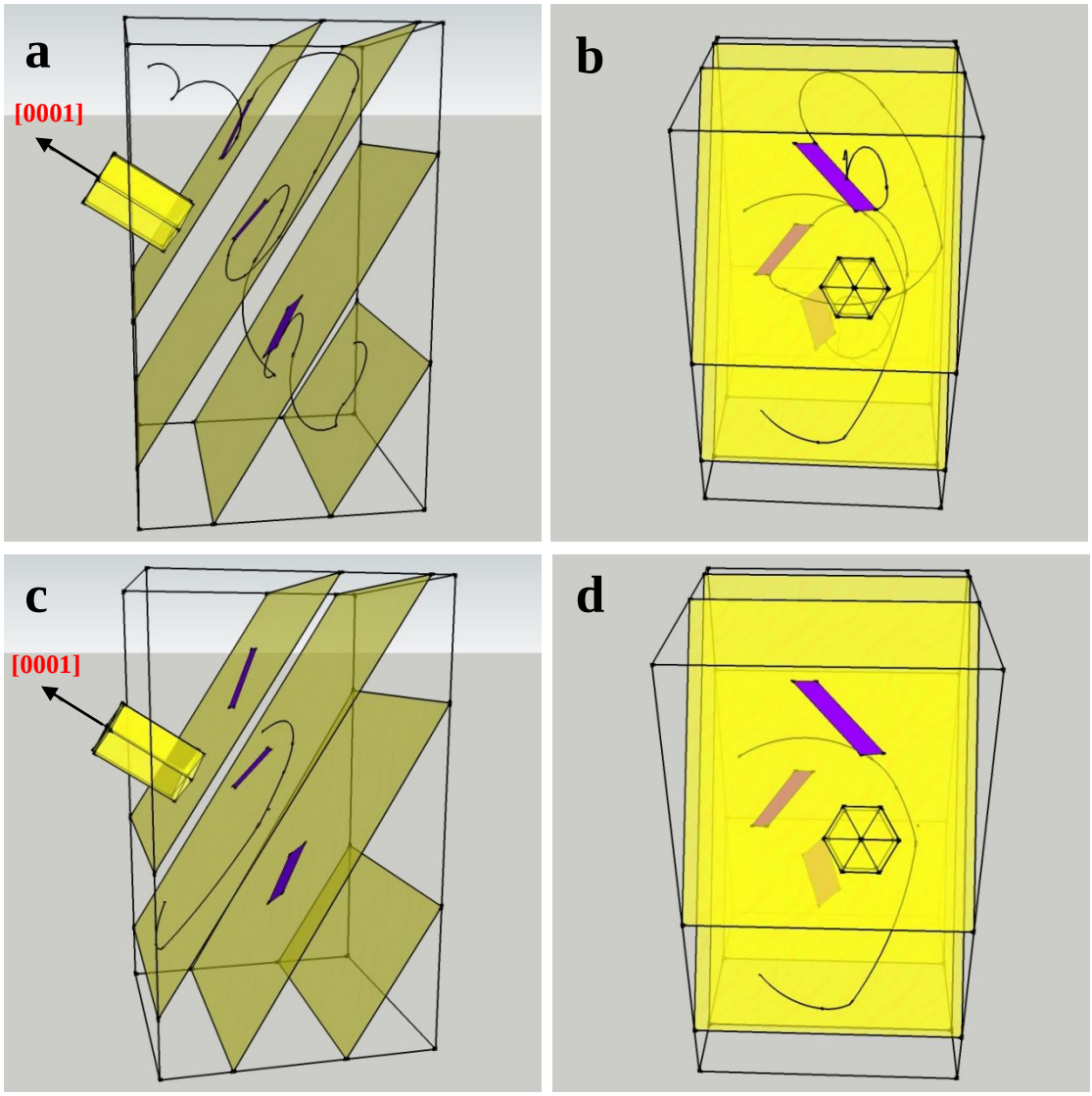

Figure 6.13. 3D schematic diagrams showing the two dislocations separately. (a) and (b) show the morphology of the spiral dislocation; (c) and (d) show the morphology of the U shaped dislocation. (a) and (c), (b) and (d) have the same viewing directions, respectively.In (c) and (d), the view direction is along the [0001].

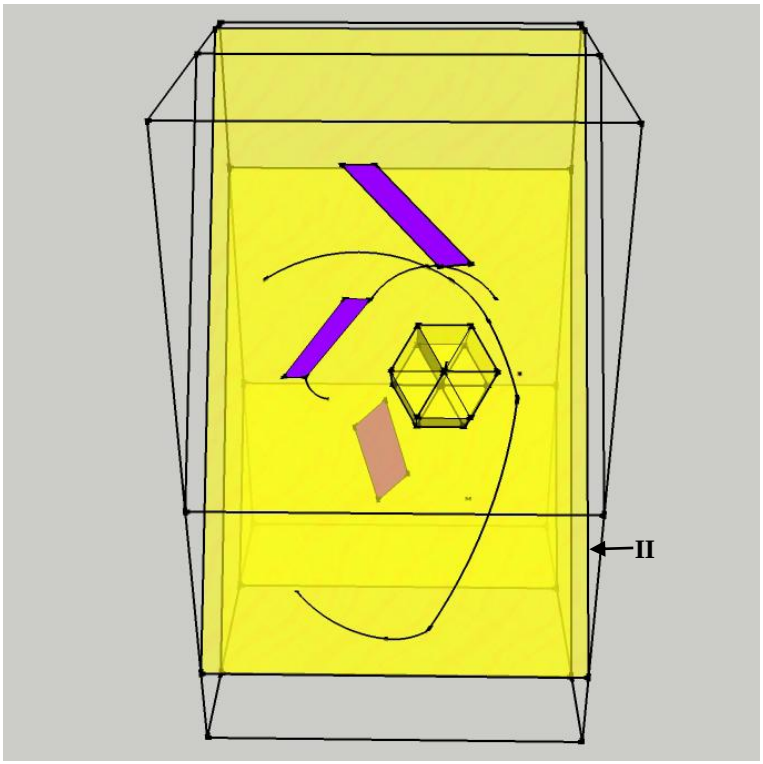

Figure 6.14. A schematic diagram showing the interaction between the spiral dislocation on the basal plane II and the U shaped dislocation.

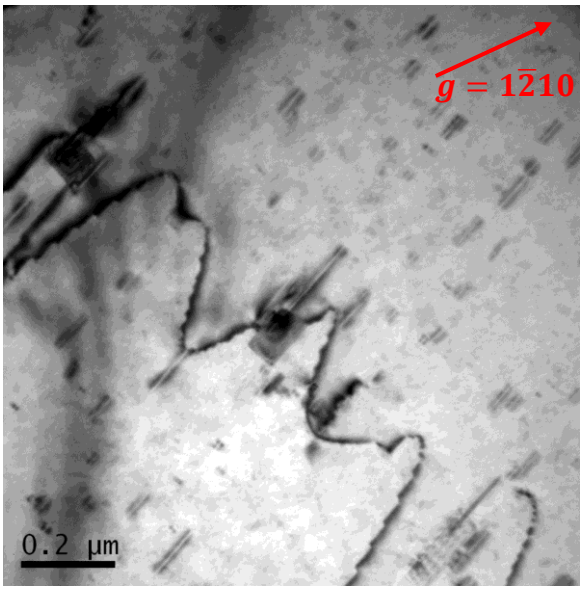

Figure 6.15. A BF-TEM image showing the stair-like structure of a W shaped dislocation in AZ91 after 0.6 % compression and ageing for 0.5h. $g = 1\bar{2}10$ (marked with a red arrow) and BD~$[10\bar{1}0]_m$.

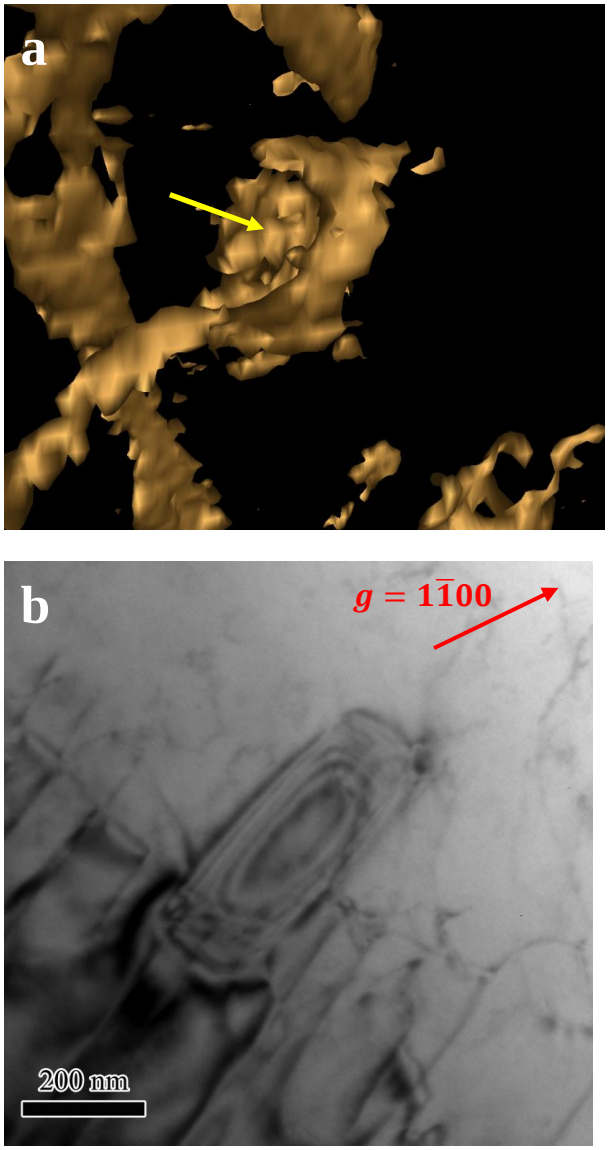

Figure 6.16. (a) A reconstructed volume showing that some parts of the reconstructed precipitate C are missing. The yellow arrow shows a hollow. (b) A typical BF-TEM image showing the strain contrast between the CPs and the Mg matrix in AZ91 aged at 200℃ for 1h. BD ~ $[11\bar{2}0]$.

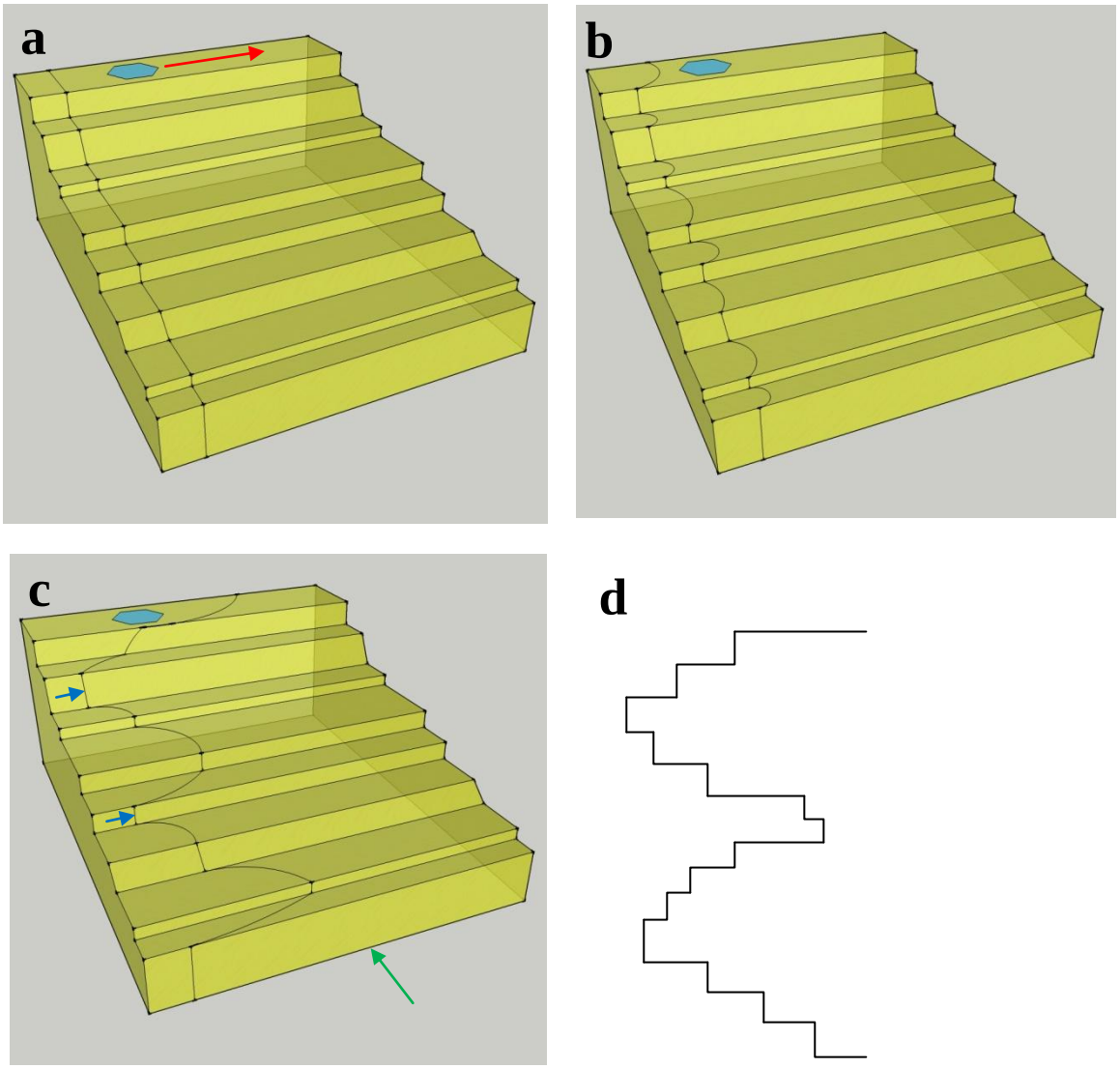

Figure 6.17. Schematic diagrams showing the formation of a spiral dislocation. The blue hexagon indicates the basal plane of the hcp unit cell. (a) A dislocation is introduced, which is composed of segments on both basal and non-basal planes. The red arrow indicates the Burgers vector and the slip direction. (b) The basal segments glide easily on the basal plane. (c) The movement of the non-basal segments begin, but with a low mobility. Some of them even remain still, as indicated with the blue arrows. (d) The dislocation presents a W shape when it is viewed along the basal plane in the direction of the green arrow in (c).

Chapter 7 Conclusions and suggestions for future work

7.1 Conclusions

The results and discussion in this thesis lead to the following conclusions:

N_V in aged AZ91

1 N_V measured in the current work is above the range in Celotto's work by one to two orders of magnitude. The $[11\bar{2}0]$ viewing direction and the existence of Al-Mn-(Mg) nano-sized particles are the main cause.

2 The crystallographic direction used for viewing the precipitates affects the overlap of the precipitates when N_V reaches a certain level. Compared with [0001], $[11\bar{2}0]$ can significantly reduce such overlap.

3 Compared with most precipitation hardenable Al alloys, N_V in AZ91 is still low. No GP zones and the relatively low diffusion rate of Al in Mg are responsible for this issue.

Modification for precipitation hardening mode of AZ91

4 In Hutchinson et al's modelling of the precipitation hardening, DP is replaced by CP, rather than being ignored. Here the DPs are ignored and CPs accord with the

metallographic evidence. With this N_V, the calculated strength from the current model is still close to the experimental results.

Precipitation hardening of the pre-deformed AZ91

5 Pre-deformation increases the hardness of the aged AZ91. 10% rolling reduction is considered to be the optimum amount of pre-deformation under the current experimental conditions, increasing the peak hardness of AZ91 by 13.7%.

6 Twins play an important role in the precipitation of deformed AZ91. Although they impede discontinuous precipitation and increase the region occupied by CPs, they promote nucleation and coarsening of $Mg_{17}Al_{12}$ nodules, which decrease the strength. The high density dislocations also increases the N_V of the CPs in the deformed AZ91.

7 Ageing of deformed AZ91 at 200℃ actually involves both precipitation (hardening) and recovery (softening). The hardness is a combined result of both hardening and softening.

Characterization of Al-Mn-(Mg) QC particles

8 Ultrafine Al-Mn-(Mg) particles have been found in sand cast AZ91. They are rod shaped and have both two-fold and pseudo five-fold symmetry. Compared with many other Al-Mn intermetallic phases in Mg-Al alloys containing Mn, these Al-Mn-(Mg) particles are small (20-200 nm).

9 Both tilting experiment and electron tomography indicate these particles are rod-shaped with either globular or a rounded rectangluar cross section. Because there is no well-defined orientation between these particles and the Mg matrix, the particles are oriented randomly, resulting in 2D projections with various shapes along a given beam direction.

10 The structure and morphology of these particles indicate that they are decagonal quasicrystals with a partially crystalline structure. A rough chemical composition, $(Al_{6.52}Mn)_{1-x}Mg_x$ ($x<0.13$), has been obtained for them, though the existence of Mg within these particles is still debatable.

Roles of Al-Mn-(Mg) QC particles in heat treatment and strength of AZ91

11 These QC particles are stable during a solution treatment at 420℃ for 72h. During ageing, $Mg_{17}Al_{12}$ precipitates on pre-existing ultrafine Al-Mn-(Mg) particles have been observed. If introduced as an even distribution and in a larger amount, these ultrafine Al-Mn-(Mg) particles should improve the mechanical performance of AZ91 at both room and elevated temperatures.

3D characterization of particles and dislocations

12 In the HAADF-STEM tomography, the end-to-end connection between the CPs and the Al-Mn-(Mg) particles and the rod shape of the Al-Mn-(Mg) are confirmed.

13 In the BF-STEM tomography, a dislocation network in the compressed AZ91 is determined in 3D. The W-shaped dislocations are found to have a spiral structure composed of lots of basal and non-basal segments. Such a spiral structure might result from the different mobility of the basal and non-basal segments during the movement of the dislocations.

7.2 Suggestions for further work

Based on the experimental results and discussion, further research may be of interest in some specific areas.

1 In the modelling of the strength of AZ91, two issues can still be improved. Firstly, the contribution of CPs to the strength of AZ91 is obtained by reducing the calculated strength from the equation by 30% (the fraction of DP area). This is just a rough approximation and whether the reduction of the strength is necessarily proportional to the area fraction of the DP still needs to be carefully investigated. Meanwhile, the total strength in the calculation is the sum of all the mechanisms. The interaction between different strengthening mechanisms needs also to be considered.

2 According to the current and previous studies [24, 45, 47], different preferential precipitation situations for $Mg_{17}Al_{12}$ happen with different defects and second phases in AZ91, as shown in Table 7.1. The different precipitation cases are due to different strains and Al concentration around these features. It would be of interest to study why they have different effects on the $Mg_{17}Al_{12}$ precipitation, since this can provide some suggestions for tailoring the microstructure to improve the strength of AZ91.If some metal or particle addition can introduce a large number of particles similar to Al-Mn-(Mg) QCs, the mechanical properties of AZ91 could be improved significantly. On the contrary, the nodules of $Mg_{17}Al_{12}$ should be avoided.

3 According to §5.4, the nano sized Al-Mn-(Mg) particles benifit the strength of AZ91, but the temperature or temperatures over which they formed during solidification are still unknown. This could be worth studying, because it can point towards the introduction of more such nano particles in AZ91 by more Mn addition.

4 According to §2.6, most Al-Mn QCs are not stable, but can be stabilized by addition of a third element. Here the nano-sized Al-Mn-(Mg) is stable during heat treatment, and therefore it may be of fundamental interest to investigate whether a Mg addition could affect the stability of the Al-Mn QCs. In addition, it would be also worth studying the orientation relationship between the Al-Mn-(Mg) QC particles and the CPs, since this may indicate the formation mechanism of CPs on the Al-Mn-(Mg) QCs.

5 In the electron tomography, a combination of DF and HAADF tomography could be tried to reproduce both the CP and Al-Mn-(Mg) particles. This may help to image both of them in 3D together.

Table 7.1. Different preferential precipitation situations for $Mg_{17}Al_{12}$ in AZ91 according to the current and previous studies [24, 45, 47]

Types of second phase or defects in AZ91	Effect on $Mg_{17}Al_{12}$ precipitation	Reference
Nano-sized Al-Mn-(Mg) QC particles	Continuous precipitation happens on these particles	Current study
SiC particles	Multiple nodules of $Mg_{17}Al_{12}$ precipitate on a SiC particle	[45]
Mg-Zn-Y-Mn QC particles	No precipitation reported	[47]
Al_8Mn_5	No precipitation found	Current study
Dislocations	Multiple CPs along a dislocation	[24]
Twinning	Multiple nodule $Mg_{17}Al_{12}$ precipitate along a twin boundary	Current study

Appendices

Appendix A: Symmetry restriction of crystals

Crystals have only 1, 2, 3, 4 and 6 fold symmetries and a five-fold symmetry is not allowed. Such a symmetry restriction is due to the lattice periodicity. Since each lattice point in crystal is identical, there is n-fold symmetry for each lattice point. It is assumed that A, B and C are three adjacent lattice points in a crystallographic plane normal to an n-fold symmetry axis, as shown in Figure A.1 (a) [138]. If the crystal are rotated clockwise through B for $\theta = \frac{2\pi}{n}$, A should reach another lattice point A′. If the crystal are rotated anti-clockwise through B for $\theta = \frac{2\pi}{n}$, C should reach another lattice point C′. Therefore,

$$|A'C'| = 2\times \cos(2\pi/n) \times |A\,B| = m \times |A\,B| \text{ (m integer)} \qquad \text{(Equation A.1)}$$

Thus

$$2\times \cos(2\pi/n) = m \qquad \text{(Equation A.2)}$$

Since $-1 \leq \cos(2\pi/n) \leq 1$, $\cos(2\pi/n) = 1, \pm 1/2, \pm 1$.

So m=1, 2, 3, 4, 6. This means that only these symmetries are allowed for crystals [138].

Meanwhile, this can also be understood using tiling of the unit cells. Taking five-fold

symmetry for example, unit cells with a pentagon shape, as shown in Figure A.1 (b), can never be assembled to fill completely space between them [69].

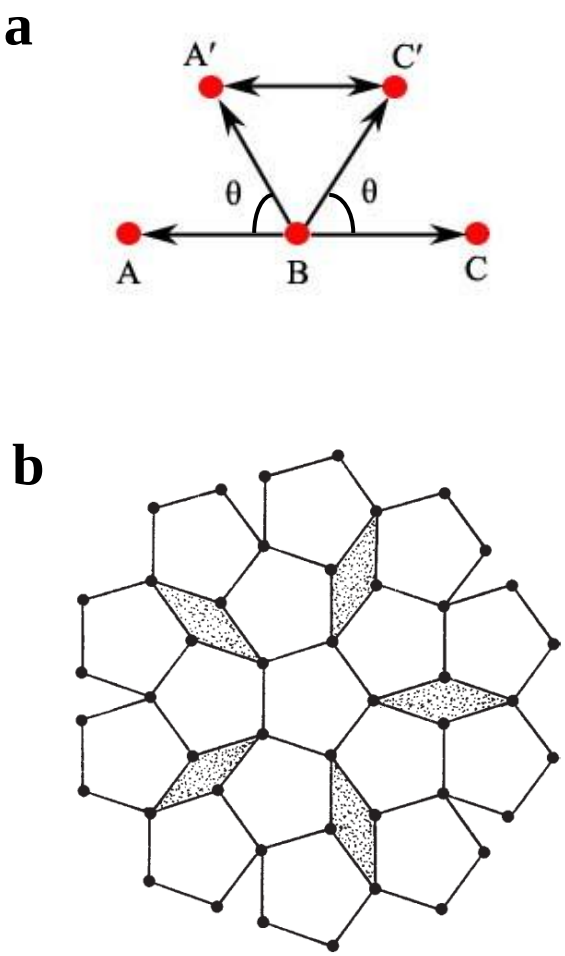

Figure A. 1 (a) Lattice points (A, B, C, A′ and B′) in a plane whose normal has n-fold symmetry; (b) Regular pentagons are assembled and the space between them cannot be filled.

Appendix B: How to tilt nano-sized Al-Mn-(Mg) particles

Some suggestions on how to tilt and perform SAD on nano-sized particles will be given in this section.

Figure B.1 shows a series of diffraction patterns from a typical Al-Mn-(Mg) particle, when it becomes dark during random tilting. Figure B.1 (a) shows an SAD pattern from the particle. Some diffraction spots from surrounding matrix are also involved in this image, but they can be distinguished according to a SAD pattern from the nearby matrix, as shown in Figure B.1 (b). Figure B.1 (c) shows a convergent beam electron diffraction (CBED) pattern from the particle. In contrast to the SAD pattern, the diffraction spots from the matrix are excluded from the CBED pattern, but the overlapping of the discs is evident. This phenomenon is even worse in some zone axes, such as the situation in Figures 5.8 (a) and (b). Similarly to the SAD pattern, few sharp Kikuchi lines can be found in the CBED pattern. Figure B.1 (d) illustrates the Kikuchi lines of the particle deduced from the SAD spots in Figure B.1 (a).

Due to the small size of the Al-Mn-(Mg) particle, the Kikuchi band of the particles, which normally occurs over a certain thickness range, is very weak, even in CBED patterns, as shown in Figure B.1 (c). In most areas of the sample, the Kikuchi bands from the matrix are much sharper than those of the particle. This makes it difficult to find the particle zone axes using a Kikuchi map. According to the author's experience, the following steps may be helpful to resolve this problem. Firstly, as mentioned in

the last paragraph, large particles close to the hole of the TEM foil should be selected. This can reduce the signal from the Mg matrix and make the Kichuchi band and diffraction pattern from the particles easy to distinguish. Secondly, the particle is tilted randomly and the sample positions when the particles become dark recorded. In these cases, the particles are either close to a zone axis, as shown in Figure B.1, or at least in a two beam condition. This provides at least a clear Kikuchi band or diffraction spot, so it would be better to start tilting from one of these positions. If the Kikuchi band from the particle is still not strong enough to guide the tilting, diffraction spots can be used to deduce the Kikuchi lines, as shown in Figure B.1 (d). Finally, the particle should be tilted using the direction of the x and y tilts in the Kikuchi map. As shown in Figure B.2, X or Y tilting of the stage is actually along a plane whose normal is one of the tilt axes. In diffraction mode, two such supposed planes indicate two “Kikuchi lines” in the Kikuchi map, likely to any atomic plane of a crystal. Since the X and Y tilt axes are fixed, the orientation of the plane is also fixed. Therefore, during X or Y tilting in a microscope, the Kikuchi map on the screen always moves along such a fixed “Kikuchi line” relative to the incident beam. Normally, the Kikuchi bands are considered as roads in orientation-space and the incident beam is understood as a car moving along the roads during tilting. If the incident beam is considered to be tilted relative to the “fixed” sample, the direction of motion of the transmitted beam relative to the Kikuchi map is also fixed. Figure B.3 illustrates the moving directions of the transmitted beam direction relative to the Kikuchi map

during x and y tilting in our JEOL 2100, indicated by orange and blue arrows respectively. The red line in Figure B.3 indicates the direction of one Kikuchi band in Figure B.1 (d). One can use +X plus –Y tilt or –X plus +Y tilt to make the transmitted beam follow the Kikuchi band and finally arrive at another zone axis.

During tilting, the key point is to keep the transmitted beam on the desired Kikuchi band all the time. In order to achieve this, on the one hand, the amounts of X and Y tilt need to be well controlled. For instance, in the case of Figure B.3, the Y tilt is much less than the X tilt, since $\tan(13° - 5.1°) \approx 0.1405$. On the other hand, it would be better to tilt the particles in image mode rather than diffraction mode. In diffraction mode, the Kikuchi line of the particle is too weak to provide the orientation information. In image mode, two phenomena may be helpful to control the tilting. One is the contrast of the particle. Once it decreases, this may indicate that the particle has moved away from the original two beam condition. When it increases, this means that it is close to a zone axis. The other is that sometimes a bend contour on the particles indicates whether the particle is in a two beam condition more or less, as shown in Figure B.4.

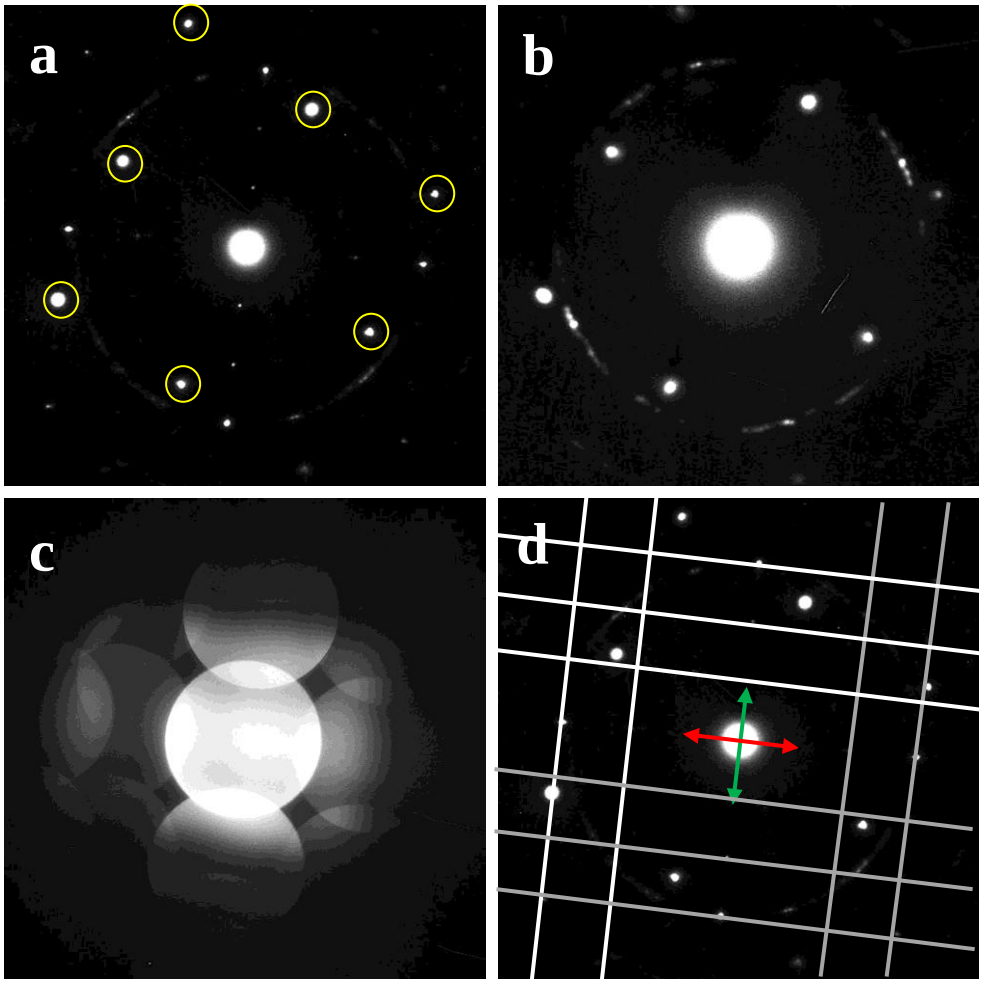

Figure B.1. Diffraction patterns from an Al-Mn-(Mg) particle when it becomes dark during random tilting: SAD patterns from (a) both the particle and matrix, (b) the matrix only; (c) CBED from the particles; (d) Kikuchi lines deduced from the diffraction pattern in (a). The circles indicate the diffraction spots from the matrix according to (b).

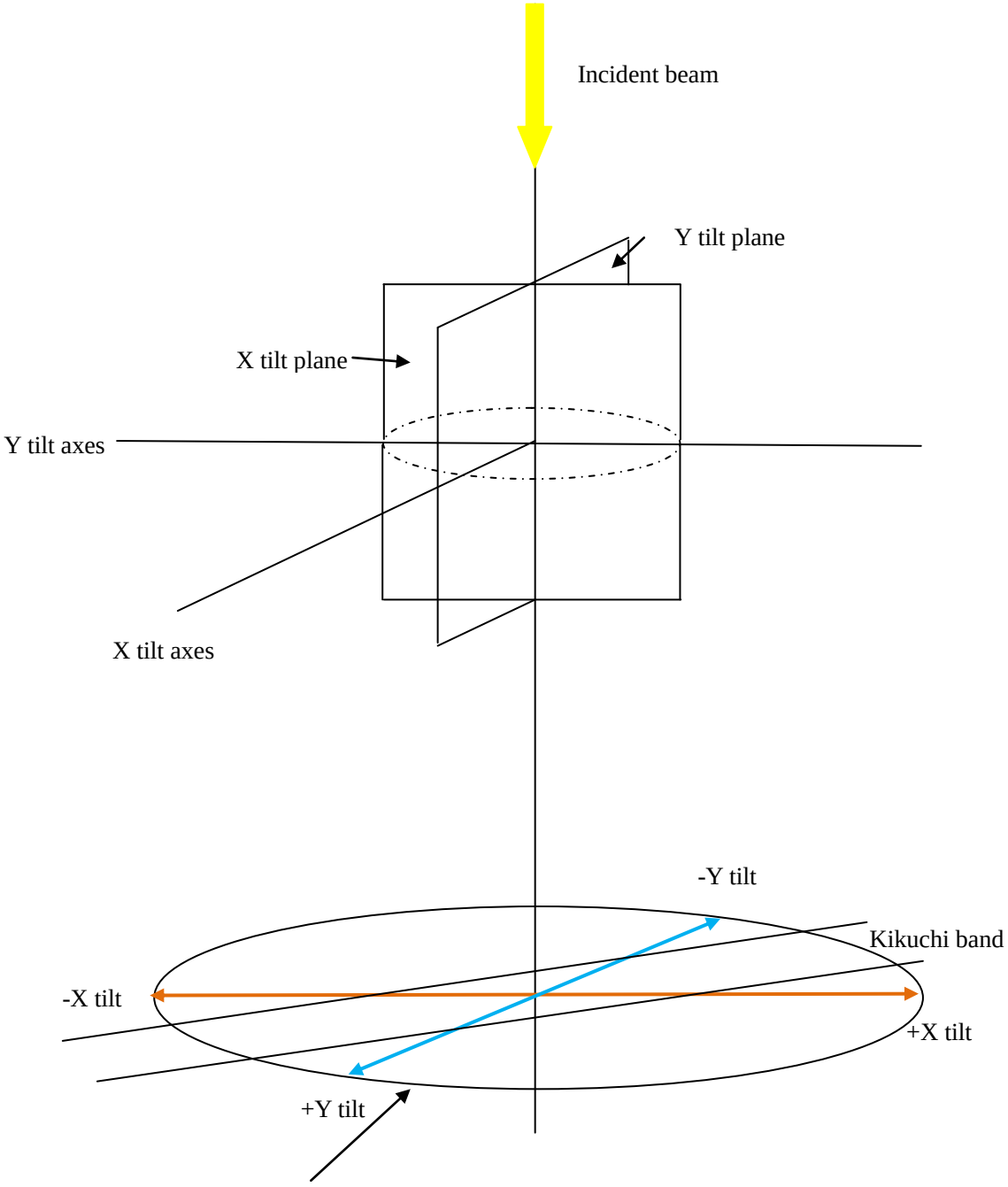

Figure B.2. A schematic diagram showing the relationship between the tilt axes, tilt plane and the direction in which the Kikuchi map moves with regards to the transmitted beam during tilting.

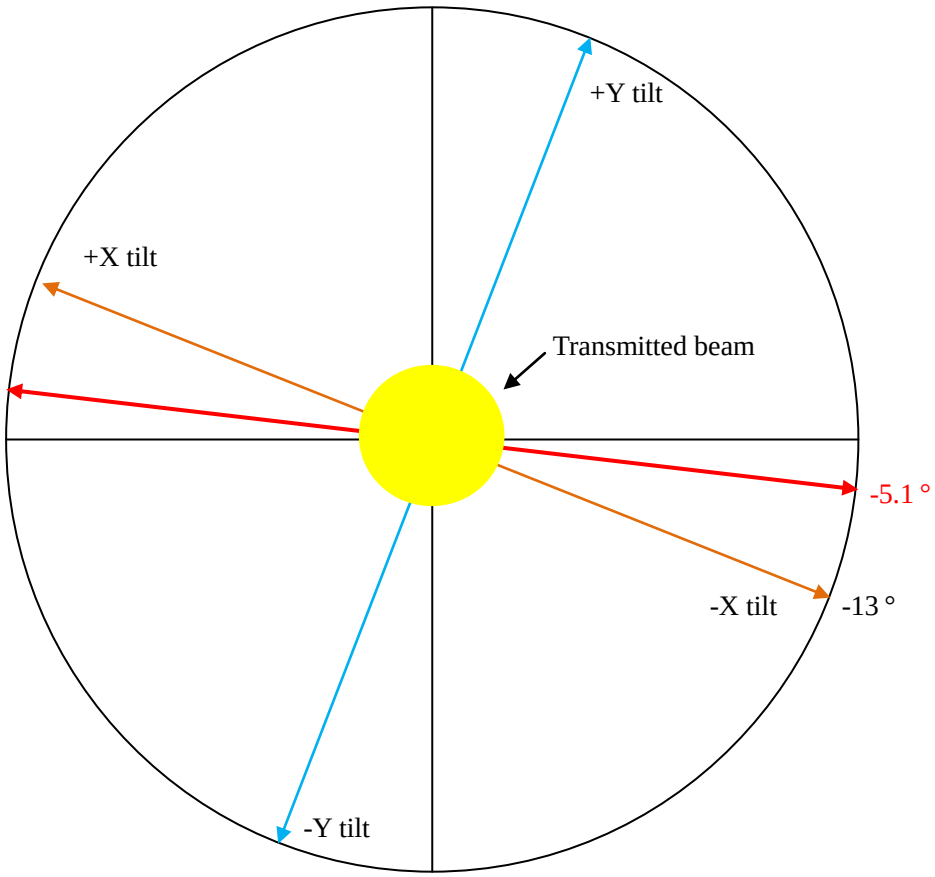

Figure B.3. An example showing how to tilt a particle along one of its Kikuchi bands using our JEOL 2100 HT. The thick red line indicates the direction of the desired Kikuchi band. The orange and blue lines indicate the direction of motion of the incident beam relative to the Kikuchi map. (Supposing that the sample is fixed and the electron beam is tilted.)

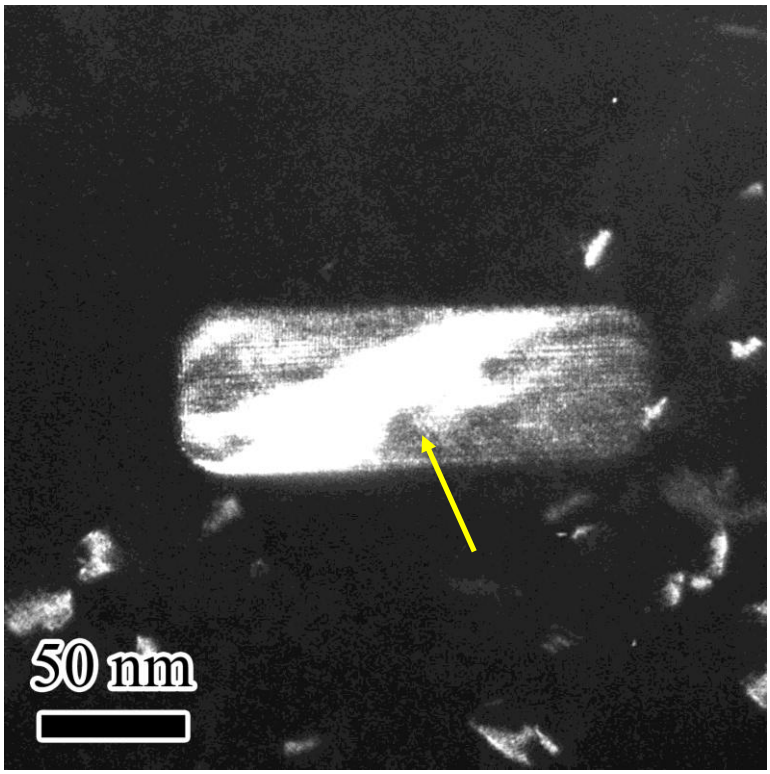

Figure B.4. A TEM dark field image showing the bend contour (indicated by a yellow arrow) on a rod-shaped Al-Mn-(Mg) particle. Some fringes indicating the lattice of the particle are also can be seen.

Appendix C: Design of TEM tomography holder

There are various TEM specimen holders, and they are designed with different functions for specimen analysis, including cooling, cryo-transfer, vacuum transfer, heating, multiple specimens, straining and tomography. Fischione instruments [139] and Gatan [140] are two major companies sharing the market of TEM specimen holders.

TEM specimen holders for tomography can be divided into 3 versions: single axis (α high tilt), dual axis (α high tilt + sample rotation) and triple axis (α high tilt + sample rotation + β tilt). The motion of each axis is illustrated in Figure 3.7. There have been various single and dual axis tomography holders produced by Fischione instruments [139] and Gatan [140]. The only triple axis tomography holder, called HATA (High Angle Triple Axis) holder, was designed by Hata et. al [106] and manufactured by Met-Build [105] so far.

In the current work, a dual axis tomography holder is designed. It features high tilt along the x axis and large angle rotation along the z axis inside the microscope. The rotation mechanism and the assembly of the holder are shown in attached videos. This holder is supposed to be used in two ways: (1) the 90 ^{o} rotation can be used for dual axis tomography [141] and this can reduce the missing wedge during reconstruction; (2) rotation can be also used for the diffraction alignment for some specific samples

whose foil normals are identical to a desired zone axis.

References

[1] A. Luo, M. Pekguleryuz, Journal of Materials Science, 29 (1994) 5259-5271.

[2] B. Mordike, T. Ebert, Materials Science and Engineering: A, 302 (2001) 37-45.

[3] M. Bamberger, G. Dehm, Annu. Rev. Mater. Res., 38 (2008) 505-533.

[4] Z. Yang, J. Li, J. Zhang, G. Lorimer, J. Robson, Acta Metallurgica Sinica (English Letters), 21 (2008) 313-328.

[5] S. Celotto, Acta materialia, 48 (2000) 1775-1787.

[6] C.R. Hutchinson, J.-F. Nie, S. Gorsse, Metallurgical and Materials Transactions A, 36 (2005) 2093-2105.

[7] M. Weyland, P.A. Midgley, Materials Today, 7 (2004) 32-40.

[8] E.F. Emley, Principles of Magnesium Technology, Pergamon Press, New York, 1966.

[9] H.E. Friedrich, B.L. Mordike, Magnesium technology: metallurgy, design data, applications, Springer, 2006.

[10] B.L. Mordike, T. Ebert, Materials Science and Engineering: A, 302 (2001) 37-45.

[11] C.S. Roberts, Magnesium and its Alloys, Wiley, 1960.

[12] R.V. Mises, ZAMM - Journal of Applied Mathematics and Mechanics / Zeitschrift für Angewandte Mathematik und Mechanik, 8 (1928) 161-185.

[13] A. Seeger, Defects in Crystalline Solids, Report of Bristol Conference (2nd edition), Physical Society, London, 1955.

[14] M. Barnett, Materials Science and Engineering: A, 464 (2007) 1-7.

[15] M. Barnett, Materials Science and Engineering: A, 464 (2007) 8-16.

[16] M.M. Avedesian, H. Baker, Magnesium and Magnesium Alloys – ASM Specialty Handbook, ASM International, Materials Park, OH 1999.

[17] S. Celotto, T.J. Bastow, Acta materialia, 49 (2001) 41-51.

[18] F.E. Hauser, C.D. Starr, L. Tietz, J.E. Dorn, Trans. ASM, 47 (1955) 102.

[19] T. Zhu, Z.W. Chen, W. Gao, Materials Characterization, 59 (2008) 1550-1558.

[20] Y. Wang, M. Xia, Z. Fan, X. Zhou, G. Thompson, Intermetallics, 18 (2010) 1683-1689.

[21] F. Czerwinski, Z. Trojanova, Z. Szaraz, P. Palcek, M. Chalupova, Croatia: In Tech, 32 (2011) 56-59.

[22] A. Guinier, Nature, 142 (1938) 569-570.

[23] G. Preston, Nature, 142 (1938) 2.

[24] J.B. Clark, Acta Metallurgica, 16 (1968) 141-152.

[25] K.N. Braszczyńska-Malik, Journal of Alloys and Compounds, 477 (2009) 870-876.

[26] J. Nie, X. Xiao, C. Luo, B. Muddle, Micron, 32 (2001) 857-863.

[27] D.A. Porter, K.E. Easterling, Phase transformations in metals and alloys, CRC Press, 1992.

[28] A. Crawley, K. Milliken, Acta Metallurgica, 22 (1974) 557-562.

[29] M.X. Zhang, P.M. Kelly, Scripta Materialia, 48 (2003) 647-652.

[30] D. Duly, W.-Z. Zhang, M. Audier, Philosophical Magazine A, 71 (1995) 187-204.

[31] J. Gjönnes, T. Östmoe, Z. Metall., 61 (1970) 604-606.

[32] D. Duly, Acta metallurgica et materialia, 41 (1993) 1559-1566.

[33] J. Nie, Scripta Materialia, 48 (2003) 1009-1015.

[34] F. Findik, Journal of Materials Science Letters, 17 (1998) 79-83.

[35] D. Duly, J. Simon, Y. Brechet, Acta metallurgica et materialia, 43 (1995) 101-106.

[36] S. Changjiang, H. Qingyou, Z. Qijie, China Foundry, 6 (2009) 93-103.

[37] F.E. Hauser, P.R. London, J.E. Dorn, AIME Transacitions, 206 (1956) 589-593.

[38] C.H. Cáceres, C.J. Davidson, J.R. Griffiths, C.L. Newton, Materials Science and Engineering: A, 325 (2002) 344-355.

[39] C. Cáceres, D. Rovera, Journal of Light Metals, 1 (2001) 151-156.

[40] A. Akhtar, E. Teghtsoonian, Acta Metallurgica, 17 (1969) 1339-1349.

[41] E. Orowan, Sympsium on the International Stresses, Inst. of Metal, London, 1947, 451.

[42] M. Gharghouri, G. Weatherly, J. Embury, J. Root, Philosophical Magazine A, 79 (1999) 1671-1695.

[43] L.M. Brown and R.K. Ham: in "Strengthening Methods in Crystals", A. Kelly and R.B. Nicholson, eds., Elsevier, London, 1971, 9-135.

[44] L. Brown, D. Clarke, Acta Metallurgica, 25 (1977) 563-570.

[45] T. Laser, M. Nürnberg, A. Janz, C. Hartig, D. Letzig, R. Schmid-Fetzer, R. Bormann, Acta materialia, 54 (2006) 3033-3041.

[46] S. Barbagallo, H. Laukli, O. Lohne, E. Cerri, Journal of Alloys and Compounds, 378 (2004) 226-232.

[47] J. Zhang, L. Pei, H. Du, W. Liang, C. Xu, B. Lu, Journal of Alloys and Compounds, 453 (2008) 309-315.

[48] A. Deschamps, F. Livet, Y. Brechet, Acta materialia, 47 (1998) 281-292.

[49] P. Ratchev, B. Verlinden, P. De Smet, P. Van Houtte, Scripta materialia, 38 (1998) 1195-1201.

[50] L. Ber, Materials Science and Engineering: A, 280 (2000) 91-96.

[51] N. Ünlü, B. Gable, G. Shiflet, E. Starke Jr, Metallurgical and Materials Transactions A, 34 (2003) 2757-2769.

[52] W.-J. Liang, Q.-L. Pan, Y.-B. He, Z.-M. Zhu, Y.-F. Liu, Materials science and technology, 23 (2007) 395-399.

[53] A. Khan, J. Robinson, Journal of Microscopy, 232 (2008) 534-538.

[54] D. Duly, M. Audier, Y. Brechet, Scripta Metallurgica et Materialia: (United States), 29 (1993) 1593-1596.

[55] I. Polmear, Light alloys: from traditional alloys to nanocrystals, Butterworth-Heinemann, 2005.

[56] J. Hirsch, G. Gottstein, B. Skrotzki, Aluminium Alloys, Wiley-VCH, 2008.

[57] V.Y. Gertsman, J. Li, S. Xu, J.P. Thomson, M. Sahoo, Metallurgical and Materials Transactions A: Physical Metallurgy and Materials Science, 36 (2005) 1989-1997.

[58] P. Cao, M. Qian, D.H. StJohn, Scripta Materialia, 54 (2006) 1853-1858.

[59] S. Lun Sin, D. Dubé, R. Tremblay, Materials Characterization, 58 (2007) 989-996.

[60] D. Shechtman, I. Blech, D. Gratias, J.W. Cahn, Physical Review Letters, 53 (1984) 1951-1953.

[61] L. Bendersky, Physical Review Letters, 55 (1985) 1461-1463.

[62] D. Shechtman, I.A. Blech, Metallurgical Transactions A, 16 (1985) 1005-1012.

[63] K. Kimura, T. Hashimoto, K. Suzuki, K. Nagayama, H. Ino, S. Takeuchi, Journal of the Physical Society of Japan, 55 (1986) 534-543.

[64] L.A. Bendersky, Materials Science and Engineering, 99 (1988) 331-334.

[65] O. Kido, H. Suzuki, Y. Kimura, T. Sato, Y. Saito, C. Kaito, Physica E: Low-dimensional Systems and Nanostructures, 25 (2005) 619-624.

[66] H.-R. Trebin, Quasicrystals, Wiley-VCH, 2006.

[67] C. Kittel, P. McEuen, Introduction to solid state physics, Wiley New York, 1996.

[68] F. Samavat, M.H. Tavakoli, S. Habibi, B. Jaleh, P.T. Ahmad, Open Journal of Physical Chemistry, 2 (2012) 7-14.

[69] P.W. Stephens, A.I. Goldman, Scientific American, 264 (1986) 10.

[70] W. Steurer, Chemical Society Reviews, 41 (2012) 6719-6729.

[71] R. Penrose, Chapter 2 - Tilings and Quasi-Crystals: a Non-Local Growth Problem?, in: V.J. Marko (Ed.) Aperiodicity and Order, Elsevier, 1989, pp. 53-79.

[72] Quasicrystals, available: http://www.jcrystal.com/steffenweber/qc.html (13 April 2013).

[73] S. Ranganathan, K. Chattopadhyay, Annual Review of Materials Science, 21 (1991) 437-462.

[74] S. Ranganathan, K. Chattopadhyay, A. Singh, K.F. Kelton, Progress in Materials Science, 41 (1997) 195-240.

[75] J. Guo, T. Sato, E. Abe, H. Takakura, A. Tsai, Philosophical Magazine Letters, 80 (2000) 495-502.

[76] A.-P. Tsai, Accounts of Chemical Research, 36 (2003) 31-38.

[77] T. Ishimasa, H.-U. Nissen, Y. Fukano, Physical Review Letters, 55 (1985) 511-513.

[78] D. Bae, M. Lee, K. Kim, W. Kim, D. Kim, Journal of Alloys and Compounds, 342 (2002) 445-450.

[79] A. Singh, M. Nakamura, M. Watanabe, A. Kato, A. Tsai, Scripta Materialia, 49 (2003) 417-422.

[80] A. Singh, A.P. Tsai, M. Nakamura, M. Watanabe, A. Kato, Philosophical Magazine Letters, 83 (2003) 543-551.

[81] A. Singh, M. Watanabe, A. Kato, A. Tsai, Science and Technology of Advanced Materials, 6 (2005) 895-901.

[82] K. Mihama, Thin Solid Films, 163 (1988) 61-66.

[83] S.-L. Chang, W. Chin, C.-M. Zhang, C. Jenks, P. Thiel, Surface science, 337 (1995) 135-146.

[84] J.-M. Dubois, Chemical Society Reviews, 41 (2012) 6760-6777.

[85] D. Lutz, The Industrial Physicist, 2 (1996) 26-31.

[86] A. Inoue, H. Kimura, T. Zhang, Materials Science and Engineering: A, 294 (2000) 727-735.

[87] J. Frank, Electron tomography: methods for three-dimensional visualization of structures in the cell, Springer Science+ Business Media, 2006.

[88] J. Banhart, Advanced tomographic methods in materials research and engineering, Oxford University Press, New York, 2008.

[89] J. Radon, Ber. der Sachische Akademie der Wissenschaften Leipzig,(Germany), 69 (1917) 262-277.

[90] P. Midgley, M. Weyland, Ultramicroscopy, 96 (2003) 413-432.

[91] G. Möbus, B.J. Inkson, Materials Today, 10 (2007) 18-25.

[92] J. Sharp, Electron tomography of defects, Ph. D thesis, University of Cambridge, 2010.

[93] H. Zhang, A. Takaoka, K. Miyauchi, Review of scientific instruments, 69 (1998) 4008-4009.

[94] I. Arslan, J.R. Tong, P.A. Midgley, Ultramicroscopy, 106 (2006) 994-1000.

[95] R. Phelan, J. Holmes, N. Petkov, Journal of Microscopy, 246 (2012) 33-42.

[96] X. Xu, Z. Saghi, R. Gay, G. Möbus, Nanotechnology, 18 (2007) 225501.

[97] K. Inoke, K. Kaneko, M. Weyland, P.A. Midgley, K. Higashida, Z. Horita, Acta materialia, 54 (2006) 2957-2963.

[98] K. Kaneko, K. Inoke, K. Sato, K. Kitawaki, H. Higashida, I. Arslan, P. Midgley,

Ultramicroscopy, 108 (2008) 210-220.

[99] J. Barnard, J. Sharp, J. Tong, P. Midgley, Science, 313 (2006) 319-319.

[100] D.B. Williams, C.B. Carter, Transmission Electron Microscopy: A Textbook for Materials Science, Springer US, 1996.

[101] J. Sharp, J. Barnard, K. Kaneko, K. Higashida, P. Midgley, Dislocation tomography made easy: a reconstruction from ADF STEM images obtained using automated image shift correction, in: Journal of Physics: Conference Series, IOP Publishing, 2008, pp. 012013.

[102] M. Tanaka, K. Higashida, K. Kaneko, S. Hata, M. Mitsuhara, Scripta Materialia, 59 (2008) 901-904.

[103] C. Chuang, Microstructure and mechanical properties of the ECAP processed AZ91 and AZ80, Ph. D thesis, University of Auckland, 2009.

[104] ImageJ, available: http://rsbweb.nih.gov/ij/ (18 April 2013).

[105] Mel-Build, available: http://melbuildhost.ehost-services124.com/ (13 April 2013).

[106] S. Hata, H. Miyazaki, S. Miyazaki, M. Mitsuhara, M. Tanaka, K. Kaneko, K. Higashida, K. Ikeda, H. Nakashima, S. Matsumura, Ultramicroscopy, 111 (2011) 1168-1175.

[107] IMOD, available: http://bio3d.colorado.edu/imod/ (18 April 2013).

[108] J.R. Kremer, D.N. Mastronarde, J.R. McIntosh, Journal of structural biology, 116 (1996) 71-76.

[109] E. Nembach, Particle strengthening of metals and alloys, Wiley-Interscience, 1997.

[110] P. Kelly, A. Jostsons, R. Blake, J. Napier, Physica status solidi (a), 31 (1975) 771-780.

[111] D. Bailey, W. Flanagan, Philosophical Magazine, 15 (1967) 43-49.

[112] N. Stanford, J. Geng, Y. Chun, C. Davies, J. Nie, M. Barnett, Acta materialia, 60 (2012) 218-228.

[113] W.-J. Lai, Y.-Y. Li, Y.-F. Hsu, S. Trong, W.-H. Wang, Journal of Alloys and Compounds, 476 (2009) 118-124.

[114] C. Cáceres, P. Lukáč, Philosophical Magazine, 88 (2008) 977-989.

[115] N. Hort, Y.-D. Huang, K.U. Kainer, Advanced Engineering Materials, 8 (2006) 235-240.

[116] U. Dahmen, Acta Metallurgica, 30 (1982) 63-73.

[117] R.E. Smallman, R.J. Bishop, Modern physical metallurgy and materials engineering, Butterworth-Heinemann, 1999.

[118] J. Nie, B. Muddle, Acta materialia, 48 (2000) 1691-1703.

[119] K. Yamada, Y. Okubo, M. Shiono, H. Watanabe, S. Kamado, Y. Kojima, Materials transactions, 47 (2006) 1066-1070.

[120] M. Yamasaki, M. Sasaki, M. Nishijima, K. Hiraga, Y. Kawamura, Acta materialia, 55 (2007) 6798-6805.

[121] T. Ozaki, Y. Kuroki, K. Yamada, H. Hoshikawa, S. Kamado, Y. Kojima,

Materials transactions, 49 (2008) 2185-2189.

[122] S. Brennan, K. Bermudez, N.S. Kulkarni, Y. Sohn, Metallurgical and Materials Transactions A, 1-10.

[123] S. Fujikawa, K. Hirano, Materials Science and Engineering, 27 (1977) 25-33.

[124] P. Yang, L.-N. Wang, Q.-G. Xie, J.-Z. Li, H. Ding, L.-L. Lu, International Journal of Minerals, Metallurgy, and Materials, 18 (2011) 338-343.

[125] C.H. Caceres, AFS Transactions, 110 (2002) 1163-1169.

[126] B. Tang, I. Jones, W. Lai, D. Bacon, Philosophical Magazine, 85 (2005) 1805-1817.

[127] K. Ishizuka, Ultramicroscopy, 90 (2002) 71-83.

[128] S. Pennycook, Ultramicroscopy, 30 (1989) 58-69.

[129] T. Walther, C. Humphreys, Journal of crystal growth, 197 (1999) 113-128.

[130] K. Hagihara, A. Kinoshita, Y. Fukusumi, M. Yamasaki, Y. Kawamura, Materials Science and Engineering: A, 560 (2013) 71-79.

[131] M. Kunst, A. Fischersworring-Bunk, G. L'Esperance, P. Plamondon, U. Glatzel, Materials Science and Engineering: A, 510–511 (2009) 387-392.

[132] B. Li, S.P. Joshi, O. Almagri, Q. Ma, K.T. Ramesh, T. Mukai, Acta Materialia, 60 (2012) 1818-1826.

[133] X.H. Shao, Z.Q. Yang, X.L. Ma, Acta Materialia, 58 (2010) 4760-4771.

[134] J. Yan, Y. Sun, F. Xue, S. Xue, Y. Xiao, W. Tao, Materials Science and Engineering: A, 524 (2009) 102-107.

[135] D. Hull, D.J. Bacon, Introduction to dislocations, Butterworth-Heinemann, 2001.

[136] Y. Terada, D. Itoh, T. Sato, Materials Science and Engineering: A, 523 (2009) 214-219.

[137] Y. Terada, D. Itoh, T. Sato, Materials Chemistry and Physics, 117 (2009) 331-334.

[138] C. Giacovazzo, Fundamentals of crystallography, Oxford University Press, USA, 2002.

[139] Fischione Instruments, Inc., available: http://www.fischione.com/ (20 April 2013).

[140] Gatan, Inc., available: http://www.gatan.com/ (20 April 2013).

[141] D.N. Mastronarde, Journal of structural biology, 120 (1997) 343.